3D-Printed Metal-only High-gain Antennas made of Quasi-periodic Arrangements of Waveguide-type Phoenix Cells

Zhihang An

COLLEGE MATHS, TELECOMS
DOCTORAL INFORMATIQUE, SIGNAL
BRETAGNE SYSTEMES, ELECTRONIQUE

INSA INSTITUT NATIONAL DES SCIENCES APPLIQUÉES RENNES

THESE DE DOCTORAT DE

L'INSTITUT NATIONAL DES SCIENCES APPLIQUEES RENNES

ECOLE DOCTORALE N° 601
Spécialité : *Electronique*

Par
« Zhihang AN »

« 3D Printed Metal-only High-gain Antennas made of Quasi-periodic Arrangements of Waveguide-type Phoenix Cells»

Thèse présentée et soutenue à « INSA RENNES », le « 15/05/2023 »
Unité de recherche : IETR
Thèse N° : 23ISAR 11 / D23 - 11

Rapporteurs avant soutenance :

Xavier BEGAUD	Professeur, Télécom ParisTech
Paola PIRINOLI	Professeur, Politecnico Turino Italie
Régis GUINVARC'H	Professeur, Centrale Supélec Paris

Composition du Jury :

Président :	Régis GUINVARC'H	Professeur, Centrale Supélec Paris
Examinateurs :	Xavier BEGAUD	Professeur, Télécom ParisTech
	Paola PIRINOLI	Professeur, Politecnico Turino Italie
Dir. de thèse :	Raphaël GILLARD	Professeur, INSA Rennes
Co-dir. de thèse :	María GARCIA VIGUERAS	HDR, INSA Rennes
	Tony MAKDISSY	Docteur-Ingénieur, SOITEC, Besançon
Invité(s)		
	Sébastien VAUDREUIL	Professeur, Université Euromed de Fès

3D Printed Metal-only High-gain Antennas made of Quasi-periodic Arrangements of Waveguide type Phoenix Cells

RÉSUMÉ

Table des matières

RÉSUMÉ 2

1. Introduction 3

2. Analyse et modélisation de cellules unitaires basées sur des guides d'ondes 5

2.1 Cellule simple 5
2.2 Cellule phénix 6
2.3 Circuit équivalent 8

3. Antenne bi-bande composée de cellules simples (20/40GHz) 9

4. Antennes monobande constituées de cellules phénix (20GHz). 11

4.1 MORA fait de cellules phénix 11
4.2 Réseau de transmetteur-réflecteur composé de cellules phénix 13

5. RR bi-bande et double faisceau constitués de cellules phénix modifiées. 14

5.1 Réseau réflecteur bi-bande 15
5.2 Réseau réflecteur Double faisceau 16

6. Conclusion 17

RÉSUMÉ

1. Introduction

Les transmissions à longue distance nécessitent des antennes à gain élevé, qui peuvent être obtenues grâce à des réflecteurs paraboliques et des réseaux phasés, parmi d'autres types d'antennes [1]. Au cours des dernières années, un nouveau type d'antenne à gain élevé, l'antenne réseau réflecteur (RA), est devenue progressivement populaire. Un RA peut être considéré comme une combinaison entre antenne réflecteur et antenne réseau. Il présente les avantages d'un gain élevé, d'un faible encombrement, d'un coût réduit et d'une fabrication facile. De plus, il est possible de manipuler la forme et la direction du faisceau principal en contrôlant la géométrie des cellules unitaires constituant le réseau. Cette opération s'effectue beaucoup plus simplement que pour un réseau à rayonnement direct où elle nécessite de concevoir un répartiteur de puissance complexe.

Les RAs sont généralement implémentés en technologie microruban, qui se compose de résonateurs métalliques imprimés sur un substrat diélectrique supporté par un plan de masse. Les RAs microruban ont l'avantage d'être peu coûteux et légers. Parmi les solutions possibles, la cellule phoenix (PC pour Phoenix Cell en anglais) est une topologie de cellule RA avec un fort potentiel. Dans sa version originale [5], elle se compose de deux anneaux concentriques carrés entourant un patch lui-même carré. Parce qu'elle permet de revenir à la géométrie initiale après un cycle complet de 360°, la PC permet d'éviter les brusques variations de géométrie sur l'ouverture rayonnante.

Dans la littérature, les PCs sont imprimées sur des couches diélectriques. Cependant, les matériaux diélectriques utilisés peuvent causer beaucoup de problèmes. Tout d'abord, les matériaux diélectriques peuvent limiter le gain en raison des pertes qu'ils engendrent, surtout à haute fréquence. Dans [3], le gain d'une antenne patch en microruban est augmenté après le remplacement du matériau diélectrique par une couche d'air. De plus, l'utilisation de matériaux diélectriques réduit les possibilités des antennes pour certaines applications opérant dans des environnements sévères, tels que l'espace [4]. Enfin, les matériaux diélectriques limitent également la capacité de gestion de puissance de l'antenne. En raison de tous ces problèmes, il y a un réel intérêt pour les antennes composées uniquement de métal. Par exemple, un réseau entièrement en métal (MO pour Metal-only en anglais) fait d'éléments patch est conçu dans [5] pour résister aux conditions de température et de niveau de radiation sévères dans l'espace.

Plus récemment, l'intérêt pour les réseaux entièrement métalliques s'est porté sur les RAs. En effet, les MORAs combinent les avantages classiques des réseaux réflecteurs imprimés avec ceux des antennes entièrement métalliques. Dans ce contexte, la conception d'une PC pour MORA présente évidemment un grand intérêt. Une première démonstration, une PC de type fente, a été proposée dans [6]. Cependant, il s'agit encore d'une structure plane assez classique (seule la couche diélectrique a été retirée comparativement à une structure imprimée classique). Bien qu'elle évite les inconvénients liés à l'utilisation de matériaux diélectriques, cette première version n'apporte rien de nouveau en termes de capacités de conception.

Au contraire, la fabrication additive (AM pour Additive Manufacturing en anglais) offre de nouvelles possibilités pour construire des antennes MO 3D plus complexes, avec de nombreux degrés de liberté géométriques pour améliorer leurs performances. À mesure que l'AM se développe, son coût diminue et sa précision s'améliore. L'AM a déjà été largement utilisée dans la fabrication d'antennes telles que les antennes cornets dans [7-9], une antenne à lentille dans [10] et des réseaux à guide d'ondes dans [11-12].

Dans cette thèse, notre objectif est d'explorer les possibilités offertes par l'impression 3D pour concevoir de véritables antennes MO 3D. Plus spécifiquement, notre travail est consacré aux MORA constitués de PC 3D. L'objectif principal est donc d'étendre la PC qui a été proposée il y a quelques années dans notre laboratoire [2] depuis sa version originale plane vers une version 3D et d'étudier les nouvelles capacités apportées par la troisième dimension.

Cette thèse a été réalisée à l'IETR, en France, dans le cadre d'une collaboration avec l'Université Antonine, au Liban et l'Université de Fez, au Maroc. La technologie d'impression 3D de fusion laser sélective est disponible dans le laboratoire partenaire à Fez.

La cellule PC 3D proposée dans cette thèse est une cellule de type guide d'ondes car elle peut être vue comme une courte section de guide d'ondes métallique (avec une terminaison en court-circuit). Sa section transversale et sa hauteur offrent de nombreux degrés de liberté pour contrôler le mode de fonctionnement et donc la façon dont elle réfléchit une onde incidente. C'est donc une cellule de déphasage intéressante pour application aux RA. De plus, d'autres configurations prometteuses sont possibles : si la terminaison en court-circuit est remplacée par une terminaison ouverte, la PC aura le potentiel de manipuler également la phase de transmission, ce qui suggère que des réseaux transmetteurs (TA pour Transmit Arrays en anglais) peuvent être conçus. Enfin, lorsqu'elle fonctionne en-dessous de la coupure, la cellule de type guide d'ondes se comporte presque comme un conducteur parfait (sans onde entrant dans le guide d'ondes), et elle peut être utilisée pour réaliser un réflecteur métallique assez classique. Toutes ces options supplémentaires élargissent encore davantage le champ de recherche de cette thèse. Par conséquent, cette thèse propose également des conceptions hybrides combinant réflecteur parabolique, RA et TA.

La thèse est structurée comme suit.

Le premier chapitre présente l'état de l'art des structures RA et TRA existantes, ainsi que l'introduction de la technologie d'impression 3D.

Le chapitre 2 présente deux cellules différentes basées sur des guides d'ondes (cellule simple (SC en anglais) et PC). Chaque cellule a deux configurations différentes selon la terminaison appliquée. Comme déjà mentionné, la configuration court-circuitée est applicable pour les RA tandis que celle à extrémité ouverte permet également de produire un faisceau transmis. Le principe de fonctionnement des cellules est analysé en détail. De plus, la PC est modélisée par un circuit équivalent.

Un antenne bi-bande qui combine les fonctionnalités d'un réflecteur parabolique et d'un RA est proposée dans le chapitre 3. Elle est synthétisée à l'aide de la SC. À la fois la cellule unitaire utilisée et l'antenne bi-bande proposée sont étudiées en détail. Enfin, l'antenne bi-bande est fabriquée et mesurée pour valider ses performances.

Un RA composé de PC avec une hauteur fixe est conçu, fabriqué et mesuré dans le chapitre 4. Ses performances sont encore améliorées en variant la hauteur de chaque cellule pour minimiser l'erreur de phase moyenne. De plus, deux réseau transmetteur-réflecteurs (TRAs pour-Treflect-arrays en anglais) sont conçues à l'aide de cette PC. Les TRAs conçus peuvent générer à la fois un faisceau transmis et un faisceau réfléchi simultanément.

Enfin, deux PC modifiées sont proposése dans le chapitre 5 pour améliorer encore leur comportement. La première variante est utilisée pour concevoir un RA pour une opération bi-bande tandis que la deuxième variante est utilisée pour concevoir un RA qui génère deux faisceaux avec des polarisations orthogonales à la même fréquence.

Une conclusion générale est tirée dans le chapitre 6.

2. Analyse et modélisation de cellules unitaires basées sur des guides d'ondes

Dans ce chapitre, des structures entièrement métalliques à base de guides d'ondes carrés sont utilisées pour concevoir des cellules RA et des cellules TA. Leur principe est analysé en détail et leurs performances sont évaluées par des résultats de simulation électromagnétique. Un modèle de circuit équivalent est également proposé.

2.1 Cellule simple

Comme le montre la Fig.2.1, une cellule constituée d'un guide d'onde carré avec un bloc métallique est proposée dans cette section. La dimension externe (L_c) est fixée à 7,5 mm ($\lambda_0/2$ à la fréquence centrale que nous avons fixée à 20 GHz pour cette démonstration) pour éviter les lobes de réseau dans une configuration en réseau. La taille du bloc métallique (L_r) est modifiée pour contrôler le comportement de la cellule, c'est-à-dire pour faire varier la phase de l'onde réfléchie (ou transmise) lorsqu'elle est éclairée par une onde incidente. Étant donné que la structure proposée (voir Fig.2.1) est plus simple que la structure présentée dans la section suivante, elle est appelée cellule simple.

La cellule simple peut fonctionner comme une cellule TA ou RA selon la terminaison utilisée au port 2. Dans la configuration RA, une terminaison en court-circuit est utilisée et l'onde incidente au port 1 est totalement réfléchie. Dans la configuration TA, une terminaison ouverte est utilisée à la place et la majeure partie de l'onde incidente est transmise à travers la cellule.

Le coefficient de réflexion simulé à l'entrée de la cellule simple avec terminaison en court-circuit à 20 GHz est illustré à la Fig.2.2. La courbe blanche est associée aux résonances qui sont causées par la propagation et la réflexion du mode quasi TE_{10}. De plus, on peut voir que la plage de phase obtenue est inférieure à 255° pour chaque h fixe. La plage de phase complète ne peut être obtenue qu'en faisant varier simultanément h et L_r. Les paramètres S simulés de la cellule simple avec terminaison ouverte à 20 GHz sont illustrés à la Fig.2.3. Ils présentent des régions à très faible réflexion ou transmission (lignes bleu foncé). Elles sont associées à des sauts de phase, comme on peut le voir sur la Fig. 2.3a. Ces résonances peuvent être expliquées à partir des paramètres S théoriques d'un tronçon de ligne où des réflexions multiples entre les deux ports sont prises en compte.

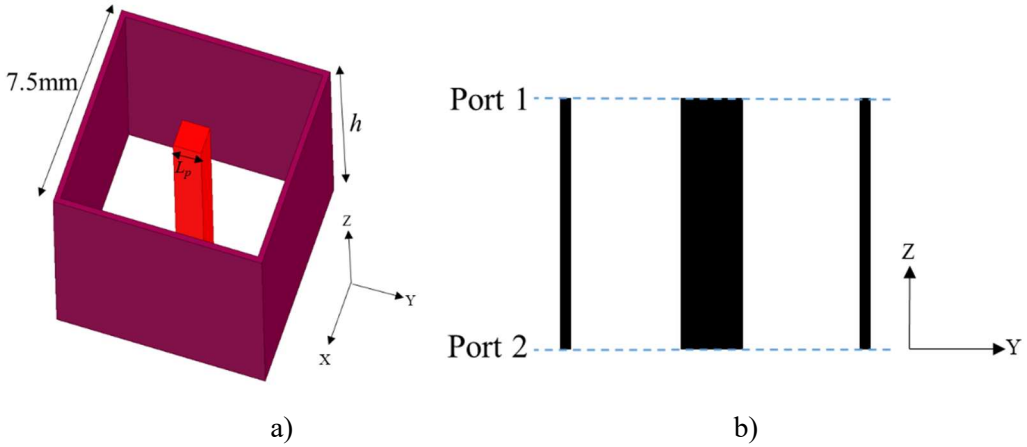

Fig.2.1 Modèle de simulation de la cellule simple. a) Vue 3D. b) Vue en coupe.

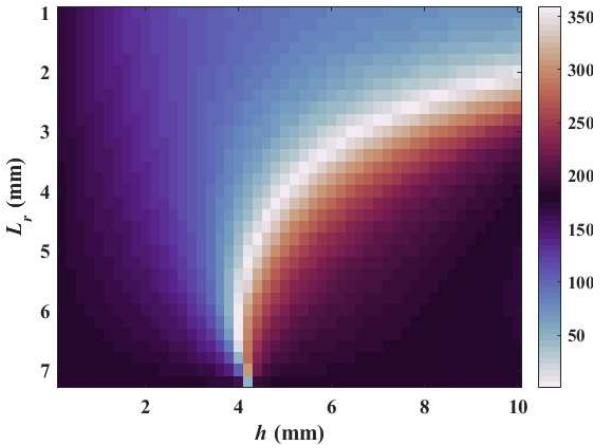

Fig.2.2 Phase du coefficient de réflexion à 20GHz (incidence normale).

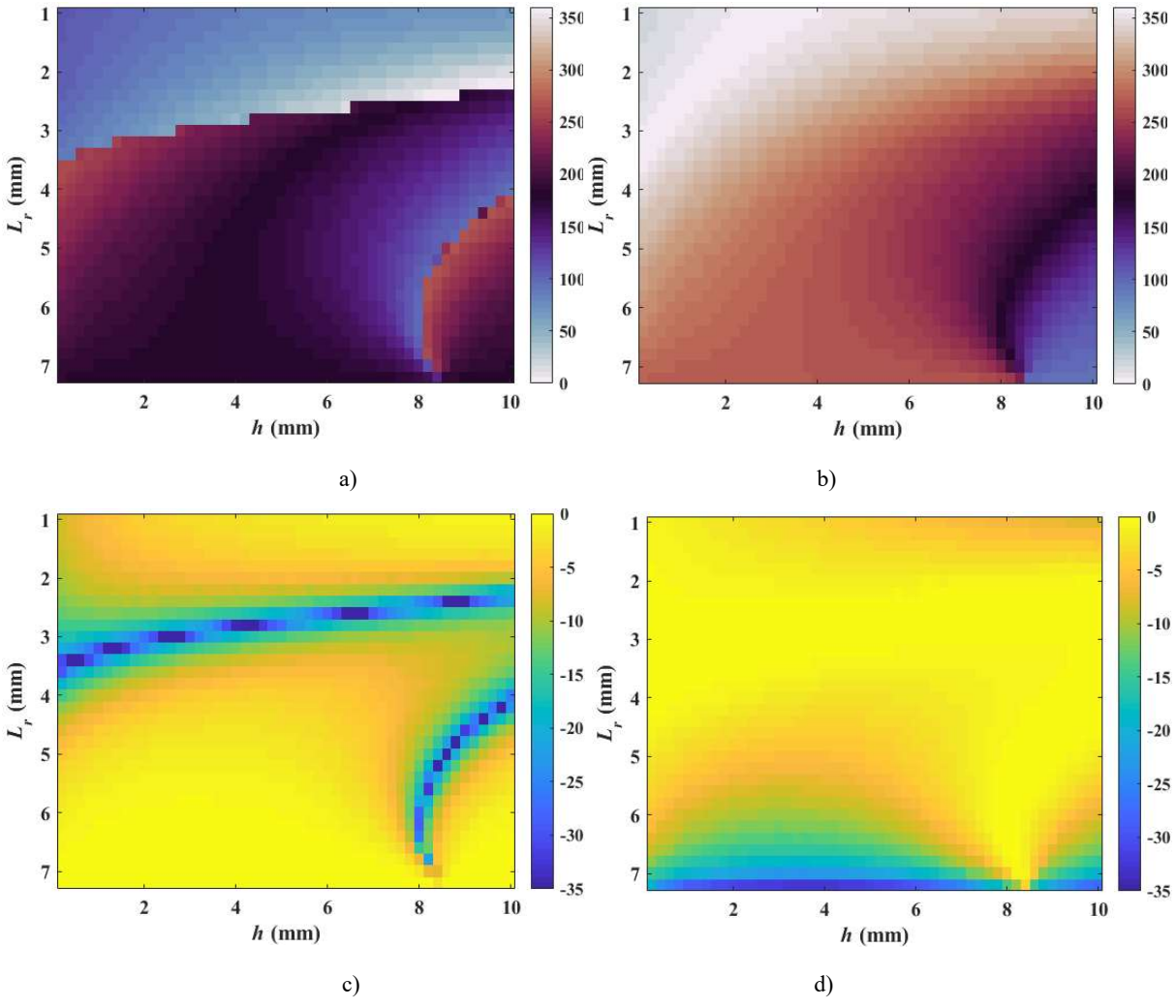

Fig.2.3 S-Paramètres simulés de la cellule simple avec guide d'onde ouvert à 20 GHz (polarisation selon x, incidence normale). a) Phase (S_{11}). b) Phase (S_{21}). c) Mag (S_{11}). d) Mag (S_{21}).

2.2 Cellule phénix

Dans cette section, une PC 3D, comme le montre la Fig.2.4, est proposée. La différence avec la cellule simple est que la PC remplace le bloc métallique variable par un guide d'onde variable et un bloc métallique fixe. La taille du guide d'onde interne (L_r) est variée pour contrôler le comportement de la cellule phénix. Le cycle de variation est représenté sur la Fig.2.5. Au stade initial (voir Fig.2.5), la taille

du guide d'onde interne est égale à la taille du bloc métallique central (ce qui signifie qu'il n'y a plus de guide d'onde interne). Le guide d'onde interne apparaît alors lorsque L_r augmente. Au stade final, la taille du guide d'ondes interne est égale à la taille du guide d'ondes externe et le guide d'ondes interne disparaît à nouveau. La cellule retrouve ainsi sa géométrie initiale.

De même que la cellule simple, la PC fonctionne comme une cellule TA ou RA selon la terminaison utilisée au port 2. Un avantage évident de la PC est cette capacité de revenir à la même géométrie après un cycle complet de 360°, ce qui peut judicieusement être exploité pour limiter les variations géométriques brutales à la surface du réseau entre deux cellules successives.

La phase réfléchie simulée de la cellule simple avec terminaison en court-circuit est illustrée à la Fig.2.6. On peut voir que la plage de phase complète de 360° (phase vs L_r) peut facilement être atteinte lorsque h est supérieur à 4 mm.

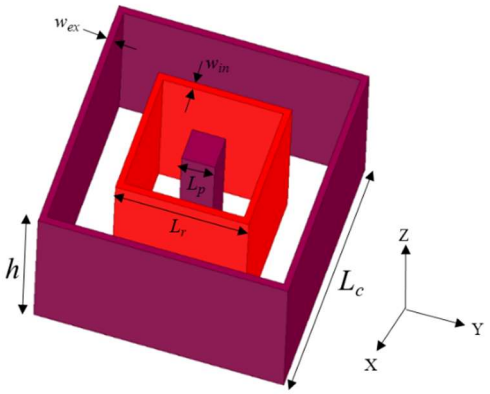

Fig.2.4 La PC 3D proposée.

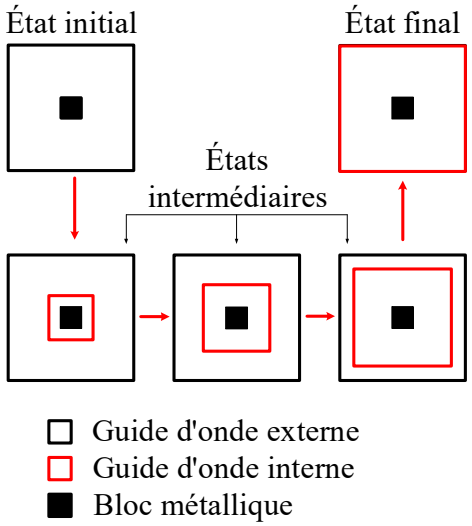

Fig.2.5 Le mécanisme de variation de la PC 3D (vue de dessus).

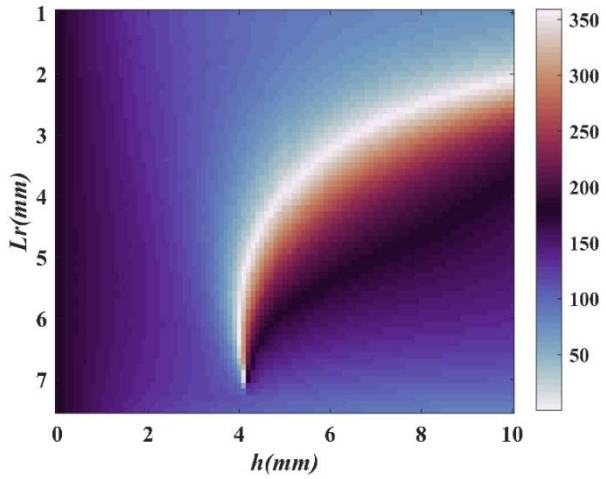

Fig.2.6 Phase réfléchie de la PC avec terminaison en court-circuit à 20GHz

La PC à guide d'ondes ouvert est simulée pour mieux illustrer son principe de fonctionnement. La hauteur (h) est fixée à 10 mm. La Fig.2.7 montre les paramètres S simulés à 20 GHz. Pour des valeurs de L_r inférieures à 2 mm, l'amplitude de S_{21} est assez faible à cause de l'adaptation imparfaite à l'entrée. Étant donné que la majeure partie de l'onde incidente est réfléchie, la cellule peut fonctionner comme une cellule RA. Avec l'augmentation de L_r, l'impédance caractéristique du guide d'onde externe diminue et se rapproche de celle de l'espace libre. Ainsi, l'onde incidente est maintenant couplée au guide d'onde externe. Dans ce cas, $|S_{21}|$ se rapproche de 1 et la PC à guide d'ondes ouvert peut fonctionner comme une cellule TA. Pour L_r supérieur à 4,5 mm, l'impédance caractéristique du guide d'ondes externe diminue à nouveau, le guide d'ondes externe est désadapté et la PC peut fonctionner comme une cellule RA. Ces résultats suggèrent qu'un TRA pourrait être conçu sur la base de la théorie des réseaux lacunaires où certaines cellules sont utilisées pour contrôler le faisceau réfléchi et les autres sont utilisées pour contrôler le faisceau transmis.

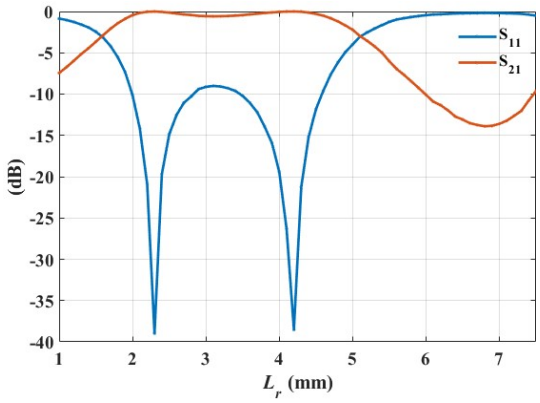

Fig.2.7 Amplitude des paramètres S de la PC à guide d'ondes ouvert

(h=10 mm, f=20GHz, polarisation x).

2.3 Circuit équivalent

Afin d'avoir une compréhension globale de la PC 3D, un circuit équivalent est proposé. Comme indiqué précédemment, il existe deux modes différents pour la PC 3D. Dans cette section, à titre d'illustration, le circuit équivalent est uniquement dérivé pour la PC en court-circuit. Comme la PC en court-circuit est constituée de deux guides d'ondes, son admittance d'entrée dépend principalement de leurs admittances d'entrée. De plus, trois admittances parallèles sont utilisées à l'entrée des deux guides

d'ondes pour modéliser les effets de discontinuité. En conséquence, le circuit équivalent peut être représenté comme indiqué sur la Fig.2.8.

La comparaison des phases réfléchies entre les simulations électromagnétiques et le circuit équivalent est illustrée à la Fig.2.9 lorsque h varie. On notera que le circuit équivalent conduit à deux solutions différentes (notées 1 et 2) du fait de la résolution d'un système d'équations de degré deux. On peut voir que l'accord entre simulations électromagnétiques et circuit équivalent est assez bon. Plus précisément, les erreurs de phase pour la plupart des cas (L_r, h) sont inférieures à 10 degrés. Ces résultats démontrent que le circuit équivalent proposé peut être utilisé pour prédire la phase de réflexion de la PC en court-circuit.

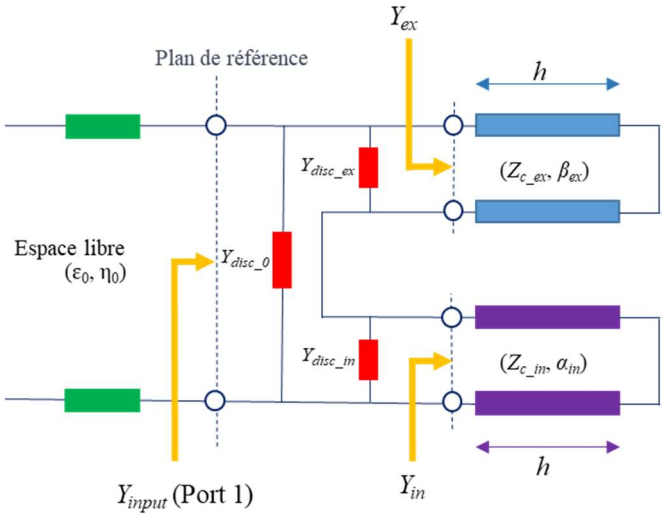

Fig.2.8 Circuit équivalent de la PC en court-circuit

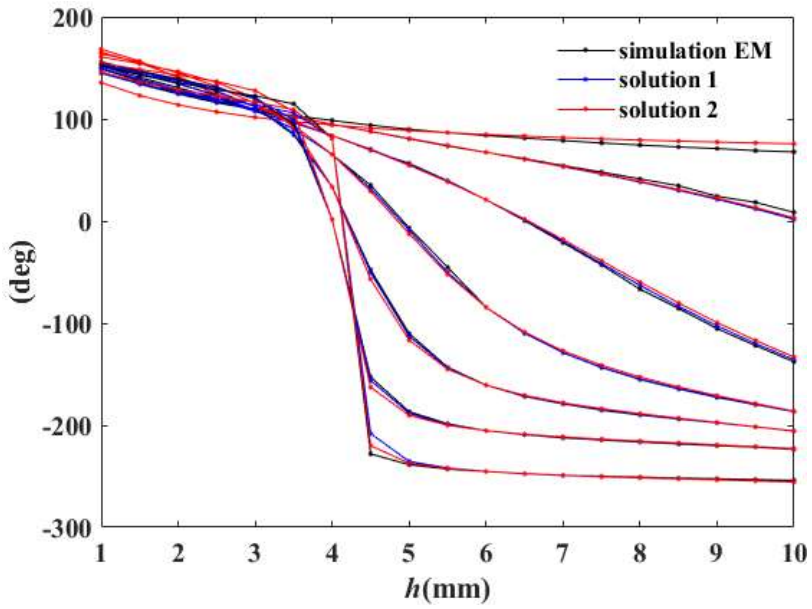

Fig.2.9 Phase réfléchie

3. Antenne bi-bande composée de cellules simples (20/40GHz)

Le principe de l'antenne bi-bande est représenté sur la Fig.3.1. L'antenne bi-bande proposée est constituée de guides d'ondes métalliques en court-circuit. Les guides d'ondes sont logés de telle sorte que leur surface supérieure forme approximativement un paraboloïde. Si la fréquence de l'onde incidente

de l'antenne d'alimentation est inférieure à la fréquence de coupure de ces guides d'onde, l'onde incidente sera réfléchie directement à l'entrée de chaque guide d'onde. Dans ce cas, l'onde incidente n'est collimatée que par la forme de l'ouverture et le mécanisme de fonctionnement est le même que celui d'un réflecteur parabolique. Il implique un mécanisme de retard en temps réel, ce qui signifie qu'il n'a aucune limitation de bande passante. Si la fréquence de l'onde incidente est supérieure à la fréquence de coupure des guides d'onde, l'onde incidente se propage à l'interne et on obtient un déphasage supplémentaire dont la valeur dépend de la longueur de chaque guide d'onde. En conséquence, une antenne bi-bande peut être conçue. Une fois la forme de l'ouverture déterminée dans la bande de fréquence inférieure, le faisceau réfléchi dans la bande de fréquence supérieure est obtenu grâce à la répartition de phase produite par les cellules unitaires de l'antenne. Notez que les directions des faisceaux principaux peuvent être différentes dans les deux bandes de fréquences. Sur la base du principe de l'antenne bi-bande proposée, un grand rapport de fréquence entre les deux bandes peut être atteint. À titre d'exemple, une antenne bi-bande fonctionnant à 20/40 GHz est conçue dans ce chapitre. L'antenne conçue est appelée réseau réflecteur/ antenne réflecteur (RRA pour Reflector-reflectarray antenna en anglais).

Le RRA conçu est représenté sur la Fig.3.2 avec son champ rayonné. On peut voir que les faisceaux principaux de 20 GHz et 40 GHz sont dans des directions différentes, ce qui prouve que l'antenne conçue peut fonctionner dans les deux bandes de fréquences.

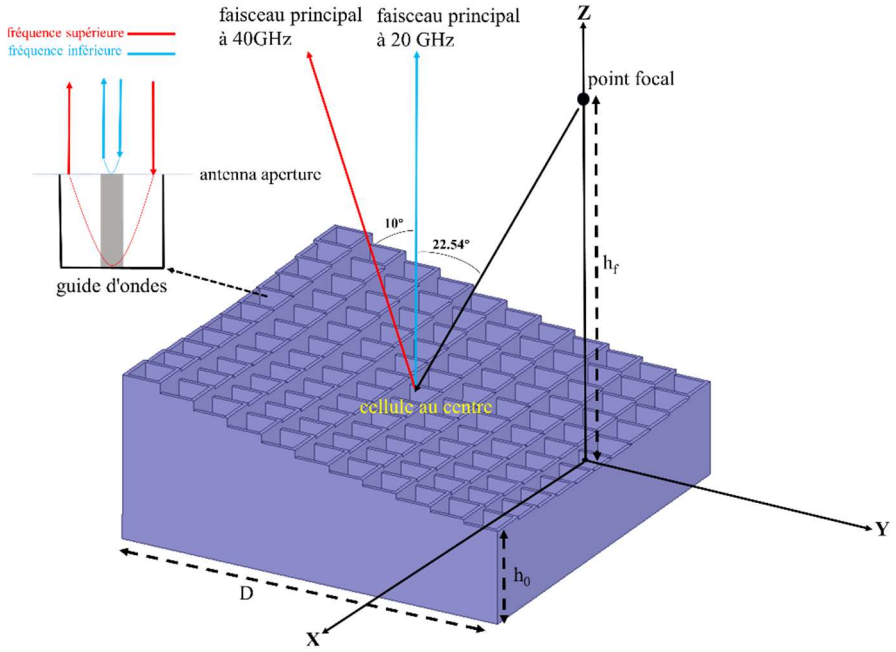

Fig.3.1 Le principe et la configuration de l'antenne bi-bande proposée

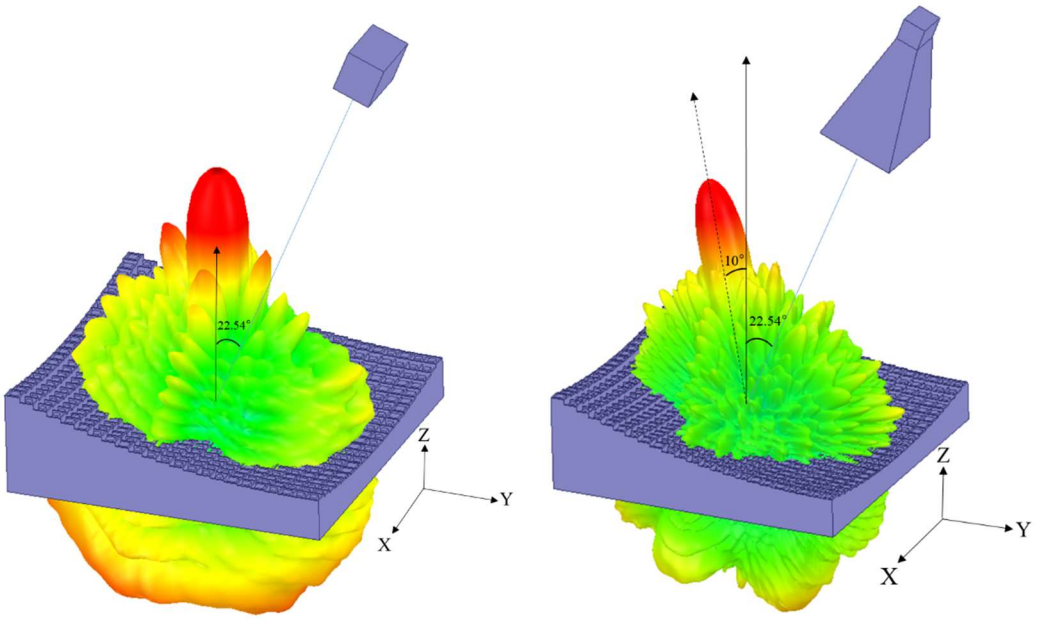

a) b)

Fig.3.2 L'antenne bi-bande proposée avec champs rayonnés. a) 20 GHz. b) 40 GHz.

4. Antennes monobande constituées de cellules phénix.

Dans le chapitre 2, deux cellules différentes basées sur des guides d'ondes (cellule simple et cellule phénix) sont introduites. La cellule simple avec terminaison en court-circuit est utilisée comme cellule de déphasage pour synthétiser les RRA au chapitre 3. Dans ce chapitre, la capacité de la PC est démontrée en l'utilisant pour synthétiser des RA et des TRA.

La section 4.1 décrit la conception, la fabrication et la mesure d'un MORA fonctionnant à 20 GHz. La conception et la simulation de deux MOTRA différentes sont abordées à la section 4.2. La section 4.3 présente une analyse détaillée de l'effet de la hauteur de la PC sur la performance des MORA et fournit une approche de conception améliorée.

4.1 MORA fait de cellules phénix

Dans cette section, un MORA constitué de cellules phénix avec des guides d'ondes en court-circuit est synthétisé en minimisant l'erreur de phase moyenne à 19,5 et 20,5 GHz. Le MORA conçu avec champ rayonné est illustré à la Fig.4.1. Le faisceau principal est à 25° de la normale du panneau RA. Le MORA conçu est fabriqué à l'aide de la technologie d'impression 3D par fusion laser sélective. Les antennes RA et cornet fabriquées sont illustrées à la Fig.4.2. On peut voir que le MORA réalise une variation douce des géométries cellulaires. La Fig.4.3 montre les photographies du MORA fabriqué et sa configuration de mesure. La réponse en gain et l'efficacité de surface sont illustrées à la Fig.4.4. L'écart de gain est inférieur à 0,53 dB de 18 GHz à 22 GHz, ce qui est tout à fait acceptable. Le gain réalisé mesuré à 19,5 GHz est de 30,3 dBi avec une efficacité d'ouverture maximale de 51,17 %. La largeur de bande de gain mesurée de 1 dB est de 15 % (de 19 à 22 GHz).

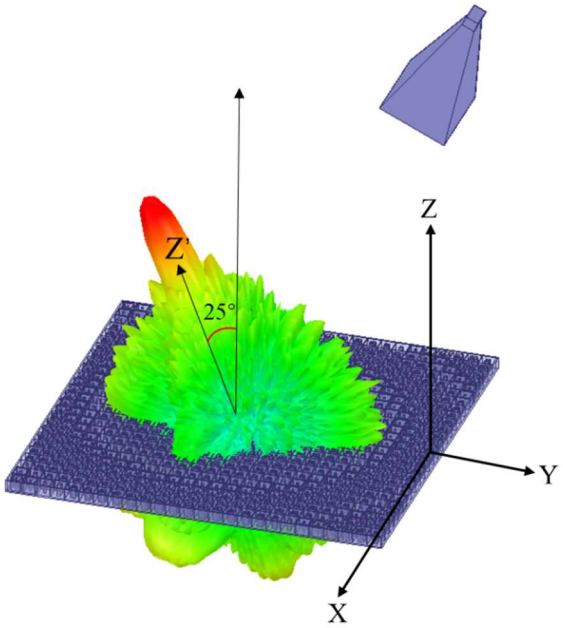

Fig.4.1 Champ de rayonnement du RA conçu à 20 GHz

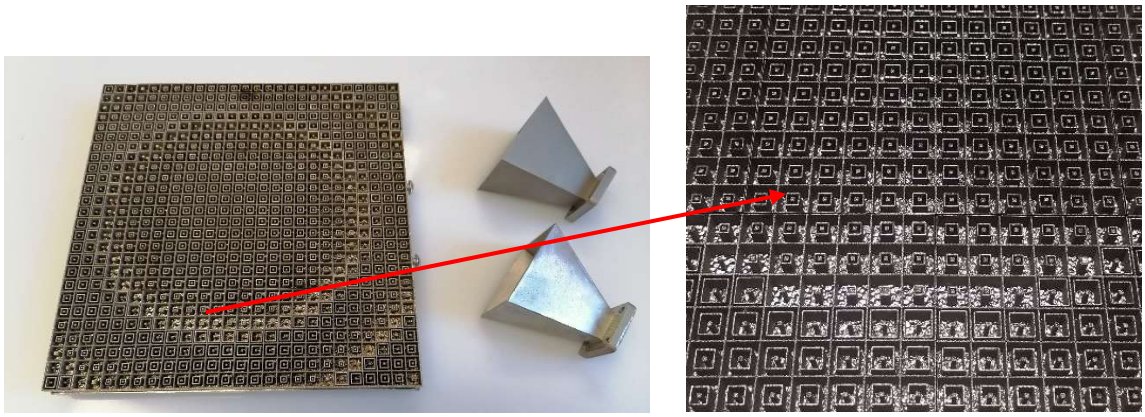

Fig.4.2 Les antennes RA et cornet fabriquées.

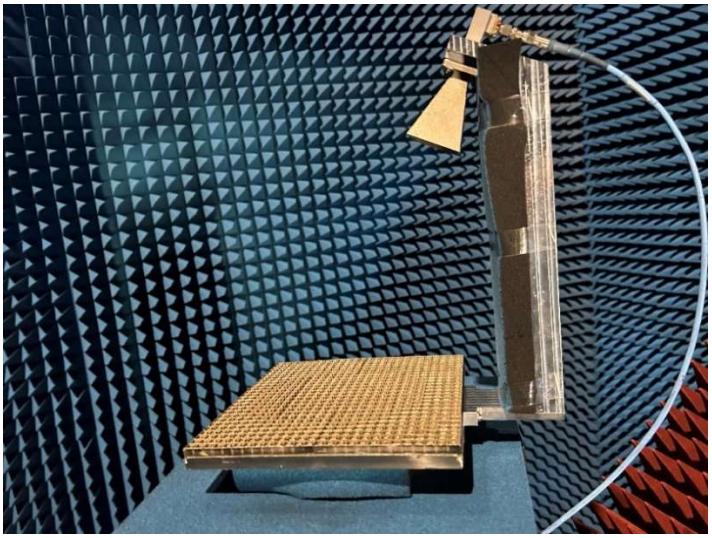

Fig.4.3 Photographies du MORA fabriqué et de sa configuration de mesure.

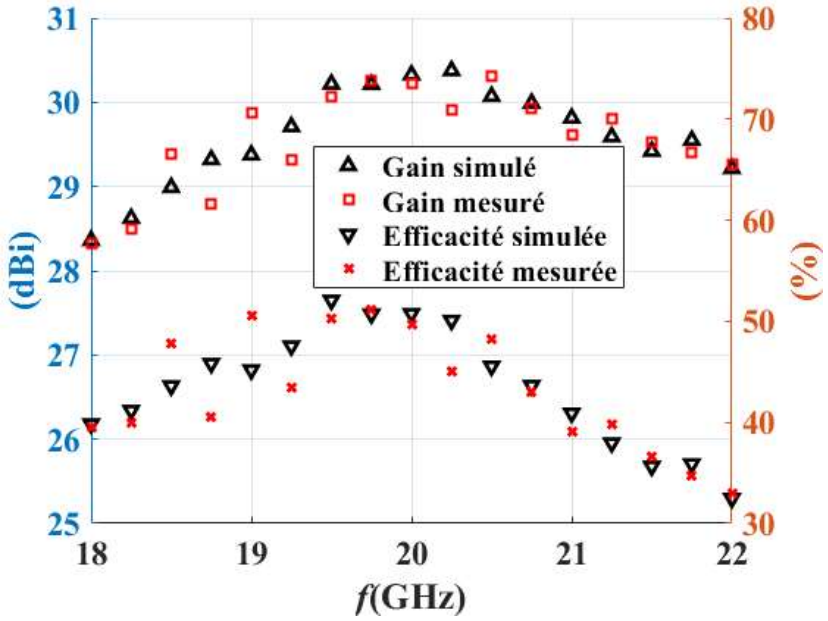

Fig.4.4 Réponse en gain (à gauche) et efficacités de surface (à droite).

4.2 Réseau de transmetteur-réflecteur composé de cellules phénix

Deux TRAs constitués de cellules phénix à guide d'ondes ouvert sont maintenant conçus pour valider cette configuration de la cellule. Les faisceaux transmis et réfléchi du 1er réseau (TRA1) sont symétriques alors qu'ils ne le sont pas dans le second (TRA2). Les deux TRAs sont synthétisés en minimisant l'erreur de phase moyenne.

La base de données simulée à 20 GHz est donnée à la Fig.4.5. Elle montre que certaines cellules (typiquement celles avec $|S_{11}|$>-2dB) semblent mieux adaptées à la réflexion et d'autres ($|S_{21}|$>-2dB) à la transmission. Les autres ne sont optimales ni pour la réflexion ni pour la transmission.

La Fig. 4.6 montre TRA1 avec le champ rayonné associé à 20 GHz. On peut voir que les faisceaux transmis et réfléchis sont produits simultanément. Les gains et les efficacités de surface en fonction de la fréquence des deux faisceaux TRA1 sont résumés à la Fig.4.7a. On constate que les performances du faisceau transmis sont globalement meilleures que celles du faisceau réfléchi. Le gain obtenu pour la transmission et la réflexion à 20 GHz est respectivement de 26,4 dBi et 25,7 dBi. L'efficacité de surface correspondante est de 20,55 % et 17,29 % respectivement. L'efficacité de surface totale de TRA1 est définie à partir de la somme du faisceau réfléchi et du faisceau transmis. Par conséquent, l'efficacité totale obtenue pour TRA1 est de 37,84 %.

Les gains et les efficacités de surface en fonction de la fréquence des deux faisceaux de TRA2 sont résumés à la Fig.4.7b. Comme pour TRA1, le faisceau transmis par TRA2 est globalement meilleur que le faisceau réfléchi. La différence de gain entre les deux faisceaux est d'environ 3dB. Les gains obtenus pour la transmission et la réflexion à 20 GHz sont respectivement de 26,1 dBi et 23,1 dBi (voir Fig.4.7b). L'efficacité de surface totale correspondante est de 28,53 %. L'efficacité d'ouverture obtenue de TRA2 est réduite par rapport à TRA1.

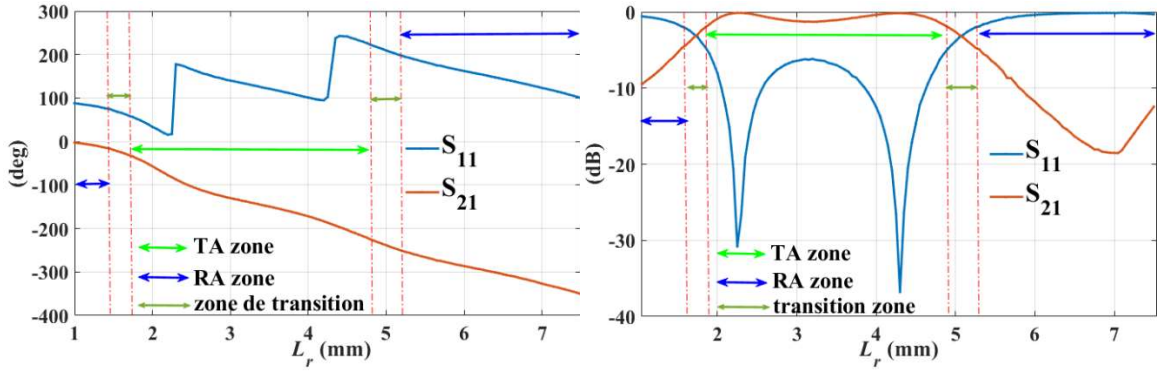

a) b)

Fig.4.5 Les paramètres S simulés de la PC avec des guides d'ondes ouverts (h=10 mm, pas=0,05 mm, f=20 GHz, polarisation x, ϕ_{inc}=90°, θ_{inc}=25°). a) Phase. b) Amplitude.

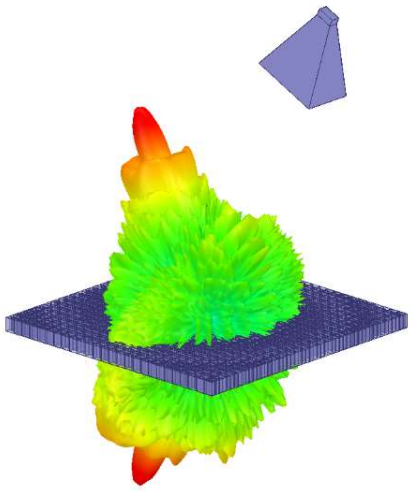

Fig.4.6 TRA1 avec faisceaux symétriques à 20GHz et antenne cornet.

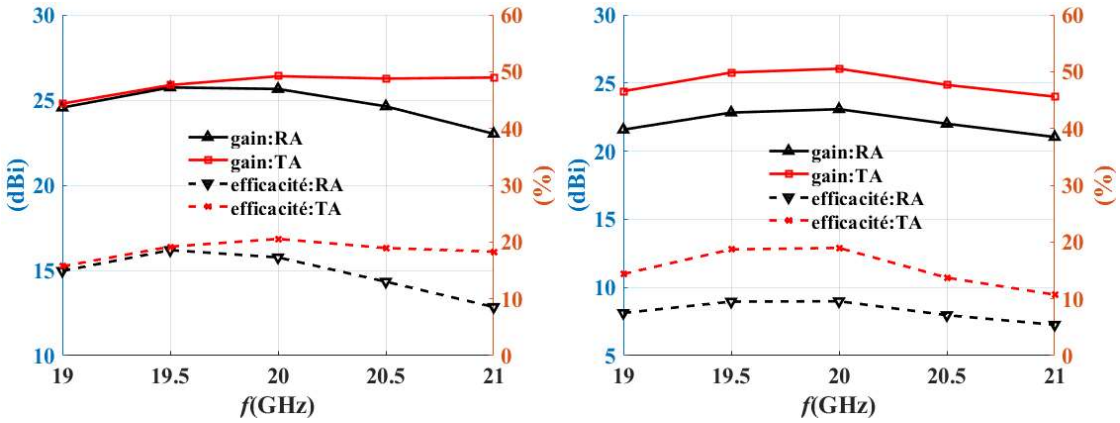

a) b)

Fig.4.7 Gain et efficacité de surface. a) TRA1. b) TRA2.

5. RR bi-bande et double faisceau constitués de cellules phénix modifiées.

Le précédent chapitre a permis de valider les deux principaux modes de fonctionnement de la PC 3D et fourni une validation expérimentale. Ce chapitre tente d'explorer davantage les capacités de cette cellule en étudiant des degrés de liberté supplémentaires ou des topologies légèrement modifiées. Plus

précisément, deux nouvelles versions de la PC en court-circuit sont discutées, conduisant à deux nouvelles conceptions RA.

Tout d'abord, il ressort de la section 2.2 que la PC est constituée de deux guides d'ondes imbriqués. Dans toutes les conceptions précédentes, les hauteurs des deux guides d'ondes sont identiques. Cependant, si nous les accordons indépendamment, un autre degré de liberté est obtenu pour contrôler la phase réfléchie. C'est ce qui est fait dans la section 5.1 où une antenne bi-bande (20/25 GHz) est conçue en tirant parti des deux hauteurs de guide d'ondes disponibles. Deuxièmement, la section 5.2 propose une topologie modifiée pour contrôler les deux polarisations linéaires séparément. En tant qu'application, un RA qui génère deux faisceaux différents avec des polarisations linéaires orthogonales à 25 GHz est conçu. Par manque de temps, seules des simulations sont réalisées dans ce chapitre à vocation exploratoire.

5.1 Réseau réflecteur bi-bande

Cette sous-section présente une PC modifiée avec un guide d'ondes en court-circuit utilisé pour concevoir un MORA bi-bande. Comme le montre la Fig.5.2, la cellule proposée se compose de deux guides d'ondes carrés et d'un bloc métallique au centre (comme la PC avec un guide d'ondes en court-circuit sur la Fig.2.4). La seule nouveauté ici est que la section transversale de la cellule est fixe et que la phase de réflexion est réglée en faisant varier les hauteurs des deux guides d'ondes.

Un RA bi-bande est maintenant conçu pour valider la cellule proposée. La géométrie de cellule de chaque cellule est sélectionnée pour minimiser l'erreur de phase moyenne à 20 et 25 GHz afin de réaliser une fonctionnalité bi-bande. Le RA bi-bande avec ses champs rayonnés 3D est représenté sur la Fig.5.2 comme une illustration préliminaire de son comportement. On peut voir que le RA proposé peut fonctionner à 20 et 25 GHz.

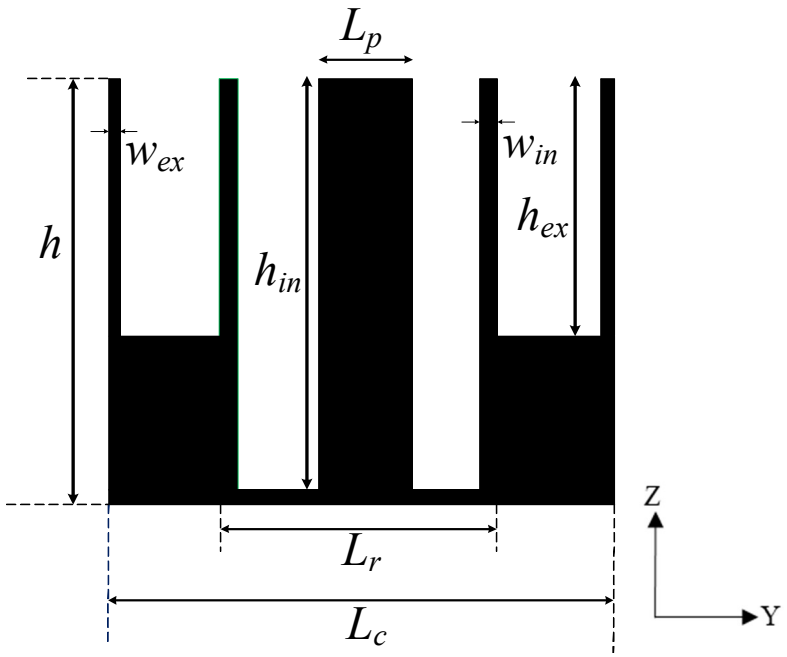

Fig.5.1 Cellule bi-bande proposée (vue en coupe).

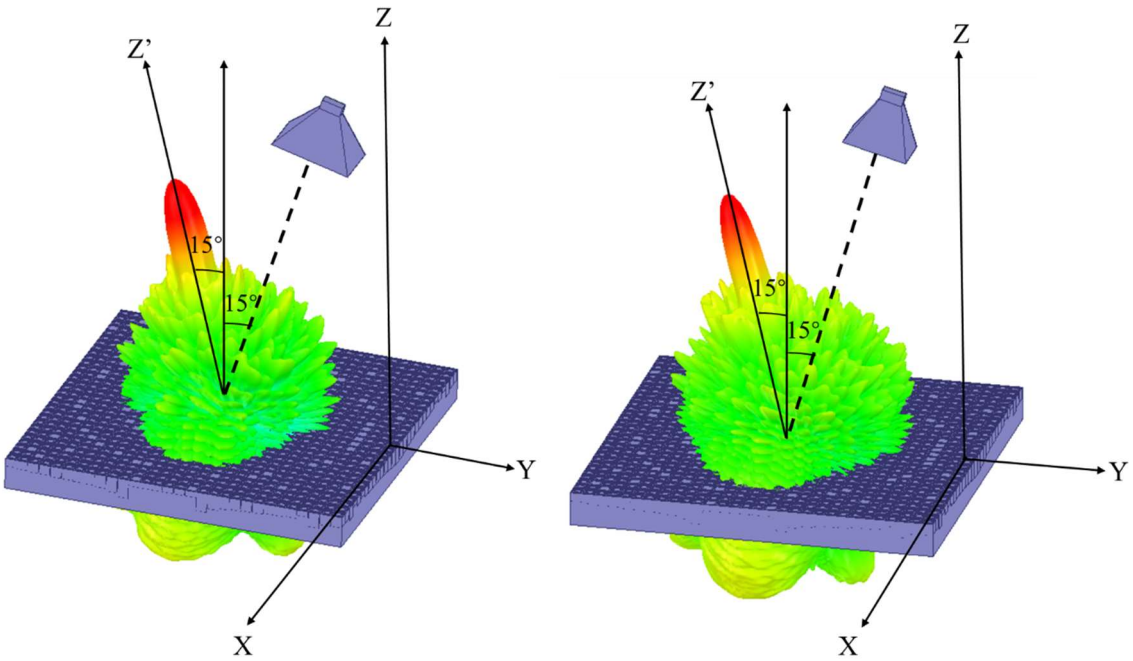

a) b)

Fig.5.2 Antenne bi-bande avec champ de rayonnement. a) 20 GHz. b) 25 GHz.

5.2 Réseau réflecteur Double faisceau

Cette section propose un MORA permettant de générer deux faisceaux rayonnés avec des polarisations orthogonales. La cellule unitaire est similaire à la cellule à bi-bande de la Fig.5.1. La seule différence, comme le montre la figure 5.3, est que quatre murs sont ajoutés pour diviser les deux guides d'ondes en deux parties. Cette modification permet à la cellule proposée de contrôler indépendamment les ondes incidentes avec des polarisations linéaires orthogonales. De plus, la phase réfléchie est contrôlée en réglant indépendamment les hauteurs des deux guides d'ondes (h_{in} et h_{ex}).

Les hauteurs h_{in} et h_{ex} de chaque cellule sont sélectionnées une par une pour répondre aux distributions de phase requises pour les deux faisceaux (h_{in} pour le faisceau (15°, 315°) et h_{ex} pour (15°, 225°)). Le RA à double faisceau avec ses champs rayonnés à 25 GHz est illustré à la Fig.5.4. On constate que la direction du faisceau principal dépend de la polarisation de l'onde incidente, ce qui est conforme aux attentes.

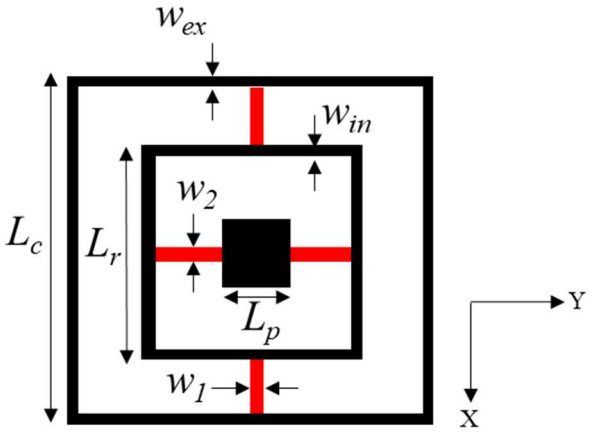

Fig.5.3 Vue de dessus de la cellule à double faisceau.

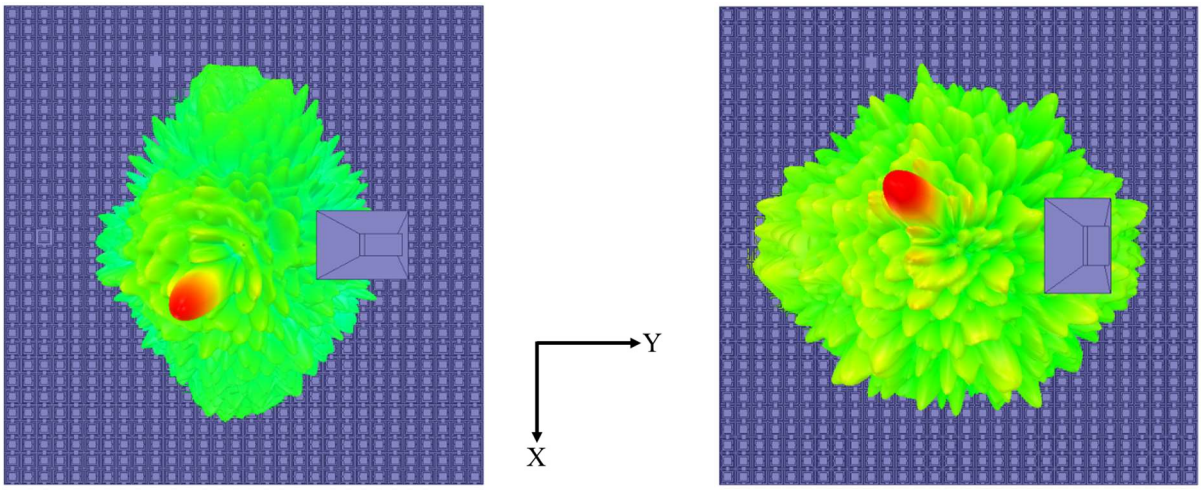

a) b)

Fig.5.4 RA avec champs rayonnés à 25GHz. a) Faisceau contrôlé par le guide d'onde interne (excitation à polarisation selon x). b) Faisceau contrôlé par un guide d'onde externe (excitation à polarisation selon y).

6. Conclusion

Dans cette thèse, les capacités des PC 3D ont été étudiées et différentes conceptions d'antennes ont été proposées en conséquence. Étant donné que la technologie de fusion sélective par laser est disponible dans le laboratoire partenaire à Fez, certaines des antennes conçues dans cette thèse ont été fabriquées et mesurées, offrant ainsi une validation expérimentale complète.

Plus précisément, les principales contributions de cette thèse sont les suivantes :

Un nouveau concept de PC basé sur un guide d'ondes MO, y compris sa version simplifiée, est proposé. La PC proposée est analysée en détail. Son principe est expliqué en observant la distribution de champ électrique. Les phénomènes de résonance sont expliqués par des paramètres S théoriques et des solutions sont données pour se débarrasser de ces résonances ou limiter leur impact. Un circuit équivalent pour la PC est établi pour prédire la phase réfléchie. Un bon accord entre le circuit équivalent et les résultats de simulation électromagnétique est obtenu. Différents degrés de liberté (section droite et hauteur) dans la PC sont étudiés. Les performances sont évaluées par les résultats de simulation.

Une antenne double bande TRA (fonctionnant à la fois à 20 et 40 GHz) est conçue, simulée, fabriquée et mesurée. Le profil de l'antenne double bande est considérablement réduit en faisant pivoter le système de coordonnées. L'antenne double bande est fabriquée à l'aide de la technologie de la fusion laser sélective. L'accord entre les résultats simulés et mesurés est assez bon.

Une antenne simple bande MORA (fonctionnant à 20 GHz) est conçue, simulée, fabriquée et mesurée. L'antenne est conçue en minimisant l'erreur de phase moyenne. Une méthodologie d'optimisation est également proposée, et la largeur de bande de gain à 1 dB est améliorée de 3 % après l'optimisation. Un bon accord entre les simulations et les mesures est obtenu. Deux différents TRAs (fonctionnant à 20 GHz) sont conçus et simulés comme première démonstration de cette topologie d'antenne lors de l'utilisation de PC. Les antennes sont synthétisées en minimisant l'erreur de phase totale. Les résultats de simulation montrent que les TRAs proposés peuvent produire simultanément des faisceaux transmis et réfléchis, et les faisceaux produits peuvent être symétriques ou asymétriques.

Une PC modifiée pour une application double bande est proposée, et une antenne double bande MORA (fonctionnant à la fois à 20 et 25 GHz) est conçue et simulée. Ses performances sont évaluées par des simulations. L'antenne double bande est synthétisée en minimisant l'erreur de phase moyenne. Les résultats de simulation montrent qu'elle peut fonctionner dans deux bandes de fréquences différentes.

Une PC modifiée pour une double polarisation est également proposée, et une antenne double faisceau (fonctionnant à 25 GHz) est conçue et simulée. La cellule unitaire peut régler indépendamment les phases réfléchies pour deux polarisations linéaires orthogonales. Ses performances sont évaluées par des simulations. L'antenne est synthétisée en sélectionnant la géométrie correspondante pour chaque faisceau respectivement. Les résultats de simulation montrent que la direction du faisceau principal peut être modifiée en changeant la polarisation de l'onde incidente.

Les principales conclusions sont les suivantes :

Les résultats de cette thèse montrent que différentes fonctionnalités peuvent être réalisées en utilisant pleinement les différents degrés de liberté dans la PC, tels que la section droite de la PC et la hauteur des différents guides d'ondes dans la PC.

La PC 3D peut être utilisée dans de nombreuses configurations différentes (RA, TA, RA/TA, RA/ réflecteur parabolique), ce qui suggère que des études supplémentaires sont encore nécessaires pour explorer pleinement toutes ses capacités.

La cellule offre de nombreux degrés de liberté, ce qui nécessite également une attention particulière lors de la conception d'un réseau. Tout d'abord, sa section transversale doit être choisie avec soin car elle contrôle la fréquence de coupure des modes de propagation. Deuxièmement, la hauteur peut être impliquée dans le déclenchement de résonances parasites. Enfin, la meilleure solution pour régler la phase consiste à combiner des variations de hauteurs et de sections droites, mais un compromis est nécessaire pour préserver une variation géométrique lisse sur l'ouverture du réseau. Pour l'instant, des schémas d'optimisation avancés sont encore nécessaires pour gérer pleinement le processus de synthèse.

Les futures lignes de recherche possibles sont les suivantes :

Tout d'abord, la thèse se concentre sur les cellules unitaires basées sur des guides d'ondes métalliques carrés. D'autres types de guides d'ondes pourraient être considérés pour ajuster la phase, par exemple les guides d'ondes à plaque parallèle.

Dans le chapitre 2, seule la PC est modélisée par un circuit équivalent. Les autres cellules peuvent également être représentées par des circuits équivalents. De cette manière, une compréhension complète des cellules proposées basées sur des guides d'ondes peut être obtenue.

Étant donné que la PC proposée possède plusieurs degrés de liberté, des études supplémentaires sont nécessaires pour trouver la meilleure façon de sélectionner la géométrie de chaque cellule afin de concevoir des antennes offrant les meilleures performances, par exemple trouver le meilleur compromis entre perte minimale, erreur minimale et géométrie régulière.

Des antennes offrant davantage de fonctionnalités peuvent être conçues en exploitant pleinement les différents degrés de liberté offerts par la PC.

Table of contents

General Introduction....23

Chapter 1 - State of the art....26

1.1 Introduction to high gain antennas....26

1.1.1 Reflector antennas....26
1.1.2 Array antennas....26
1.1.3 Reflectarray antennas....26
1.1.3.1 Phase-shift distribution on the reflectarray aperture....27
1.1.3.2 Advantages of reflectarray antenna....28
1.1.3.3 Disadvantages of reflectarray antenna....29
1.1.4 Transmitarray antennas....29
1.1.5 Conclusion....29

1.2 Different reflectarray antennas....30

1.2.1 The first reflectarray antenna....30
1.2.2 Microstrip reflectarray antennas....30
1.2.2.1 Reflectarray cells with time delay line.....31
1.2.2.2 Reflectarray cells with variable size....31
1.2.2.3 Reflectarray cells with variable rotation angle....33
1.2.3 Metal-only reflectarray antennas....33
1.2.3.1 Metal-only reflectarray antennas using slot-type cells....34
1.2.3.2 Metal-only reflectarray antennas using waveguide-type cells....36
1.2.3.3 Metal-only reflectarray antennas using metallic blocks....40
1.2.4 Comparison between different reflectarray antennas....41

1.3 Different transmit-reflect-arrays....43

1.4 Fabrication of reflectarray antennas....43

1.3.1 Introduction of different additive manufacturing technologies....44
1.3.1.1 Fused deposition modeling....44
1.3.1.2 Stereolithography....45
1.3.1.3 Material Jetting 3D printing....45
1.3.1.4 Selective Laser Sintering....46
1.3.1.5 Metal 3D printing....47
1.3.1.6 Binder Jetting....48
1.3.1.7 Reasons for choosing selective laser meting 3D printing technology .49
1.3.2 Reflectarray antennas using 3D printing technologies....49

1.5 Conclusion 51

Chapter 2 - Analysis and Modeling of Waveguide-based Phoenix Cell 53

2.1 Simple cell. 53

2.1.1 Simple cell with short-ended waveguide 57
2.1.2 Simple cell with open-ended waveguide 59
2.1.3 Conclusion 61

2.2 Phoenix cell 61

2.2.1 Phoenix cell using short-ended waveguides 63
2.2.2 Phoenix cell using open-ended waveguides 64
2.2.3 Conclusion 66

2.3 Equivalent circuit of the 3D phoenix cell 66

2.3.1 Derivation process 67
2.3.2 Verification of the equivalent circuit 68
2.3.3 Conclusion 70

2.4 Resonances analysis 70

2.4.1 Waveguide with losses 71
2.4.2 Unit cell with losses 71
2.4.3 Conclusion 72

2.5 Conclusion 72

Chapter 3 - Dual Band Antenna made of Simple Cells 74

3.1 Introduction 74

3.2 Proposed concept of dual band antenna 74

3.3 Analysis of the unit cell 75

3.3.1 Initial analysis 75
3.3.2 Unit cell under oblique incidence 77
3.3.3 Solutions to avoid TEM resonance 82
3.3.4 Conclusion 84

3.4 Preliminary design of dual band antenna 84

3.4.1 Description of the design process 84
3.4.2 Design of two feed antennas 86
3.4.3 Performances of the designed dual band antenna 88
3.4.4 Conclusion 93

3.5 Optimized design 1 of dual band antenna 94

3.5.1 Comparison between three different RRAs 94
3.5.2 Conclusion 97

3.6 Optimized design 2 of dual band antenna 98
3.6.1 Description of two operation modes 98
3.6.2 Performances of two different modes 99
3.6.3 Conclusion....101

3.7 Modification of RRA0 for reduced profile....101
3.7.1 Principle of profile reduction 101
3.7.2 Performances evaluation 104
3.7.3 Conclusion....107

3.8 Fabrication and measurements 108
3.8.1 Antenna fabrication 108
3.8.2 Antenna measurement 111
3.8.3 Optimized antenna made of unit cells with fixed cross-section....1115

3.9 Conclusion 117

Chapter 4 - Single Band Antennas made of Phoenix Cells 120

4.1 Introduction 120

4.2. Metal-only reflectarray antenna using 3D phoenix cell 121
4.2.1 Design process of metal-only reflectarray antenna 121
4.2.2 Horn antenna design....121
4.2.3 Performances evaluation 123
4.2.4 Fabrication and measurements 125
4.2.3 Conclusion....129

4.3. Transmit-reflect-arrays using 3D phoenix cells 129
4.3.1 Design process 129
4.3.2 Performances analysis 132
4.3.3 Conclusion....139

4.4 Bandwidth enhancement of metal-only reflectarray antennas 140
4.4.1 Database 140
4.4.2 Initial design approach and analysis 141
4.4.3 Improved design approach and analysis 141
4.4.4 Conclusion....145

4.5 Conclusion 146

Chapter 5 - Dual Band and Dual Beam Antennas made of Modified Phoenix Cells..147

5.1 Introduction 148

5.2 Dual band Metal-only reflectarray antenna 149
5.2.1 Cell analysis 149

5.2.2 Horn antenna design....151
5.2.3 Dual band reflectarray antenna design and analysis....153
5.2.4 Performances evaluation....155
5.2.5 Conclusion....158

5.3 Dual beam metal-only reflectarray antennas....159

5.3.1 Cells Description....159
5.3.2 Cells performances....159
5.3.3 Antenna synthesis and analysis....160
5.3.4 Conclusion....164

5.4 Conclusion....164

General Conclusion....166

References....168

Appendix 1: Acronyms....178

General Introduction

Long-distance transmissions require high-gain antennas, which can be achieved by parabolic reflectors and phased arrays, among other types of antennas [1]. In recent years, a new type of high-gain antenna, the reflectarray antenna (RA), has gradually become popular. RA can be seen as a combination of reflector antenna and array antenna. It has the advantages of high gain, low profile, low cost and easy manufacturing. Also, it is able to manipulate the main beam, including its shape and direction, by controlling the geometrical pattern of the unit cell. In contrast to phased array antennas, such manipulation of the radiation is obtained in RA without increasing the complexity of any beamforming network.

RAs are usually implemented in microstrip technology, which consists of metallic resonators printed on a dielectric substrate backed by a ground plane. Microstrip RAs have the advantages of low-cost and low mass. Among possible solutions, the phoenix cell (PC) is a topology of RA cell with high potential. In its original version [2], it consists of two square concentric rings enclosing a square patch. The geometric variation over the RA aperture is smoothed out owing to the rebirth ability of the PC.

In the literature, PCs are printed on top of dielectric layers. However, the used dielectric materials may cause a lot of problems. First of all, dielectric materials may limit the gain due to the losses they bring, especially at high frequency. In [3], the gain of a microstrip patch antenna is increased after the dielectric material is replaced by air substrate. In addition, the use of dielectric materials makes PCs not optimal for some applications operating in severe environments, such as space [4]. Finally, dielectric materials also limit the power handling capability of the antenna. Due to all these problems, there is a real interest in antennas made only of metal. As an example, a metal-only (MO) array made of patch elements is designed in [5] to withstand harsh temperature condition and radiation levels in space.

More recently, the interest on MO arrays has been devoted to RAs themselves. Indeed, MORAs combine the classical advantages of RAs with the ones of MO antennas. As one of the first demonstrations, a slot-type PC has been proposed in [6] to design a MORA. However, it is still a quite classical planar structure (only the dielectric layer has been removed compared to a classical printed structure). Although it prevents from the drawbacks associated to the use of dielectric materials, it does not bring anything new regarding design capabilities.

On the contrary, additive manufacturing offers new possibilities to build more complex 3D MO antennas, with numerous geometrical degrees of freedom to improve their performance. As additive manufacturing (AM) develops, its cost is also getting lower while its accuracy is getting better. AM has been widely used in the fabrication of antennas e.g., horn antennas in [7-9], a lens antenna in [10], and waveguide-based arrays in [11-12].

In this thesis, we aim at exploring the possibilities offered by AM for designing actual 3D MO antennas. More specifically, our work is devoted to MORAs made of 3D PCs. The main objective is thus to extend the PC that has been proposed in our lab a few years ago [2] from its planar original version to a 3D one and to investigate the new capabilities brought by the third dimension.

This thesis has been done in IETR, France, in the frame of a collaboration with the Antonine University, Lebanon and University of Fez, Morocco. The selective laser melting (SLM) 3D printing technology is available in our collaborative lab in Fez.

The 3D cell proposed in this thesis is a waveguide-type cell since it can be seen as a short length of metal waveguide (with a short-circuit termination). Both its cross-section and its height provide many degrees of freedom to control the operating mode and consequently the way it reflects an incident wave. It is thus an interesting phase-shifting cell for RA applications. In addition, other promising configurations are possible: if the short-circuited termination is replaced by an open one, the PC will

have the potential to also manipulate the transmission phase, which suggests transmitarrays (TA) can be designed. Finally, when working below cut-off, the waveguide-type cell almost behaves as a perfect conductor (with no wave entering into the waveguide), and it can be used to achieve a quite classical metal reflector. All these additional options further enlarge the research scope of this thesis. Consequently, this thesis also proposes some hybrid designs combining parabolic reflector, RA and TA.

The thesis is structured as follows.

The first chapter presents the state of the art of existing RA and TRA structures, as well as the introduction of 3D printing technologies. Chapter 2 introduces two different waveguide-based cells (simple cell (SC) and PC). Each cell has two different configurations depending on the applied termination. As already said, the short-circuited configuration is applicable for RA while the open-ended one also enables to produce a transmitted beam. The operation principle of the cells is analyzed in detail. Also, the PC is modeled by an equivalent circuit.

A dual band antenna that combines the functionality of a parabolic reflector and a RA is proposed in chapter 3. It is synthesized using the SC. Both the used unit cell and the proposed dual band antenna are investigated in detail. Finally, the dual band antenna is fabricated and measured to validate its performance. A RA made of PCs with fixed height is designed, fabricated and measured in chapter 4. Its performance is further improved by varying the height of each cell to minimize the average phase error. Also, two transmit-reflect-arrays (TRAs) are designed using this PC. The designed TRA can generate both a transmitted beam and a reflected beam simultaneously.

Finally, two modified PC are proposed in chapter 5 to further enhance its behavior. The first variant is used to design a RA for dual band operation while the second variant is used to design a RA that generates two beams with orthogonal polarizations at the same frequency. A general conclusion is drawn in chapter 6.

Chapter 1 - State of the Art

1.1 Introduction to high gain antennas 26
1.1.1 Reflector antennas 26
1.1.2 Array antennas 26
1.1.3 Reflectarray antennas 26
1.1.3.1 Phase-shift distribution on the reflectarray aperture 27
1.1.3.2 Advantages of reflectarray antenna 28
1.1.3.3 Disadvantages of reflectarray antenna 29
1.1.4 Transmitarray antennas 29
1.1.5 Conclusion 29

1.2 Different reflectarray antennas 30
1.2.1 The first reflectarray antenna 30
1.2.2 Microstrip reflectarray antennas 30
1.2.2.1 Reflectarray cells with time delay line. 31
1.2.2.2 Reflectarray cells with variable size 31
1.2.2.3 Reflectarray cells with variable rotation angle 33
1.2.3 Metal-only reflectarray antennas 33
1.2.3.1 Metal-only reflectarray antennas using slot-type cells 34
1.2.3.2 Metal-only reflectarray antennas using waveguide-type cells 36
1.2.3.3 Metal-only reflectarray antennas using metallic blocks 40
1.2.4 Comparison between different reflectarray antennas 41

1.3 Different transmit-reflect-arrays 43

1.4 Fabrication of reflectarray antennas 43
1.3.1 Introduction of different additive manufacturing technologies 44
1.3.1.1 Fused deposition modeling 44
1.3.1.2 Stereolithography 45
1.3.1.3 Material Jetting 3D printing 45
1.3.1.4 Selective Laser Sintering 46
1.3.1.5 Metal 3D printing 47
1.3.1.6 Binder Jetting 48
1.3.1.7 Reasons for choosing selective laser meting 3D printing technology 49
1.3.2 Reflectarray antennas using 3D printing technologies 49

1.5 Conclusion 51

Chapter 1 - State of the Art

1.1 Introduction to high gain antennas

The long-distance transmission requires high-gain antennas, which can be achieved, among other antenna solutions, by both parabolic reflector and phased array [1]. In recent years, two new types of high-gain antenna, the RA and the TA, have gradually become popular. In this section, reflector antennas, phased array antennas, RAs and TAs, along with their advantages and disadvantages, are described respectively.

1.1.1 Reflector antennas

Reflectors are one of the most practical types of electrically large antennas. When wireless communication was first demonstrated experimentally by Hertz in 1887, a dipole-fed cylindrical parabolic antenna, which is believed to be the first reflector antenna, was used. Since then, reflectors have become the most widely used high-gain antenna in communications, radio astronomy, remote sensing, and radar [13]. In addition, reflector antennas have the advantages of structural simplicity, low mass and mature design [14]. The common shape of reflector antennas is parabolic and its principle is shown in Fig.1.1a. It can be seen that the parabolic surface reflects the incident waves from a feed antenna and collimate the beam (pencil beam) in a direction determined by the reflector's geometry. There is no bandwidth limitation for the parabolic reflector owing to the true time delay provided by the reflector itself. Nevertheless, it is the curved surface that makes the parabolic reflector difficult to fabricate, in particularly at higher microwave frequencies.

1.1.2 Array antennas

Array antenna, which is formed by using several smaller antennas, is an alternative approach to realize a large radiating aperture [15]. The first array antenna was reported over 100 years ago [16]. The unique characteristics of array antenna were explored by several other scientists [17-19]. Since then, array antenna engineering evolved rapidly. The microstrip patch antenna proposed by Deschamps in 1953 [20] revolutionized array engineering. Microstrip antenna arrays have since then been widely used in modern phased array systems.

In most cases, the elements of an array are identical and arranged periodically. The radiation of an array antenna is the combination of the radiations of all elements in the array. It is determined by the spacing between two adjacent elements, the magnitude and the phase of the excitation applied to each element and the radiation pattern of single element. To achieve wide-angle beam scanning electronically, an array antenna must be equipped with controllable phase shifters, which make the array antenna become expensive due to its complicated beamformer and many high-cost amplifier modules. The amplifier modules must be used to alleviate the problem associated with power inefficiency that occurs in the high-loss beamformer and phase shifters [21].

1.1.3 Reflectarray antennas

The reflectarray [22, 23] is an antenna consisting of either a flat or a slightly curved reflecting surface and an illuminating feed antenna as shown in Fig.1.1b. RA can be seen as a combination of planar arrays and parabolic reflectors with the advantages of high gain, low profile, low cost and easy manufacturing.

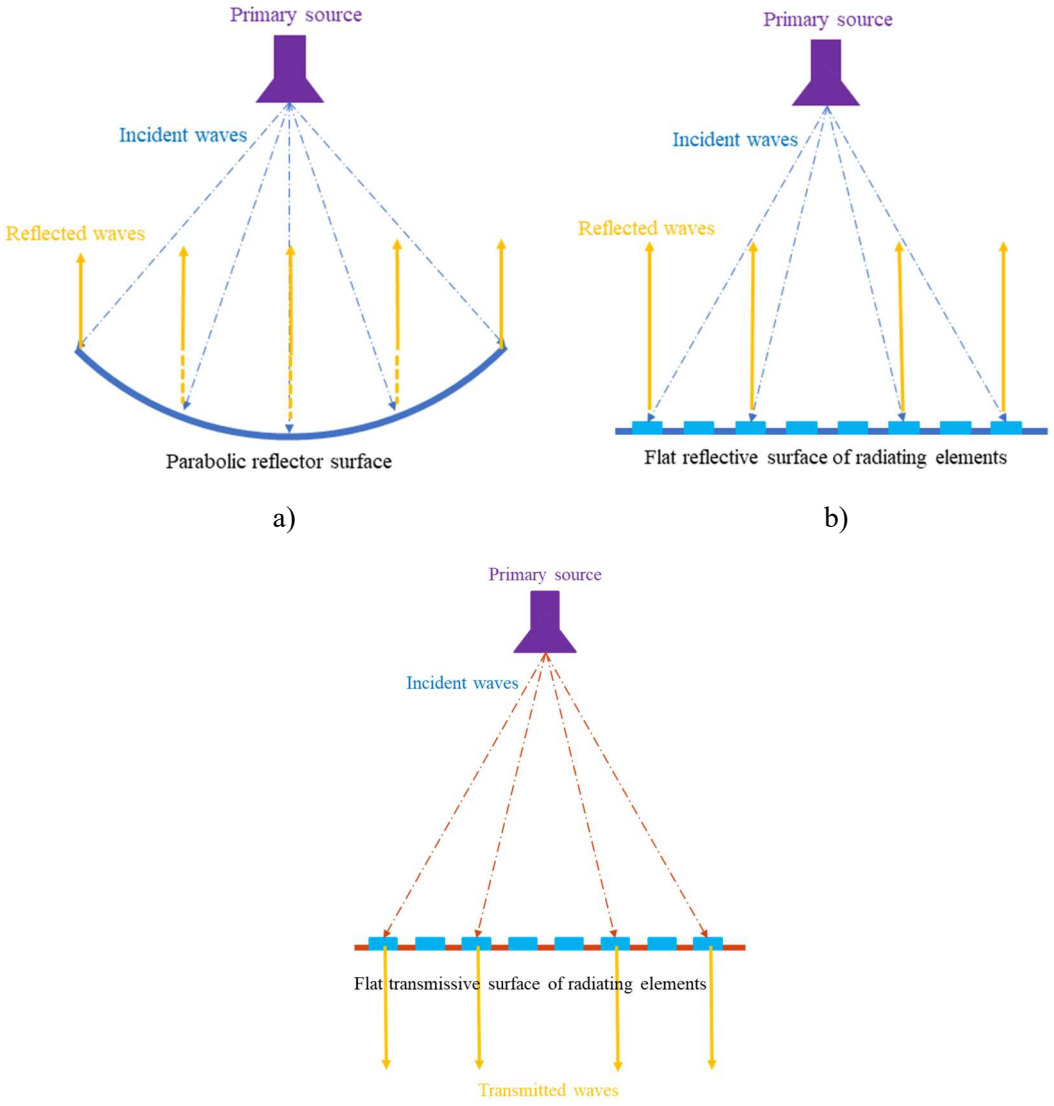

Fig.1.1 Principle of: a) Parabolic reflector. b) Reflectarray. c) Transmitarray.

1.1.3.1 Phase-shift distribution on the reflectarray aperture

The parabolic reflector antenna collimates the reflected beam by using its geometric surface. The RA is more like an array antenna whose beam is collimated in a certain direction by assigning a progressive phase distribution to the cells [24-25]. The geometrical parameters of a RA are shown in Fig.1.2. Typically, a horn antenna pointing to the center of RA is used as a feed antenna. The cells in the RA are assumed to be in the far field of the horn antenna and the incident electromagnetic field on each cell in the RA is approximated by a plane wave with a certain incident angle. The electromagnetic fields radiated by the horn antenna propagate as a spherical wave which originates from the phase center of the horn antenna. Therefore, the incident electromagnetic fields on the reflectarray aperture have a phase proportional to the distance they have traveled, which is referred to as spatial phase delay [26]. In this thesis, the phase shift of incident electromagnetic field caused by the cell in the RA is referred to as reflection phase.

The reflection phase of a cell in the RA should compensate for the spatial phase delay. It is given by:

$$\emptyset_{spd} = -k_0 R_i \tag{1.1}$$

where R_i is the distance between the phase center of the feed and the i^{th} cell in the RA and k_0 is the wave number in free space at the center frequency. To scan the collimated beam in any direction, a progressive phase should be added to the aperture. Its vector form is given by:

$$\emptyset_{pp} = -k_0 \vec{r_i} \cdot \hat{r}_0 \tag{1.2}$$

where $\vec{r_i}$ is the position of the i^{th} cell in the RA and $\hat{r}_0$ is the direction of main beam as shown in Fig.1.2. The position of each cell in the RA is expressed as (x_i, y_i, z_i) and the direction of main beam is expressed as (θ_0, φ_0). The required phase shift on the reflectarray aperture needs to compensate for the spatial phase delay and add the progressive phase to the aperture. The required phase shift of the ith cell, which is used to produce a pencil beam in a desired direction, can thus be given by:

$$\phi_i^{des} = -\emptyset_{spd} + \emptyset_{pp} = k_0\big(R_i - (x_i sin\theta_0 cos\varphi_0 + y_i sin\theta_0 sin\varphi_0 + z_i cos\theta_0)\big) + \emptyset_{off} \tag{1.3}$$

where $\emptyset_{off}$ is a relative phase added to all the cells in the reflectarray aperture and its value is a constant. Note that the equation (1.3) can be used for both flat and non-flat RA. The z_i coordinate is usually set to zero in the case of a flat RA by properly locating the origin of the coordinate system. In addition, for shaped beams, the progressive phase in equation (1.2) should be replaced by an appropriate phase distribution.

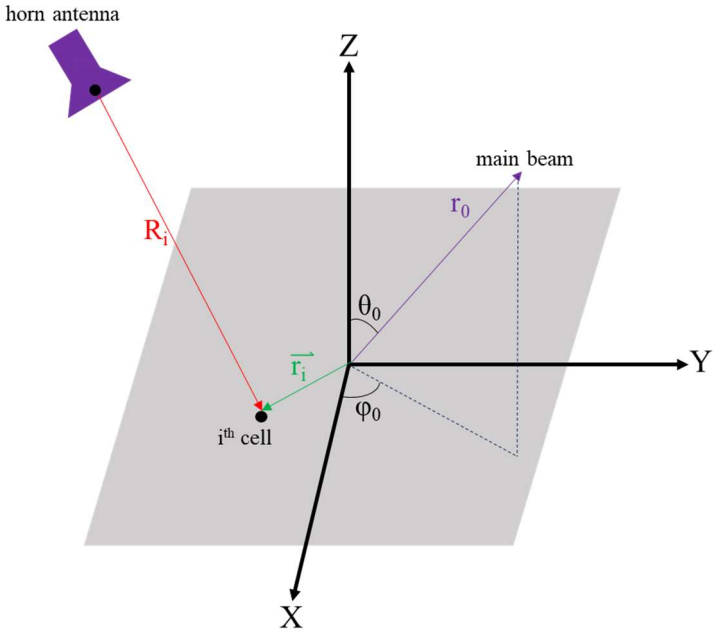

Fig.1.2 Geometrical parameters of a RA.

1.1.3.2 Advantages of reflectarray antenna

Similar to a parabolic reflector, the RA can achieve very good efficiency (typically greater than 50 percent) for a very large aperture since no power divider is needed and thus very little resistive insertion loss is encountered here [21]. On the other hand, very similar to an array antenna, the RA can have its main beam designed to tilt at a large angle (> 50°) from its broadside direction [21].

However, compared to the parabolic reflector, the RA has a planar reflecting surface (or slightly curved reflecting surface), which makes it easier to be fabricated. In addition, it replaces the complex feed network used in an array antenna with a simple feed antenna.

Another major feature of this antenna is that, with a large number of elements in a RA having elemental phase adjustment capability, it can achieve very accurate contour beam shape by using a phase

synthesis technique [27-28]. Also, a multi-beam RA with single feed can be realized using the alternating projection method [29].

1.1.3.3 Disadvantages of reflectarray antenna

Unlike the infinite bandwidth of parabolic reflector, the RA has a distinct disadvantage of narrow bandwidth. The narrow bandwidth is affected by both the narrow bandwidth of the phase shifting cell, which will be discussed later, and the flat nature of the reflectarray aperture. The flat surface of RA leads to a differential spatial phase delay [21], which can be explained by referring to Fig.1.3. The phases of incident field when it reaches the center cell and the edge cell are expressed as:

$$\varphi_1^{inc} = \frac{-2\pi}{\lambda_0} S_1 \tag{1.4}$$

$$\varphi_2^{inc} = \frac{-2\pi}{\lambda_0} S_2 \tag{1.5}$$

where S_1 and S_2 are two paths from the feed to the cells in the reflectarray. The difference between the two phases is thus given by:

$$\Delta\varphi = \varphi_2^{inc} - \varphi_1^{inc} = \frac{-2\pi}{\lambda_0} \Delta S \tag{1.6}$$

where ΔS is the difference between two paths. Its value may be multiples of the wavelength at the center frequency. The phase difference $\Delta\varphi$ varies with frequency. The cells in the RA, however, are designed only to compensate the spatial phase delay at the center frequency. A frequency excursion error thus occurs in the re-radiated phase front, which will result in gain reduction, pattern deterioration, and ultimately, bandwidth limitation of the designed RA. A method to increase the bandwidth is to use, instead of a completely flat reflectarray surface, a concavely curved reflectarray with piecewise flat surfaces [21].

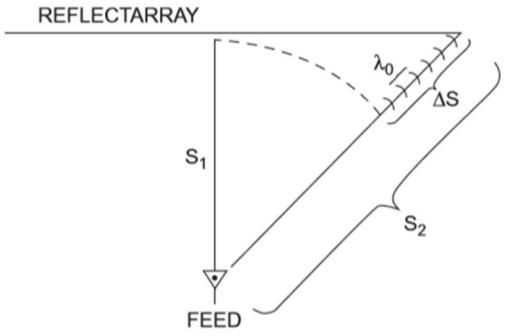

Fig.1.3 Differential spatial phase delay of flat reflectarray[21].

1.1.4 Transmitarray antennas

A transmitarray is an antenna consisting of an illuminating feed source and a thin transmitting surface [30] as shown in Fig.1.1c. As an emerging concept, the TA combines the favorable features of optic theory and antenna array techniques, leading to a low profile conformal design with high radiation efficiency and versatile radiation performance [30]. The main difference with RA is that a RA produces a reflected beam while a TA generates a transmitted one. At the same time, TAs can avoid certain limitations associated to RA, such as feed-blockage.

1.1.5 Conclusion

This section first introduces the parabolic reflector and the phased array. After describing their advantages and disadvantages, the concept of RA is introduced. RA combines the parabolic reflector and the phased array. It is used to produce a collimated beam by varying the phase distribution on the

RA aperture. It has the advantages of high gain, low profile, low cost and easy manufacturing. The main disadvantage of RA is narrow bandwidth. The narrow bandwidth is affected by both the narrow bandwidth of the phase shifting cell and the flat nature of the RA aperture. Also, the functionality of TAs is introduced. Instead of a reflected beam, a transmitted beam can be produced by a TA. In addition, the feed blockage can be completely avoided by a TA.

1.2 Different reflectarray antennas

Equation (1.3) illustrates the calculation of the required phase shift distribution in a desired direction. In order to collimate the beam in any direction and provide a good performance, the unit cell in a RA must be able to achieve a full cycle of phase shift (360°). The previous subsection introduced the concept of RA, while this subsection will give a brief introduction of the development of reflectarray and different phase-shifting cells. More precisely, this subsection focuses on the microstrip RAs and MORAs.

1.2.1 The first reflectarray antenna

The first RA (see Fig.1.4) was designed during the early 1960s using short-ended waveguides with variable heights [22]. It is a MORA. The incident electromagnetic waves from the feed antenna enter the waveguides from the open ends and propagate inwards. They are reflected back by the shorted-ends and re-radiated out from the open-ends. The desired beam can be controlled by varying the height of each waveguide. However, the operating frequency strongly affects the size of these waveguides. At that period, the microwave frequencies used in many wireless communication systems were relatively low. Therefore, the realized RA was so bulky and heavy that it was not attractive compared to other antennas.

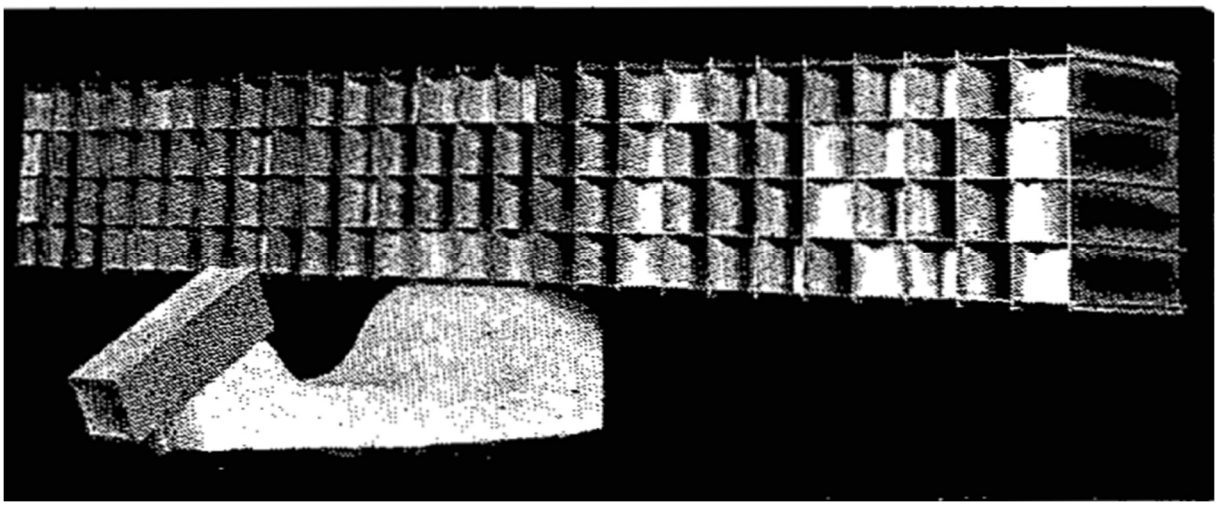

Fig.1.4 The first reflectarray antenna [22].

1.2.2 Microstrip reflectarray antennas

With the development of the printable microstrip antennas, the microstrip RAs were investigated and the first microstrip RA was designed by Malagisi [31] in 1978. The microstrip RA has become the most common RA. Compared to the first RA [22], the advantages of low mass and low profile can be easily achieved by the microstrip antennas. The different microstrip RAs are introduced respectively based on their phase tuning methodologies. There are three main different approaches to tune the phase of reflectarray cells [26]:

1) Reflectarray cells with time delay line.

2) Reflectarray cells with variable size.

3) Reflectarray cells with variable rotation angle.

Next, these three approaches are briefly introduced.

1.2.2.1 Reflectarray cells with time delay line

The cells with time delay lines are shown in Fig.1.5. The unit cell consists of a patch and a variable time delay line [32-34]. When the incident wave reaches the surface of the patch, it is received by the patch and transferred into a guided wave. The guided wave propagates in the time delay line and is reflected back by the open-end. Finally, it is reradiated by the patch. The reflection phase is thus determined by the length of time delay line. For this type of unit cell, the time delay line must match the patch, if not, part of the guided wave will be reflected by the patch before going into the time delay line. In this case, the reflected wave will be the superposition of two components and the reflection phase will no longer vary linearly with the length of time delay line.

The time delay line, however, always takes up a large space, which inevitably reduces the aperture efficiency of the RA. An improved structure was proposed by moving the transmission line downwards below the ground [35-36]. The space thus can be saved by etching a slot in the ground plane to make the transmission line couple to the patch through it.

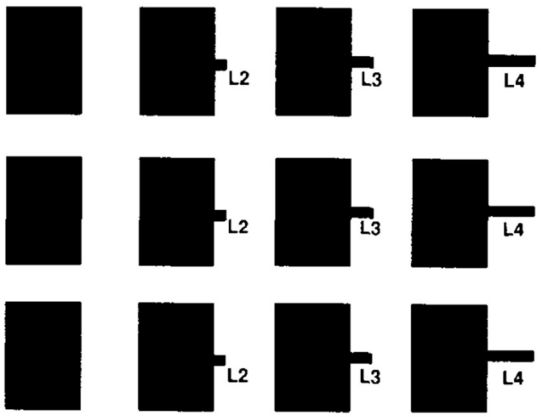

Fig.1.5 Schematic models of reflectarray cells with time delay lines of different lengths [33].

1.2.2.2 Reflectarray cells with variable size

The reflectarray cells with variable size were first designed in [37-38] for printed crossed dipoles and rectangular patches (see Fig.1.6). For this type of cell, each size corresponds to a resonant frequency. If the size of a patch is tuned, its resonant frequency will be changed and so the reflection phase. Compared to the cells with time delay lines, the cells with variable size can suppress the cross polarization caused by the parasitic radiation from time delay lines and increase the aperture efficiency. Since the reflection phase is controlled by the size of the patch and is sensitive to it, a precise fabrication technique is required for the RA made of this type of cells.

Ideally, one single resonance allows one complete phase cycle (360°). The phase range actually achieved, however, is often less than 360°, which may degrade the performance of the designed RA such as bandwidth and gain. One of the most effective solutions is to use multi-layer stacked patches (see Fig.1.7) which can improve the bandwidth by a few percent or more than ten percent [39-40]. This multi-layer configuration can provide not only a phase range far in excess of 360°, but also a smooth phase-versus-size characteristic owing to the introduced multiple resonances. However, the multi-layer cell, especially its multi-layer substrates, makes the fabrication more complex. The single-layer multi-resonance reflectarray cells [2, 41-42] are thus proposed to reduce the fabrication cost and increase the gain and bandwidth of RA. As shown in Fig.1.8, the unit cell in [2] consists of two square metallic rings and a square metallic patch. The reflection phase is tuned by varying the size of inner metallic ring. The

evolution of cell geometry is illustrated in Fig.1.9. At the initial step, the metallic ring overlaps with the metallic patch and it will then arise from the square patch. At the intermediate steps, the metallic square ring gets larger, moving towards the outer border of the cell. At the final step, the metallic square ring disappears and the cell comes back to its initial step. Therefore, this cell is referred to as PC. Since the PC has a smooth evolution of cell geometry, the abrupt variation of cell geometry, which can be responsible for severe degradations in the reflectarray pattern [43], can be reduced.

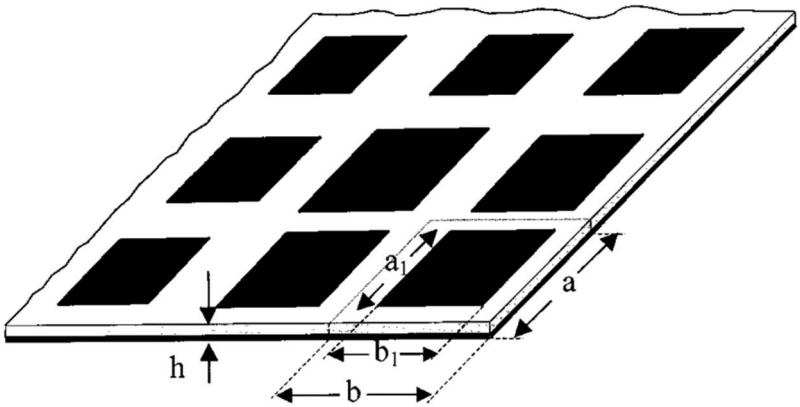

Fig.1.6 schematic models of reflectarray cells with variable size [39].

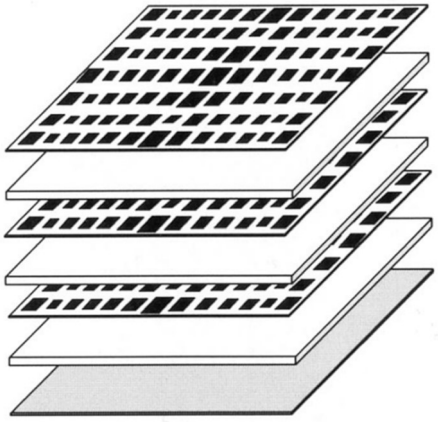

Fig.1.7 schematic model of a three-layer reflectarray using the cells with variable size [40].

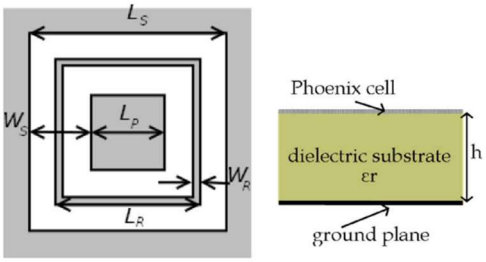

Fig.1.8 General geometry of the first phoenix cell [2].

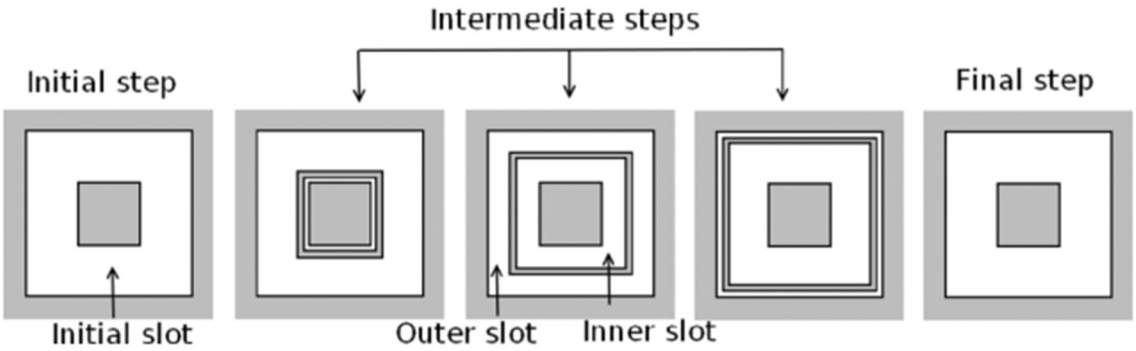

Fig.1.9 Phoenix cycle: Evolution of the cell geometry over a complete 360° cycle [2].

1.2.2.3 Reflectarray cells with variable rotation angle

Unlike the first two techniques, the cells using variable rotation technique are only for circularly polarized (CP) RA which is excited by CP electromagnetic waves. This technique is based on the fact that rotating a CP antenna element about its origin by ψ, will change the radiated phase by twice this angle where the advance or delay of the phase depends on the sense of rotation [23]. This technique was first applied to RA [44], as shown in Fig.1.10, using patch cells with attached phase delay lines. The 180-degree phase difference between the reflected waves in the orthogonal directions can be achieved by properly varying the length of two transmission lines. Therefore, 2ψ reflection phase can be achieved by rotating the patch by an angle ψ. Although this type of cell increases the complexity of the RA design, it reduces the requirements for antenna fabrication accuracy.

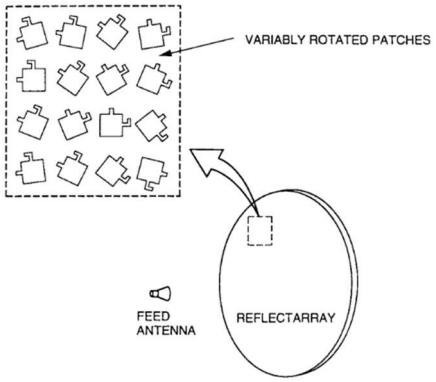

Fig.1.10 Circularly polarized microstrip reflectarray with elements having variable rotation angles [44].

1.2.3 Metal-only reflectarray antennas

The multi-layer configuration is usually used to improve the performance of microstrip RAs [39-40]. Its poor thermal behavior, however, makes it not suitable for some applications, such as multi-band operation. In addition, its multi-layer substrate significantly increases the cost of fabrication. In this case, the single-layer microstrip RAs seem more promising. Nevertheless, the dielectric materials they use may cause lots of problems. First of all, they may limit the gain due to the losses they bring, especially at high frequencies. In addition, for RAs that work in harsh environments, such as space, the use of dielectric substrates is not recommended due to undesired associated effects. One of the main concerns is a phenomenon known as outgassing [4]. For a microstrip antenna, gas may be trapped in it during the manufacturing process, and it can be released under certain conditions, such as the high-vacuum environments of space. Another concern for the dielectric materials in space is the impact of the large swings in temperature that can take place within a spacecraft or satellite and how these temperature swings can alter the dielectric materials' characteristics, such as its dielectric constant [4]. At the same time, some space applications may need to survive high-voltage conditions, with the capability of handling high dielectric breakdown voltage [4]. In such a situation, the MORA is preferred as it avoids

the intrinsic problems brought by dielectric materials. The MORAs in this thesis are roughly categorized into three groups:

1) MORAs using slot-type cells

2) MORAs using waveguide-type cells

3) MORAs using metallic blocks

This part makes a detailed introduction to these different MORAs.

1.2.3.1 Metal-only reflectarray antennas using slot-type cells

The slot-type cells have one or more slots machined in a metallic sheet. The incident wave is coupled to these slots and re-radiated out. A metallic ground plane is placed under the metallic sheet so that the incident wave is totally reflected. The geometry of these slots is used to tune the reflection phase. Since the slot-type cells use no supporting dielectric substrate, they must be unified as a whole piece of metallic structure. They therefore lose some degrees of freedom of design compared to slots with dielectric support. Instead, their simple structure leads to a very simple fabrication process, such as the conventional machining technologies.

The first slot-type MO cell, as shown in Fig.1.11, was reported in [45]. It consists of a slot in a metallic sheet and many metallic stubs which are backed by a metallic ground plane. The reflection phase is tuned by the length of metallic stubs. However, the achieved phase range is only 221°, which will degrade the performance of the MORA.

A slot-type MO PC was proposed in paper [6]. The concept of PC was first conceived in paper [2] for the design of broadband RA. Compared with the cell in paper [6], the complete phase circle can be easily realized by MOPC. The MOPC and its full element changing cycle are shown in Fig.1.12. It consists of double square loops, a square patch, and a connecting stub that unites them into a whole piece. The reflection phase is tuned by the size of middle loop. The slot-type MORA has the same evolution of cell geometry as the microstrip PC in [2]. At the initial stage, the size of middle loop is equal to the size of the square patch. The middle loop then appears as its size increases. At the final stage, the size of middle loop is equal to the size of outer loop and the middle loop disappears again. The cell thus comes back to its initial geometry, which justifies the appellation of PC. Unfortunately, compared to the original PC in [2], since the dielectric layer has been removed, there is no support anymore for the different isolated metal elements and this is why a connecting strip is needed to attach them together. As a consequence, the PC loses in this case its 90° rotational invariance and subsequently its capability to deal with dual linear polarizations.

Fig.1.11 Metal-only slot cell [45].

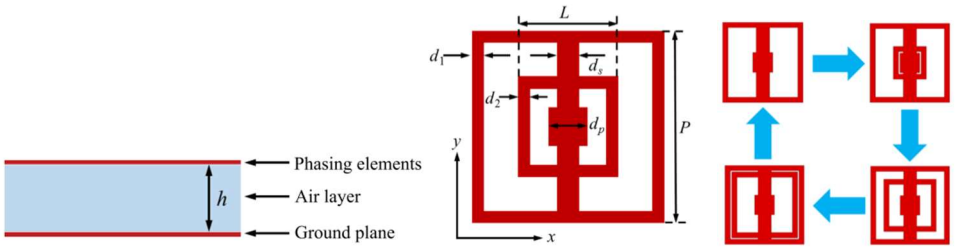

a) b) c)

Fig.1.12 Slot metal-only phoenix cell [6]: a) sectional view, b) top view, c) evolution of cell geometry.

The previous two cells are designed to deal with linear polarizations. Hence, a slot-type MO cell supporting both left-hand circular polarization (LHCP) and right-hand circular polarization (RHCP) is proposed in [46]. The proposed MO cell (see Fig.1.13) consists of a square slot at the center of the unit cell and four L-slots, each of which is composed of two connected straight slots of different physical lengths with each L-slot of equal electrical length. The length of the L-slots is adjusted to tune the reflection phase of the MO cell. The measurement results, however, show that the proposed MORA has a narrow bandwidth of 6.85% (defined for a 1dB-decrease in the antenna gain).

To increase the bandwidth, a MORA with separated layers, as shown in Fig.1.14, is proposed in [47]. A dumbbell-cross slot cell (see Fig.1.14) is used in the proposed MORA. The reflection phase is tuned by the size of 'dumbbell'. Since the field distribution over the aperture has a Fresnel structure and the range of reflection phase is limited, the presence of phase errors due to frequency changing is inevitable. The mentioned phase errors can be improved by taking advantage of the spatial separation of the antenna layers. As shown in Fig.1.14 (c), the proposed MORA consists of 3 separated layers. The distance between top layer and middle layer is half a wavelength at the center frequency, which corresponds to a phase shift of 2π. The bottom layer is a ground plane. The achieved 3-dB gain bandwidth is 18%.

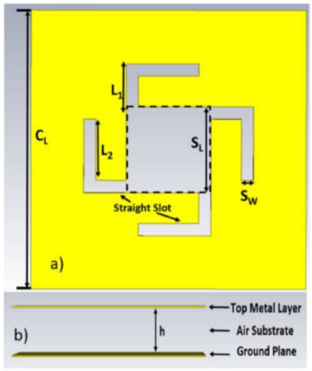

Fig.1.13 The MO cell in [46]: a) top view, b) sectional view.

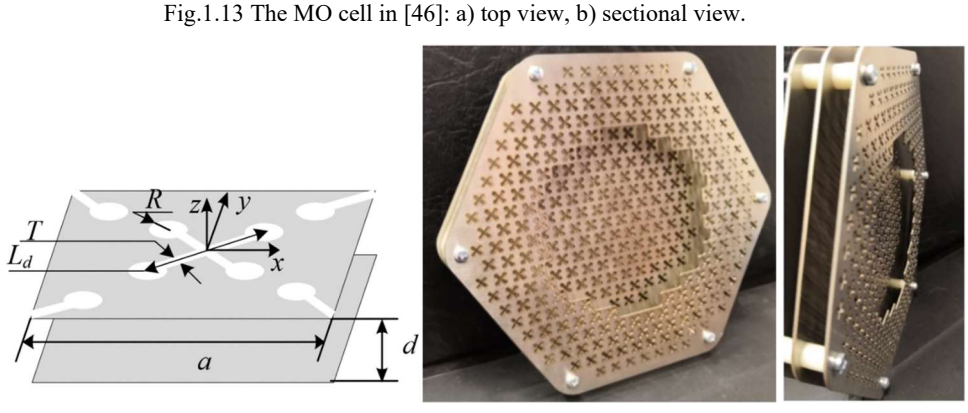

a) b) c)

Fig.1.14 MORA with separated layers in [47]: a) MO cell, b) front view of prototype, c) side view.

A MORA using new slot-type cells is designed in [48]. As illustrated in [45, 6, 46, 47], the unit cells described above use a shared air substrate. The MORA in [48], however, isolates the air substrate and forms separated cavities for each cell. As shown in Fig.1.15, the unit cell in [48] consists of slots shaped in a circular pattern and backed with a cavity. It is an inductive cell of order one and the reflection phase is controlled by the length of the slot. The proposed unit cell is a bit more complex than the previous slot-type cells [45, 6, 46, 47], since it requires a vertical metal. Therefore, it does not only belong to slot-type cells, but also to full 3D structures. A CP three-panel deployable MORA is designed. The analytical results show a maximal directivity of 28 dBi with a half-power beam width of 8°.

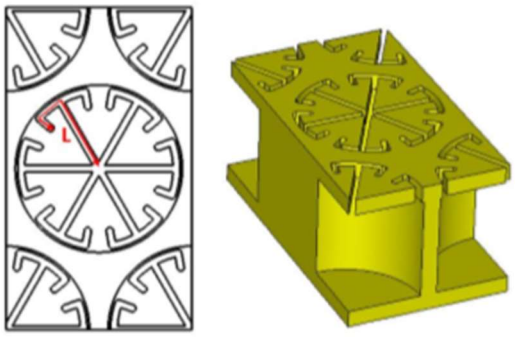

a) b)

Fig.1.15 Schematic view of the unit cell in [48]: a) top view, b) 3D view.

1.2.3.2 Metal-only reflectarray antennas using waveguide-type cells

The waveguide-based unit cells are widely used in MORAs. Furthermore, the first RA [22] used a waveguide as its phase-shifting cell. Their principle is similar to the unit cells with time delay lines (see section 1.2.2.1). Typically, these unit cells consist of an open-ended waveguide (rectangular waveguide, circular waveguide or parallel plate waveguide…) with a short circuit termination. The waveguide receives the electromagnetic wave, and transfers it into a guided wave along the waveguide which operates as a transmission line. The guided wave reflects back from the short circuit termination and is re-radiated by the waveguide. The difference between the waveguide-type cell and the cell with time delay line is that the characteristic impedance of the waveguide may not match the wave impedance in free space, which makes part of the incident wave reflect before entering the waveguide. The overall reflected wave thus is a combination of two different reflection processes and the reflection phase does no longer vary linearly with the length of the waveguide. Since the waveguide-type cell is a 3D structure, it provides more degrees of freedom to design MORAs. The MORAs made of waveguide-type cells can be fabricated by both conventional machining technologies and 3D printing technologies.

Two 2D MORAs consisting of rectangular metallic grooves are designed in papers [49-50]. As shown in Fig.1.16, the unit cell in [50] consists of a section of parallel plate waveguide with a short-circuit termination. These waveguides allow the propagation of TEM mode electromagnetic waves. Its reflection phase is tuned by the width and depth of the groove. After an optimization for the width of the groove, the reflection phase varies smoothly with the depth of the groove. At the end, endfire radiation can be achieved with out-of-phase cells and by using a half wavelength inter-element spacing.

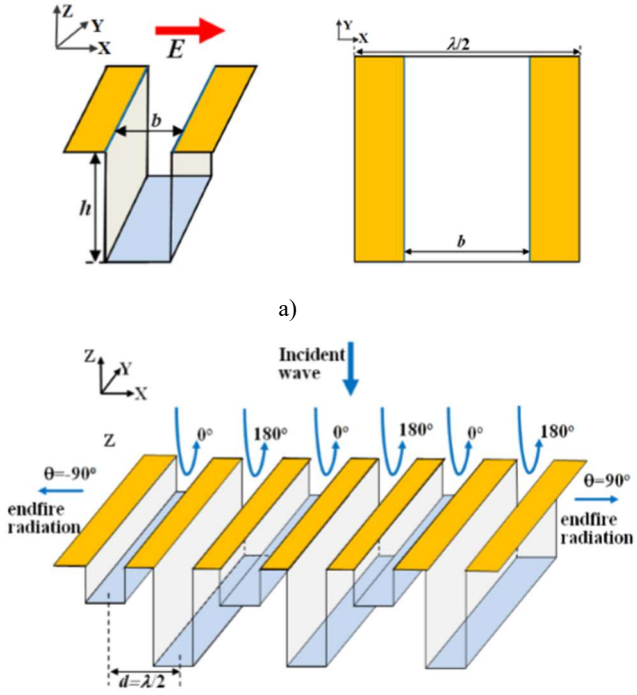

Fig.1.16 MORA made of rectangular metallic grooves: a) geometry of the unit cell. b) global view of the MORA with endfire radiation [50].

The MORA in paper [51] is also composed of multiple rectangular grooves. The difference from the previous two MORA, as shown in Fig.1.17, is that the unit cell is based on a rectangular waveguide instead of a parallel plate waveguide. Similarly, the depth of metallic groove is used to control the reflection phase. The rectangular waveguide allows the propagation of the fundamental TE_{10} mode. Unlike the TEM mode in parallel plate waveguide, there is a limitation of cutoff frequency for the TE_{10} mode in rectangular waveguide. In order to enable the propagation of the fundamental mode, the width of the metallic groove is set to a value that is greater than the half wavelength at its central frequency, which may result in grating lobes.

Paper [52] proposes a MO unit cell (see Fig.1.18) consisting of a square base and metallic cylinder with a cuboid-shaped notch. The cuboid shaped notch corresponds to a section of parallel plate waveguide and the reflection phase is tuned by its width and depth. As illustrated in Fig.1.18, the TM polarization can penetrate into the cuboid-shaped notch but TE polarization cannot. Based on this principle, the 1-bit reflection phase (0 and 180 degrees) is achieved by simply rotating the cell by 90° around Z axis. Then a linearly polarized MORA made of such cells was designed.

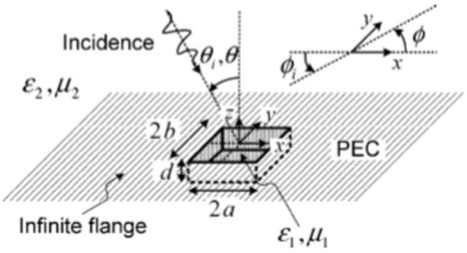

Fig.1.17 Geometry of a metallic rectangular groove in a perfectly conducting plane [51].

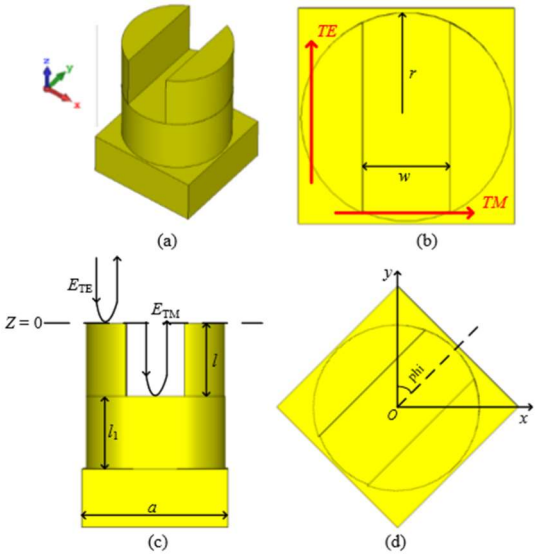

Fig.1.18 Geometries of the proposed cell in [52]: a) perspective view, b) top view, c) side view, d) top view with a phi angle offset.

The previous MORAs were designed for linear polarization, while the MORAs in paper [53-56] support circular polarization. As illustrated in Fig.1.19, the unit cell in [53] consists of a cuboid metallic base and a radiating structure which are connected to each other through a supporting rod. The radiating structure is composed of a H-shaped structure, in which there are a split circular slot and a rectangular slot. In this case, the unit cell is equivalent to a short-ended circular waveguide with two ridges. The 90 degrees phase difference between x-polarized and y-polarized reflected waves (the condition for circular polarization) is achieved by selecting appropriate geometries for the unit cell. A circular polarized MORA is thus designed by applying the variable rotation technique. The simulation results show that the antenna has a maximum gain of 33.1 dBi and a maximum aperture efficiency of 58.76%. A similar MORA cell, as shown in Fig.1.20, is proposed in paper [54]. The unit cell consists of a circular outer waveguide, an elliptical inner conductor and a hexagonal base. There is a phase difference between the reflection phases of x-polarized wave and y-polarized reflected waves owing to the presence of the elliptical conductor in the center. A circular polarized MORA is synthesized by using the same process as in [53]. The measurement results show that a maximum gain of 26.2dBi and a maximum aperture efficiency of 66% are achieved.

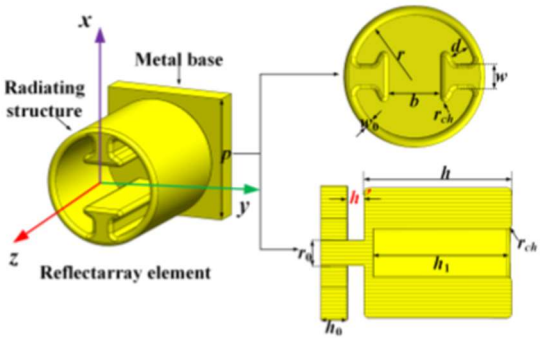

Fig.1.19 Geometry of the unit cell in [53].

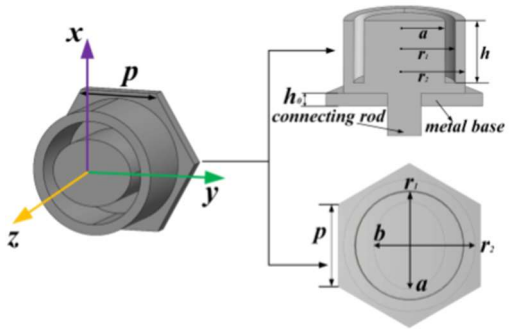

Fig.1.20 Geometry of the unit cell in [54].

The MORA in paper [55] has the capability to independently control the RHCP and LHCP incident waves. As shown in Fig.1.21 a), the unit cell consists of a metal waveguide in the bottom and a septum blade-liked structure above it. As illustrated in Fig.1.21 b), LHCP incidence cannot penetrate into the waveguide and the reflected wave is collimated only by rotating the cells in the MORA. Instead, the RHCP incidence is able to penetrate into the waveguide and the reflected wave is collimated by both rotating the cells and varying the length of the waveguide. Therefore, the LHCP and RHCP can be controlled independently.

In paper [56], a wideband CP MORA is proposed. The difference with the MORAs in paper [53-56] is that the CP wave is achieved by independently controlling orthogonal polarizations without using the variable rotation technique. Fig.1.22 illustrates the geometric evolution of the MORA unit cell from its original design. The unit cell is a combination of vertical and horizontal parallel plates whose groove depths are varied independently for each polarization. Unlike the unit cell introduced in [49-50], the unit cell in [56] allows the propagation of TEM mode for both orthogonal polarizations. At the same time, it provides a fairly linear phase response along frequency. A CP MORA using a linearly polarized feed is thus synthesized. Compared to the circular polarized MORA in paper [53-55], a wideband characteristic (a 1.5dB bandwidth of 43.9%) is realized.

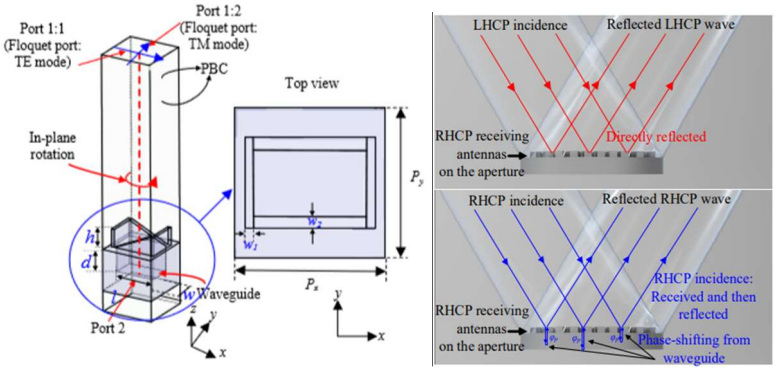

a) b)

Fig.1.21 MORA in [55]: a) unit cell geometry, b) operating principle of the MORA.

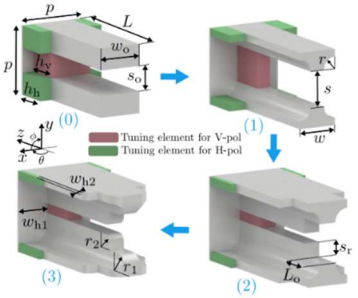

Fig.1.22 Design evolution of the unit cell in [56]

The previously mentioned RAs were only used to collimate the incident waves from a feed antenna. The RA in [57], however, does not only deal with the collimation, but it also achieves a filtering functionality where only the incident wave in the target frequency band is collimated. The proposed unit cell consists of two-section open-ended metallic waveguides as shown in Fig.1.23 a). The operating frequency band is between the cutoff frequencies of two waveguides. As illustrated in Fig.1.23 b), if the operating frequency is less than the cutoff frequency of upper waveguide, the incident wave is directly reflected back, which is equivalent to the incident wave being "filtered out". If the operating frequency is greater than the cutoff frequency of bottom waveguide, the incident wave propagates through both waveguides and is finally radiated from the bottom open-end, which is also equivalent to the incident wave being "filtered out". If the operating frequency is greater than the cutoff frequency of upper waveguide and less than the cutoff frequency of bottom waveguide, the incident wave propagates in the upper waveguide and is totally reflected back at the entrance of bottom waveguide. In this case, the reflection phase of the unit cell is tuned by the height of upper waveguide and a collimated beam is generated in this frequency band. As a conclusion, when the incident wave has a frequency outside the operating frequency band of the RA, it is reflected directly or radiated at bottom end, which means the incident wave is not collimated. When the incident wave has a frequency within the operating frequency band of the RA, a collimated beam is produced. It is thus a filtering RA.

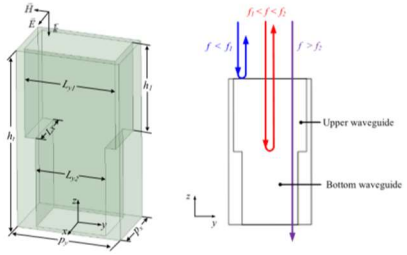

a) b)

Fig.1.23 Unit cell in [57]: a) geometry of the two-section waveguide cell, b) principle of the unit cell.

1.2.3.3 Metal-only reflectarray antennas using metallic blocks

For the cells using metallic blocks, the incident waves are directly reflected back by their metallic surface. Compared with previous MO cells, these cells are non-resonant cells, which leads to low losses. The phase of the incident wave is reversed by the metallic surface that can be viewed as a short circuit termination. The reflection phase is tuned simply by varying the height of metallic block or directly moving the metallic block. Unlike previous MORAs, the MORAs made of metallic blocks are non-planar structures in the sense the height varies from one cell to the other. They can be fabricated using both conventional machining technologies and 3D printing technologies.

The phase-shifting cells in papers [58-62] are made of metallic blocks. The unit cell in paper [58] consists of a circular cylinder and two pairs of auxiliary stubs which are supported by a metal layer with uniform thickness (see Fig.1.24). The reflection phase is varied by adjusting the height of circular cylinder and stubs. The unit cells in papers [59] and [60] consist of only one cuboid metallic block (see Fig.1.25). The reflection phase is compensated by the height of this metallic block. The unit cell in [61] and [62] is similar to the one in [58]. It has a different cross-section which is implemented for easy manufacturing (see Fig.1.26). The first five unit cells [58-62] are designed to deal with linear polarization in a single frequency band while the unit cell in [63] allows manipulating the reflection phase of CP wave in two frequency bands. It consists of an anisotropic metal brick mounted on a full metal ground (see Fig.1.27). Actually, the metal bricks between two adjacent cells form a parallel plate waveguide. The reflection phase thus can be tuned by properly adjusting the geometry of the metal brick. Since this unit cell does not exhibit any 90° rotational invariance, there is a phase difference between the reflected waves of orthogonal polarizations in both frequency bands. This characteristic means the unit cell is able to deal with CP by rotating the cell. In addition, the reflection phase of circularly

polarized waves is affected by the position of the cell and can be tuned by moving the cell along Z axis. Therefore, there are two different degrees of freedom to control the reflection phase in both frequency bands. A dual band circularly polarized MORA is synthesized using this cell.

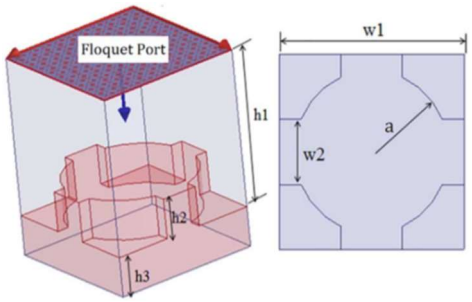

Fig.1.24 Geometry of unit cell in [58].

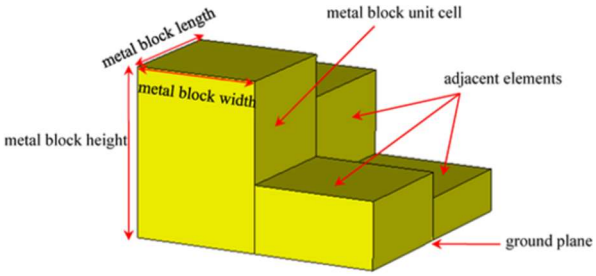

Fig.1.25 Geometry of unit cell in [59].

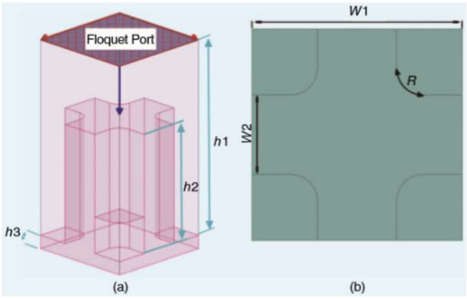

Fig.1.26 Geometry of unit cell in [61]

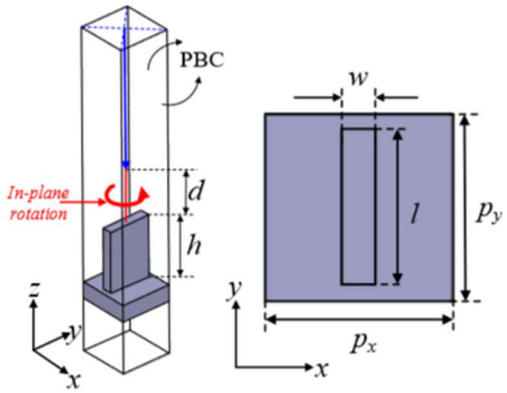

Fig.1.27 Geometry of unit cell in [63]

1.2.4 Comparison between different reflectarray antennas

The first RA is a MORA made of waveguide-type cells. It is bulky and heavy due to the low operating frequency. Microstrip RAs are the most common RAs. The advantages of low-mass and low profile can be easily achieved by the microstrip antennas. Nevertheless, as introduced in the previous

subsection, the dielectric materials they use may cause lots of problems. In such a situation, MORA is preferred. They are devided into three different categories: the MORA using slot-type cells, the MORA using waveguide-type cells and the MORA using metallic blocks. Table 1.1 summarizes the performances of different MORAs. The MORAs using slot-type cells can be easily fabricated by the conventional machining technologies. Since the dielectric material layer is removed, the top layer must be unified as a whole piece of metallic structure, which makes the slot-type cells lose some degrees of freedom of design. In addition, as shown in Table 1.1, the center frequencies of the MORAs using slot-type cells are lower than 22GHz, which may be limited by the used fabrication technologies. For the MORAs using metallic blocks, their performances are only determined by the height of each cell in the MORA. They need to combine the features of other cells to improve their functionality. For example, the unit cell in [63] achieves the dual band functionality by combining the waveguide-type cells and the cells using metallic block. Compared with the MORAs using slot-type cells, the operating frequency of the MORA using metallic block in [59] is significantly increased and the achieved frequency is 100GHz. At the same time, the achieved aperture efficiency of MORAs using metallic blocks is quite high (for example 50% and 50.1% in [58-59]) as they are non-resonant cells. A main disadvantage of the cells using metallic block is that they have only one degree of freedom, height, to tune the reflection phase. The waveguide-type cells, however, lead to many degrees of freedom to manipulate their characteristics. The reflection phase of these cells is affected by both their cross-sections and their lengths. The rectangular waveguides are used to tune the reflection phase of the cells in [51, 55]. To make the incident wave better propagate in the waveguide, the width of rectangular waveguide is increased to a value greater than the half wavelength at the center frequency. In this case, however, such a width may lead to grating lobes. To achieve a CP MORA, the variable rotation technique is used in [55]. Circular waveguides with asymmetric ridges are used in [53, 54] to synthesize CP MORA. The achieved aperture efficiency in [54] is 66%. In addition, the used ridges can effectively reduce the cutoff frequency and reduce the periodicity to avoid grating lobes. In order to avoid the restriction of cutoff frequency, parallel plate waveguides are used in [52, 56]. The unit cell in [56] has a very linear phase response and the achieved 3-dB bandwidth of MORA in [56] is very large (40.90%). As a summary, the waveguide-type cells have a better performance than the slot-type cells and the cells using metallic blocks. Therefore, the MORAs using waveguide type cells are the topic of this thesis.

Table 1.1 The performances of different MORAs

	Type	**Polarization**	**Freq (GHz)**	**Peak Gain (dBi)**	**1-dB Gain Bandwidth (%)**	**3-dB Gain Bandwidth (%)**	**3-dB Axial Ratio Bandwidth (%)**	**Aperture Efficiency (%)**	**3D printing**
[45]	slot	Linear	12.5	32.5	8.3	-	-	-	No
[6]	slot	Linear	12.5	33.9	12.8	-	-	53.8	No
[46]	slot	Circular	20	31.4	6.85	10.15	32.5	35	No
[47]	slot	linear	22	-	-	18	-	-	No
[48]	slot	Circular	8.2	28 (simulation)	-	-	-	-	No
[51]	waveguide	linear	75	42.3	-	-	-	30.2	No
[52]	waveguide	linear	26	18.9	20 (1.5-dB Gain Bandwidth)	-	-	-	No
[53]	waveguide	circular	10	33.05 (simulation)	-	-	-	58.76 (simulation)	No
[54]	waveguide	circular	10	26.2	-	-	-	66	No
[55]	waveguide	circular	27	24	-	-	22.2%	-	Yes
[56]	waveguide	circular	41	-	-	40.96	43.9	55.4	Yes
[57]	waveguide	linear	60	27.9	-	-	-	40.5	Yes
[58]	Metallic block	linear	12.2	33.2	-	-	-	50	No
[59]	Metallic block	linear	100	28	-	-	-	50.1	No
[63]	Metallic block	circular	24/32	24.3/24.5	-	10/9.3		38/26	Yes

1.3 Different transmit-reflect-arrays

As introduced before, a RA produces a reflected beam while a TA generates a transmitted one. The combination of both RA and TA functionalities in a single-feed high-gain TRA has been found of great interest to implement bi-directional radiated beams. For example, [64] proposes a TRA (see Fig.1.28) based on a multilayer amplitude–phase-modulated stack-up and employing sparse-array concepts. Similar antennas that combine TA and RA are proposed in [65-70]. For these antennas, however, the bidirectional beams are not produced simultaneously, and their operation modes depend on polarization and frequency. Moreover, all the aforementioned examples use dielectric materials [64-70]. A design of MOTRA is proposed in [71] that consists of Babinet-inverted defected square slot cells etched on a single-layer thin metallic sheet (see Fig.1.29).

Since there is only one published MOTRA made of slot-type cells, this thesis tries to use waveguide-based cells to design 3D MOTRAs.

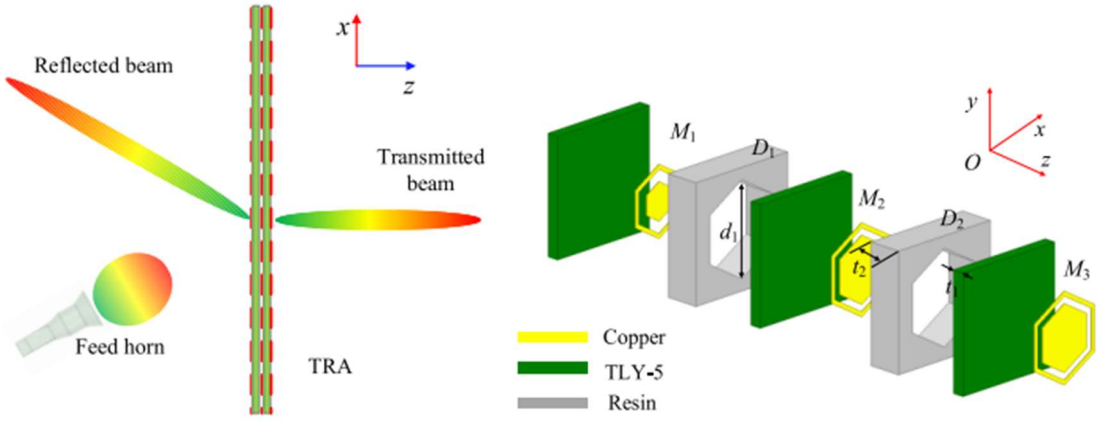

a) b)

Fig.1.28 Principle of TRA in [64]: a) configuration of TRA, b) configuration of unit cell.

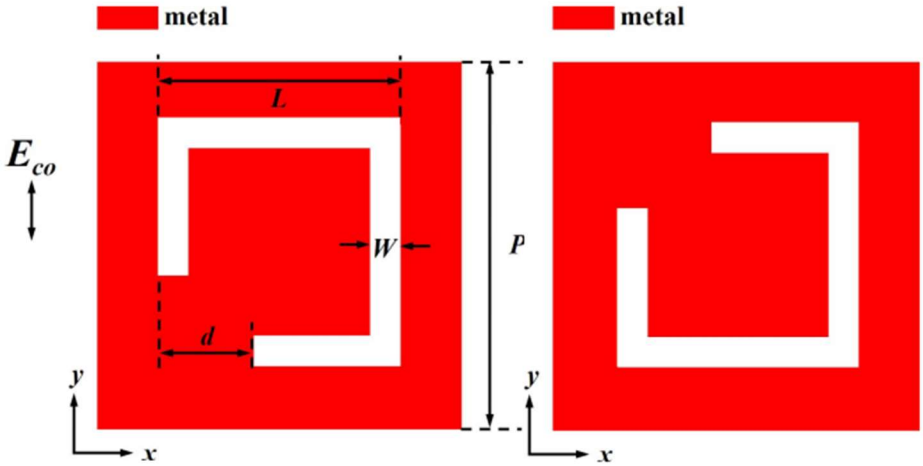

Fig.1.29 Configuration of unit cell in [71].

1.4 Fabrication of reflectarray antennas

After analyzing the different RAs, TRAs and phase shifting cells, the fabrication of them will be discussed in this section. The technologies used for printed microstrip RAs are not suitable for the fabrication of MORAs. There are two types of technologies that can be used for MORAs, namely AM and subtractive manufacturing. Subtractive manufacturing involves cutting away from a solid block of material. AM, also known as 3D printing, is a method of manufacturing where layers of material are

built up one at a time to create a solid object. Compared with the subtractive manufacturing, AM has the advantages of low cost and high material efficiency. Also, AM was known as rapid prototyping because it allowed people to create a scale model of the final object quickly, without the typical setup process and costs involved in creating a prototype. The most important is that the AM is more suitable for some parts with complex structures, which provides more freedom in antenna design. Therefore, this thesis focuses on the AM technology.

In this section, different AM technologies are introduced first. Then, the applications of AM technologies in the fabrication of antennas, especially RAs, are summarized.

1.3.1 Introduction of different additive manufacturing technologies

In this thesis, AM technologies are divided into two different categories, one is non-metal 3D printing (such as fused deposition modeling) and the other one is metal 3D printing (such as SLM). At the same time, there are two AM technologies (selective laser sintering and binder jetting) that can print both metal parts and non-metal parts. These technologies, along with their advantages and disadvantages, are described in details in the following subsections. The introduction of these technologies mainly refers to [72-74].

1.3.1.1 Fused deposition modeling

Fused deposition modeling (FDM) is a material extrusion AM process to produce prototypes, functional parts, and conceptual models [75]. FDM uses digital design files that are uploaded to the machine itself and translates them into physical dimensions. Materials for FDM include some polymers which the machine feeds as threads through a heated nozzle. A spool of this thermoplastic filament is first loaded into the printer. Once the nozzle hits the desired temperature, the printer feeds the filament through an extrusion head and nozzle. This extrusion head is attached to a three-axis system that allows it to move across the X, Y and Z axes. The printer extrudes melted material in thin strands and deposits them layer by layer along a path determined by the design. Once deposited, the material cools and solidifies. Fans can be attached to the extrusion head to accelerate cooling in some cases. To fill an area, multiple passes are required. When the printer finishes a layer, the build platform descends and the machine begins work on the next layer. In some machine setups, the extrusion head moves up. This process repeats until the part is finished.

FDM printers cannot deposit molten thermoplastic on thin air. Certain part geometries require support structures which are usually printed in the same material as the parts themselves. Oftentimes, removing support structures can be difficult, so it's often far easier to design parts in such a way that minimizes the need for support structures. Support materials that dissolve in liquid are also available, but they are generally used in tandem with higher-end FDM 3D printers. Using dissolvable supports increases the overall cost of a print.

FDM is widely approached for its simplicity, relatively low costs, minimal material wastage, and high processing speed [76]. The one main disadvantage of FDM 3D printing is that it has the lowest resolution compared to other 3D printing technologies. This makes it a less viable option for parts with very small details.

FDM is used to print non-metallic materials. Most antennas, especially metal antennas, however, require metallic conductors. For example, a horn antenna requires an all-metal metallic surface while a microstrip antenna requires one or more metallic patches. The FDM 3D printing technology cannot be used directly to fabricate these antennas. In this case, it should be followed by additional technology to print metals on these non-metallic materials. Therefore, many antennas are printed using both FDM and another metallization technology.

The paper [77] introduced a half-wave dipole antenna fabricated using FDM and then metalized using microdispensing. Some patch antennas are introduced in [78-83] where the substrates are printed using FDM while the metal traces are deposited using another technology such as microdispensing, pneumatic dispensing technique and thermal spray. A pyramidal horn antenna in [84] is fabricated using FDM and metalized using conductive copper paint. Note that the printed metal antennas, for example a horn antenna with all-metal surface, are not MO antennas as the non-metallic materials still exist after the metallization process.

1.3.1.2 Stereolithography

Stereolithography (SLA) 3D printing is the first successful AM process applied in commercial field, and presents fast forming speed and outstanding resolution [85]. The materials used in SLA are photosensitive thermoset polymers that come in a liquid form. Its working process is shown below:

1). SLA 3D printing works by first positioning the build platform in the tank of liquid photopolymer, at a distance of one layer height for the surface of the liquid.

2). A ultraviolet（UV) laser creates the next layer by selectively curing and solidifying the photopolymer resin.

3). During the solidification part of the photopolymerization process, the monomer carbon chains that compose the liquid resin are activated by the light of the UV laser and become solid, creating strong unbreakable bonds between each other.

4). The laser beam is focused in a predetermined path using a set of mirrors, called galvos. The whole cross-sectional area of the model is scanned, so the produced part is fully solid.

5). After printing, the part is in a not-fully-cured state. It requires further post-processing under UV light if very high mechanical and thermal properties are required.

A support structure is always required in SLA. Support structures are printed in the same material as the part and must be manually removed after printing. The orientation of the part determines the location and amount of support. It is recommended that the part is oriented so that the visually critical surfaces do not come in contact with the support structures. SLA 3D printing has many advantages, for example, it can produce parts with very high dimensional accuracy and with intricate details. Also, its parts have a very smooth surface finish, making them ideal for visual prototypes. Nevertheless, the SLA 3D printing also has some disadvantages. SLA parts are generally brittle and not suitable for functional prototypes. At the same time, the mechanical properties and visual appearance of SLA parts will degrade over time when the parts are exposed to sunlight. In addition, support structures are always required and post-processing is necessary to remove the visual marks left on the SLA part.

Similar to FDM technology, SLA technology needs to be followed by another metallization technology so that it could be used to print antenna with metal conductor.

Three horn antennas [7-9] are fabricated using SLA technology and then metallized using another technology. A Ka band antenna in [86] is fabricated using SLA technology followed by metal coating.

1.3.1.3 Material Jetting 3D printing

Material Jetting (MJ) is an additive manufacturing process that operates in a similar fashion to 2D printers. In material jetting, a printhead (similar to the printheads used for standard inkjet printing) dispenses droplets of a photosensitive material that solidifies under UV light, building a part layer-by-layer. The materials used in MJ are thermoset photopolymers (acrylics) that come in a liquid form. Unlike most other 3D printing technologies, MJ deposits material in a line-wise fashion.

MJ creates parts of high dimensional accuracy with a very smooth surface finish. Multi-material printing and a wide range of materials (such as rubber-like and fully transparent materials) are available in Material Jetting. These characteristics make MJ a very attractive option for both visual prototypes and tooling manufacturing.

These are the main steps in the MJ 3D printing process:

1). First, the liquid resin is heated to 30 – 60°C to achieve optimal viscosity for printing.

2). Then the printhead travels over the build platform and hundreds of tiny droplets of photopolymer are jetted/deposited to the desired locations.

3). A UV light source that is attached to the printhead cures the deposited material, solidifying it and creating the first layer of the part.

4). After the layer is complete, the build platform moves downwards one layer height and the process repeats until the whole part is complete.

Since photosensitive materials are used, the parts created with MJ have poor mechanical properties and their mechanical properties degrade over time, which makes them not suitable for some functional prototypes. In addition, the high cost of the technology may make MJ financially not viable for some applications. A 3-D Luneburg lens antenna in [10] is fabricated using MJ technology. The printed 3D lens antenna is an all-dielectric antenna.

1.3.1.4 Selective Laser Sintering

Selective Laser Sintering (SLS) is an additive manufacturing process that belongs to the Powder Bed Fusion family [87]. It can be used to fabricate both metal parts and non-metal parts depending on the material used. SLS 3D printing uses a laser to sinter small particles of polymer powder or metal powder. The entire cross-section of the component is scanned, so the part is built solid. The process works as follows:

1). The powder bin and the build area are first heated to just below the melting temperature of the powder.

2). A re-coating blade spreads a thin layer of powder over the build platform.

3). A CO2 laser then scans the contour of the next layer and selectively sinters—fuses together—the particles of the powder.

4). When a layer is complete, the build platform moves downwards and the blade re-coats the surface. The process then repeats until the whole part is complete.

5). After printing, the parts are fully encapsulated in the unsintered powder. The powder bin must cool before the parts can be unpacked, which can take a considerable amount of time—sometimes up to 12 hours.

6). The parts are then cleaned with compressed air or another blasting media, then they are ready to use or further post-process.

SLS parts have good, isotropic mechanical properties, making them ideal for functional parts and prototypes. SLS requires no support, so designs with complex geometries can be easily produced. The manufacturing capabilities of SLS is excellent for small to medium batch production. All remaining unsintered powder is collected and can be reused. However, SLS technology also has some disadvantages. Only industrial SLS systems are currently widely available, so lead times are longer than other 3D printing technologies, such as FDM and SLA. SLS parts have a grainy surface finish and internal porosity that may require post processing, if a smooth surface or watertightness are required.

Large flat surfaces and small holes cannot be printed accurately with SLS, as they are susceptible to warping and oversintering.

If polymer powder is used, SLS technology, similar to previous non-metal 3D printing technologies, should combine another metallization technology to print antenna with metal conductor. If metal powder is used, SLS technology can be used to directly print MO antennas.

A stepped-reflector antenna [88] is fabricated using SLS 3D printing technology. In the post processing, the reflector was iteratively sprayed with a primer and sanded to form a smooth surface, then spray-painted with silver-based *APPLICOAT ES210* to make it reflective, and finally a layer of clear coat was applied. A low-profile magnetic dipole antenna [89] is fabricated using SLS technology and silver paste painting. A 4×4 array antenna and two WR90 [90-91] waveguides are fabricated using SLS metal 3D printing technology.

1.3.1.5 Metal 3D printing

The first few AM technologies are for non-metal parts, and now the metal 3D printing is introduced. Metal 3D printing has been widely used in the aerospace and medical industries in the last decade, which is still growing [92-93]. SLM and Direct Metal Laser Sintering (DMLS) are two metal AM processes that belong to the powder bed fusion 3D printing family. The two technologies have a lot of similarities: both use a laser to scan and selectively fuse (or melt) the metal powder particles, bonding them together and building a part layer-by-layer. Also, the materials used in both processes are metals that come in a granular form. The differences between SLM and DMLS come down to the fundamentals of the particle bonding process: SLM uses metal powders with a single melting temperature and fully melts the particles, while in DMLS the powder is composed of materials with variable melting points that fuse on a molecular level at elevated temperatures. Essentially, SLM produces parts from a single metal, while DMLS produces parts from metal alloys. The difference between SLM and SLS metal printing is that the metal powder in SLS metal printing is only sintered and not completely melted. The SLS metal 3D printing is almost the same as DMLS and they both print parts by sintering alloys.

The basic fabrication process is similar for both SLM and DMLS. Here's how it works:

1). The build chamber is first filled with inert gas (for example argon) to minimize the oxidation of the metal powder and then it is heated to the optimal build temperature.

2). A thin layer of metal powder is spread over the build platform and a high-power laser scans the cross-section of the component, melting (or fusing) the metal particles together and creating the next layer. The entire area of the model is scanned, so the part is built fully solid.

3). When the scanning process is complete, the build platform moves downwards by one layer thickness and the recoater spreads another thin layer of metal powder. The process is repeated until the whole part is complete.

When the build process is finished, the parts are fully encapsulated in the metal powder. Unlike the polymer powder bed fusion process (such as SLS), the parts are attached to the build platform through support structures. Support in metal 3D printing is built using the same material as the part and is always required to mitigate the warping and distortion that may occur due to the high processing temperatures.

When the bin cools to room temperature, the excess powder is manually removed and the parts are typically heat treated while still attached to the build platform to relieve any residual stresses. Then the components are detached from the build plate via cutting or machining and are ready for use or further post-processing.

The dimensional accuracy for metal 3D printing is ± 0.1 mm, which is better than previously introduced non-metallic printing technologies. Support structures are always required in metal printing,

due to the very high processing temperature and they are usually built using a lattice pattern. Various post-processing techniques are used to improve the mechanical properties, accuracy, and appearance of the metal printed parts. Compulsory post-processing steps include the removal of the loose powder and the support structures, while heat treatment (thermal annealing) is commonly used to relieve the residual stresses and improve the mechanical properties of the part. Computer numerical control machining can be employed for dimensionally crucial features (such as holes or threads). Media blasting, metal plating, polishing, and micro-machining can improve the surface quality and fatigue strength of a metal printed part.

Metal 3D printing processes can be used to manufacture complex, bespoke parts with geometries that traditional manufacturing methods are unable to produce. Metal 3D printed parts can be topologically optimized to maximize their performance while minimizing their weight and the total number of components in an assembly. Metal 3D printed parts have excellent physical properties and the available material range includes difficult-to-process otherwise materials, such as metal superalloys. However, the material and manufacturing costs connected with metal 3D printing are high, so these technologies are not suitable for parts that can be easily manufactured with traditional methods. Also, the build size of the metal 3D printing systems is limited, as precise manufacturing conditions and process control are required.

Compared to non-metallic printing, the 3D metal printing can be used directly to print MO parts without applying any metallization process. The SLM 3D printing technology has been widely used in the fabrication of horn antennas and filters [94-99]. At the same time, some horn antennas and waveguide-based antennas are fabricated using DMLS 3D printing technology [100-106]. The mainly difference between these antennas is that the metal alloys, instead of single metal, are used in the DMLS 3D printing technology.

1.3.1.6 Binder Jetting

Binder Jetting can be used to fabricate both metal parts and non-metal parts depending on the material used. The materials commonly used in Binder Jetting are metals, sand, and ceramics that come in a granular form. Binder Jetting is used in various applications, including the fabrication of full-color prototypes, the production of large sand casting cores and molds and the manufacture of low-cost 3D printed metal parts. These are the main steps in the binder jetting 3D printing process:

1). First, a recoating blade spreads a thin layer of powder over the build platform.

2). Then, a carriage with inkjet nozzles passes over the bed, selectively depositing droplets of a binding agent (glue) that bond the powder particles together. In full-color Binder Jetting, the colored ink is also deposited during this step. The size of each drop is approximately 80 μm in diameter, so good resolution can be achieved.

3). When the layer is complete, the build platform moves downwards and the blade re-coats the surface. The process then repeats until the whole part is complete.

4). After printing, the part is encapsulated in the powder and is left to cure and gain strength. Then the part is removed from the powder bin and the unbound, excess powder is cleaned via pressurized air.

A key advantage of Binder Jetting over other 3D printing processes is that bonding occurs at room temperature. This means that dimensional distortions connected to thermal effects (such as warping in FDM, SLS, SLM or curling in SLA) are not a problem in Binder Jetting.

Moreover, Binder Jetting requires no support structures: the surrounding powder provides to the part all the necessary support (similar to SLS). This is a key difference between metal Binder Jetting and other metal 3D printing processes, which usually require extensive use of support structures, and allows for the creation of freeform metal structures with very few geometric restrictions. Geometric

inaccuracies in metal Binder Jetting come mainly from the post-processing steps. The manufacturing capabilities of Binder Jetting are excellent for low to medium batch production.

For the metal Binder Jetting, it is up to 10x more economical than other metal 3D printing processes (DMSL/SLM). Moreover, the build size of Binder Jetting is considerably large and the produced parts require no support structures during printing, enabling the creation of complex geometries. This makes metal Binder Jetting a very appealing technology for low-to-medium metal production. The main drawback of metal Binder Jetting parts are their mechanical properties, which are not suitable for high-end applications.

Metal Binder Jetting parts require a secondary process after printing, like infiltration or sintering, to achieve their good mechanical properties, as the as-printed parts basically consist of metal particles bound together with a polymer adhesive.

Infiltration: After printing, the part is placed in a furnace, where the binder is burnt out leaving voids. At this point, the part is approximately 60% porous. Bronze is then used to infiltrate the voids via capillary action, resulting in parts with low porosity and good strength.

Sintering: After printing is complete, the parts are placed in a high temperature furnace, where the binder is burnt out and the remaining metal particles are sintered (bonded) together, resulting in parts with very low porosity.

The post-processing step can also be the source of inaccuracies. For example, during sintering, the part is heated to a high temperature and becomes softer. In this softer state, unsupported areas might deform under their own weight. Moreover, as the part shrinks during sintering, there is friction between the plate of the furnace and the lower surface of the part, which may lead to warping.

Similar to the metal printing, the metal binder jetting can be directly used to print metal parts. It has been used to fabricate waveguide-based antennas and horn antennas [107-110].

1.3.1.7 Reasons for choosing selective laser meting 3D printing technology

In this subsection, four different AM technologies used for non-metal parts are first introduced. They can be used to print substrate for some patch antennas or to print some antennas made only of dielectric materials. Although the 3D printed parts can be metallized using another technology, they are not suitable for some applications in harsh environment as they are not real MO antennas. The metal Binder Jetting technology could be a candidate for printing the antennas in this thesis, but the metal Binder Jetting parts have lower mechanical properties than DMSL/SLM parts, due to their higher porosity. In addition, only the rough details can be printed with Binder Jetting as the post processing may cause undesired deformation or warping. Compared with DMSL and SLS technologies, the SLM technology prints parts by melting the metal powder, rather than sintering, which gives the printed parts better mechanical properties. Furthermore, the SLM technology is available in our collaborative lab in Fez. Therefore, the SLM 3D printing technology is adopted to fabricate the antennas in this thesis.

1.3.2 Reflectarray antennas using 3D printing technologies

The 3D printing technologies have been applied to the fabrication of RAs. Two 3D printed linearly polarized RAs consisting of dielectric cubes with variable height are introduced in [111-112]. Their principle is similar to the MORA in [59], which is to change the reflection phase by adjusting the distance between feed antenna and unit cells. The reflection phase is completely controlled by the height of dielectric cube. After these, two 3D printed circularly polarized RAs are introduced in [113-114]. The unit cell (see Fig.1.30) in [113] consists of a cross-shaped dielectric block and a metallic ground. The two dielectric blocks have different width and length, which leads to a phase difference between two orthogonal components of reflected electric field. The unit cell (see Fig.1.31) in [114] consists of an air-perforated dielectric stub and a metallic ground. Since it is an asymmetric structure, similar to the unit

cell in [113], different reflection phases of TE and TM polarizations can be achieved. These two RAs are synthesized to collimate the linearly polarized incident waves to a CP pencil beam in a desired direction. A 3D printed dual-band all-dielectric RA (see Fig.1.32) is proposed in [115]. The proposed dual band RA consists of two dielectric mirrors. The upper-band reflectarray is on the top, which can reflect and collimate the electromagnetic wave at V-band and allow the K-band electromagnetic wave to pass. The bottom reflectarray reflects and collimates the K-band wave. The dielectric mirror is formed by periodically stacking dielectric layers and air layers. At low frequencies, the wavelength is much longer than the periodicity, the wave propagates through the structure as if the structure was homogenous with the corresponding effective refractive index. As the frequency increases, multiple partial reflections from the boundaries (between two materials with different refractive indexes) become important and all these partially reflected waves interfere with each other and give rise to a significant overall reflection. As a results, a dual band RA is designed based on this principle.

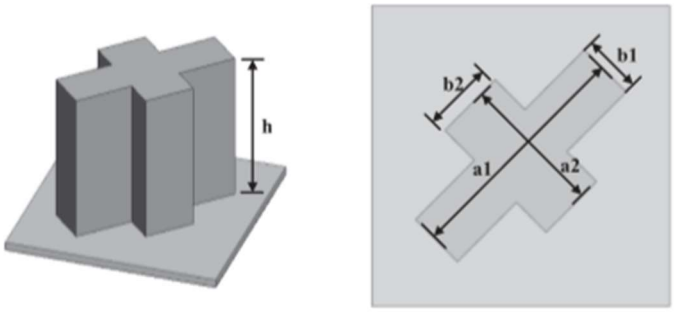

Fig.1.30 Geometry of the cross shaped dielectric cell in [113].

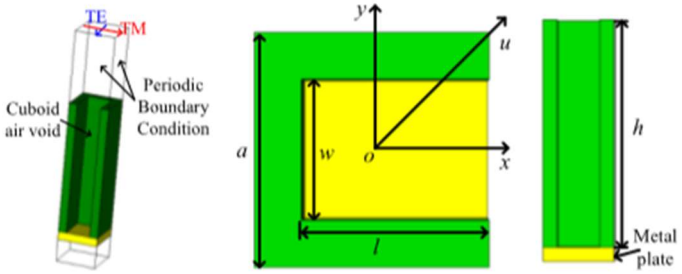

Fig.1.31 Geometry of the unit cell in [114].

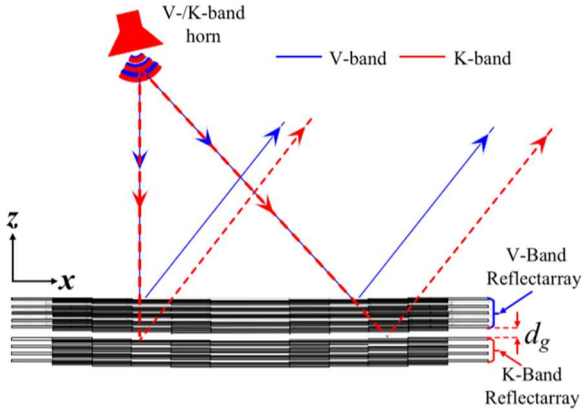

Fig.1.32 Configuration of the dual-band all-dielectric reflectarray in [115].

The aforementioned 3D printed RAs use dielectric materials as the phase shifting cells, while the metallic materials are used to design phase shifting cells for 3D printed RAs in [55-57, 63]. These RAs

have been introduced in a previous subsection. The RAs in [56, 57] are fabricated using non-metal 3D printing technologies and then metallized. To be precise they are not true MORAs, which makes them not suitable for some applications in harsh environment. Instead, the MORAs in [55, 63] are fabricated using metal 3D printing technologies and the used material is ALSi10Mg powder.

1.5 Conclusion

First, the concepts of reflector antenna, array antenna, RA and TA were introduced. All of these are high gain antennas. The reflector has, in theory, an infinite bandwidth but its curved surface is expensive to fabricate, particularly at higher microwave frequency and for shaped beams. Array antenna is an alternative approach to achieve a high gain. Although it allows a flexible design to implement the beam scanning capability, high-cost transmit/receive amplifier modules and the complicated high-loss beamforming network are unacceptable in some applications. RA is a combination of reflector antenna and array antenna. It effectively avoids the aforementioned problems of reflector antenna and array antenna. It has the advantages of high gain, low profile, low cost and easy manufacturing. Also, it is able to manipulate the main beam, including its shape and direction, like an array antenna. Its bandwidth, however, is strongly limited by its flat nature. A RA produces a reflected beam while a TA generates a transmitted one. In addition, TAs can avoid certain limitations associated to RA, such as feed-blockage.

Since the RA consists of many phase-shifting cells, the phase-shifting cell used to design a RA must be selected carefully. In the second subsection, the different microstrip RAs and MORAs were introduced respectively. The microstrip RAs were categorized into three groups based on the approaches they applied to tune the reflection phase, including using the attached time delay line, varying the cell geometry and rotating the cell. The MORAs in this chapter were classified into three types, including the MORAs using slot-type cells, the MORAs using waveguide-type cells and the MORAs using metallic blocks. The principles of these antennas were analyzed in detail. The MORA is preferred in some specific applications, such as space, as it avoids the use of dielectric material. For the microstrip RAs, the dielectric materials they use may cause lots of problems. First of all, they may limit the gain due to the losses they bring, especially at high frequencies. In addition, for RAs that work in harsh environment, such as space, the use of dielectric substrates is not recommended due to undesired associated effects, such as outgassing, temperature-dependent dielectric constant and the dielectric breakdown. In such a situation, the MORA is preferred as it avoids the intrinsic problems brought by dielectric materials. Also, after comparing different MORAs, the waveguide-type cells show a better performance than the slot-type cells and the cells using metallic blocks. Therefore, the MORAs using waveguide type cells are the topic of this thesis.

The combination of both RA and TA functionalities in a single-feed high-gain TRA has been found of great interest in order to implement bi-directional radiated beams. Since there is only one published MOTRA made of slot-type cells, this thesis tries to use waveguide-based cells to design MOTRAs.

After studying the different RAs, TRAs and phase-shifting cells, seven different 3D printing technologies and their application in antennas were introduced in detail. FDM, SLA and MJ 3D printing technologies are used for non-metal parts, while SLM and DMLS are used for metal parts. In addition, SLS and Binder Jetting technologies can be used for both metal and non-metal parts. The non-metal 3D printing technologies can be used directly for the printing of dielectric RAs and indirectly for the printing of metal RAs (followed by another metallization technology). The metal 3D printing technologies can be used for the fabrication of MORAs. After some comparisons, SLM technology was chosen to fabricate the antennas in this thesis.

Chapter 2 - Analysis and Modeling of Waveguide-based Phoenix Cell

2.1 Simple cell. 53

2.1.1 Simple cell with short-ended waveguide 57
2.1.2 Simple cell with open-ended waveguide 59
2.1.3 Conclusion 61

2.2 Phoenix cell 61

2.2.1 Phoenix cell using short-ended waveguides 63
2.2.2 Phoenix cell using open-ended waveguides 64
2.2.3 Conclusion 66

2.3 Equivalent circuit of the 3D PC 66

2.3.1 Derivation process 67
2.3.2 Verification of the equivalent circuit 68
2.3.3 Conclusion 70

2.4 Resonances analysis 70

2.4.1 Waveguide with losses 71
2.4.2 Unit cell with losses 71
2.4.3 Conclusion 72

2.5 Conclusion 72

Chapter 2 - Analysis and Modeling of Waveguide-based Phoenix Cell

A waveguide is a structure that guides waves, such as electromagnetic waves or sound, with minimal loss of energy by restricting the transmission of energy to one direction. The concept of waveguide was first proposed by J.J. Thomson in 1893 [116]. It was then promoted by Lord Rayleigh who performed the first mathematical analysis of electromagnetic waves in a metal cylinder [117], and Sommerfeld who established theoretical analysis on different modes [118]. Rectangular waveguides were one of the earliest types of transmission lines used to transport microwave signals, and they are still used for many applications [119].

In this chapter, rectangular waveguides are used to design RA cells and TA cells. They consist of one or two waveguides. Their principles are analyzed in details and their performances are evaluated by full wave simulation results. Also, one of them is modelled by an equivalent circuit. At the end, the resonances in these cells are analyzed.

2.1 Simple cell.

As introduced in chapter 1, the rectangular waveguide has been used as a phase shifting cell [51]. It allows the propagation of the fundamental TE_{10} mode. Unlike the TEM mode in parallel plate waveguide, there is a limitation of cutoff frequency for the TE_{10} mode in rectangular waveguide. In order to enable the propagation of the fundamental mode, the width of the rectangular waveguide in [51] is set to a value that is greater than half wavelength at its central frequency, which may result in grating lobes. To avoid grating lobes, its width should not be greater than the half wavelength. Another solution is to introduce a metallic block in the center. The presence of the metallic block in the center decreases the cut-off frequency of the fundamental TE_{10} and TE_{01}-like modes in the waveguide surrounding the metallic block. As shown in Fig.2.1, a cell consists of a square waveguide with a metallic block is proposed in this section. The external dimension (L_c) is set to 7.5 mm ($\lambda_0/2$ at the central frequency we have set to 20 GHz for this demonstration) to prevent from grating lobes in an array configuration. The size of the metallic block (L_r) is varied to control the cell behavior, i.e. to vary the phase of the reflected wave when it is illuminated by an incident wave. Since the proposed structure (see Fig.2.1) is simpler than the structure introduced in next section, it is referred to as SC.

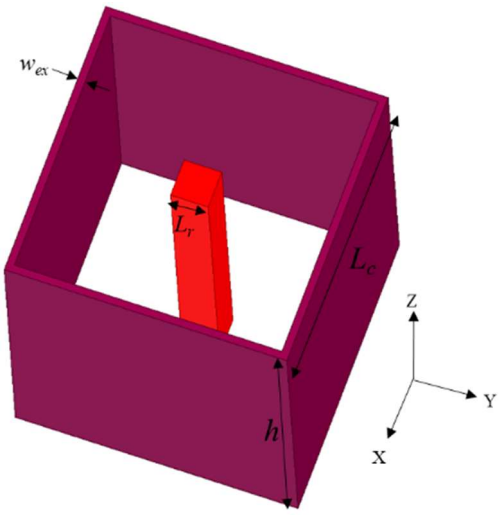

a)

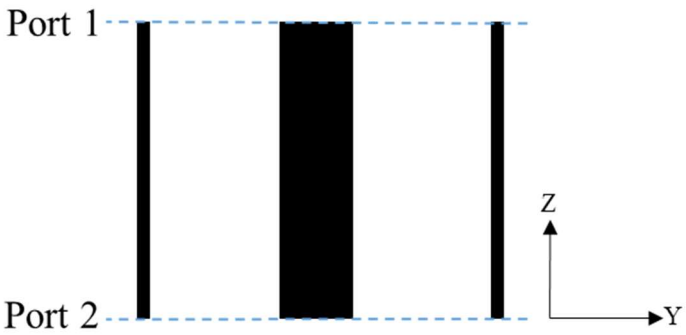

b)

Fig.2.1 The proposed 3D MO SC. a) 3D view. b) Sectional view.

Table 2.1 Detailed parameters of the SC

Parameter	L_c	w_{ex}
Value (mm)	7.5	0.1

The electric field inside the SC is first simulated to analyze the effect of this central metallic block. Simulation model of the SC is shown in Fig.2.2. In the simulations, all metal parts are considered as Perfect Electric Conductors (PEC). Floquet ports are used at input and output and the periodic boundary condition (PBC) is assigned on the lateral faces to mimic a cell in a periodic infinite environment. The SC is simulated using HFSS® under normal incidence. Here, h is fixed at 10 mm for these simulations. Fig.2.3 shows the complex magnitude of electric field in the XZ plane at 16 GHz for different values of L_r. Note that the 3D SC is designed so that the cutoff frequency of the empty waveguide (i.e. without any metallic block) is 20.54GHz which is a bit higher than 20GHz due to the wall thickness. Then, the observation of the electric field at a lower frequency (16GHz here) gives some insights on the effect of L_r on this cutoff frequency. It can be seen from Fig.2.3 that the amplitude of the electric field inside the waveguide is almost zero for the lower value of L_r and it then gradually increases with L_r. Initially, the incident wave does not penetrate into the waveguide because it is under cutoff. Then, the increase in the amplitude of electric field means the incident wave can propagate better in the waveguide. In other words, the presence of metallic block can reduce the cutoff frequency of the waveguide surrounding it.

Note that the SC can be equivalent to a coaxial transmission line that supports the TEM mode. However, the propagation of the TEM mode in the SC is only allowed under oblique incidence, which will be explained later. The SC supports only the TE_{10} mode under normal incidence.

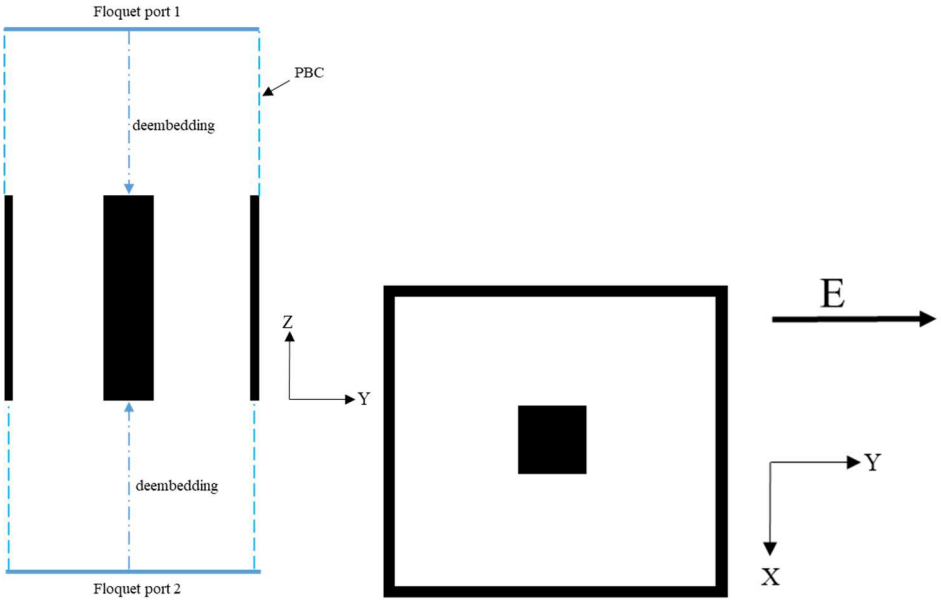

a) b)

Fig.2.2 Simulation model of the SC. a) Sectional view. b) Top view.

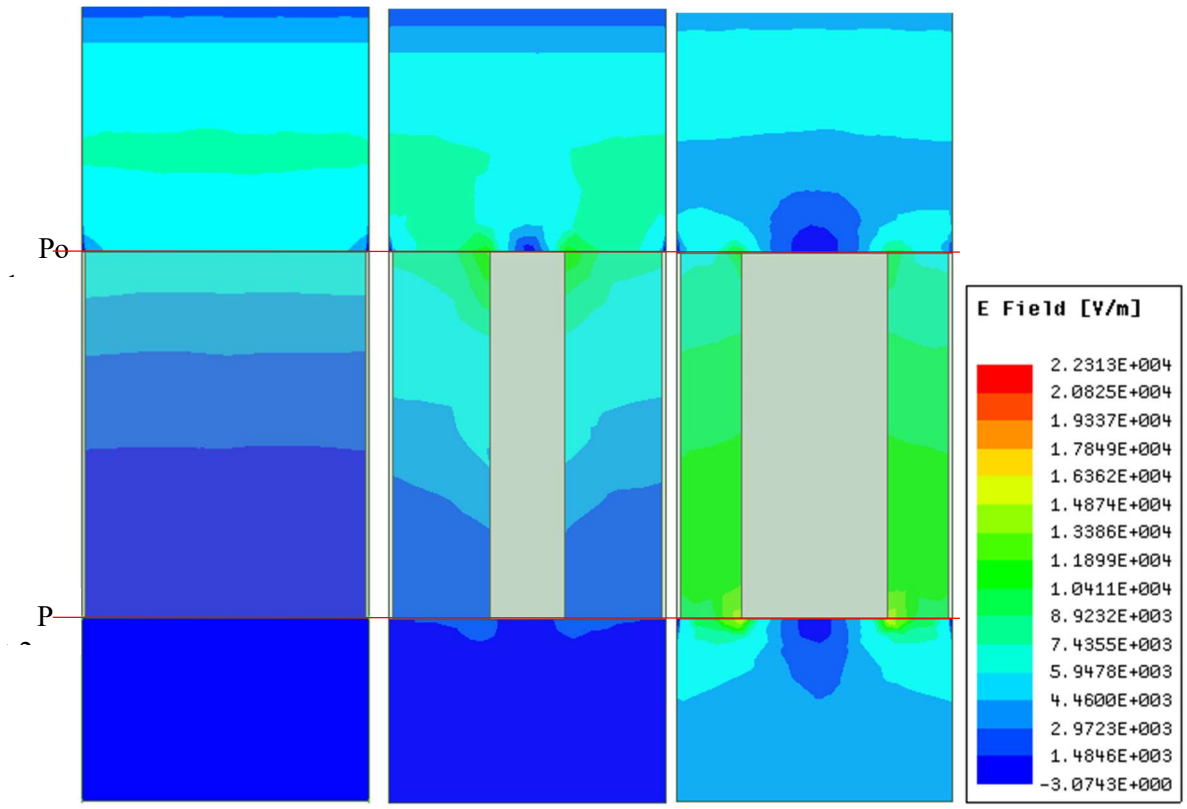

a) b) c)

Fig.2.3 The complex magnitude of electric field (XZ plane, middle of the waveguide, normal incidence, y-polarization, f=16GHz, h=10 mm). a) L_r=0. b) L_r=2 mm. c) L_r=4 mm.

To better analyze its principle, the characteristics of the waveguide in the SC are simulated. The waveguide is composed of two conductors (inner wall and external wall) as shown in Fig.2.4a. It cannot be recognized as a waveguide by HFSS because a metallic waveguide in HFSS should have one and only one conductor. Fortunately, the existence of a vertical symmetry axis at the center of the waveguide for the fundamental mode (here assuming horizontal polarization) enables to connect both inner and

external conductors (as shown in Fig.2.4b). Consequently, as shown in Fig.2.4, the initial O-shape configuration (see Fig. 2.4a) can finally be transformed to H-shape (Fig. 2.4c), which is equivalent but composed of only one conductor. The precise simulation configuration that is used for the waveguide is shown in Fig.2.5. It is simulated by applying two wave ports at the two ends of the waveguide. Here, the length of the waveguide is 100 mm (6.67 wavelengths at 20GHz). The characteristic impedance (Z_{c_ex}), the propagation constant (β_{ex}) and the cutoff frequency of the waveguide are summarized in Fig.2.6. Also, the wave impedance of free space (Z_0) is added to Fig.2.6 to make the analysis in the following subsections easier. Note that index ex is used only for uniformity with the following sections where this waveguide will be called the "external" one. Since the waveguide operates in propagative mode at 20GHz and there is no loss of material, the imaginary part of the characteristic impedance and the real part of the propagation constant are equal to 0. It can be seen that increasing the size of the metallic block reduces the cutoff frequency and the characteristic impedance (real part) of the waveguide and increases its propagation constant (imaginary part).

Also, it can be seen that the waveguide in the SC always operates in the propagative mode when the value of L_r is greater than 1 mm.

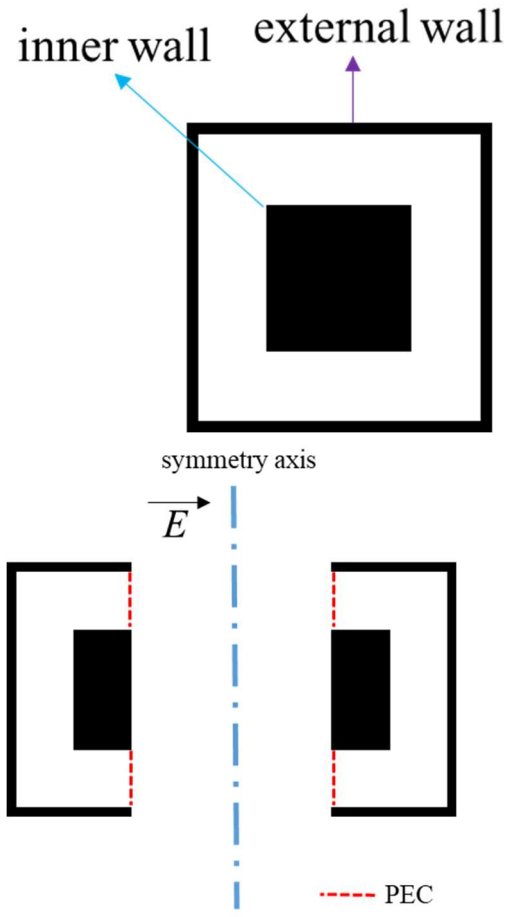

a) b)

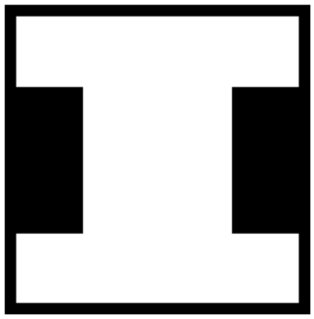

c)

Fig.2.4 Top view of the 3D SC. a) The whole cell. b) Two symmetrical parts. c) H-shape.

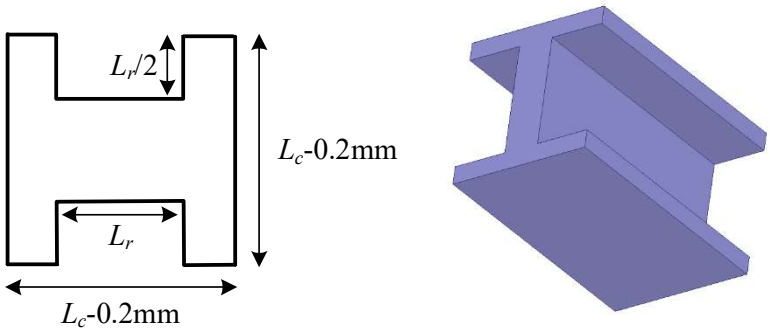

a) b)

Fig.2.5 Simulation model of the waveguide in the SC. a) Top view. b) 3D view.

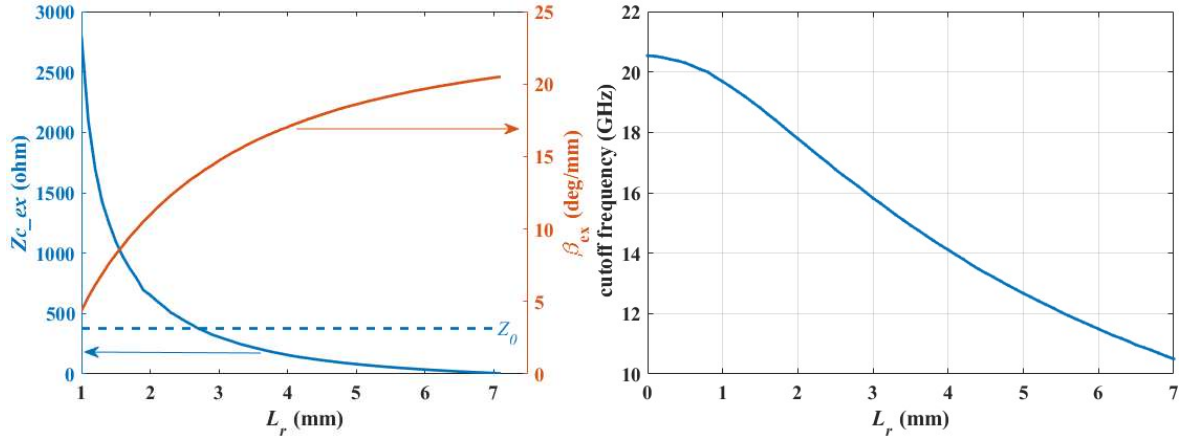

a) b)

Fig.2.6 Characteristics of the waveguide in the SC at 20GHz. a) Propagation constant and characteristic impedance. b) Cutoff frequency.

As we will see, the cell can work as a TA or RA cell depending on the termination that is used at bottom end. In the RA configuration, a short-circuit termination is used and the incident wave at port 1 is totally reflected. In the TA configuration, an open-ended termination is used instead and most of the incident wave is transmitted through the cell.

2.1.1 Simple cell with short-ended waveguide

The simple cell with short-ended waveguide (SCSW) is shown in Fig.2.7. The presence of the short-circuit termination enables the control of the reflected wave. More precisely, when an incident electromagnetic wave impinges on top end, it is partly reflected at the entrance and partly transmitted into the waveguide. The transmitted wave is then reflected by the short-circuit and it returns back to the

top end, where it is radiated in the backward direction (half space above the top end). Note that multiple reflections may occur at both ends due to imperfect matching. In addition, the SCSW can deal with both x- and y-polarized incident waves.

The simulated reflection coefficient at the input of the SCSW at 20GHz is shown in Fig.2.8a. As a comparison, the theoretical approximation of this reflection coefficient using simple transmission line theory is given by:

$$S_{11}^{SCSW\_th} = \Gamma_{ex} + \frac{(\Gamma_{ex}^2-1)e^{-2j\beta_{ex}h}}{1-\Gamma_{ex}e^{-2j\beta_{ex}h}} = \frac{\Gamma_{ex}-e^{-2j\beta_{ex}h}}{1-\Gamma_{ex}e^{-2j\beta_{ex}h}} \tag{2.1}$$

where Γ_{ex} expresses the mismatch between the waveguide and free space:

$$\Gamma_{ex} = \frac{Z_{c\_ex}-Z_0}{Z_{c\_ex}+Z_0} \tag{2.2}$$

Note that (2.2) is only an approximation as discontinuity effects, which will be explained in section 2.3, also arise at the entrance. Fig.2.8b plots this theoretical reflection coefficient where the variations of both Z_{c_ex} and β_{ex} versus L_r are taken into account (from Fig.2.6, using full-wave simulations of the waveguide in the SC). The agreement between the theoretical and the full-wave simulations of the whole SCSW itself is quite good, in spite of the approximations in the theoretical model. This suggests equation (2.1) can basically represent the SCSW, at least qualitatively.

It can be seen from Fig.2.8 that the phase range is less than 255° for each fixed h. The complete phase range can be achieved only by varying both h and L_r simultaneously. In addition, Fig.2.8 shows a 'white curve' that is very close to the case where $\beta_{ex}h$ is equal to π/2. Actually, it is a resonant phenomenon and the corresponding reflection coefficient can be given by:

$$S_{11}^{SCSW\_th}|_{\beta_{ex}h=\frac{\pi}{2}} = \frac{\Gamma_{ex}+1}{1+\Gamma_{ex}} = 1 \tag{2.3}$$

In this case, the reflection coefficient is a real number and the 'white curve' thus corresponds to a reflection phase of 0° (see Fig.2.8).

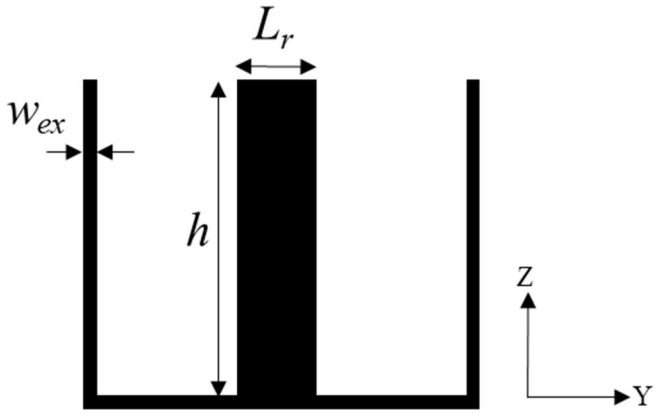

Fig.2.7 Sectional view of the SCSW

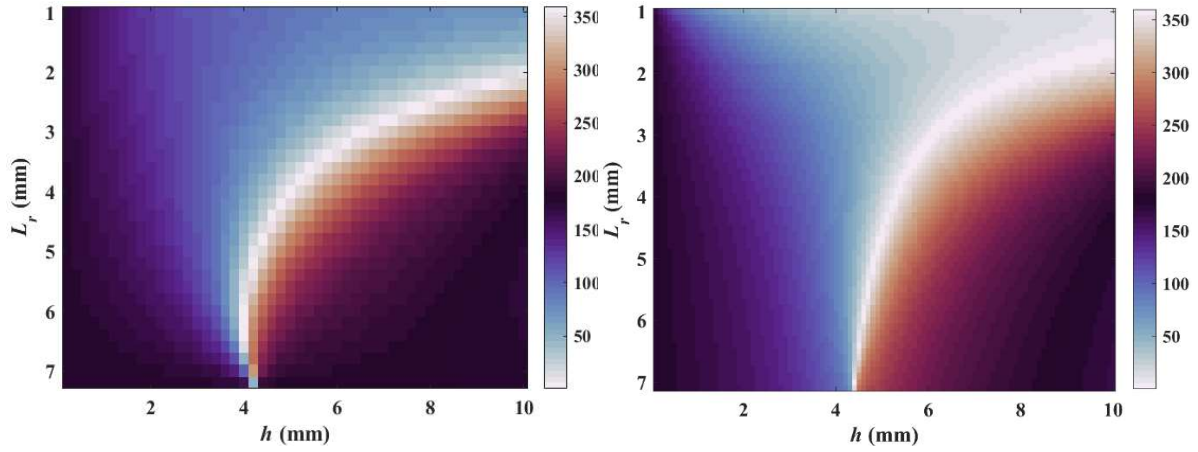

a) b)

Fig.2.8 Phase of reflection coefficient at 20GHz (normal incidence). a) Full wave simulation results. b) Theoretical model.

2.1.2 Simple cell with open-ended waveguide

The simple cell with open-ended waveguide (SCOW) is shown in Fig.2.9. Compared to the SCSW, there are two differences. Firstly, the short-circuit termination at the bottom of the cell is replaced by an open-ended one in order to let the transmitted wave within the waveguide be radiated through the bottom end. Secondly, since the short-circuit termination has been removed, a transverse metallic wall is added at the middle of the cell to hold all metallic parts together. Therefore, contrarily to the SCSW, the SCOW can only be used for x-polar (see Fig.2.9).

Apart from these differences, the principle of the cell is comparable to that of the SCSW. When an incident electromagnetic wave impinges on the top end, both transmitted and reflected waves are produced. Now, the transmitted wave is radiated at the bottom end in the forward direction (half space beyond the cell). As previously, multiple reflections may occur, making the overall process more complex. The simulated S-parameters of the SCOW at 20GHz are shown in Fig.2.10. It exhibits regions with very low reflection or transmission (dark blue lines). They are associated with phase jumps, as can be seen in Fig. 2.10a. In order to have a deeper insight into these resonant phenomena, multiple reflections have to be considered. Similarly to the SCSW, the theoretical approximations of the S-parameters of the SCOW are given by:

$$S_{21}^{SCOW\_th} = \frac{(1-\Gamma_{ex}^2)e^{-j\beta_{ex}h}}{1-\Gamma_{ex}^2 e^{-2j\beta_{ex}h}} \tag{2.4}$$

$$S_{11}^{SCOW\_th} = \frac{\Gamma_{ex}(1-e^{-2j\beta_{ex}h})}{1-\Gamma_{ex}^2 e^{-2j\beta_{ex}h}} \tag{2.5}$$

Fig.2.11 plots the theoretical S-parameters where the variations of both Z_{c_ex} and β_{ex} versus L_r are taken into account. The agreement with Fig. 2.10 (full-wave simulations of the whole cell itself) is quite good, in spite of the approximations in the theoretical model. This suggests equations (2.4) and (2.5) provides a comprehensive means to analyze the cell, at least qualitatively.

The top curve (dark blue line) in Fig.2.11c is obtained for L_r equal to 2.7 mm. It can be seen from Fig.2.6 that this value corresponds to the case where the characteristic impedance of the waveguide is equal to Z_0, leading to a perfect matching and a total transmission. Now, the bottom curve in Fig.2.11c involves L_r values ranging from 4 mm to 7 mm and h values ranging from 8 mm to 10 mm. For such values of L_r, the characteristic impedance of the waveguide varies from 7.10 Ω to 157.86 Ω, which corresponds to a quite large magnitude of Γ_{ex}. Then, a Fabry-Perot resonance occurs as soon as $\beta_{ex}h$ is equal to π. As a result, $|S_{21}|$ gets close to 1, meaning $|S_{11}|$ is minimal.

Next the performance of the SCOW as a TA cell is analyzed. It can be seen from Fig.2.10d that the losses are significantly increased when the value of L_r is very high. This can be explained by the low characteristic impedance of the waveguide (see Fig.2.6). In this case, most of the incident wave is directly reflected back at the top end of the cell. However, the achieved phase range (about 200°, phase vs h) is significantly increased due to the high β_{ex}. In addition, it can be seen from Fig.2.10c and Fig.2.10d that the SCSW provides both high phase range (290°) and high transmission magnitude when h is close to the resonant transmission (h>8 mm). The high phase range is due to the large h.

For a planar TA, the h of all the cells must be identical. Obviously, in this case, the SCOW cannot provide a complete phase range for each given h.

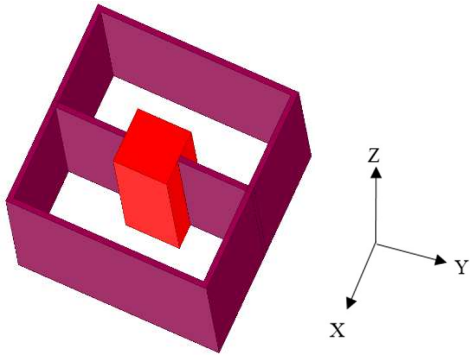

Fig.2.9 3D view of the SCOW

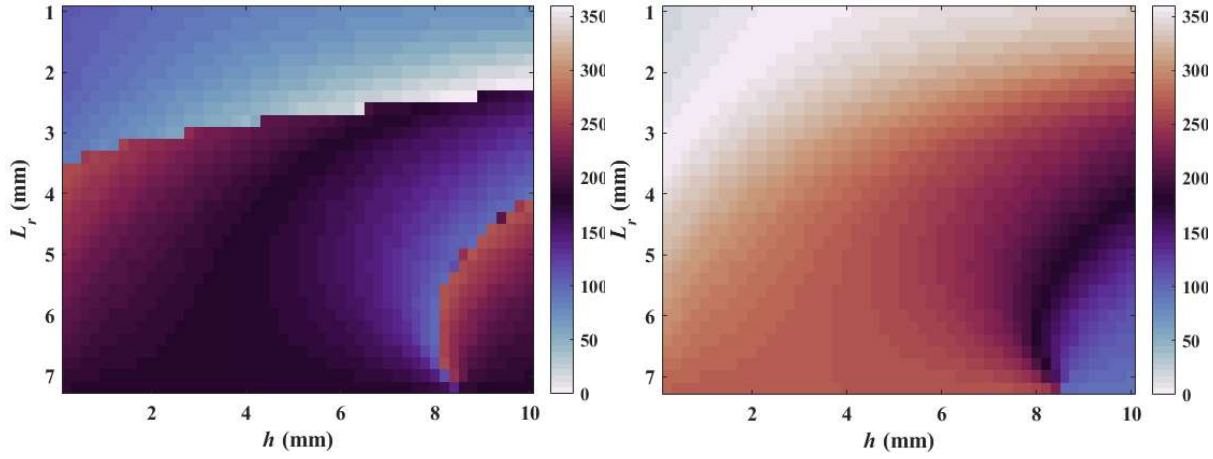

a) b)

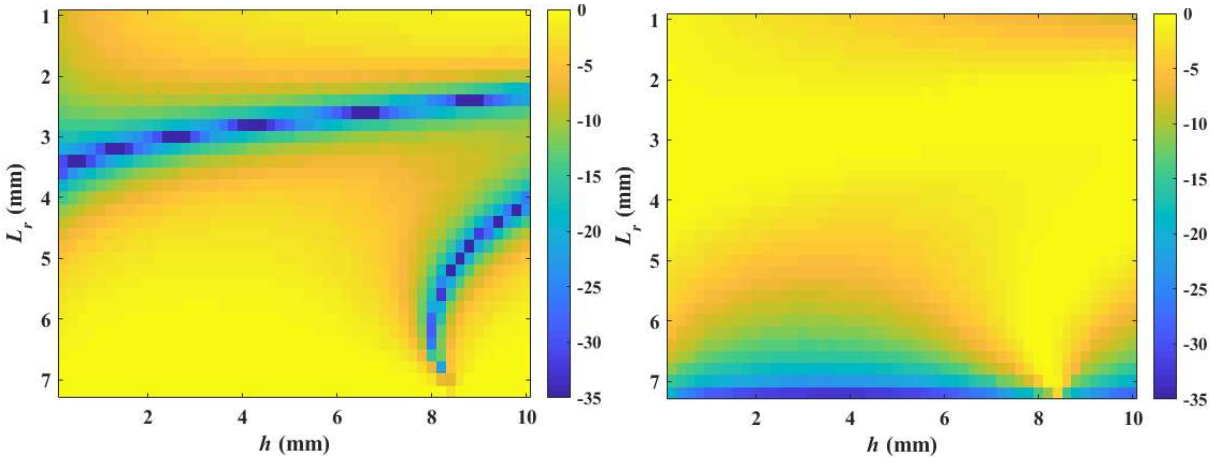

c) d)

Fig.2.10 Simulated S parameters of the SCOW at 20GHz (x-polarization, normal incidence). a) Phase (S_{11}). b) Phase (S_{21}). c) Mag (S_{11}). d) Mag (S_{21}).

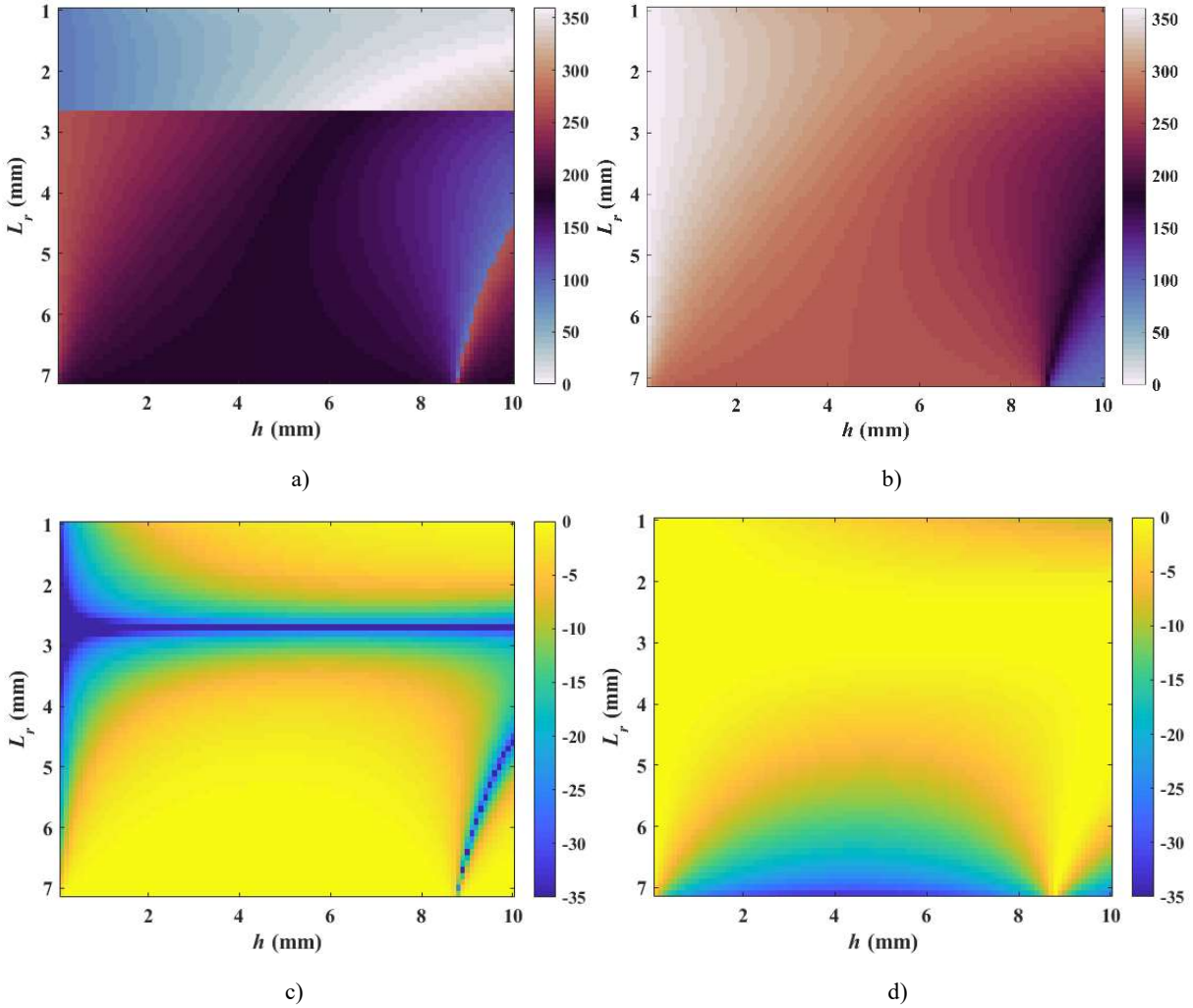

Fig.2.11 Theoretical S parameters of the SCOW at 20GHz. a) Phase (S_{11}). b) Phase (S_{21}). c) Mag (S_{11}). d) Mag (S_{21}).

2.1.3 Conclusion

In this section, the SC with a waveguide and a metallic block is introduced. The distribution of the complex magnitude of the electric field inside the SC is simulated to illustrate the effects of the metallic block. The SC operates as a TA cell or a RA cell depending on the termination at the bottom end. The SCSW enables to control the reflection phase while the SCOW allows to manipulate both the reflection phase and the transmission phase. Their simulated characteristics can be approximated by theoretical S-parameters of the waveguide. In addition, the resonances in the SCOW are analyzed using theoretical S-parameters. For both SCSW and SCOW, however, the achieved phase ranges are not sufficient, which drives us to design new cells.

2.2 Phoenix cell

The SC consisting of a waveguide and a metallic block was introduced in the previous section. The characteristics of the SC are mainly affected by its length (h) and by the size of the metallic block (L_r) in the center. As L_r increases, however, the weight of the SC increases significantly due to the large metallic block. It significantly increases the cost of fabrication. More importantly, the achieved phase ranges of the SC are not sufficient.

In this section, a 3D PC, as shown in Fig.2.12, is proposed. The detailed parameters of the PC are summarized in Table 2.2. The difference with the SC is that the PC replaces the variable metallic block with a variable waveguide and a fixed metallic block. Note that the size of the variable waveguide in this section and the size of the variable metallic block in the previous section use the same index *r*. The waveguide between L_c and L_r is referred to as external waveguide which is equivalent to the waveguide in the SC. Meantime, the waveguide between L_r and L_p is referred to as inner waveguide. The introduction of the inner waveguide can increase the phase ranges of the SC, which will be verified later. Note that the characteristics of the external waveguide in the PC are exactly the same as the waveguide in the SC (see Fig.2.6).

The size of the inner waveguide (L_r) is varied to control the behavior of the PC. The variation cycle is shown in Fig.2.13. At the initial stage (see Fig.2.13), the size of the inner waveguide is equal to the size of the central metallic block (which means there is no more inner waveguide). The inner waveguide then appears as L_r increases. At the final stage, the size of inner waveguide is equal to the size of external waveguide and the inner waveguide disappears again. The cell thus comes back to its initial geometry.

The characteristics of the inner waveguide are summarized in Fig.2.14. It is simulated using the similar model shown in Fig.2.5. L_p provides a possible additional degree of freedom for tuning. In this section, it is set to 1 mm and, at 20GHz, the inner waveguide is under cut-off all over the cycle (see Fig.2.14).

Similarly to the SC, the PC works as a TA or RA cell depending on the termination that is used at the bottom end. One obvious advantage of the PC is that the sharp geometrical variation over the RA aperture might be reduced owing to its rebirth ability.

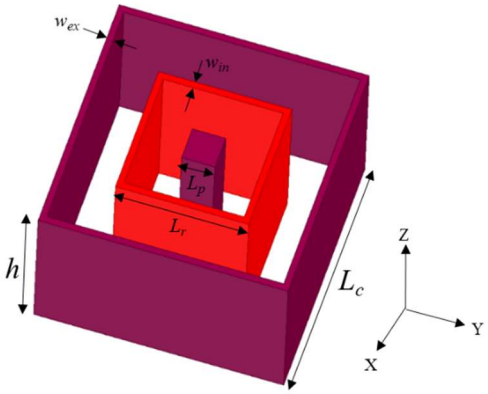

Fig.2.12 The proposed 3D PC.

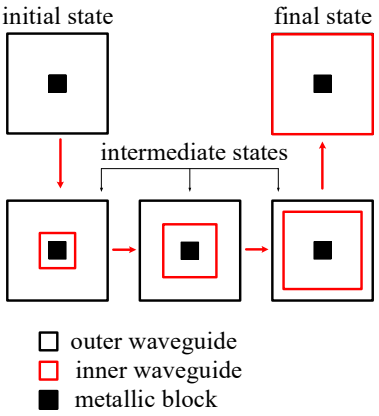

Fig.2.13 The variation mechanism of the 3D PC (the top view)

Table 2.2 Detailed parameters of the 3D MO PC

Parameter	L_c	L_r	L_p	w_{in}	w_{ex}
Value (mm)	7.5	1-7.5 (step=0.1)	1	0.2	0.1

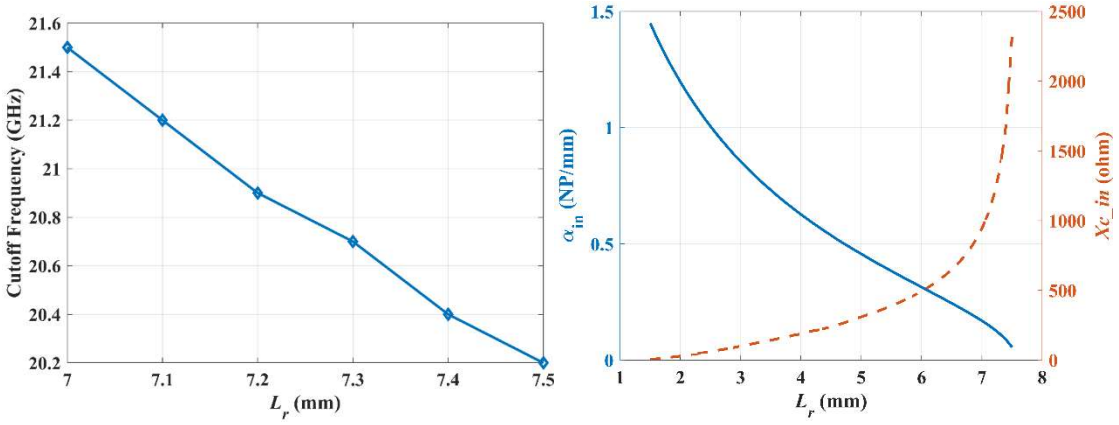

a) b)

Fig.2.14 Characteristics of the inner waveguide. a) Cutoff frequency. b) Imaginary characteristic impedance (Z_{c_in}=jX_{c_in}) and attenuation constant (α_{in}) at 20GHz.

2.2.1 Phoenix cell using short-ended waveguides

The phoenix cell using short-ended waveguide (PCSW) is shown in Fig.2.15. Similarly to the SCSW, the PCSW is able to control the reflection phase owing to the presence of the short circuit termination below the cell.

Before we analyze the actual capabilities of this cell, we would like to compare it with the alternative MO PC cell that has been proposed in [6] and that involves a slot-based configuration. Indeed, this slot-based configuration requires a connecting strip to attach all its metallic parts together since, compared to the original PC in [2], the dielectric layer has been removed and there is no physical support anymore. As a consequence, the PC in [6] loses its 90° rotational invariance and subsequently its capability to deal with dual linear polarization. For our PCSW, the metal rings are replaced by square waveguides. Since these waveguides are supported by the ground plane itself, such connecting elements are not needed and the PCSW recovers the 90° rotational invariance. Therefore, it is a dual-linearly polarized RA cell.

Now, we will have a detailed insight on the cell performance. The simulated reflection phase of the PCSW is shown in Fig.2.16. It can be seen that the complete 360° phase-range (phase vs L_r) can easily be achieved when h is greater than 4 mm. As shown in Fig.2.8a, the achieved phase range (phase vs L_r) of the SCSW is less than 255° for each given h. Obviously the achieved phase range (phase vs L_r) of the PCSW is significantly increased due the introduction of the inner waveguide.

It can be clearly deduced that a small value of h reduces the propagation distance of the guided wave in the external waveguide. In this case, the reflection phase is mainly affected by the variation of characteristic impedances of the waveguides when L_r is changed. The complete 360° phase-range thus cannot be achieved when h is less than 4 mm (see Fig.2.16). For the cases where L_r is very small or very large, most of the incident wave is reflected back due the imperfect matching at the top end. In this case, the reflection phase is hardly affected by h (see Fig.2.16).

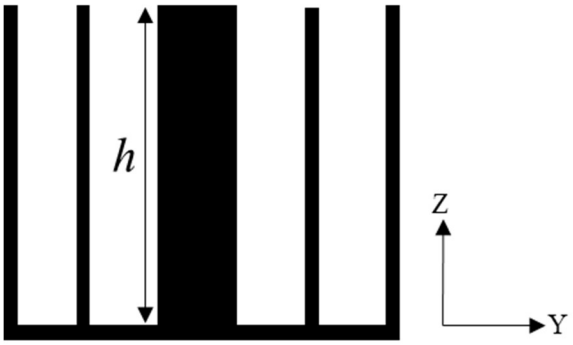

Fig.2.15 Sectional view of the PCSW

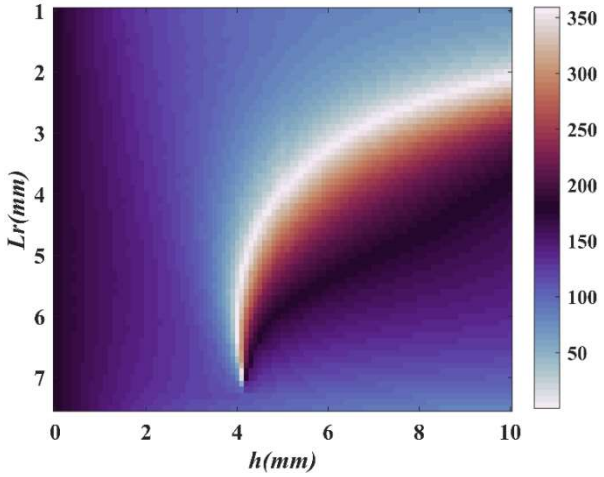

Fig.2.16 Reflection phase of the PCSW at 20GHz

2.2.2 Phoenix cell using open-ended waveguides

The phoenix cell using open-ended waveguide (PCOW) is shown in Fig.2.17. Contrarily to the PCSW that is dual-polarized, the PCOW only enables x-polarization. Compared to the SCOW, the only difference is that an additional waveguide, the inner waveguide, is introduced. Then, if the length of the cell is not long enough, some power can couple reactively from the top end to the bottom end through the inner waveguide. Apart from these differences, the principle of the cell is comparable to that of the SCOW. Since the inner waveguide always operates under the cutoff mode, the theoretical S-parameters of the SCOW (equation (2.4-2.5)) can also be used to analyze the PCOW.

The PCOW is simulated to better illustrate its operation principle. It is illuminated under normal incidence by a x-polarized wave. The height (h) is set to 10 mm. Fig.2.18 shows the simulated S-parameters at 20 GHz. For values of L_r lower than 2 mm, the magnitude of S_{21} is quite small. This is explained by the high characteristic impedance of the external waveguide, as shown in Fig.2.6. Since most of the incident wave is reflected back, the cell can operate as a RA cell. With the increase of L_r, the characteristic impedance of external waveguide decreases and approaches that of free space, Z_0 (see again in Fig.2.6). Thus, the incident wave is now coupled to the external waveguide. In this case, $|S_{21}|$ gets close to 1 and the PCOW can operate as a TA cell. For L_r larger than 4.5 mm, the characteristic impedance of external waveguide decreases further (see Fig.2.6), the external waveguide is mismatched and the PCOW can operate as a RA cell again. These results suggest that a TRA could be designed based on sparse-array theory where some cells are used to control the reflected beam and the other ones are used to control the transmitted beam.

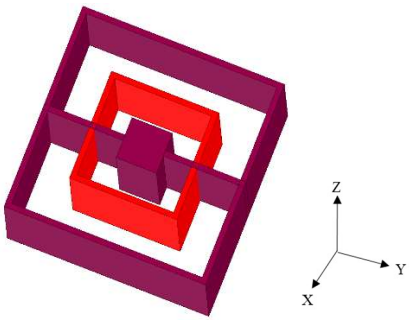

Fig.2.17 3D view of the PCOW.

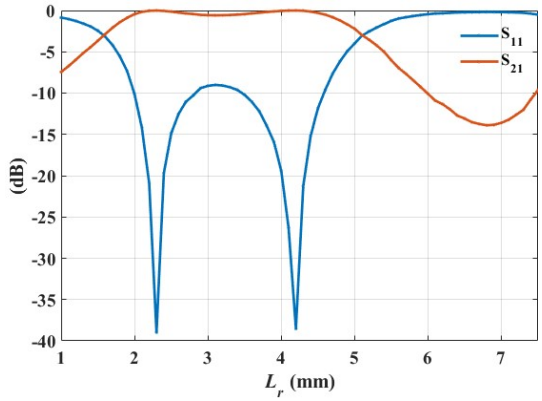

Fig.2.18 Magnitude of S-parameters of the PCOW (h=10 mm, f=20GHz, x-polarized incidence).

In order to have a more global view, both h and L_r are now varied. The simulated S-parameters of the PCOW at 20 GHz are shown in Fig.2.19. On the one hand, it appears that the region where the cell can best be used for reflection is when $4<L_r<7$ mm with $h<8$ mm (left bottom region of plot 2.19c, where $|S_{11}|$ is close to 1). In this region, the characteristic impedance of the external waveguide is far from Z_0 (see Fig.2.6) and most of the incident wave is reflected back directly at the top end of the cell. Unfortunately, a direct consequence of this mechanism is that the range of achievable reflected phase is quite reduced since the incident wave does not penetrate into the cell. On the other hand, the appropriate region for transmission is either when $L_r<4$ mm or, best, when $h>8.6$ mm. The latter case not only provides a magnitude of $|S_{21}|$ close to 1 but also a full 360° range for the transmitted phase. Compared to the maximum achieved phase range of SCOW (290°, phase vs h, see Fig.2.10b), the phase ranges of the PCOW are significantly increased.

Fig 2.19c and d also exhibit dark blue lines. The two dark blue curves in Fig 2.19c has been explained using the theoretical S-parameters in the previous section. Now, the dark blue line in Fig. 2.19d is analyzed, which corresponds to a minimum of transmission. Its equivalent in Fig. 2.11d is not a straight line but still a region of low transmission. It is essential to highlight that Fig. 2.11d agreed well with Fig. 2.10d but the agreement with Fig. 2.19d is not so good. This suggests a strong effect of the inner waveguide here. Once again, the imperfect agreement is due to the used approximations in the theoretical model. Indeed, in this case, the value of L_r is close to that of L_c, which means the cut-off frequency of the inner waveguide is not far from the operating frequency and its effect is not negligible any longer. However, equation (2.2) suggests this low-transmission region is associated to a value of Γ_{ex} such that $\Gamma^2_{ex}\approx 1$, which is consistent with the low values of Z_C in this range of L_r.

Finally, it is worth pointing out that the interesting region for transmission ($h>8.6$ mm) is quite well predicted in Fig. 2.19d. As already mentioned, it is related to the Fabry-Perot resonance (bottom dark blue curve in Fig. 2.19c, which highlights the importance of this phenomenon in the achievement of a full 360° range for transmitted phase.

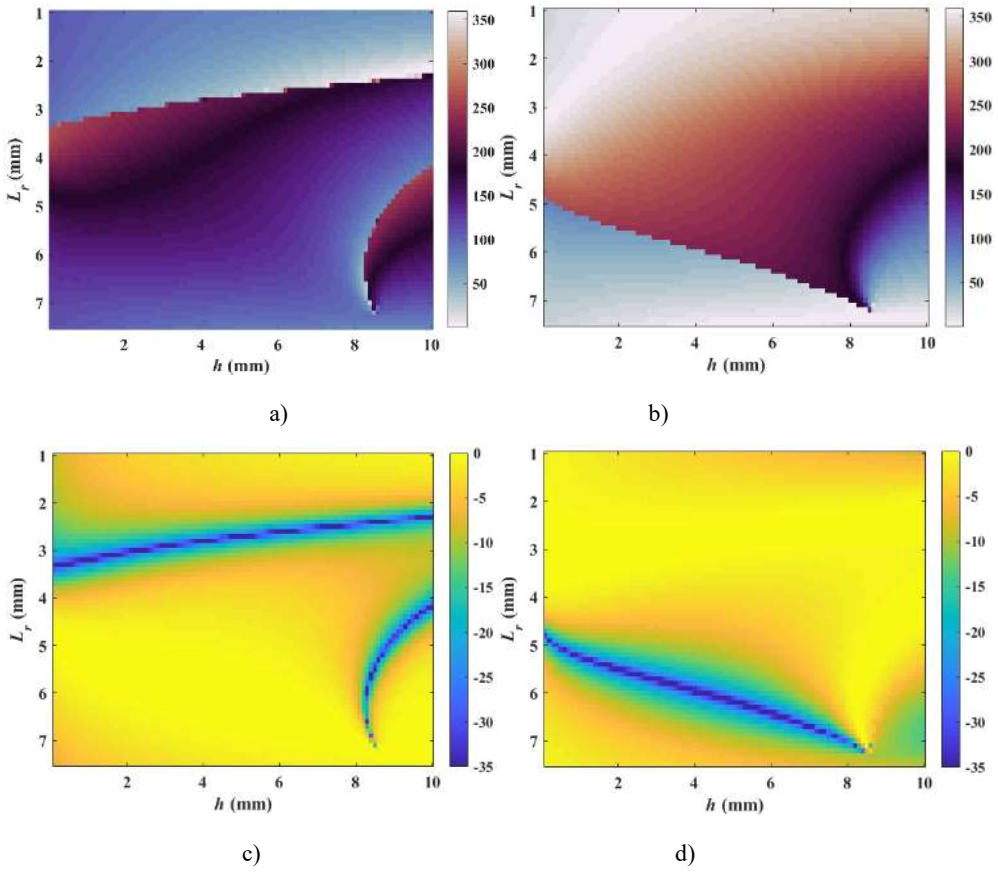

Fig.2.19 Simulated S-parameters of the PCOW at 20 GHz. a) Phase (S_{11}) (deg). b) Phase (S_{21}) (deg). c) Mag (S_{11}) (dB). d) Mag (S_{21}) (dB).

2.2.3 Conclusion

In this section, a 3D PC with the rebirth ability is proposed. It has two different operation modes. The PCSW is a dual-linearly polarized RA cell while the PCOW is a single-linearly polarized cell which can be used to design a TRA. Compared to the SC, the phase ranges of the PC are significantly increased due to the introduction of an additional waveguide. The 'dark blue lines' of the PCOW can be well explained using the theoretical S-parameters.

2.3 Equivalent circuit of the 3D phoenix cell

In previous sections, it is shown that there is a difference between the simulated S-parameters and the theoretical S-parameters due to the discontinuity effects at the top and bottom ends of the cell. In order to have a comprehensive understanding of the 3D PC, an equivalent circuit is proposed. As introduced before, there are two different modes for the 3D PC. In this section, the equivalent circuit is derived for the PCSW only as an illustration. The derivation could easily be extended to the PCOW, but this has not been done for time reasons. The derivation is also done at a single frequency (20GHz).

As the PCSW consists of two waveguides, its input admittance mainly depends on their input admittances. In addition, three shunt admittances are used at the entrance of both waveguides to model the discontinuity effects. As a result, the equivalent circuit can be represented as shown in Fig.2.20. The corresponding input admittance is given by:

$$Y_{input} = Y_{disc\_0} + \frac{1}{\frac{1}{Y_{in}+Y_{disc\_in}}+\frac{1}{Y_{ex}+Y_{disc\_ex}}} \tag{2.6}$$

where Y_{disc_in}, Y_{disc_ex} and Y_{disc_0} are three discontinuity admittances which characterize the reactive excitation of all higher order modes, including higher order modes in the waveguide and Floquet harmonics, and the coupling between them. Note that the two waveguides are connected in series.

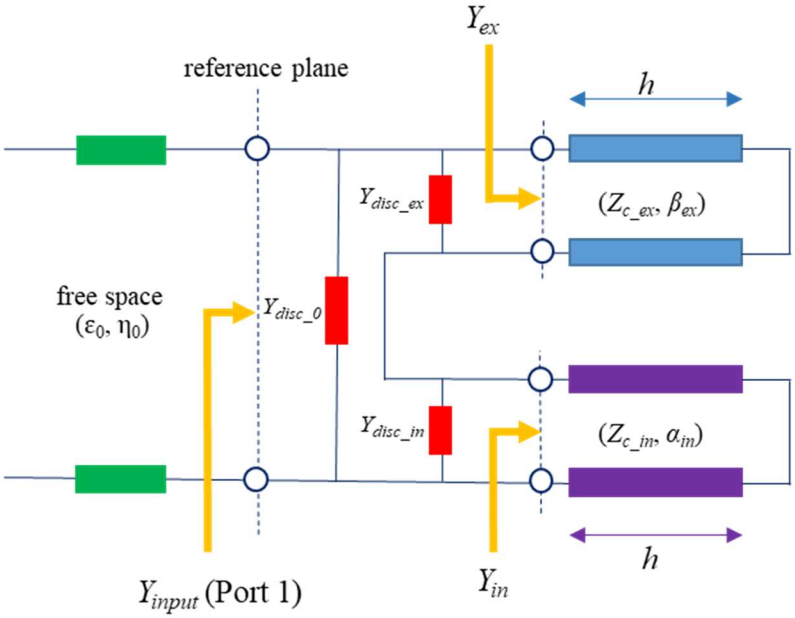

Fig.2.20 Equivalent circuit of the PCSW

2.3.1 Derivation process

In this subsection, the different elements in the equivalent circuit are derived. The derivation has to be repeated for each value of L_r. Once the equivalent elements for a given L_r have been derived, the response of the cell for any value of h can be obtained without any additional full-wave simulation.

The derivation process itself requires only three full-wave simulations corresponding to three different values of h_i (i=1 to 3). Each full-wave simulation yields a given value of Y_{input}, called Y_{input_i}. Y_{in_i} and Y_{ex_i} can be calculated analytically for each value of h_i, using simple transmission line theory and the simulated characteristics of two waveguides (see Fig.2.6 and Fig.2.14).

Then Y_{input_i} can be expressed from Y_{in_i}, Y_{ex_i}, Y_{disc_0}, Y_{disc_in} and Y_{disc_ex} using (2.5). We thus obtain a system of three equations with three unknowns (Y_{disc_0}, Y_{disc_in} and Y_{disc_ex}):

$$Y_{input1} = Y_{disc\_0} + \frac{1}{\frac{1}{Y_{in1}+Y_{disc\_in}} + \frac{1}{Y_{ex}+Y_{disc\_ex}}} \tag{2.7}$$

$$Y_{input2} = Y_{disc\_0} + \frac{1}{\frac{1}{Y_{in2}+Y_{disc\_in}} + \frac{1}{Y_{ex2}+Y_{disc\_ex}}} \tag{2.8}$$

$$Y_{inpu} = Y_{disc\_0} + \frac{1}{\frac{1}{Y_{in}+Y_{disc\_in}} + \frac{1}{Y_{ex3}+Y_{disc\_ex}}} \tag{2.9}$$

We can first address the specific case where L_r <1.4 mm or L_r >7.3 mm. In these cases, one of the two waveguides disappear completely. Then, there will be only one discontinuity admittance (corresponding to either $Y_{disc\_0} // Y_{disc\_in}$ or $Y_{disc\_0} // Y_{disc\_ex}$) in the equivalent circuit. As a consequence, a single equality is enough to derive the discontinuity. It is given by:

$$Y_{disc\_0} = Y_{input} - Y_{in1} \tag{2.10}$$

or:

$$Y_{disc\_0} = Y_{input1} - Y_{ex1} \tag{2.11}$$

In the general case, we have to consider all three discontinuity-admittances. Obviously, equations (2.7-2.9) are nonlinear equations, which makes the resolution a bit tricky. A judicious choice of some of the values of h_i can facilitate the process. For example, if:

$$h_1 = \lambda_{ex} \tag{2.12}$$

the associated value of Y_{ex} is infinite and:

$$Y_{input1} = Y_{disc\_0} + Y_{in1} + Y_{disc\_in} \tag{2.13}$$

Substituting equation (2.13) into equation (2.8) and equation (2.9), gives:

$$\begin{aligned}\left(Y_{input2} - Y_{input1} + Y_{in1}\right)(Y_{in2} + Y_{ex2}) - Y_{in2}Y_{ex2} + \left(Y_{inp} \quad - Y_{input1} + Y_{in1} + Y_{in2}\right)Y_{disc\_in} + \\ Y_{disc\_in}^2 = \left(Y_{input1} - Y_{input2} - Y_{in1} + Y_{in2}\right)Y_{disc\_ex}\end{aligned} \tag{2.14}$$

$$\begin{aligned}\left(Y_{input3} - Y_{input1} + Y_{in1}\right)(Y_{in3} + Y_{ex3}) - Y_{in3}Y_{ex3} + \left(Y_{input3} - Y_{input1} + Y_{in1} + Y_{in3}\right)Y_{disc\_in} + \\ Y_{disc\_in}^2 = \left(Y_{input1} - Y_{input3} - Y_{in1} + Y_{in3}\right)Y_{disc\_ex}\end{aligned} \tag{2.15}$$

In the end, there remains only two unknowns in equation (2.14-15). Therefore, Y_{disc_in} and Y_{disc_ex} can be obtained by solving these equations. In addition, the equations (2.14-15) are quadratic equations of Y_{disc_in}. As a results, we can get two different sets of solutions for Y_{disc_in} and Y_{disc_ex}. In the following, we will call them analytical solution 1 and analytical solution 2. Analytical solution 1 corresponds to the + signs in equations (2.16-2.17) while analytical solution 2 correspond to the – signs.

$$Y_{disc\_in} = \frac{\frac{Y_{input2}-Y_{input1}+Y_{in1}+Y_{in2}}{Y_{input1}-Y_{input2}-Y_{in1}+Y_{in2}} + \frac{Y_{input3}-Y_{inpu}\ \ +Y_{in1}+Y_{in}}{Y_{input}\ -Y_{inpu}\ \ -Y_{in1}+Y_{in}}}{2\left(\frac{1}{Y_{input}\ -Y_{input}\ -Y_{in1}+Y_{in2}} - \frac{1}{Y_{inpu}\ \ -Y_{input3}-Y_{in}\ +Y_{in3}}\right)} \pm \frac{\sqrt{\left(\frac{Y_{inpu}\ \ -Y_{input1}+Y_{in1}+Y_{in2}}{Y_{input1}-Y_{inp}\ \ -Y_{in}\ +Y_{in}} - \frac{Y_{inpu}\ \ -Y_{input1}+Y_{in1}+Y_{in}}{Y_{input1}-Y_{input3}-Y_{in1}+Y_{in3}}\right)^2 - 4\left(\frac{1}{Y_{input1}-Y_{inpu}\ \ -Y_{in1}+Y_{in2}} - \frac{1}{Y_{inpu}\ \ -Y_{input3}-Y_{in1}+Y_{in}}\right)\cdot \left(\frac{\left(Y_{inpu}\ \ -Y_{input1}+Y_{in1}\right)(Y_{in2}+Y_{ex2})-Y_{in}\ Y_{ex}}{Y_{inpu}\ \ -Y_{inpu}\ \ -Y_{in1}+Y_{in}} - \frac{\left(Y_{input}\ -Y_{inpu}\ \ +Y_{in1}\right)(Y_{in3}+Y_{ex}\ )-Y_{in3}Y_{ex}}{Y_{input1}-Y_{input3}-Y_{in}\ +Y_{in3}}\right)}}{2\left(\frac{1}{Y_{inpu}\ \ -Y_{input2}-Y_{in}\ +Y_{in}} - \frac{1}{Y_{input1}-Y_{input3}-Y_{in1}+Y_{in3}}\right)} \tag{2.16}$$

$$Y_{disc\_ex} = \frac{\left(Y_{inpu}\ \ -Y_{input1}+Y_{in1}\right)(Y_{in}\ +Y_{ex2})-Y_{in2}Y_{ex}\ +\left(Y_{input2}-Y_{inpu}\ \ +Y_{in}\ +Y_{in2}\right)Y_{disc\_in}+Y_{disc\_in}^2}{\left(Y_{inpu}\ \ -Y_{input2}-Y_{in}\ +Y_{in}\ \right)} \tag{2.17}$$

After solving the Y_{disc_in}, Y_{disc_0} can be solved from equation (2.13):

$$Y_{disc\_0} = Y_{inpu}\ \ - Y_{in1} - Y_{disc\_in} \tag{2.18}$$

2.3.2 Verification of the equivalent circuit

The derivation process was presented in the previous subsection. It is now applied for L_r in the range from 1 to 7 mm with a step of 1 mm, which means it is repeated 7 times. For the case where L_r equals to 1mm, equation (2.11) is used to derive the equivalent circuit. The selected h is 5.5mm, which is a medium value. For other values of L_r, equations (2.16-18) are used. As already said, h_1 is chosen as the wavelength in the external waveguide. The two other heights should be selected far away from integer multiples of half this wavelength in order to obtain a system with independent equations. In this section, three different combinations of heights, as summarized in table 2.3, are used to derive the equivalent circuits so that the reliability of the proposed equivalent circuit can be verified.

Table 2.3 Heights used to derive the equivalent circuit

	h_1 (mm)						h_2 (mm)	h_3 (mm)
L_r	2mm	3mm	4mm	5mm	6mm	7mm	-	-
Combination 1	32.99	24.51	21.13	19.38	18.30	17.62	4	6
Combination 2							7.5	4
Combination 3							7	6

The reflection phases produced by the equivalent circuits for the three different combinations and for the two analytical solutions are shown in Fig.2.21 when h is varied. They are compared to the ones given by full wave simulations. It can be seen that the agreement between the full wave simulations and the equivalent circuits is quite good, which demonstrates the reliability of the proposed equivalent circuits. The phase errors between equivalent circuit and full wave simulation results for most cases (L_r, h) are less than 10 degrees. These results demonstrate that the proposed equivalent circuit can be used to predict the reflection phase of the PCSW.

In addition, the obtained values for the discontinuity admittances are summarized in table 2.4. It can be seen that analytical solution 2 for combination 1, analytical solution 1 for combination 2 and analytical solution 1 for combination 3 are very close. Similarly, analytical solution 1 for combination 1, analytical solution 2 for combination 2 and analytical solution 2 for combination 3 are very close. These results demonstrate that the two analytical solutions in equation (2.16-2.18) may lead to same solutions. In other words, both solutions are acceptable.

Table 2.4 Discontinuity admittances

			L_r (mm)					
			2	3	4	5	6	7
Y_{disc_0}	Combination 1	Analytical Solution 1	-0.0043i	-0.0015i	-0.0002i	0.0003i	0	0.0020i
		Analytical Solution 2	-0.0419	-0.0532i	-0.0423i	-0.0268i	-0.0150i	-0.0097i
	Combination 2	Analytical Solution 1	-0.0421i	-0.0528i	-0.0419i	-0.0263i	-0.0145i	-0.0102i
		Analytical Solution 2	-0.0041i	-0.0016i	-0.0003i	0.0001i	-0.0003i	0.0029i
	Combination 3	Analytical Solution 1	-0.0424i	-0.0522i	-0.0416i	-0.0262i	-0.0141i	-0.0094i
		Analytical Solution 2	-0.0037i	-0.0019i	-0.0003i	0.0002i	0.0005i	0.0023i
Y_{disc_in}	Combination 1	Analytical Solution 1	0.0168i	-0.0154i	-0.0154i	-0.0100i	-0.0053i	-0.0044i
		Analytical Solution 2	0.0543i	0.0363i	0.0267i	0.0171i	0.0097i	0.0072i
	Combination 2	Analytical Solution 1	0.0545i	0.0359i	0.0263i	0.0166	0.0092i	0.0078i
		Analytical Solution 2	0.0165i	-0.0153i	-0.0153i	-0.0098	-0.0050i	-0.0053i
	Combination 3	Analytical Solution 1	0.0548i	0.0353i	0.0260i	0.0164i	0.0088i	0.0070i
		Analytical Solution 2	0.0161i	-0.0150i	-0.0154i	-0.0099i	-0.0047i	-0.0047i

Y_{disc_ex}	Combination 1	Analytical Solution 1	0.0030i	0.0011i	0.0010i	0.0023i	0.0054i	0.0068i
		Analytical Solution 2	-0.0349i	-0.0518i	-0.0424i	-0.0253i	-0.0090i	-0.0006i
	Combination 2	Analytical Solution 1	-0.0356i	-0.0506i	-0.0412i	-0.0237i	-0.0075i	-0.0046i
		Analytical Solution 2	0.0027	0.0012i	0.0010i	0.0025i	0.0057i	0.0017i
	Combination 3	Analytical Solution 1	-0.0363i	-0.0489i	-0.0404i	-0.0241i	-0.0110i	-0.0078i
		Analytical Solution 2	0.0024i	0.0014i	0.0010i	0.0023i	0.0030i	0.0164i

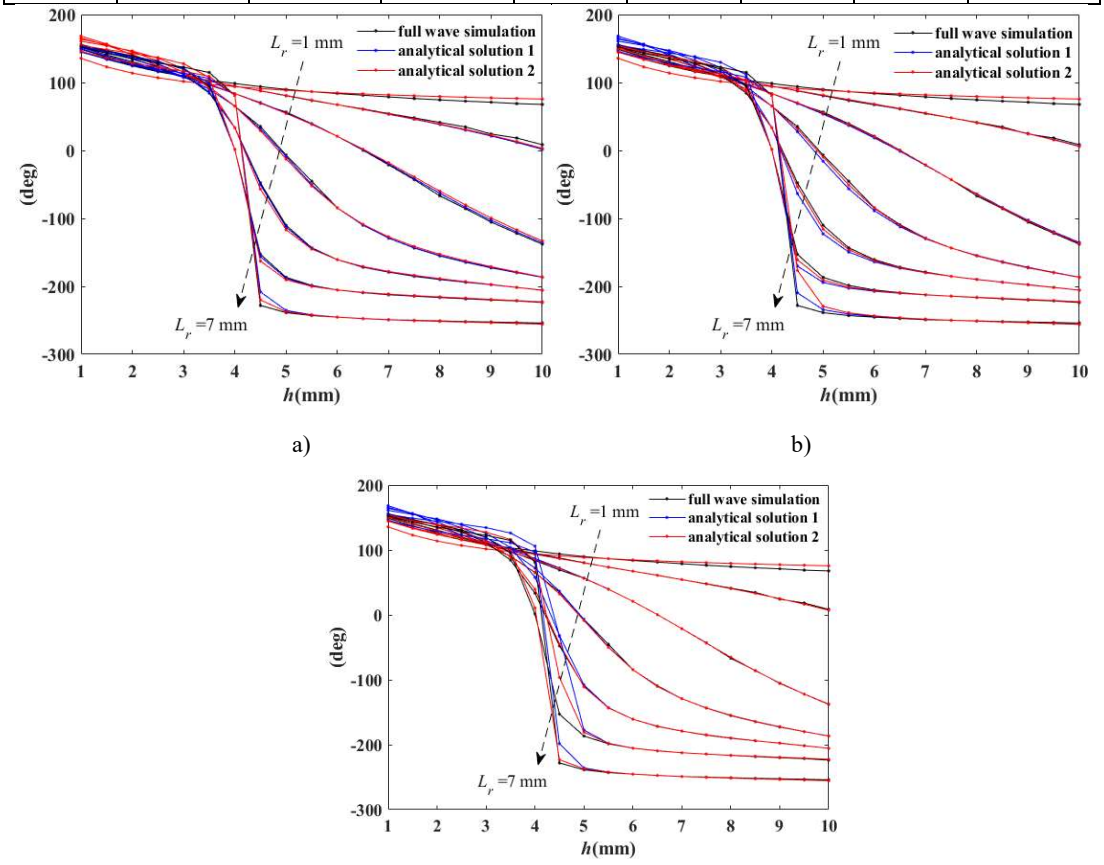

Fig.2.21 Reflection phase. a) Combination 1. b) Combination 2. c) Combination 3.

2.3.3 Conclusion

In this section, an equivalent circuit considering the discontinuity effects is proposed. Different elements in the equivalent circuit are derived respectively. The reflection phases of the derived equivalent circuits are compared with the full wave simulation results. It shows that the proposed equivalent circuit can be used to predict the reflection phase. Also, the reliability of the proposed equivalent circuit is verified.

2.4 Resonances analysis

In previous simulations, the material of the unit cells is PEC, which neglects the losses caused by real materials. In this section, the SCSW (see Fig.2.7) is simulated again to analyze the effect of a real metal on the losses of the waveguide-based cells. Stainless steel with a conductivity of 1.33×10^6 S/m is

chosen as it will be the used metal for breadboards in future chapters. A single waveguide is analyzed first and then the SCSW is analyzed.

2.4.1 Waveguide with losses

The waveguide defining the SCSW is simulated using the same set-up as the one shown in Fig.2.5. The only difference is that the metal walls are now made of stainless steel with a thickness of 0.2 mm. The simulated characteristics of the waveguide are shown in Fig.2.22. α and β'_{ex} are the real part and imaginary part of the propagation constant respectively. Obviously, the losses get high when L_r gets close to L_c (meaning the gap between metal walls is small).

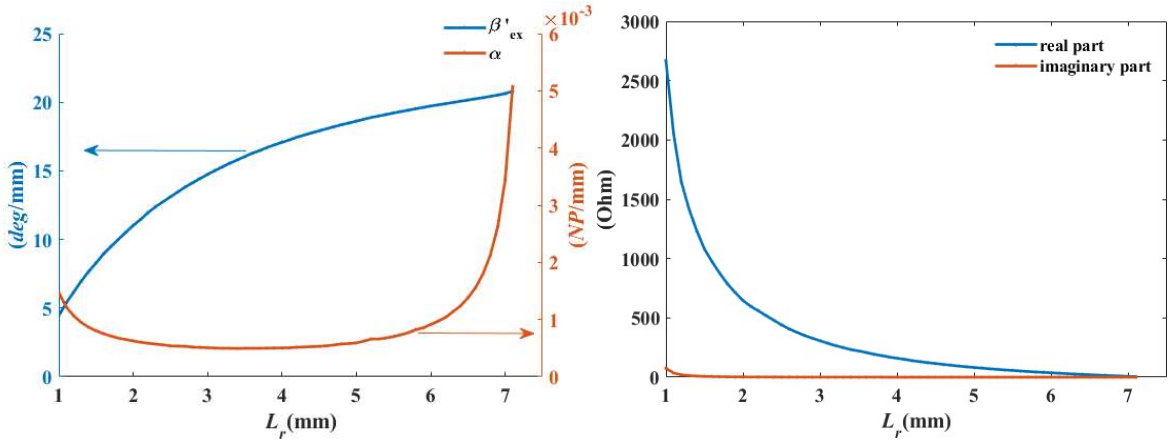

a) b)

Fig.2.22 Characteristics of the waveguide at 20GHz. a) Propagation constant. b) Characteristic impedance.

2.4.2 Unit cell with losses

Now the SCSW with a realistic material is simulated. Its reflection coefficients are summarized in Fig.2.23. It can be seen that the resonances ('white curve' in Fig.2.23a) may increase the losses of the SCSW. The theoretical reflection coefficient of the SCSW after considering the realistic material is shown in Fig.2.24. It can be seen that the agreement between Fig.2.23 and Fig.2.24 is quite good, which further verifies that the cells with high losses are caused by the resonances. However, the losses are not so large except for the case where L_r is close to L_c.

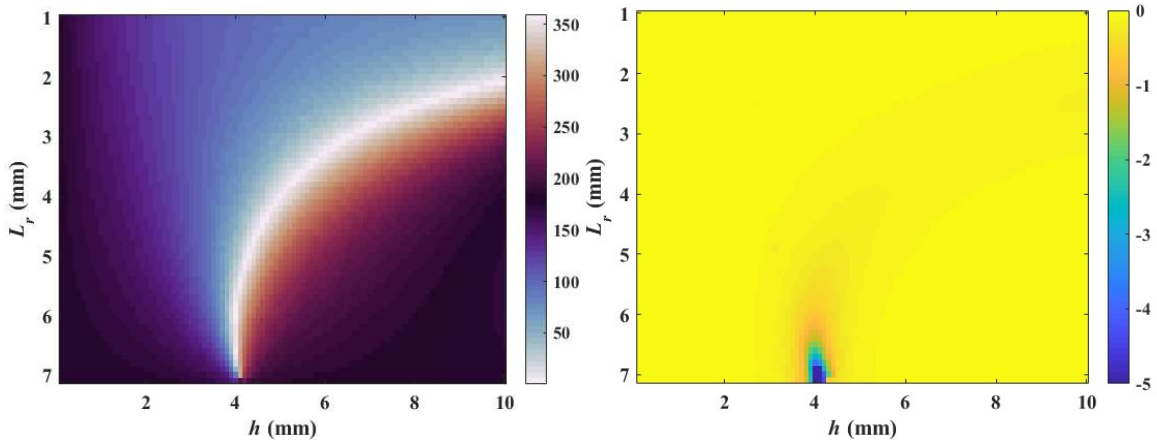

a) b)

Fig.2.23 Simulated reflection coefficient of the SCSW at 20GHz (real metal, normal incidence). a) Phase. b) Mag.

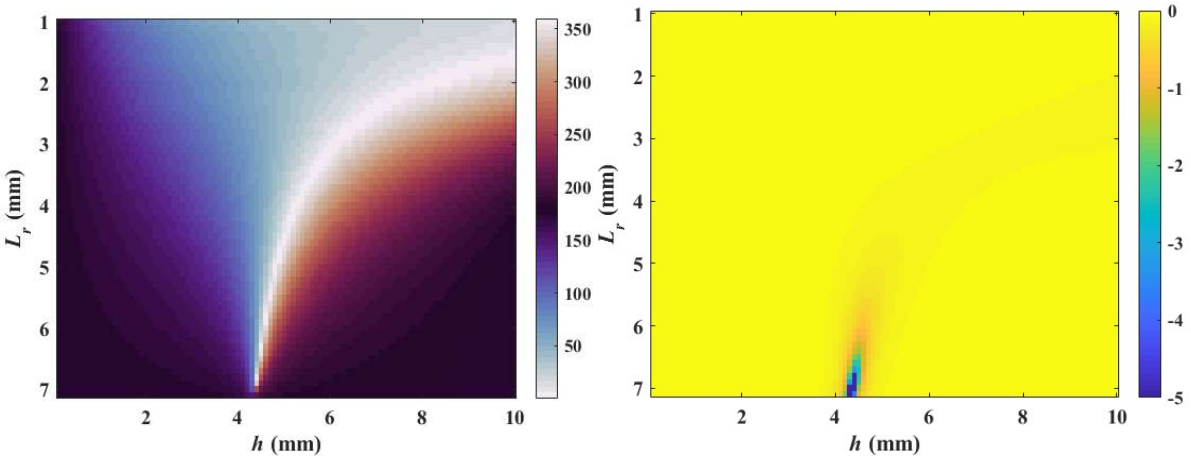

Fig.2.24 The theoretical S parameter of the SCSW at 20GHz (real metal). a) Phase (S_{11}). b) Mag (S_{11}).

2.4.3 Conclusion

In this section, the characteristics of the waveguide after considering the real material is first evaluated. It shows that the real material leads to an attenuation of the magnitude of the wave propagating in the waveguide, when L_r is close to L_c. In this situation, a prohibitive loss can be observed when the cell is resonant.

2.5 Conclusion

This chapter provides a detailed analysis of waveguide-based cells. The SC and the PC are first introduced. The SC consists of a rectangular waveguide and a metallic block while the PC consists of two concentric rectangular waveguides and a metallic block. Both of them operate as a TA cell or a RA cell depending on the termination at the bottom end. Their performances are verified by full wave simulation results. Also, their principles are analyzed using theoretical S-parameters. It shows that there is a difference between the theoretical S-parameters and the simulated S-parameters caused by the discontinuity effects. To fully understand the waveguide-based cells, an equivalent circuit is derived for the PCSW where the discontinuity effects are considered. Results show that the proposed equivalent circuit can be used to predict the reflection phase of the PCSW. Finally, the SCSW with a realistic material is studied using theoretical S-parameters. Simulations show that loss is not a major issue, even for resonant cells, except in extreme configurations (L_r close to L_c).

Chapter 3 - Dual Band Antenna made of Simple Cells

3.1 Introduction 74

3.2 Proposed concept of dual band antenna 74

3.3 Analysis of the unit cell 75

3.3.1 Initial analysis 75
3.3.2 Unit cell under oblique incidence 77
3.3.3 Solutions to avoid TEM resonance 82
3.3.4 Conclusion 84

3.4 Preliminary design of dual band antenna 84

3.4.1 Description of the design process 84
3.4.2 Design of two feed antennas 86
3.4.3 Performances of the designed dual band antenna 88
3.4.4 Conclusion 93

3.5 Optimized design 1 of dual band antenna 94

3.5.1 Comparison between three different RRAs 94
3.5.2 Conclusion 97

3.6 Optimized design 2 of dual band antenna 98

3.6.1 Description of two operation modes 98
3.6.2 Performances of two different modes 99
3.6.3 Conclusion 101

3.7 Modification of RRA0 for reduced profile 101

3.7.1 Principle of profile reduction 101
3.7.2 Performances evaluation 104
3.7.3 Conclusion 107

3.8 Fabrication and measurements 108

3.8.1 Antenna fabrication 108
3.8.2 Antenna measurement 111
3.8.3 Optimized antenna made of unit cells with fixed cross-section 115

3.9 Conclusion 117

Chapter 3 Dual Band Antenna made of Simple Cells

3.1 Introduction

In some specific applications, RAs are required to operate in two different frequency bands. The dual band RAs are often achieved using microstrip phase-shifting cells [120-132], where the reflection phases at both bands are tuned either by varying the geometry or using the variable rotation technique. In [115], an all-dielectric dual band RA is proposed where two different dielectric mirrors are used to control the reflection phase of the two frequency bands respectively. For all previously mentioned dual band RAs, a dielectric material is used, which makes these solutions not suitable for some applications in severe environment, such as space. In such a situation, as described in Chapter 1, a MORA is preferable as it avoids the intrinsic problems brought by the dielectric materials such as outgassing and temperature-dependent dielectric constant. A dual band MORA consisting of slot-type PC is thus proposed in [133]. This dual band MORA is synthesized by optimizing the total phase error at two frequency bands simultaneously. A dual band CP MORA is proposed in [63]. It consists of an anisotropic metal brick mounted on a full metal ground (see Fig.1.27). The reflection phases at both frequency bands are controlled by both rotating the cell and moving the cell up.

Nevertheless, for all these dual band RAs, the main beams of both frequency bands are completely determined by the phase distributions over the RA cells. At the same time, they are flat structures (or almost flat structures). Instead, this chapter proposes a dual band MO antenna which combines a parabolic reflector and a RA. For the sake of simplicity, it is referred to as reflector reflectarray antenna (RRA) in this thesis. Nowadays the fabrication of such structures is possible thanks to the development of 3D printing technology. The dual band MORRA is fabricated using the SLM 3D printing technology which has been introduced in Chapter 1.

Although a reflector antenna with a similar principle has been reported in [134], the proposed MORRA in this thesis is quite different. First, the used phase-shifting cell is different. In [134], the reflection phase at higher frequency is tuned only by a short-ended rectangular waveguide. Therefore the periodicity (after taking into account the cutoff frequency of the TE_{10} mode) has to be greater than half a wavelength at higher frequency, which may result in grating lobes. Next, the waveguides in [134] are integrated into the curved surface of reflector and the waveguide open-ended apertures are closely tangent to the reflector surface. In this case, the metallic walls of the waveguides may not be parallel to the vertical direction, which is not compatible with a simple AM process. The cell apertures in this PhD, however, are perpendicular to the vertical direction. In other words, the antenna in this PhD is more like a RA and more compatible with a simple AM process. Finally, the antenna in [134] has not been validated by fabrication and measurements.

In this chapter, the concept of dual band antenna is proposed first. The performances of the unit cell under normal incidence and oblique incidence are evaluated and analyzed. Then the proposed dual band antenna is synthesized. After this, three optimized designs are studied. Finally, a dual band antenna is selected to be fabricated and measured.

3.2 Proposed concept of dual band antenna

The principle of the dual band MORRA is shown in Fig.3.1. The proposed dual band RRA consists of short-ended metallic waveguides. The waveguides are accommodated in such a way that their top surface approximately forms a paraboloid. If the frequency of the incident wave from the feed antenna is less than the cutoff frequency of these waveguides, the incident wave will be reflected back directly

at the entrance of each waveguide. In this case, the incident wave is collimated only by the shape of the aperture and the operating mechanism is the same as the one of a parabolic reflector. It involves a true-time delay mechanism, which means it has no bandwidth limitation. If the frequency of the incident wave is greater than the cutoff frequency of the waveguides, the incident wave propagates inside and an additional phase shift is obtained whose value depends on the length of each waveguide. As a result, a dual band MORRA can be designed. Once the shape of the aperture is determined in the lower frequency band, the reflected beam in the upper frequency band is obtained thanks to the phase distribution produced by the unit cells of the RRA. Note that the directions of the main beams can be different in both frequency bands. Based on the principle of the proposed dual band MORRA, a very large frequency ratio between both bands can be achieved. As an example, a dual band MORRA operating at 20/40GHz is designed in this chapter.

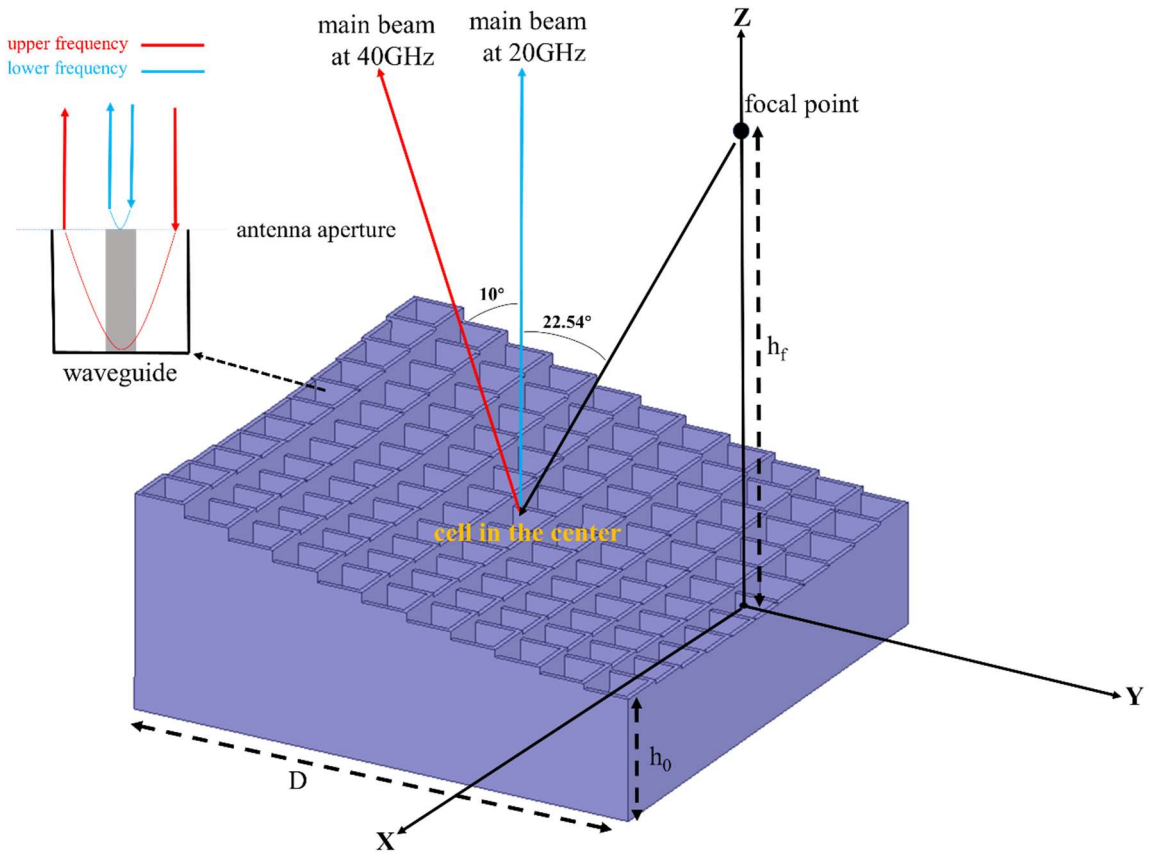

Fig.3.1 The principle and configuration of proposed dual band MORRA.

(The given angles are the ones used in the designed dual band antenna before optimization)

3.3 Analysis of the unit cell

3.3.1 Initial analysis

In this thesis, the unit cell is designed for operation at 20 and 40GHz. Based on the concept previously described, the reflection phase at 20GHz must be constant, and a complete 360° phase range is required at 40GHz. Both the SCSW and the PCSW described in the last chapter enable to control the reflection phase. Compared with the PCSW, however, the use of the SCSW at 40GHz may reduce the fabrication error as its structure is simpler. Consequently, the SCSW (see Fig.2.7) is used to design the dual band antenna in this chapter. The detailed parameters of the proposed cell are tabulated in Table 3.1.

First, the unit cell under normal incidence is simulated to initially evaluate its characteristics. In the simulations, the metal conductivity is set to 1.33×10^6 S/m (stainless) for the sake of realism. The simulated reflection phase and loss at 20/40GHz are summarized in Fig.3.2 when h and L_r are varied. It can be seen that the range of variation of the reflection phase is from 155° to 165° and the maximum loss is 0.05dB at 20GHz. The 360° phase range is achieved and the loss is less than 1.15 dB at 40GHz. These results demonstrate that the SCSW can be used to design the dual band MORRA. The frequency response of the unit cell is now simulated to evaluate the maximum frequency for which it enables the antenna to work as a parabolic reflector. In this case, the waveguide inside the unit cells should operate under cutoff or close to cutoff so that unit cells with different geometries all provide the same reflection phase (or very close ones). As we expect the cutoff of the waveguide to be affected by the value of L_r, three different L_r (1.5mm, 2mm and 2.5mm) are chosen and h is fixed at 5mm. The frequency range is varied from 10GHz to 40GHz and the simulation results are summarized in Fig.3.3. It can be seen that the phase response is almost constant up to a given frequency (depending on L_r), then the reflected phase decreases rapidly, which means cutoff has been reached and the wave penetrates into the waveguide. As could be expected, the cutoff frequency gets lower when L_r increases. For all three considered L_r, it is higher than 25GHz. Thus, the phase variation from one geometry to another is negligible up to 25GHz and the corresponding loss is less than 0.2dB, which indicates that the operating frequency band of the parabolic reflector can reach at least 25GHz. This will be verified in subsequent simulations for MORRAs. The loss after 25 GHz is caused by the propagation of the fundamental TE_{10} and TE_{01}-like modes and associated resonances, which has been demonstrated in chapter 2, section 1.4. Also note that the maximum value of L_r used here (2.5 mm) is sufficient to obtain a 360° phase range at 40 GHz (as demonstrated by Fig. 3.2b).

Table 3.1 Detailed parameters of the unit cell

Parameter	L_c	L_r	h	w_{ex}
Value (mm)	3.75	1.5-2.5	2.5-7	0.2

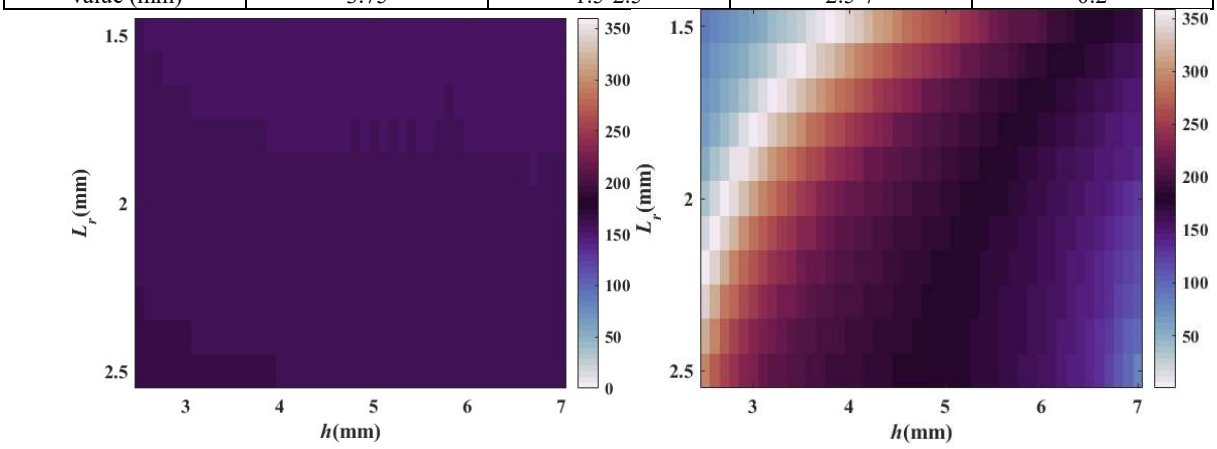

a) b)

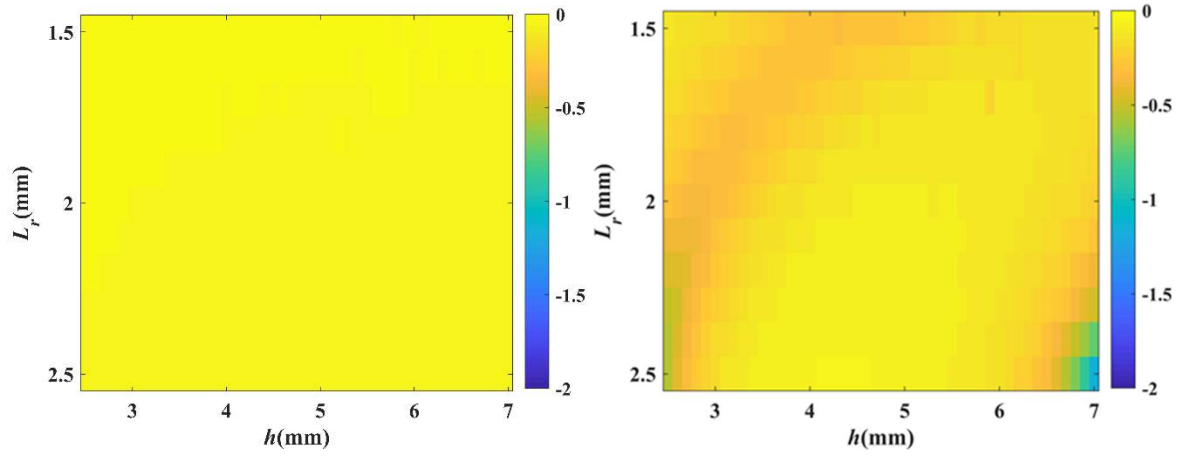

c) d)

Fig.3.2 Reflection phase and magnitude (normal incidence). a) Phase at 20GHz (deg). b) Phase at 40GHz (deg). c) Magnitude at 20 GHz(dB). d) Magnitude at 40GHz (dB).

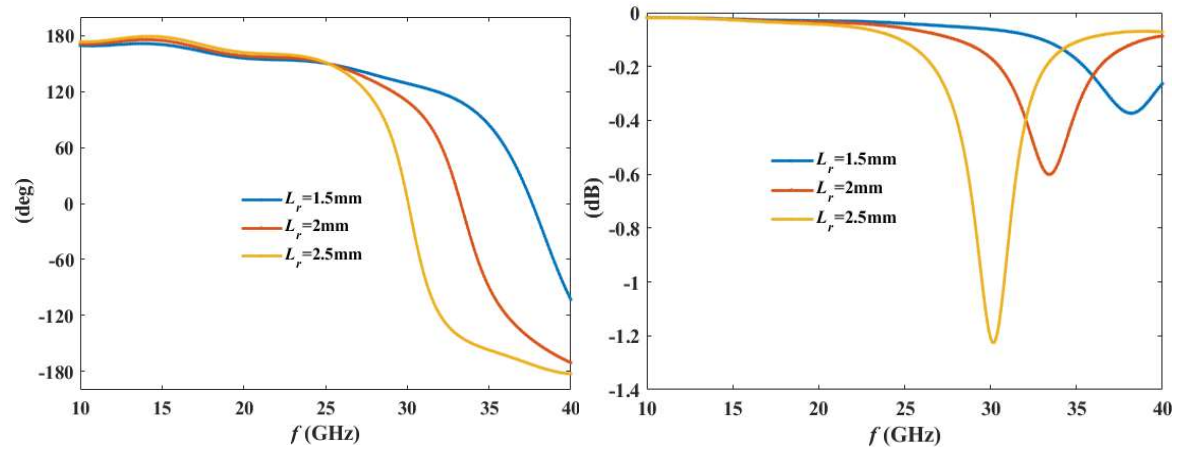

a) b)

Fig.3.3 Frequency response of the unit cell (h=5mm, normal incidence). a) Reflection phase. b) Magnitude.

3.3.2 Unit cell under oblique incidence

Next, the unit cell under oblique incidence is simulated to analyze its performances. In this simulation, the range of h is increased to better show the resonances (whose origin will be explained later in this section). The incident theta (θ_{inc}) and incident phi (ϕ_{inc}) are set to (22.54°, 90°). This specific angles correspond to the direction of arrival of the incident wave in the center of dual band RRA, as will be explained in a later subsection. Both TE and TM polarizations are considered in this simulation. Note that, in this plane, the TE case corresponds to x-polarization while the TM case corresponds to y-polarization. The simulation results are summarized in Fig.3.4 (TE case) and 3.5 (TM case).

It can be seen from the comparison of Fig.3.2 and 3.4 that the TE case is quite similar to the case of normal incidence. Note that the range of h in the case of oblique incidence is increased to 10 mm to better see the resonances that will be discussed in this section.

Now, we move to the TM case. It can be seen from Fig.3.5 that the TM case causes additional resonances associated with high losses and unstable phases. The values of h that causes these resonances (3.3mm, 5.2mm, 9mm) are almost independent of the value of L_r. This suggest they are linked to the length of the waveguide (h) but not to its cross section. To figure out these resonances, the electric field distribution of the unit cell is analyzed. A case under normal incidence (without resonance) and a case

under oblique incidence (with resonance) are shown in Fig.3.6 and Fig.3.7, respectively. Note that both cases have the same geometry and only the incident angle is different.

Actually, the waveguide inside the unit cell can be equivalent to two symmetrical back-to-back ridged waveguides (about xoz plane in this case). The complex magnitude (see Fig.3.6a) shows that the field is concentrated in the corresponding vertical halves (the one along x) of the waveguide. The direction of electric field in these areas (see Fig.3.6b, c and d) confirms that a quasi TE_{10} mode is excited there. On the contrary, Fig.3.7a shows that, in the case of oblique incidence, the electric field is not concentrated anymore in the vertical halves but quite uniformly distributed all around the central metallic block. Moreover, time-domain snapshots (especially Fig. 3.7d) suggest the configuration is that of a quasi-TEM mode.

The explanation is the following. In the case of normal incidence, the electric fields in both halves of the unit cell have the same phase (due to the symmetrical excitation) and the TEM mode cannot be excited. Similarly, the TE case under oblique incidence does not enable a TEM mode in the unit cell. On the contrary, such a mode is possible in the TM case under oblique incidence because the phases in both halves of the cell are not identical any longer. More likely, both a TE10 mode (one in each vertical half) and a TEM mode are excited simultaneously in this case and they have a different phase (and also a different magnitude). This is why the time-domain field looks like a TE10 one at some time steps (typically at ωt=0°, Fig. 3.7b) and a TEM one at other time steps (typically at ωt=90°, Fig. 3.7d). In fact, it seems there are almost in phase quadrature. In addition, an important point is that it is the introduction of the central metallic block that makes possible the excitation of a TEM mode because it provides the two independent conductors (metallic block and metallic wall) that are required to support such a mode.

Now, we will show the observed resonances in the TM case are directly linked to the excitation of this TEM mode. For simplicity, these resonances will be called ‘TEM resonances’ in the rest of this thesis.

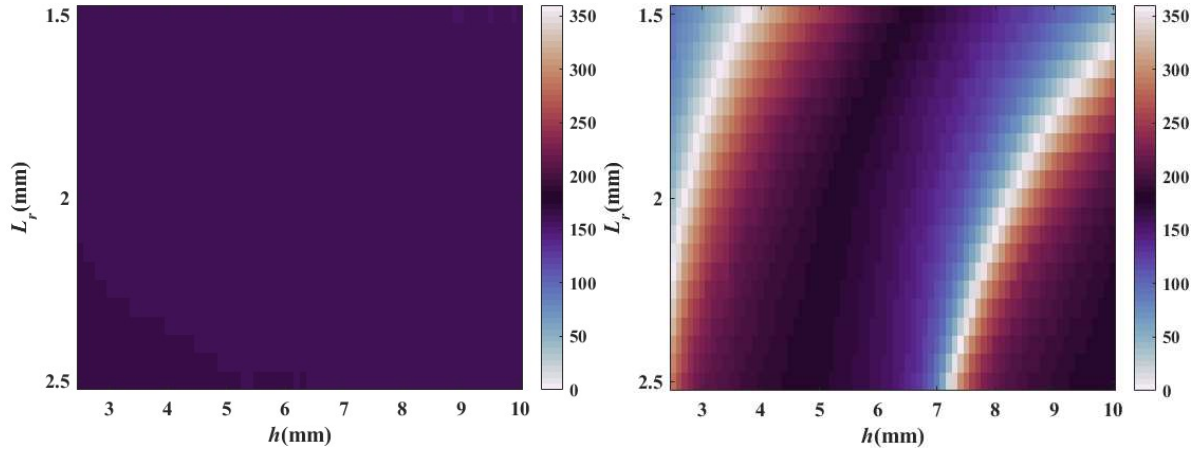

a) b)

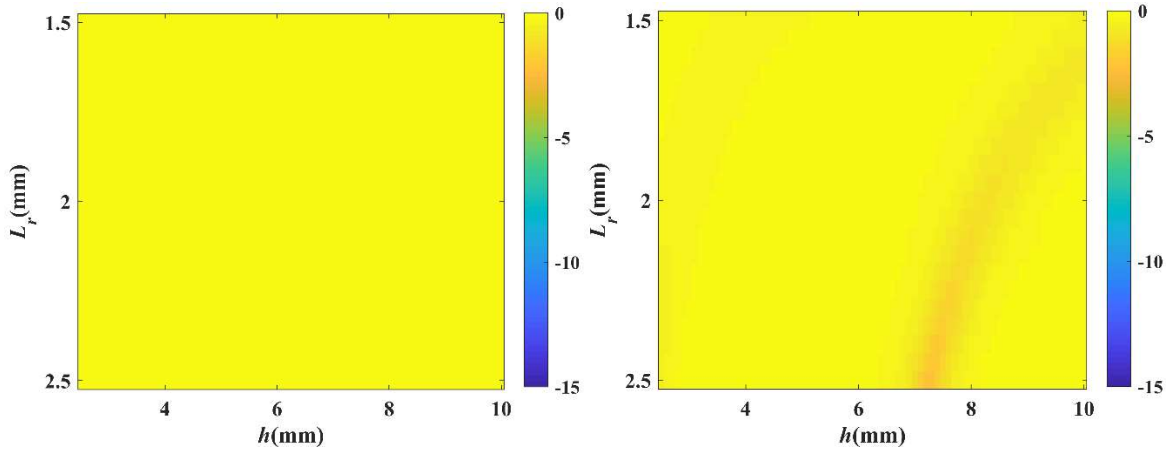

c) d)

Fig.3.4 Reflection phase and magnitude under oblique incidence (TE case, ϕ_{inc}=90°, θ_{inc}=22.54°). a) Phase at 20GHz (deg). b) Phase at 40GHz (deg). c) Magnitude at 20GHz (dB). d) Magnitude at 40GHz (dB).

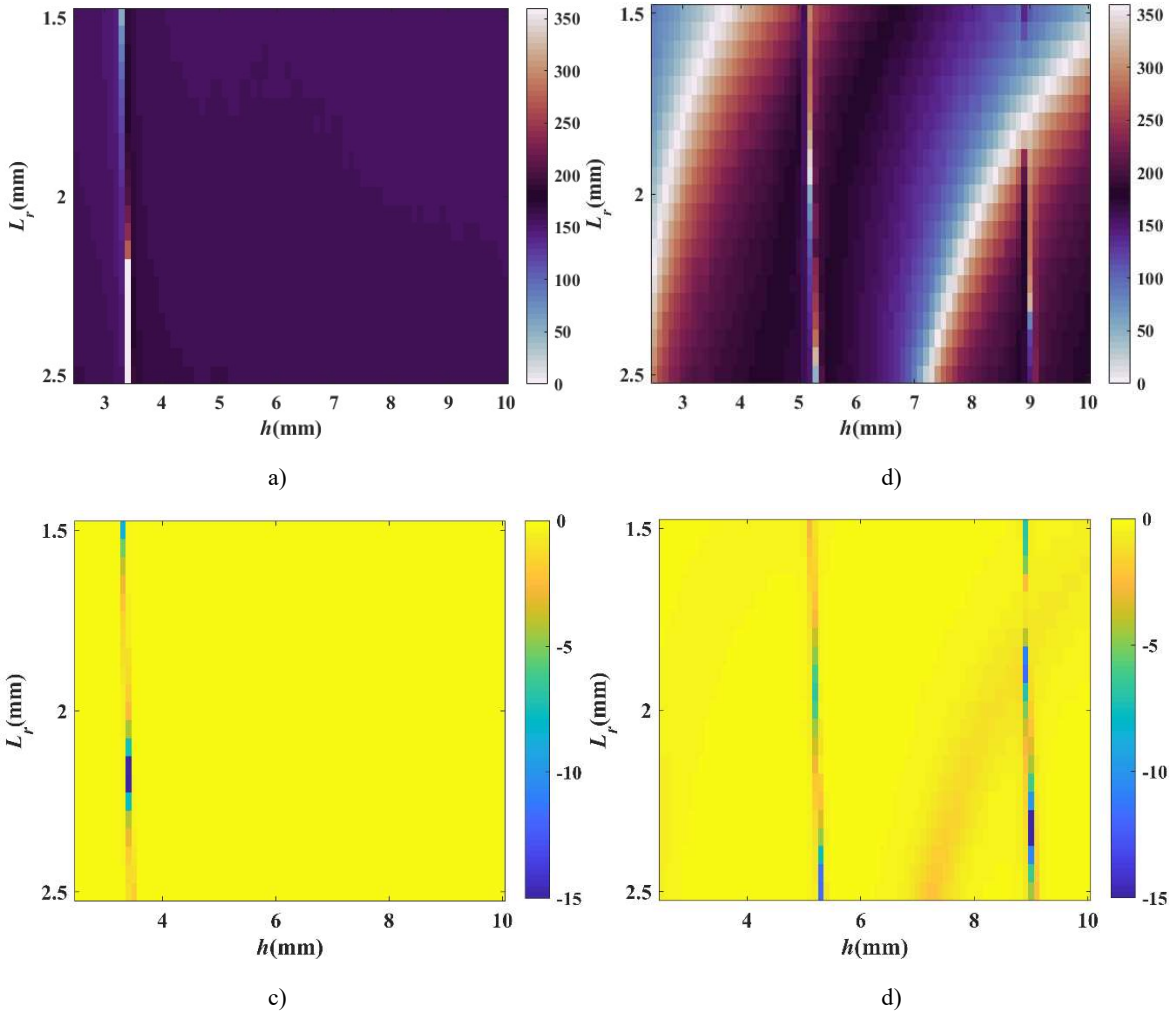

a) d)

c) d)

Fig.3.5 Reflection phase and magnitude under oblique incidence (TM case, ϕ_{inc}=90°, θ_{inc}=22.54°). a) Phase at 20GHz (deg). b) Phase at 40GHz (deg). c) Magnitude at 20GHz (dB). f) Magnitude at 40GHz (dB).

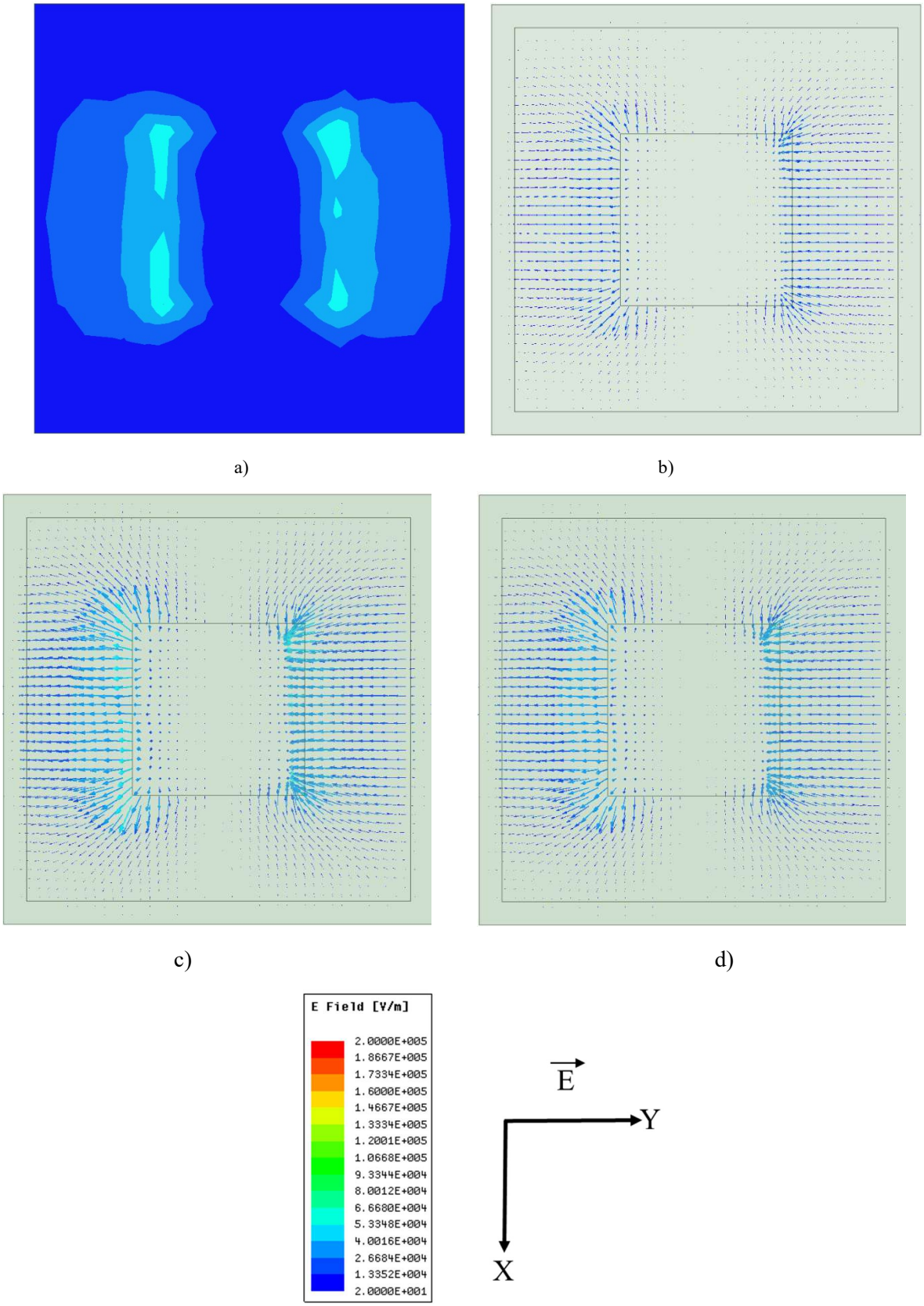

Fig.3.6 Electric field distribution of the unit cell under normal incidence (ϕ_{inc}=90°, θ_{inc}=0°, f=40GHz, h=5.2mm, L_r=1.5mm, without resonance). a) Complex magnitude. b) Time-varying field (ωt=0°). c) Time-varying field (ωt=45°). d) Time-varying field (ωt=90°). e) Scale

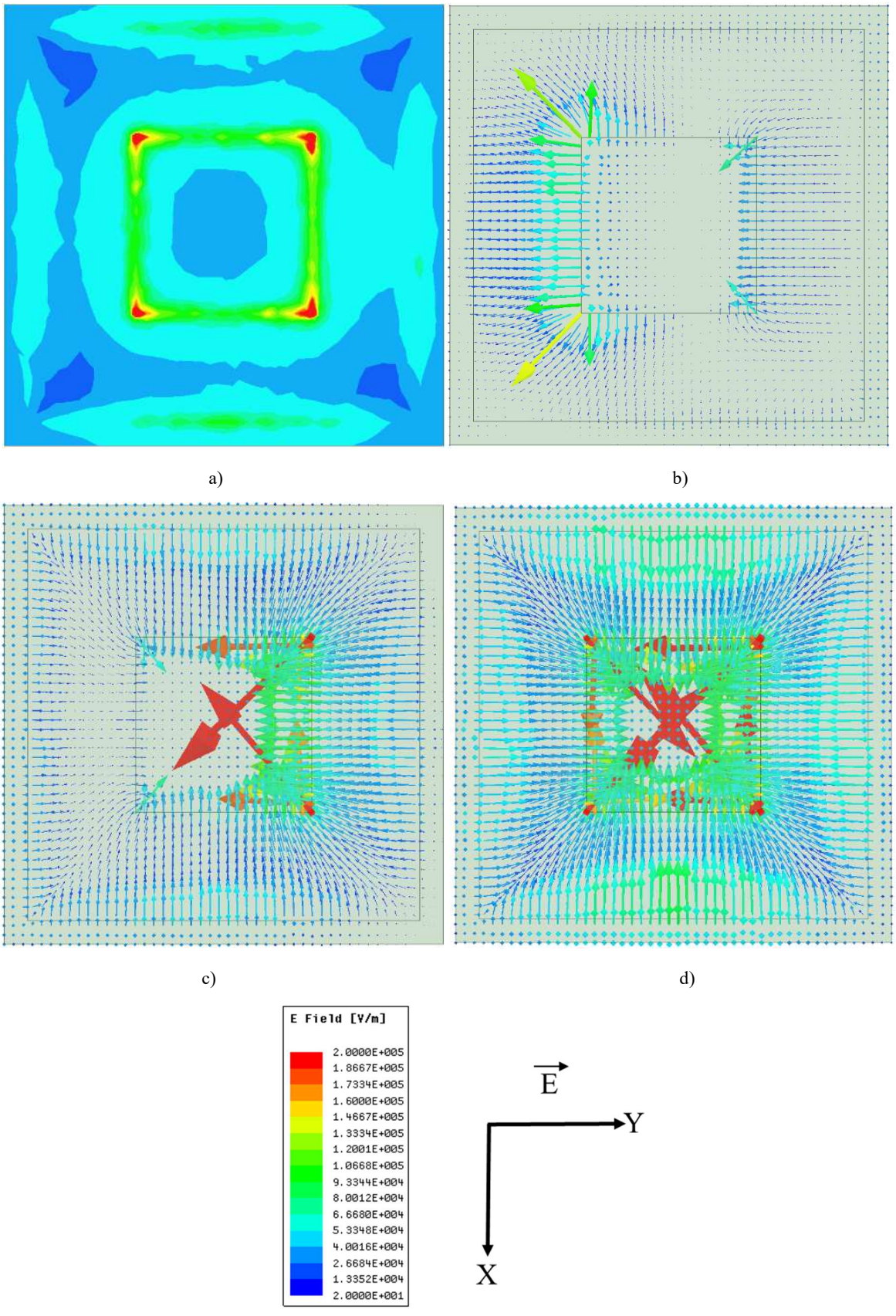

Fig.3.7 Electric field distribution of the unit cell under oblique incidence in TM case (ϕ_{inc}=90°, θ_{inc}=22.54°, f=40GHz, h=5.2mm, L_r=1.5mm, with resonance). a) Complex magnitude. b) Time-varying field (ωt=0°). c) Time-varying field (ωt=45°). d) Time-varying field (ωt=90°). e) Scale

As explained before, the structure in oblique incidence with TM polarization can support simultaneously TE_{10} modes (one in each vertical half) and a TEM mode. When h is close to an odd multiple of one-quarter wavelength in free space, the TEM mode is resonant. For example, as shown in Fig.3.5 a and b, h = 3.3 mm roughly corresponds to the one-quarter wavelength at 20 GHz (3.75 mm) and h=5.2 mm roughly corresponds to three-quarter wavelength at 40GHz (5.625 mm). The differences with theoretical values are mainly caused by the effect of the discontinuity at the top surface of the unit cell, which has been discussed in section 2.3. In addition, it can be seen from Fig.3.5b that the value of h that causes another TEM resonance at 40 GHz is around 9mm and the difference with previous h is 3.8 mm which is very close to half wavelength at 40 GHz (3.75 mm). These results suggest that the TEM resonance is predictable and the corresponding h is given by:

$$(0.25 + 0.5n)\lambda_0, \quad n = 1,2,3,\dots,N \tag{3.1}$$

where $\lambda_0 = c/f$ is the free-space wavelength at frequency f.

In order to investigate the effects of incident angle on the TEM resonance, different cells are simulated under different incident angles and the simulated results are summarized in Fig.3.8. In the simulation, L_r is fixed at 2 mm. First, as could be expected, the resonance is always obtained for the same h value (5.2 mm here). Then, it can be seen that non-resonant geometries provide responses (both magnitude and phase) that are very stable with the incident angle. Conversely, for resonant cells, a very small deviation from normal incidence (typically less than 10 degrees) is sufficient to trigger the TEM resonance. Also, the response of resonant cells is very sensitive to the incident angle. Therefore, it is highly required to stay apart from the resonant zone or to get rid of it when designing an array.

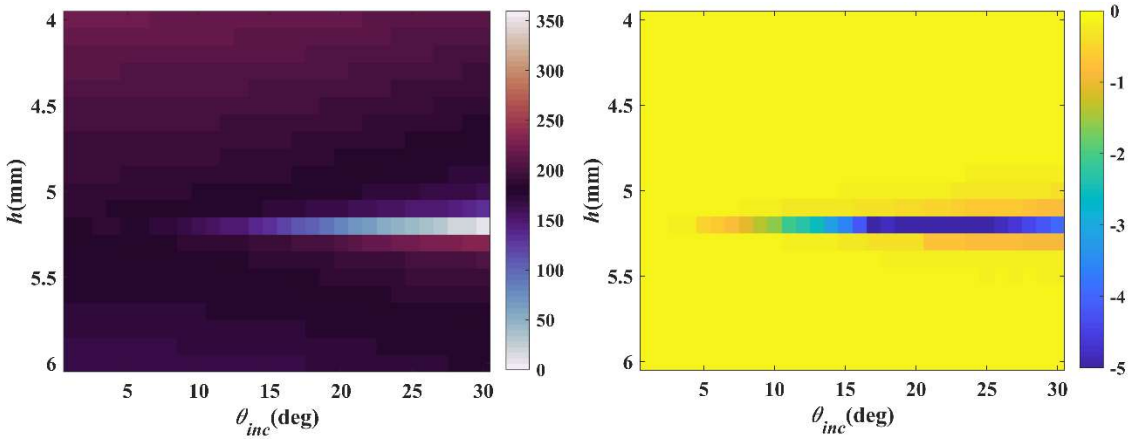

Fig.3.8 Reflection phase and magnitude under different incident theta (TM case, ϕ_{inc}=90°, 40GHz). a) Reflection phase (deg). b) Magnitude (dB).

3.3.3 Solutions to avoid TEM resonance

There are two possible solutions to avoid the TEM resonance. The first one consists to exclude all the resonant geometries from the database, whereas the second one is more drastic and requires a modification of the cell geometry.

In this thesis, the database has been obtained for the configuration of the central cell in the panel, i. e. with incident angles (θ_{inc}=22.54°, ϕ_{inc}=90°). In this subsection, we show how we can select the range of h to exclude the resonant cells from this database. The initial range of h is from 2.5-7mm as tabulated in Table 3.1. The three h that causes TEM resonance are 3.3 mm at 20GHz and 5.2 mm, 9 mm at 40GHz. There are thus two different ranges (from 3.5 mm to 5 mm and from 5.5 mm to 8.8 mm) that can be chosen to avoid the TEM resonances. For the first range of h (3.5-5mm), the achieved phase range at 40

GHz is less than 210° which may be not sufficient to design a RA. For the second range (5.5-8.8 mm), the complete phase cycle is achieved. As a consequence, it can be selected to design the array.

As for the second solution, a modified structure is proposed as shown in Fig.3.9. It can be known from the subsection 3.3.2 that the TEM mode is excited in the unit cell due to the presence of two disconnected conductors (metallic wall and metallic block). Consequently, this mode can be suppressed when the initial waveguide is split into two half ridged waveguides by the introduction of a metallic wall as shown in Fig.3.9b. Indeed, this additional metallic wall connects the different metal elements, which makes the excitation of a TEM mode impossible. As a price to pay, the metallic wall makes the unit cell unable to deal with dual polarized incident waves.

This modified unit cell is simulated under oblique incidence and the simulated results are summarized in Fig.3.10. It can be seen that the TEM resonance is completely suppressed owing to the presence of the wall in the center. Note that the high losses observed in Fig.3.10d correspond to the resonances caused by the propagation of the fundamental TE_{10} and TE_{01}-like modes in the waveguide, which has been explained in section 2.4. The loss in Fig.3.10d is higher than that in Fig.3.4d, which is due to the reduction of cross section after introducing the metallic wall. This is another drawback compared to the original unit cell.

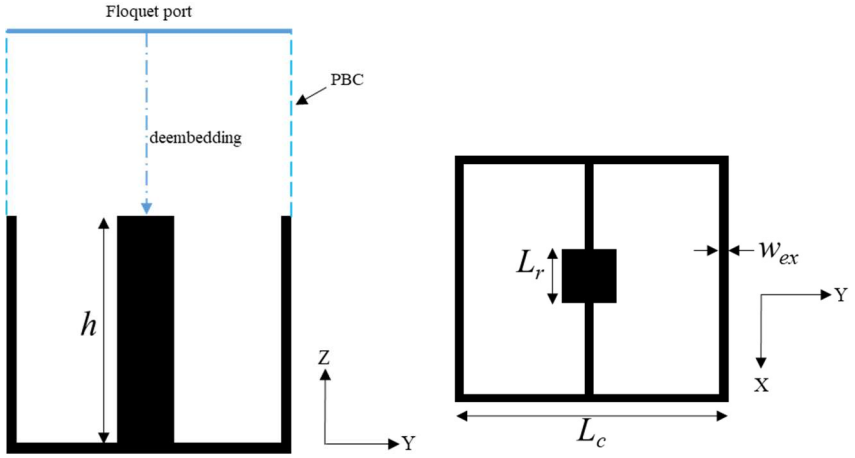

a) b)

Fig.3.9 The modified unit cell used to avoid TEM resonance. a) Sectional view. b) Top view.

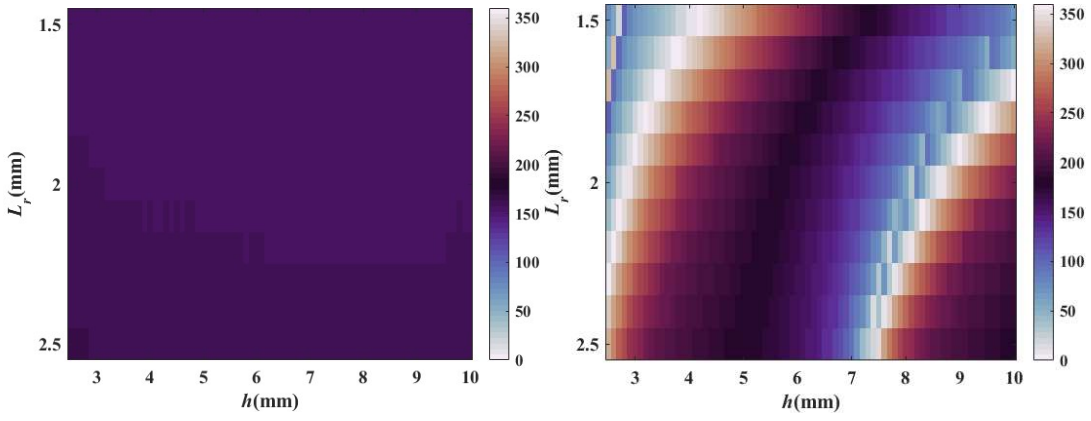

a) b)

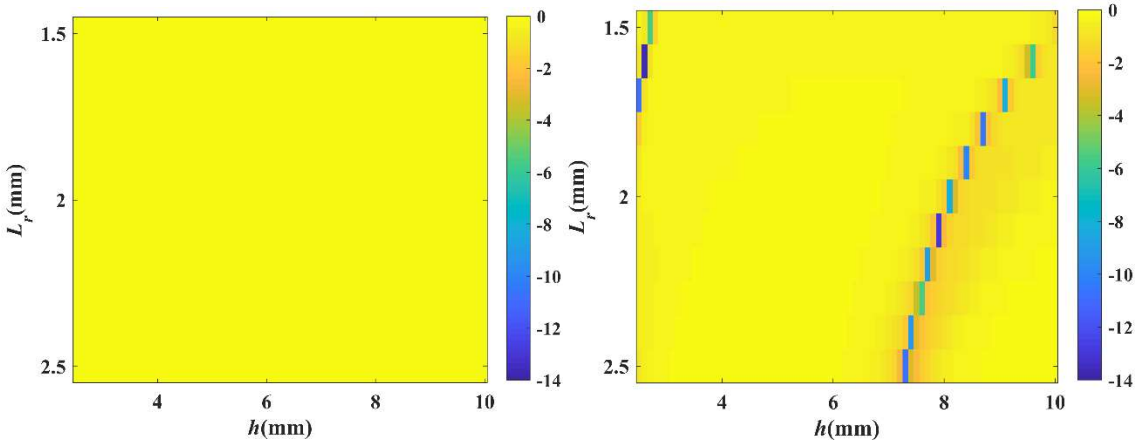

Fig.3.10 Reflection phase and magnitude of the modified unit cell (ϕ_{inc}=90°, θ_{inc}=22.54°, TM case). a) Reflection phase at 20GHz (deg). b) Reflection phase at 40GHz (deg). c) Magnitude at 20GHz (dB). d) Magnitude at 40GHz (dB).

3.3.4 Conclusion

This section first described the concept of the dual band RRA. In the upper band, the dual band antenna is a RA that collimates the reflected beam by varying the phase distribution over the cells. In the lower frequency band, the dual band antenna operates as a parabolic reflector where the reflected beam is determined by the paraboloid. The beams in the two frequency bands can be steered in two different directions. The SCSW introduced in chapter 2 is used to design the proposed dual band antenna. It provides a stable reflection phase at 20GHz and a complete phase cycle at 40GHz. Simulation results show that oblique incidence may cause additional resonances. The resonances are analyzed by observing the electric field vector on the top surface of the cell. They are referred to as TEM resonances since a TEM mode is excited in the waveguide. Two different ways are proposed and verified to avoid the TEM resonances. One is to adjust the range of h to exclude the cells with TEM resonances, the other is to modify the structure of the unit cell. Both ways will be selected to design MORRAs to analyze the effects of the TEM resonances on the performances of MORRAs (see section 3.5 and 3.6).

3.4 Preliminary design of dual band antenna

3.4.1 Description of the design process

The unit cell has been analyzed in detail in both chapter 2 and in the last section. Now, the proposed dual band MORRA is designed. The design process is divided into 2 successive steps:

1) First, the position of the focal point and the shape of RRA surface are determined. This step is to make the RRA works as a parabolic reflector in the lower frequency band. At the same time, the feed antennas are designed to provide the appropriate illumination.

2) Next, the required phase shift for each cell is calculated based on the position of the feed phase center and the coordinates of each cell in the RRA. This allows generating, in the upper frequency band, a pencil beam in a different direction than that in the lower frequency band. A RRA can be synthesized by matching the required phase shift and the geometric parameters (h and L_r) of each cell.

At the end, the designed dual band MORRA is drawn in HFSS®. Note there is a height difference between two adjacent cells. Consequently, the wall thickness might be not uniform in the designed antenna. As illustrated in Fig.3.11, a uniform value is recovered to reduce possible manufacturing errors.

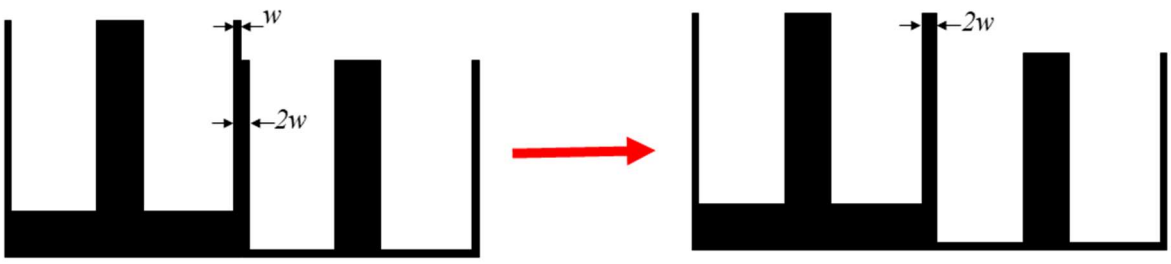

Fig.3.11 Adjustment of wall thickness of two adjacent cells in the RRAs.

The configuration of the dual band MORRA is shown in Fig.3.1. An offset configuration is used to avoid feed-blockage. As already said, the resulting incident angle at the array center is 22.54°. The radiating aperture is D×D ($11.5\lambda_{up}\times11.5\lambda_{up}$, λ_{up} being the wavelength in free space at 40GHz) while the element spacing is $0.5\lambda_{up}$. Note that the array dimensions are quite small in the lower frequency band (only $5.75\times5.75\lambda^2$ at 20GHz). As we will see later, this will be the cause of several issues (especially regarding the way such an aperture can be illuminated efficiently). However, this tradeoff was chosen to enable a full-wave simulation of the complete antenna at the higher frequency. A reserved space h_0 is used to tune the reflection phase. The position of the focal point is set to (0, 0, h_f) where h_f is equal to 1.2D. The z coordinate of cell i (the center of the top surface of the cell) can be given by:

$$z_i = \frac{x_i^2+y_i^2}{4h_f} \tag{3.2}$$

where (x_i, y_i, z_i) represents the coordinates of cell i. The calculated z coordinates for all cells are summarized in Fig.3.12.

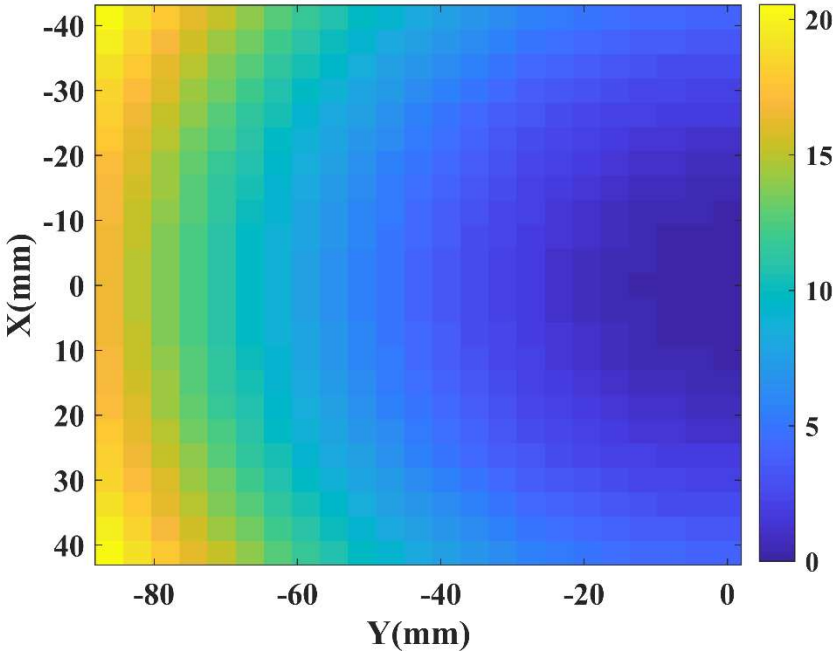

Fig.3.12 z coordinate of each cell (mm).

The proposed antenna is designed so that a pencil beam in the broadside direction is produced in the lower frequency band, owing to the presence of the parabolic surface. The direction of the main beam in the upper frequency band is set to (θ_0=10°, φ_0=270°) which is 10° away from the direction in the lower frequency band (see Fig.3.1). Then the required phase shift of the i^{th} cell in the RRA at 40GHz can be calculated using equation (1.3). Note that the relative phase offset $\emptyset_{off}$, is set to 0. Also, the calculation of the required phase shift takes into account the difference in z coordinate from one cell to

another. The required phase shift for each cell is shown in Fig.3.13. It is a simple linear phase since the compensation of the different delays from feed horn is already compensated for by the parabolic shape.

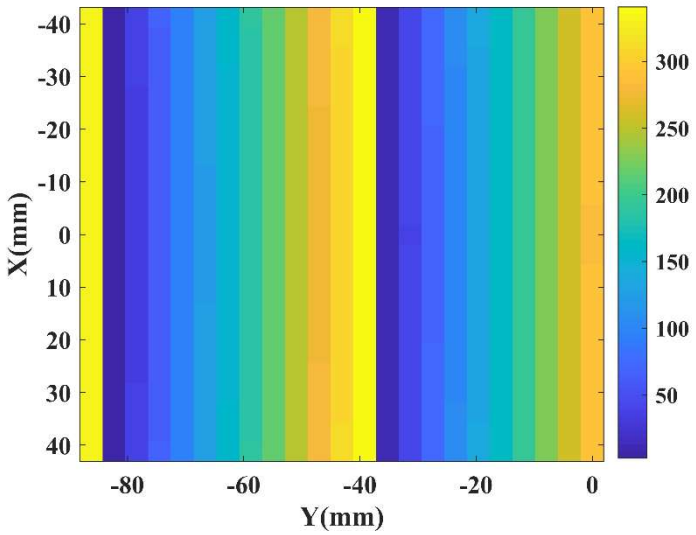

Fig.3.13 The distribution of the required phase shift at 40GHz (deg).

3.4.2 Design of two feed antennas

Before the synthesis of the dual band RRA, feed antennas are designed. Since the reflector surface is quite small, a simple rectangular waveguide (WR51 waveguide) is used to illuminate the antenna at the lower frequency. A more directive feed (such as a pyramidal horn antenna) would have required too large dimensions at this frequency, making the masking issues too critical. The consequence is that the illumination in the lower frequency band will not be optimal due to spillover. On the contrary, a pyramidal horn antenna can be used for the upper frequency band.

The design of a horn antenna is based on the following steps:

1) The field from the horn antenna is approximated by a $\cos^q$ model. First, the required value of q to produce a -10dB edge taper is calculated based on the size of the dual band antenna, the z coordinate of each cell and the position of focal point. The definition of edge taper will be explained later.

2) Then the geometry of the horn antenna is initially selected to achieve the required q. Also, its phase center is determined by conducting a parametric analysis in HFSS®.

3) Next, the designed horn antenna is validated by putting it in the required position and perform a full wave simulation to see the illumination intensity of each cell in the dual band antenna. Note that the illumination intensity is the complex magnitude of electric field at the center of the top surface of each cell. The ratio between the highest illumination intensity at the edge of the dual band antenna and the highest illumination intensity in the whole dual band antenna is referred to as edge taper. If the achieved edge taper is less than -10dB, the designed horn antenna is adopted. If not, the value of q is adjusted and the horn antenna is redesigned until the required edge taper is achieved.

The designed two feed antennas are shown in Fig.3.14 and 3.15. The simulation is done assuming metal is made of stainless steel (as it will be the case later on for fabricated breadboards). Radiation boundary conditions are used to enclose the feed antenna. The designed horn antenna at 40 GHz achieves a maximum gain of 18.3dBi. Its normalized radiation pattern and the normalized illumination intensity over the RRA cells at 40GHz are shown in Fig.3.16. It can be seen that the achieved edge taper is less than -10dB. Similarly, the performances of the used waveguide at 20GHz are shown in Fig.3.17. Obviously, the radiation pattern of the used waveguide (see Fig.3.17 a)) is flatter than that of the

designed horn antenna (see Fig.3.16 a)). Therefore, the achieved edge taper is around -5dB at 20GHz (see Fig.3.17 b)) which is significantly higher than that at 40GHz (see Fig.3.16 b)).

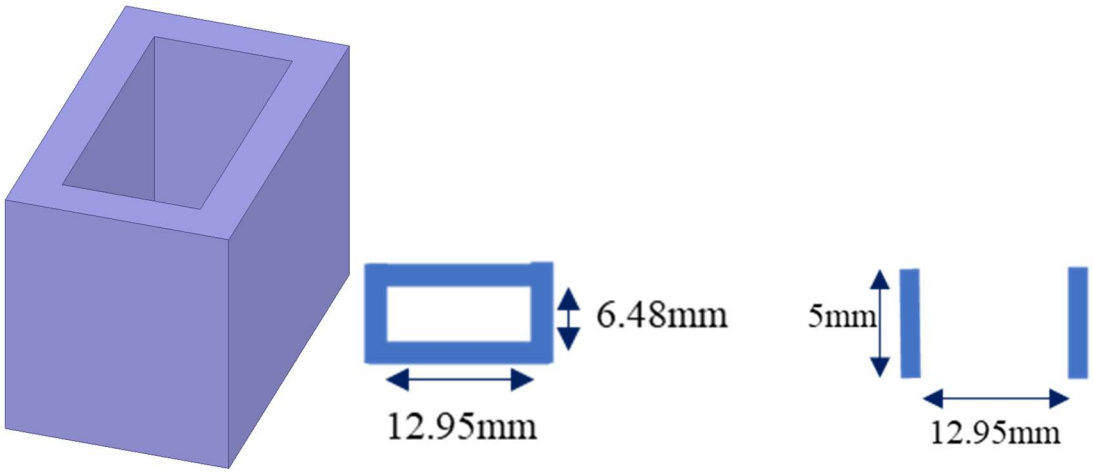

a) b) c)

Fig.3.14 Feed antenna (lower band). a) 3D view. b) Top view. c) Sectional view.

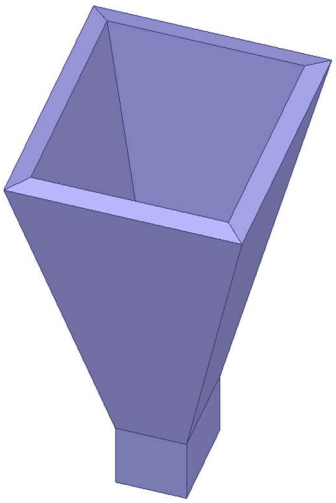

a)

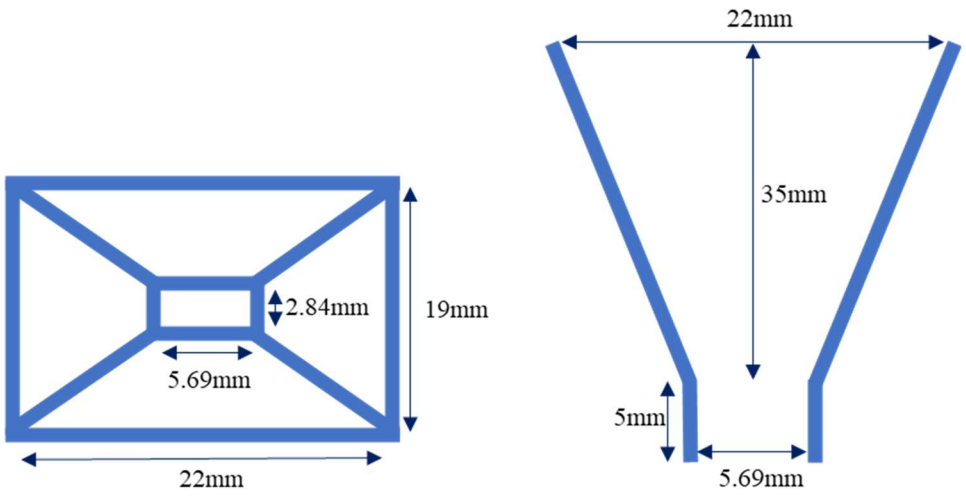

b) c)

Fig.3.15 Feed antenna (upper band). a) 3D view. b) Top view. c) Sectional view.

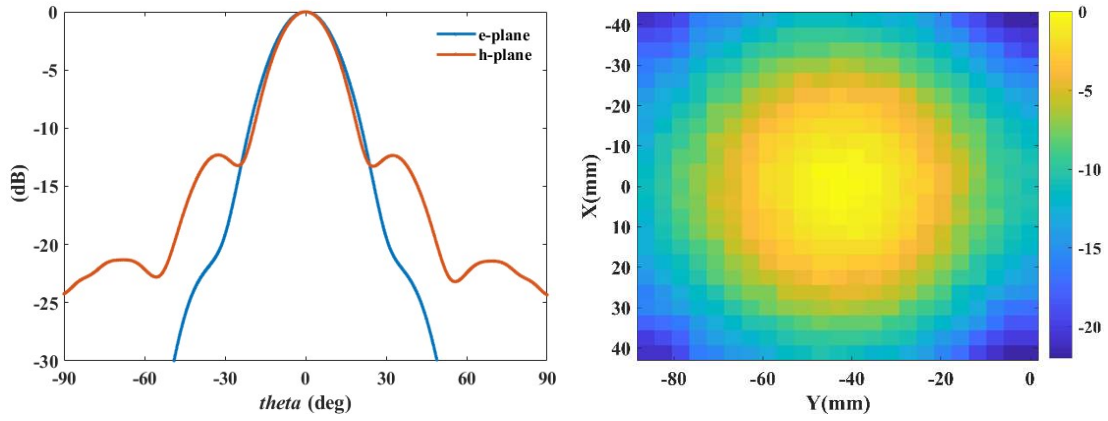

a) b)

Fig.3.16 Performances of the designed horn antenna at 40GHz. a) Normalized radiation pattern (dB). b) Normalized illumination intensity over the RRA cells (dB).

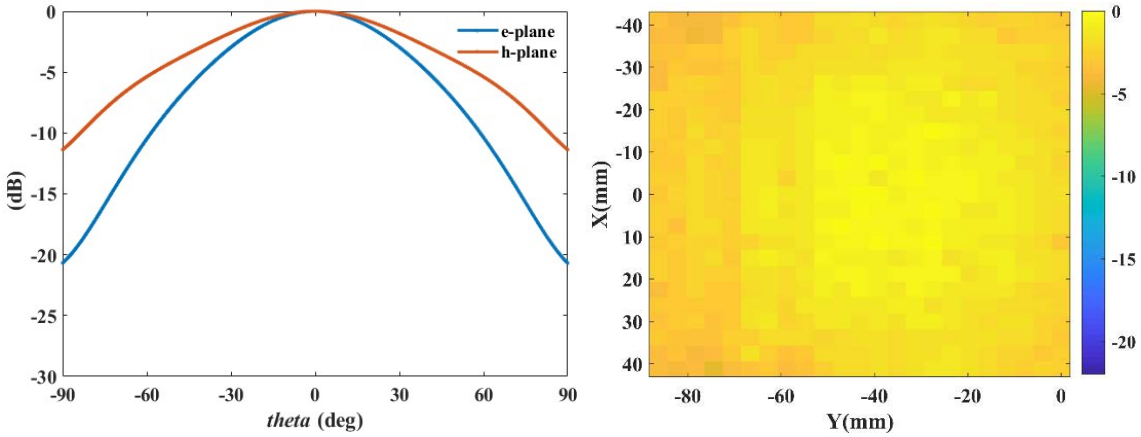

a) b)

Fig.3.17 Performances of the used waveguide at 20GHz. a) Normalized radiation pattern (dB). b) Normalized illumination intensity over the RRA cells (dB).

3.4.3 Performances of the designed dual band antenna

Since the cells in the center have stronger illumination intensity, the database of the reflection phase provided by the cell at 40GHz is established for this particular incidence angle (22.54°). The dual band antenna is synthesized using the database in Fig.3.5b (The range of h is from 2.5 to 7 mm). The synthesis process consists in minimizing the phase error of each cell in the dual band antenna at 40GHz. The phase error is defined as:

$$error = \left|\emptyset_i^{achieved} - \emptyset_i^{desired}\right| \tag{3.3}$$

where $\emptyset_i^{achieved}$ and $\emptyset_i^{desired}$ are the achieved phase and the desired phase of the i^{th} cell at 40GHz respectively.

For the sake of simplicity, the first designed antenna is referred to as RRA0 in this chapter. The cell geometries of RRA0 are shown in Fig.3.18. It can be seen from Fig.3.18 that the smoothness of the cell geometry is not very good as it is not optimized. At this stage, it must be highlighted that the database used for RRA0 did not care about the cells with TEM resonance. Indeed, this resonance was discovered after this first array wad designed. Fortunately, Fig.3.19 shows that RRA0 involves only10 cells whose loss is greater than 2dB at 20GHz and 14 cells at 40GHz. Moreover, these cells are not located in the

center of RRA0. It can be deduced that the TEM resonances do not significantly affect the performances of RRA0, which will be verified in the following sections.

RRA0 with its 3D radiated fields are shown in Fig.3.20 as a preliminary illustration of the behavior of the designed RRA. It can be observed that the main beams at 20GHz and 40GHz are globally compliant with expectations.

The more detailed performances of RRA0 in lower frequency band are summarized in Fig.3.21. It can be seen that the main beam is in the broadside direction. Simulation results also show that the achieved side lobe levels are -11.89/-11.09/-13.56 dB at 16/20/25GHz. At the same time, the achieved cross polarization levels are -27.67/-27.01/-30.38 dB at 16/20/25GHz. In addition, Fig.3.21g shows that the achieved gain increases with frequency in the frequency band from 16 to 25 GHz, which demonstrates that the designed antenna operates as a parabolic reflector in the lower frequency band. The achieved gain and aperture efficiency at 20GHz are 19.8dBi and 22.88%. The low aperture efficiency can be explained by the high edge taper (see Fig.3.17b).

The performances of RRA0 in upper frequency band are summarized in Fig.3.22. Once again, the main beam is steered in the desired direction (note that the coordinate system has been rotated in the field plots in order to place the main beam at 0°). Simulation results also show that the achieved side lobe levels are -12.41/-22.94/-15.87 dB at 38/40/41GHz. Compared with the large side lobe level of the antenna in [115] (that can be seen as competing solution), the ones obtained here are much better. At the same time, the achieved cross polarization levels are -29.49/-28.73/-25.6 dB at 38/40/41GHz. In addition, Fig.3.22 g) shows that the achieved gain at 40GHz is 29.3dBi and the corresponding aperture efficiency is 51.21%. The gain drop is less than 1.1dB in the range from 38 to 41 GHz.

The results in Fig.3.21 and Fig.3.22 demonstrate that the designed antenna can operate in two different frequency bands.

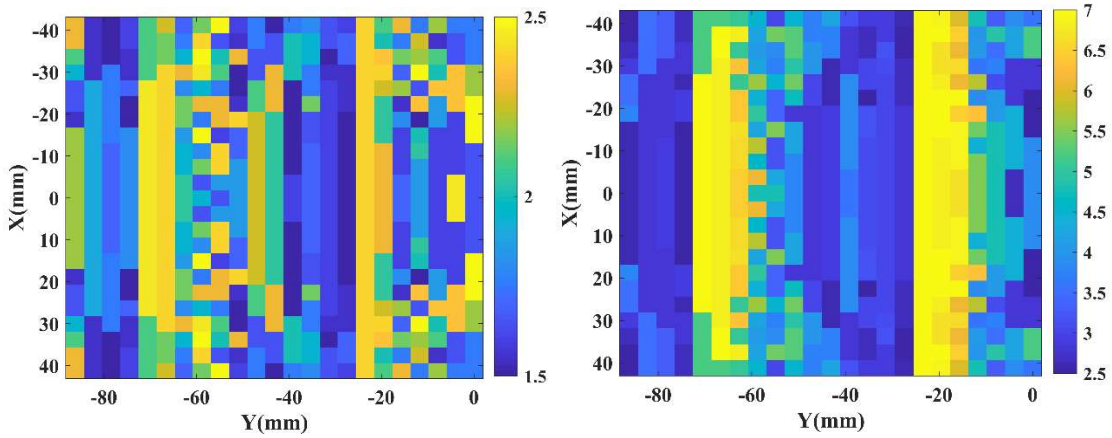

a) b)

Fig.3.18 Cell geometries of RRA0 (mm). a) L_r. b) h.

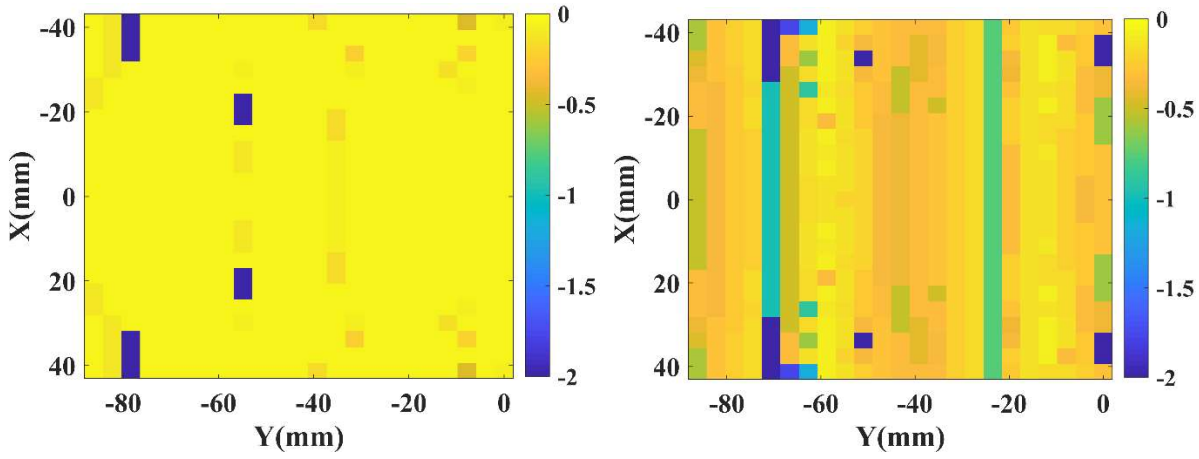

a) b)

Fig.3.19 Loss distribution over the cells in RRA0. a) 20GHz. b) 40GHz.

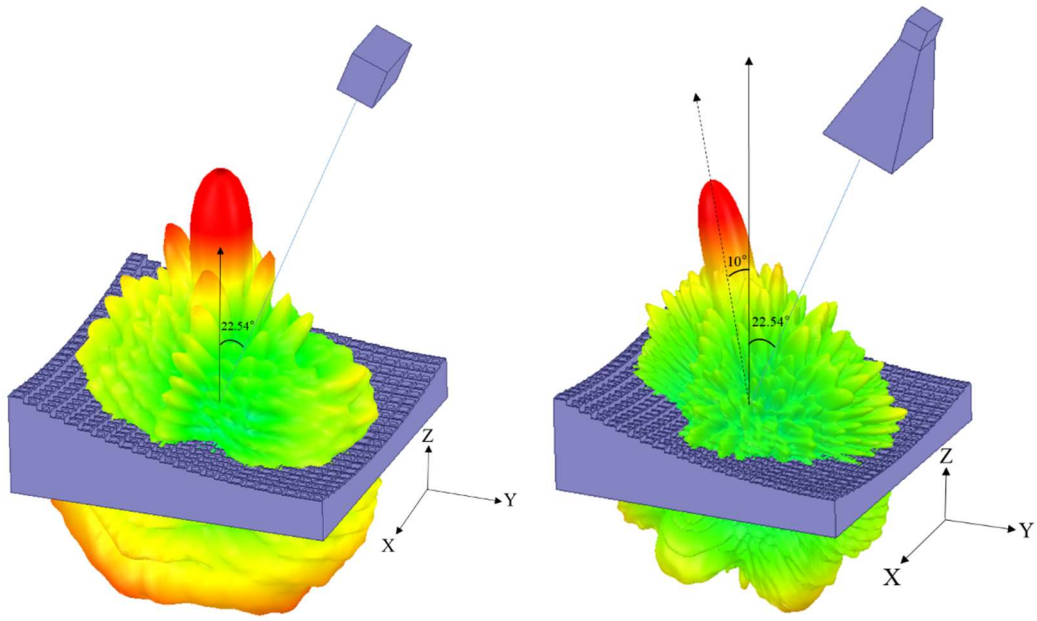

a) b)

Fig.3.20 The proposed dual band MORRA with radiation fields (RRA0). a) 20GHz. b) 40GHz.

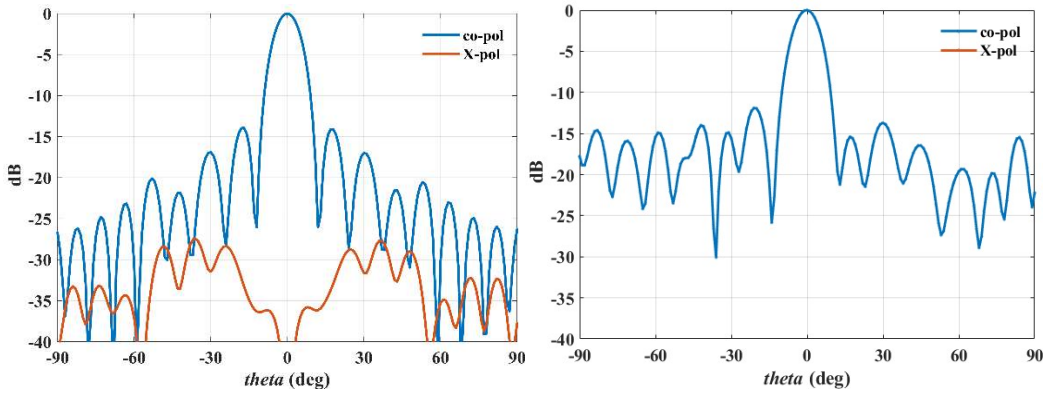

a) b)

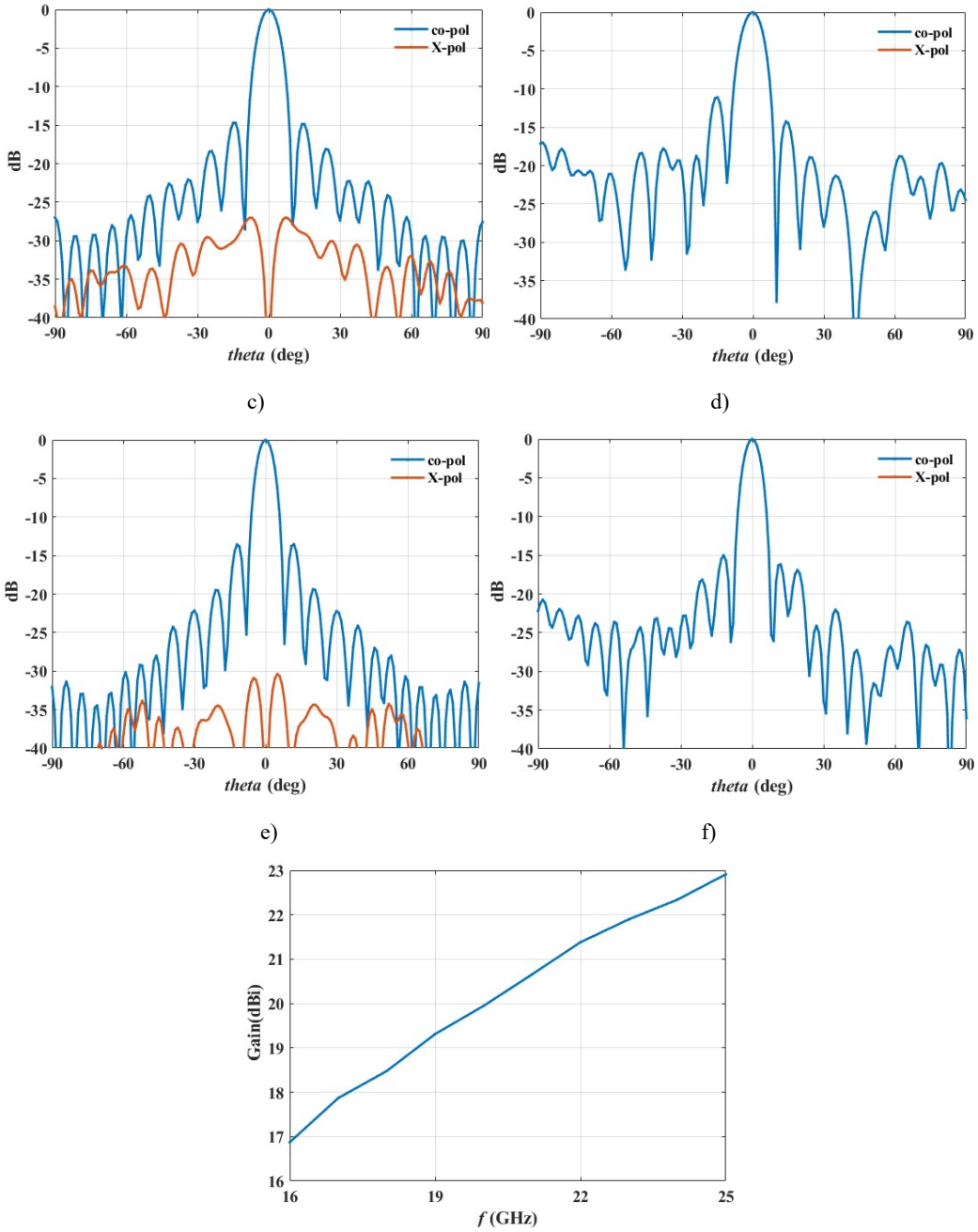

Fig.3.21 Performances of RRA0 in lower frequency band. a) Radiation pattern in xoz plane (16GHz). b) Radiation pattern in yoz plane (16GHz). c) Radiation pattern in xoz plane (20GHz). d) Radiation pattern in yoz plane (20GHz). e) Radiation pattern in xoz plane (25GHz). f) Radiation pattern in yoz plane (25GHz). g) Gain response (16-25GHz)

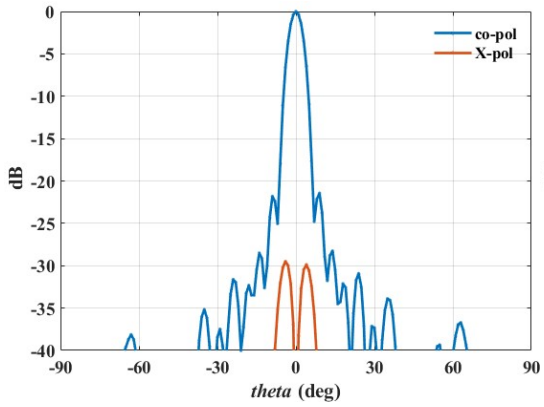
co-pol
X-pol
dB
theta (deg)

a)

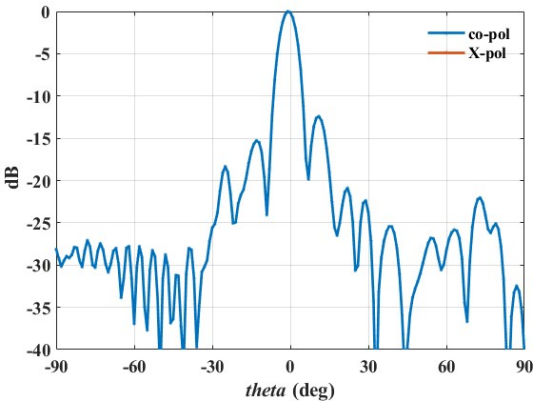
co-pol
X-pol
dB
theta (deg)

b)

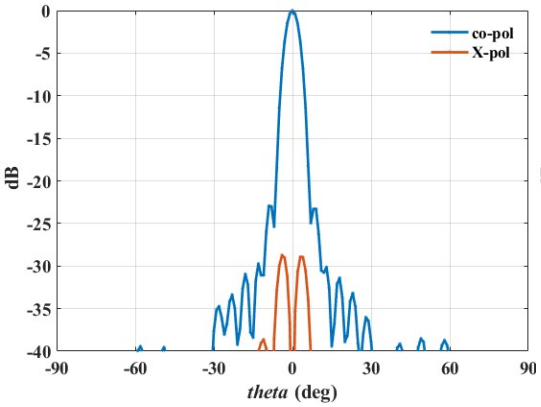
co-pol
X-pol
dB
theta (deg)

c)

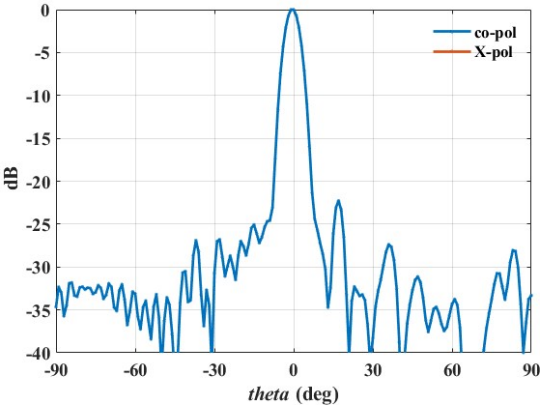
co-pol
X-pol
dB
theta (deg)

d)

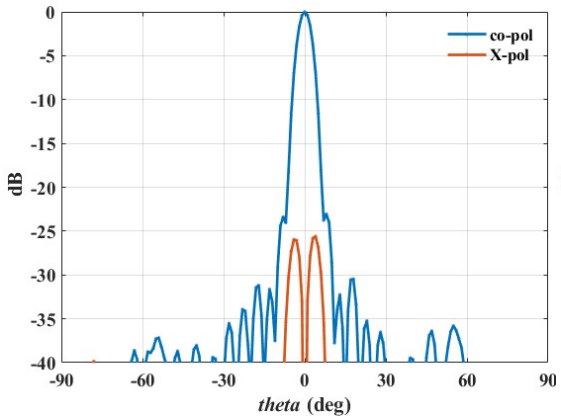
co-pol
X-pol
dB
theta (deg)

e)

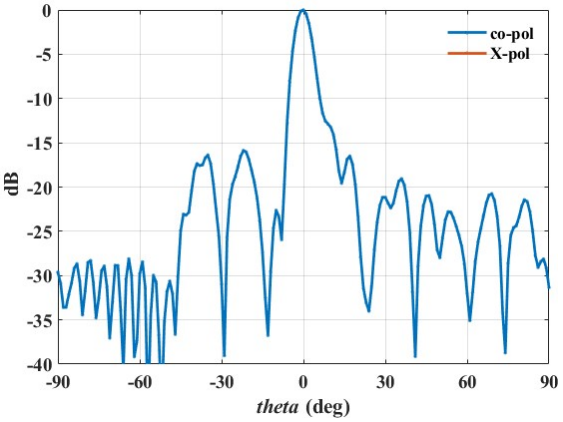
co-pol
X-pol
dB
theta (deg)

f)

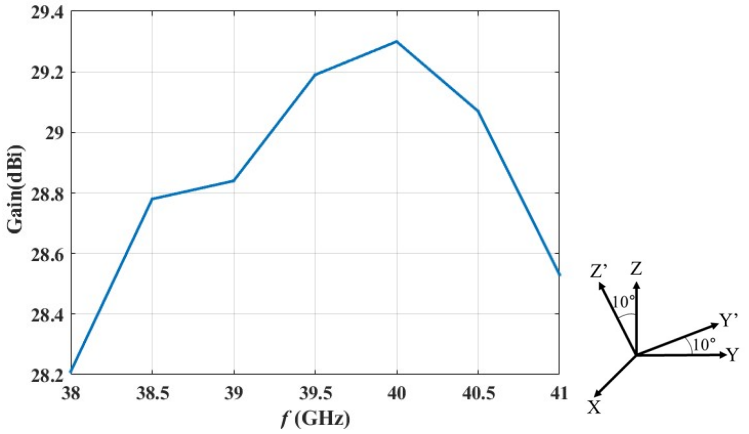
Gain(dBi)
f (GHz)
Z'
Z
10°
Y'
10°
Y
X

g)

Fig.3.22 Performances of RRA0 in upper frequency band. a) Radiation pattern in xoz' plane (38GHz). b) Radiation pattern in y'oz' plane (38GHz). c) Radiation pattern in xoz' plane (40GHz). d) Radiation pattern in y'oz' plane (40GHz). e) Radiation pattern in xoz' plane (41GHz). f) Radiation pattern in y'oz' plane (41GHz). g) Gain response (38-41GHz)

In order to analyze the capabilities of the proposed dual band MORRA further, its operating mode versus frequency is shown in Fig.3.23. The lower frequency band is from 0 to 25 GHz and is mainly controlled by the cutoff frequency of the waveguides in the MORRA. In this frequency band, the antenna operates as a parabolic reflector. The upper frequency band is from 38 to 41 GHz and is controlled by the characteristics of the cells in the MORRA. In this frequency band, it operates as a RA. What happens from 25 to 38GHz or above 41GHz is not so well controlled. Indeed, at such frequencies, a fraction of the incident power penetrates into the cells but the associated reflected phase is not controlled any longer. Then, the reflected waves from the different cells combine randomly. On the other hand, the remaining fraction of the incident power is directly reflected at the entrance of the cells and it produces a broadside beam, as it should be for a parabolic reflector. Finally, the antenna can be seen as some sort of noisy parabolic reflector where a main beam at broadside coexists with diffuse lobes due to uncontrolled phases in cells. Two different radiation patterns at intermediate frequencies are shown in Fig.3.24 to illustrate this behavior out of the two well-controlled frequency bands. It can be seen that the main beam is at broadside and the side lobe level is quite high at 32GHz. At the same time, the slide lobe gradually increases, and its level exceeds the main beam at 35GHz (see Fig.3.24b).

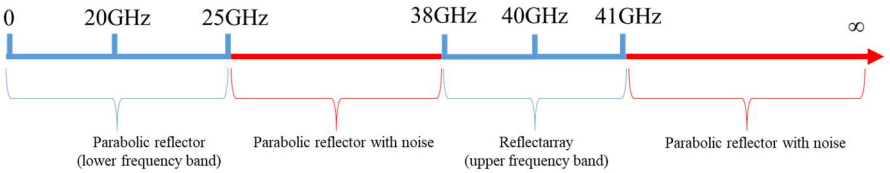

Fig.3.23 Operating modes of the proposed MORRA

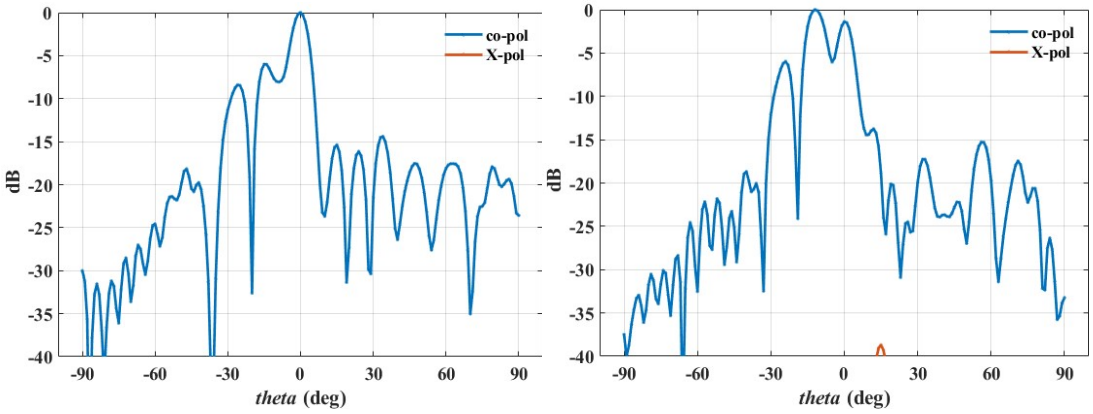

a) b)

Fig.3.24 Radiation patterns between two frequency bands (yoz plane). a) 32GHz. b) 35GHz.

3.4.4 Conclusion

In this section, a MORRA is synthesized using the database with TEM resonant cells. It is designed by achieving the functionalities of parabolic reflector and RA respectively. A pyramidal horn antenna is used to illuminate the MORRA in the upper frequency band while a WR51 waveguide illuminates the MORRA in the lower frequency band. Simulation results show that the directions of main beam in both bands are pointing in the target directions. The gain increases with frequency in the lower frequency band. The gain drop in the upper frequency band is less than 1.1dB. At the same time, the side lobe levels and the cross polarization levels in both frequency bands are acceptable. These results

demonstrate the capability of the proposed MORRA. In addition, the number of cells with a loss greater than 2dB is very small in the designed MORRA, which means the TEM resonance does not significantly affect the designed MORRA.

3.5 Optimized design 1 of dual band antenna

RRA0 is synthesized using the database with TEM resonant cells. In this section, two different RRAs are synthesized using the database excluding TEM resonances (see section 3.3.3). The difference between them is the range of *h*. For the first RRA, which is referred to as RRA1, *h* is ranging from 3.5 to 5 mm. For the second RRA, which is referred to as RRA2, *h* is ranging from 5.5 to 7.8 mm. The synthesis processes of RRA1 and RRA2 are the same as that of RRA0.

3.5.1 Comparison between three different RRAs

As it can be deduced from Fig. 3.4, limiting the range of *h* reduces the achievable phase range at 40 GHz. This means the avoidance of resonant zones may be responsible for a poorer matching of the required phase law over the aperture. In order to assess this effect, the obtained phase error for each of the three considered RRAs is shown in Fig.3.25. It can be seen that the maximum phase error of RRA0 and RRA2 is less than 10 degrees. The phase error of RRA1, however, is significantly higher than the other ones. The maximum phase error of RRA1 is 74.61° due to the fact that the achieved phase range of the database in RRA1 is only 209.38°. Cell geometries and losses distribution of RRA1 and RRA2 are summarized in Fig.3.26 and Fig.3.27. Like the RRA0 in Fig.3.18, the smoothness of the cell geometries in RRA1 and RRA2 is not very good. It can be seen from Fig.3.27c and d that RRA2 involves no cells with high losses. However, Fig.3.27b shows that RRA1 involves many cells with a loss close to 2dB at 40GHz, which will degrade the performances of RRA1. These high losses are produced due to the fact that their geometry is close to the cells with TEM resonance (*h*=3.3mm).

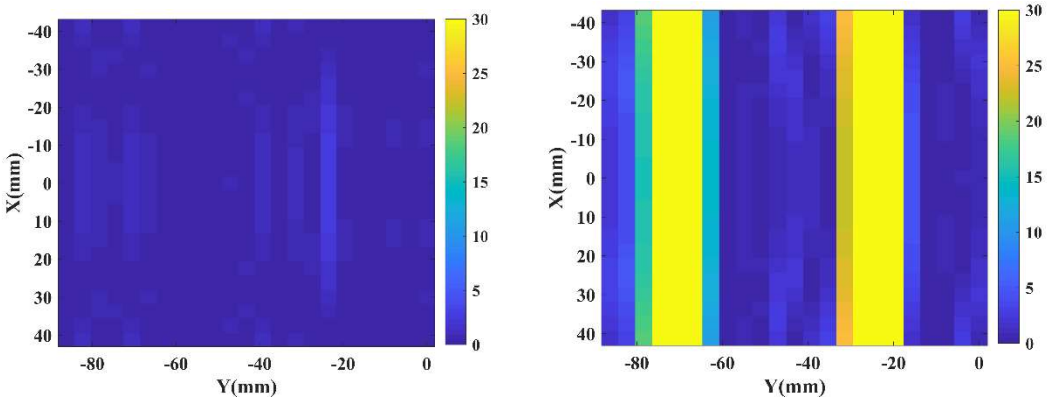

a) b)

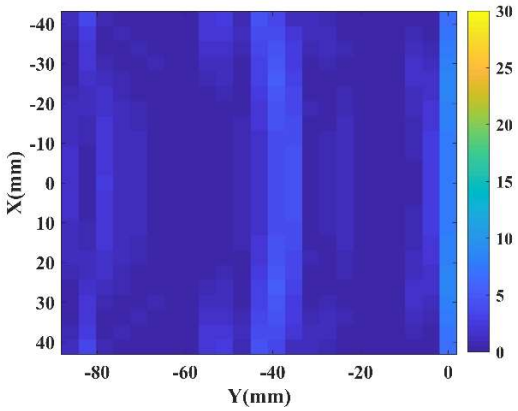

c)

Fig.3.25 Phase error distribution of 3 different RRAs at 40GHz (deg). a) RRA0. b) RRA1. c) RRA2.

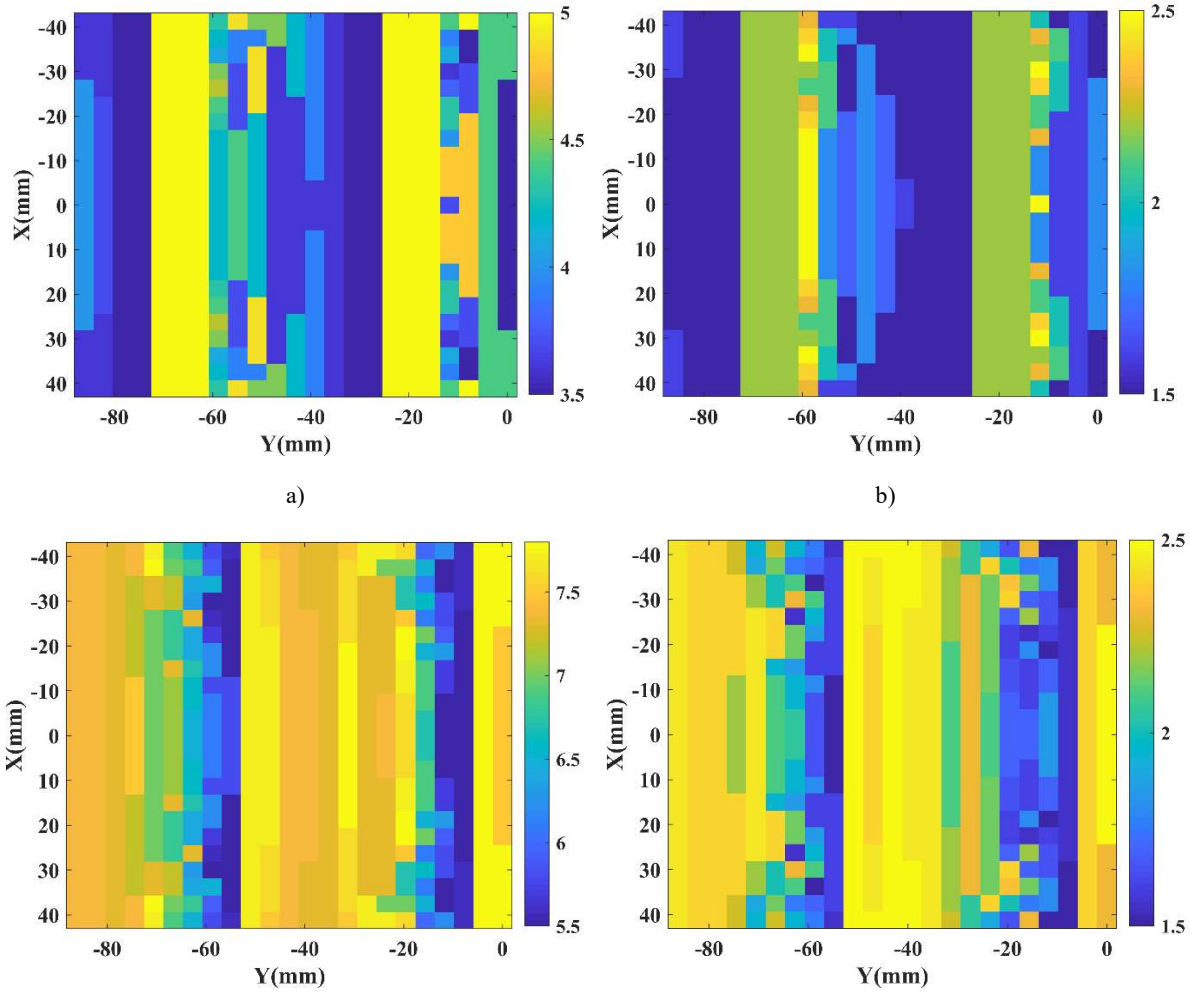

Fig.3.26 Cell geometries in RRA1 and RRA2 (mm). a) RRA1(h). b) RRA1(L_r). c) RRA2(h). b) RRA2(L_r).

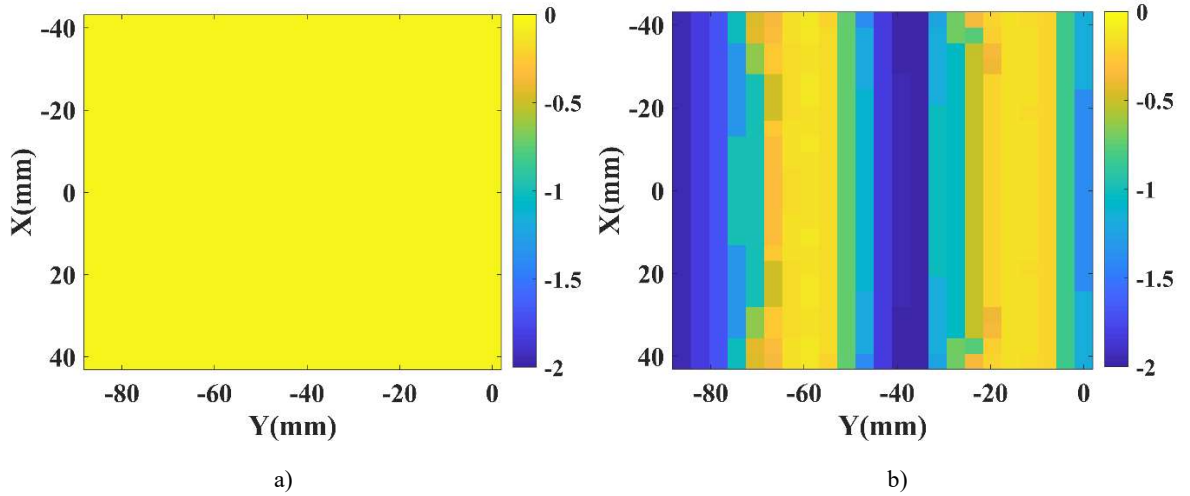

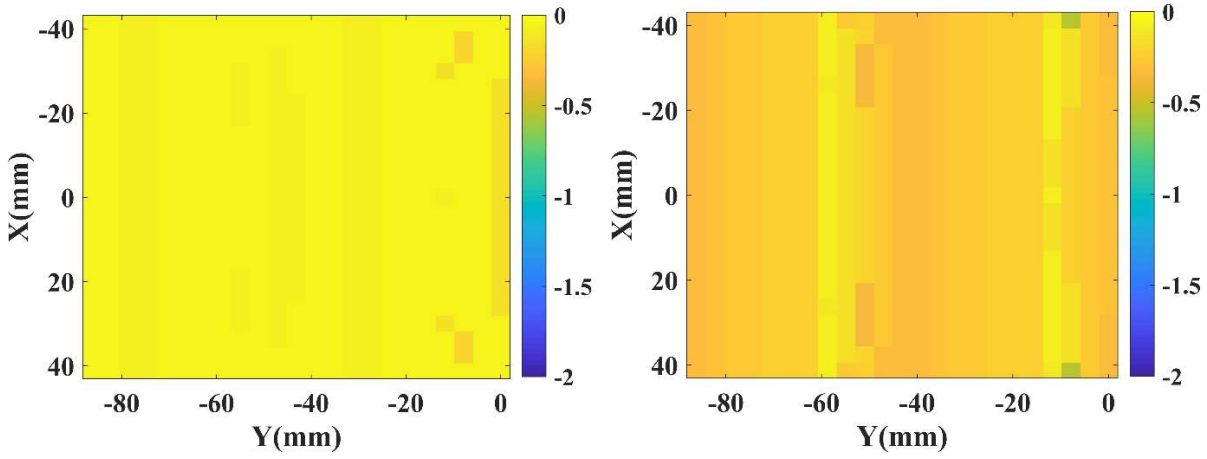

c) d)

Fig.3.27 Loss distribution over the cells in RRA1 and RRA2 (dB). a) RRA1 at 20GHz. b) RRA1 at 40GHz. c) RRA2 at 20GHz. d) RRA2 at 40GHz.

The comparison between the performances of the 3 different RRAs in the lower frequency band is summarized in Fig.3.28. Obviously, the incident wave cannot penetrate into the cells and the reflected beam thus is mainly determined by the parabolic surface. Therefore, the performances of these three RRA3 are quite close to each other.

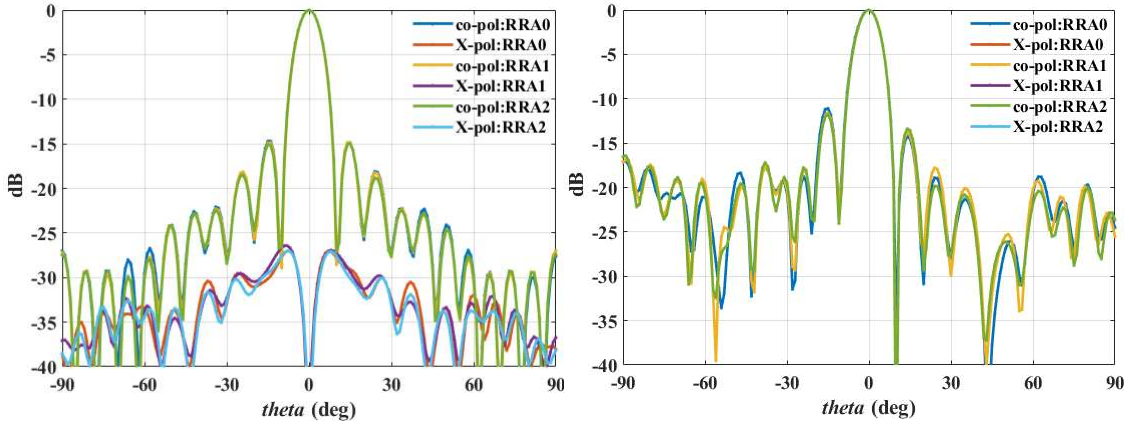

a) b)

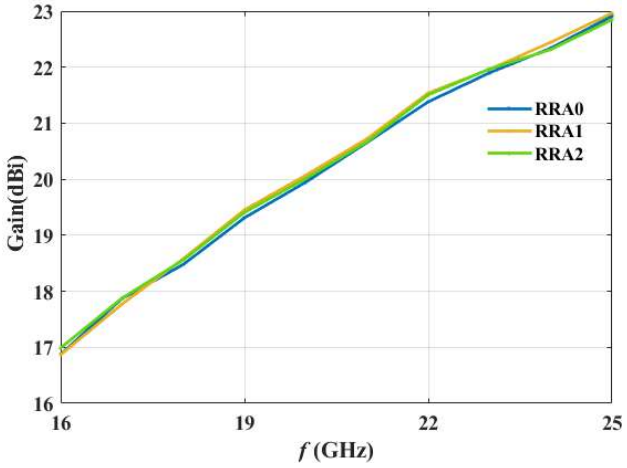

c)

Fig.3.28 Performances of 3 different RRAs in the lower frequency band. a) Radiation pattern (xoz plane). b) Radiation pattern (yoz plane). c) Gain versus frequency

Since the performances of the 3 different RRAs are similar in the lower frequency band, the comparison focuses on the higher frequency band. It can be seen from Fig. 3.29 that RRA0 has the lowest side lobe level at 40GHz. At the same time, the gain response of RRA0 is better than the other ones. RRA1 has the worst performances, which is due to its high phase error shown in Fig.3.25b and the high losses in Fig.3.27b. In addition, the performances of RRA2 is degraded compared to RRA0. On the one hand, the phase errors of RRA2 at 40GHz (see Fig.3.25) is a bit higher than that of RRA0, which degrades the gain of RRA2 at 40GHz. On the other hand, the used h in RRA2 (5.5-7.8mm) is higher than that of RRA0 (2.5-7mm), which makes the performances sensitive to frequency.

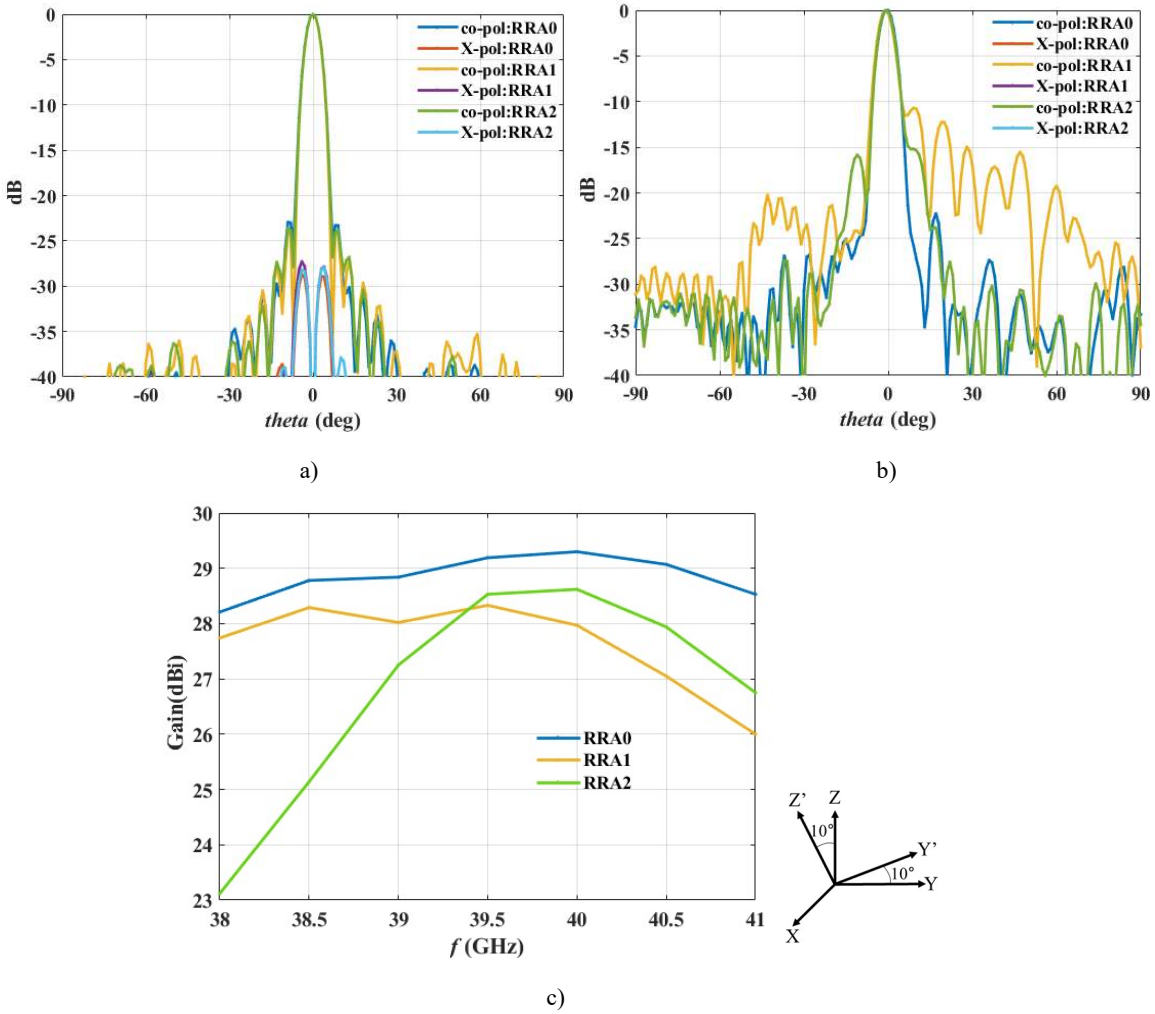

Fig.3.29 Performances of 3 different RRAs in the upper frequency band. a) Radiation pattern (xoz' plane). b) Radiation pattern (y'oz' plane). c) Gain versus frequency

3.5.2 Conclusion

In this section, 2 different RRAs are synthesized using the same process as RRA0. The used databases exclude the cells with TEM resonances by varying the range of h. It is shown that their performances are worse than that of RRA0. In that case, it is not necessary to avoid the TEM resonances by varying the range of h during the synthesis of a RRA because the initial array involves only a few cells with resonances. However, this solution could be useful in a less favorable situation.

3.6 Optimized design 2 of dual band antenna

3.6.1 Description of two operation modes

In the previous section, the range of h was varied to avoid the TEM resonances. In this section, the second proposed approach is used instead, where the structure of the unit cell is modified to avoid the TEM resonances. Thus, a new RRA is synthesized using the database in Fig.3.10d where the used range of h is from 2.5 to 7 mm. The synthesis process is the same as for RRA0. The new RRA is referred to as RRA3 in this chapter. The details of RRA3 are summarized in Fig.3.30. It can be seen that the phase error of RRA3 (see Fig.3.30c) is similar to that of RRA0 (see Fig.3.25a). In addition, the number of cells with a loss greater than 2dB in RRA3 (see Fig.3.30d) is similar to that of RRA0 (see Fig.3.19b). I recall that these losses are mainly caused by the propagation of TE_{10} mode in the waveguide.

Actually, the operation mode of the RRA3 depends on the polarization of the feed antenna. It can be deduced from Fig.3.9 that if the incident electric field is y-polarized, RRA3 exactly behaves as RRA0. However, if the incident electric field is x-polarized, it cannot penetrate into the cells, even above 25 GHz, because of the additional metallic wall. In this case, RRA3 operates as a parabolic reflector on the full frequency range (at least up to the cutoff frequency of the first higher-order mode).

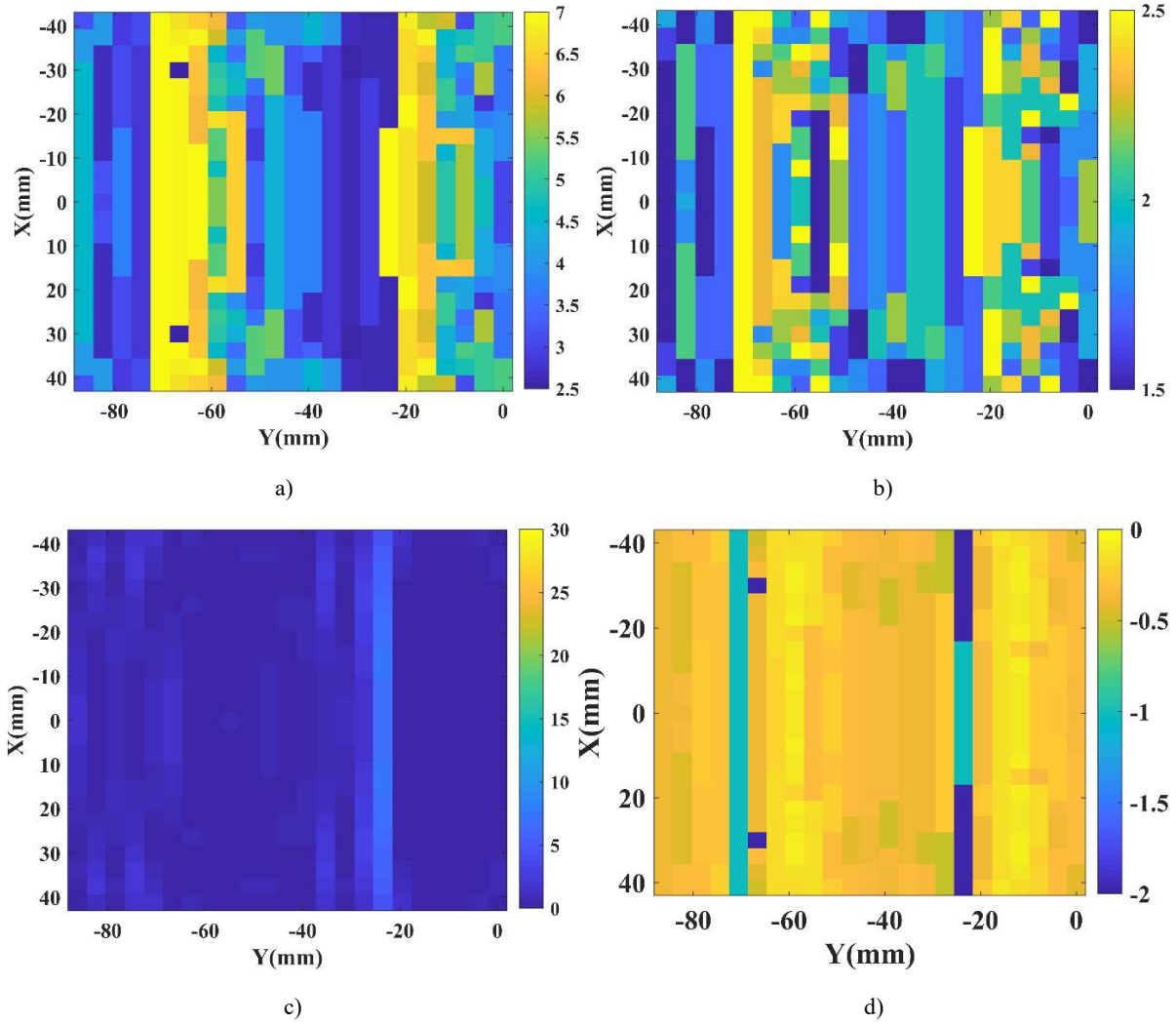

Fig.3.30 Details of RRA3. a) Cell geometries for h (mm). b) Cell geometries for L_r. c) Phase error distribution over the cells at 40GHz (deg). d) Loss distribution over the cells at 40GHz (dB).

3.6.2 Performances of two different modes

First, RRA3 under y-polar excitation is analyzed. In this case, its operation mode is the same as that of RRA0 (with the additional capability of preventing from the TEM resonances). Fig.3.31 compares the performances of RRA0 and RRA3 in the lower frequency band. Obviously, their performances are quite close to each other. Fig.3.32 compares their performances in the upper frequency band. It can be seen that the side lobe level of the RR3 is 4dB higher than that of RRA0. At the same time, the gain of RRA3 is globally lower than that of RRA0. An improvement in gain is however obtained above 40.5GHz. So, although RRA3 provides a convenient solution to prevent from potential TEM resonances, this solution does not seem appropriate here due to the fact that RRA3 involves cells with TE_{10} resonance, and we have seen in section 2.4 that the associated loss is higher when the additional metallic wall is present.

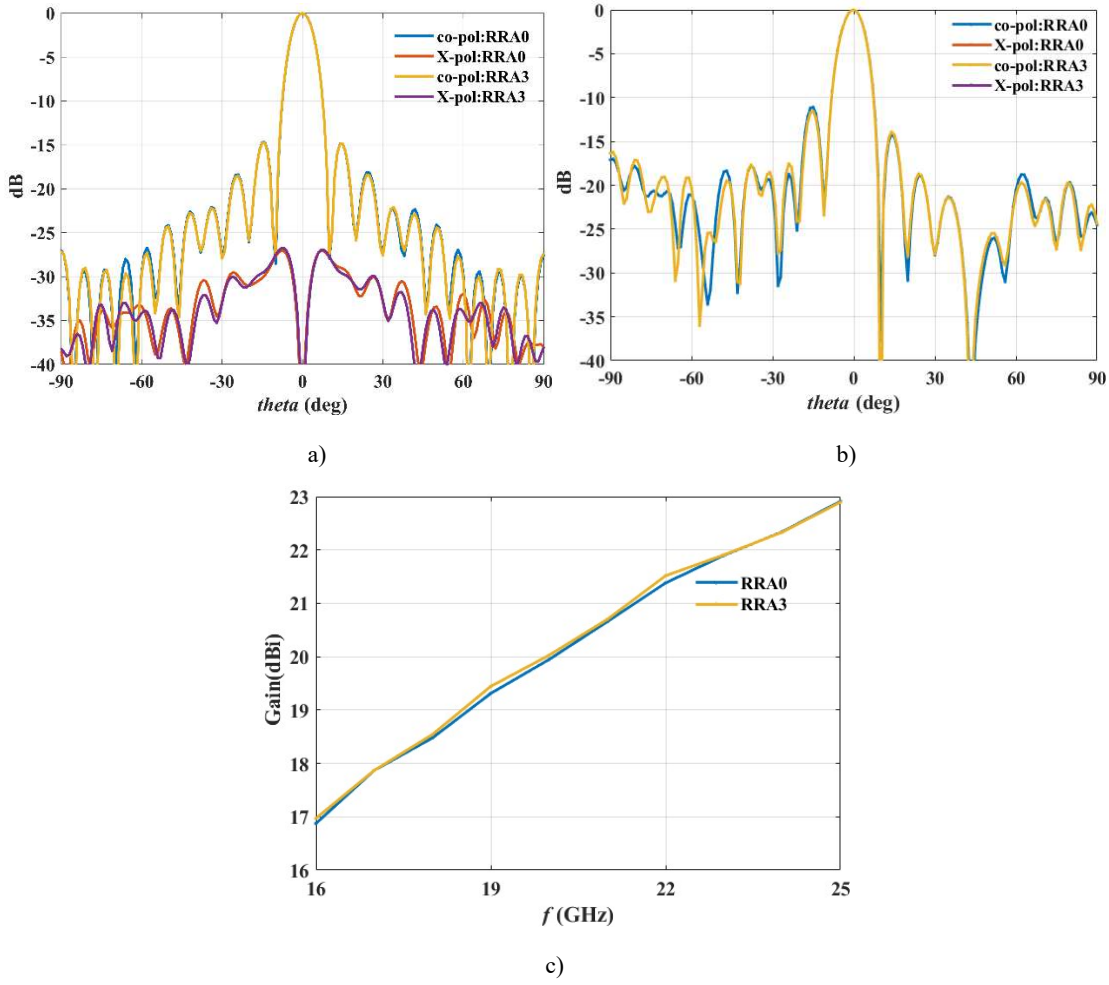

Fig.3.31 The comparison between RRA0 and RRA3 at 20GHz (y-polar excitation). a) Radiation pattern (xoz' plane). b) Radiation pattern (y'oz' plane). c) Gain versus frequency

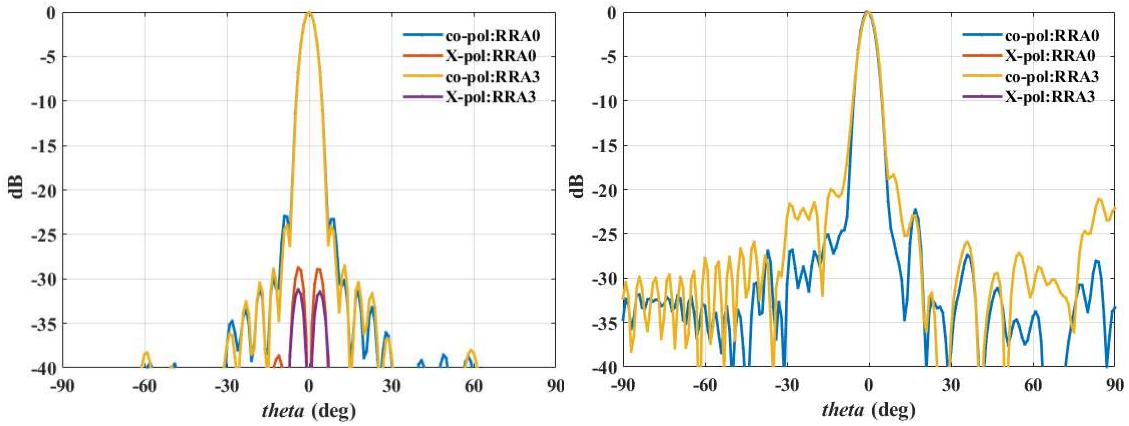

a) b)

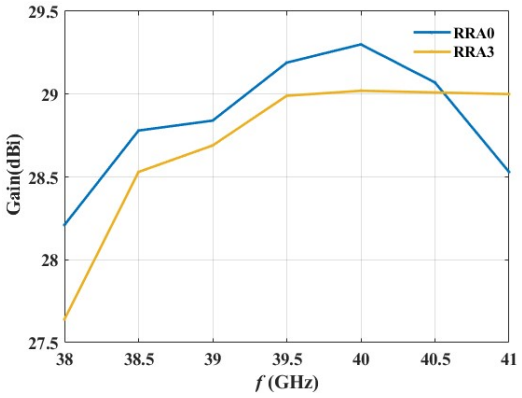

c)

Fig.3.32 The comparison between RRA0 and RRA3 at 40GHz (y-polar excitation). a) Radiation pattern (xoz' plane). b) Radiation pattern (y'oz' plane). c) Gain versus frequency

Now, the second mode of RRA3 is analyzed. In this case, RRA3 is excited by a x-polarized WR22 waveguide. Fig.3.33a shows the associated radiation at 40 GHz. As can be seen, the direction of the main beam is now in the broadside direction, as it is in the lower frequency band. At the same time, it can be seen from Fig.3.33 b) that the gain of RRA3 increases with frequency. These results demonstrate that RRA3 operates in both frequency bands as a parabolic reflector if incident wave is x-polarized. Consequently, it could be used to produce two orthogonally-polarized beams in different directions at 40 GHz.

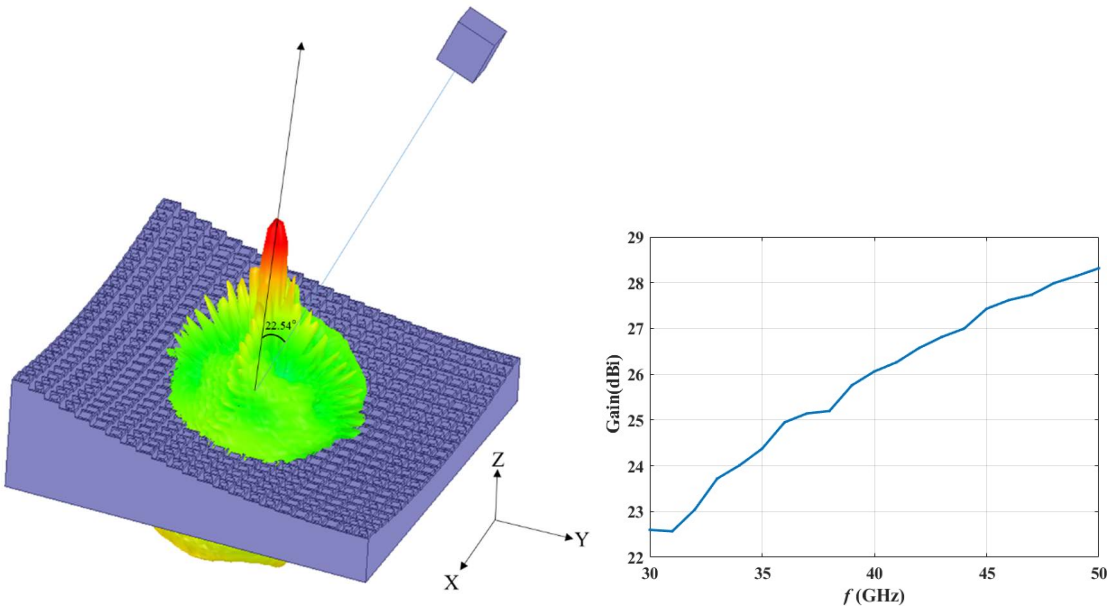

a) b)

Fig.3.33 Simulated results of RRA3 (x-polar excitation). a) Radiation field at 40GHz. b) Gain versus frequency.

3.6.3 Conclusion

This section first described the two different operation modes of RRA3 depending on the polarization of the excitation. The first mode is the same as that of RRA0 and it produces different beams in two different frequency bands. Simulation results show that its performances are not better than that of RRA0. However, a second mode of operation is possible for the orthogonal polarization, where the RRA operates as a parabolic reflector in both frequency bands.

3.7 Modification of RRA0 for reduced profile

3.7.1 Principle of profile reduction

The previous two sections compared the performances between RRA0, RRA1, RRA2 and RRA3. Results show that RRA0 has the best performances. As shown in Fig.3.20, however, RRA0 is very bulky and heavy. Indeed, it can be seen from Fig.3.12 that the z coordinate for the different cells varies from 0 mm to 20.55mm, which means there is a 20.55 mm maximum height difference. Also, after considering the 7mm reserved height for phase tuning, and the 0.2 mm thick ground plane, the achieved height of the RRA0 is 27.75mm, which is equal to 3.7 times the wavelength at 40GHz.

Before RRA0 is fabricated, a further modification is carried out to make it more compact. An efficient way to reduce the height is to rotate the coordinate system and redesign the RRA based on the new coordinate system. As illustrated in Fig.3.34, the height after rotating the coordinate system by α (in degree) around X axis is obviously lower than the height before rotation. The principle of coordinate transformation before and after rotation is shown in Fig.3.35. As a consequence, a point (x, y, z) in the original coordinate system is transferred to (x'', y'', z'') in the new one, with:

$$x'' = x \tag{3.4}$$

$$y'' = y\cos(\alpha) - z\sin(\alpha) \tag{3.5}$$

$$z'' = z\cos(\alpha) + y\sin(\alpha) \tag{3.6}$$

By substituting equation (3.2) into equation (3.5), the y-coordinate can be expressed as

$$y = \frac{\cos\alpha \mp \sqrt{(\cos\alpha)^2 - \frac{\sin}{h_f}\left(y'' + \frac{x''^2}{4h_f}\right)}}{\frac{\sin\alpha}{2h_f}} \tag{3.7}$$

For each cell in the RRA, as shown in Fig.3.1, its *y*-coordinate should not be positive. However, for the second solution (with + sign), its value is always greater than 0, provided the rotation angle (α) is in the range of 0 to 90 degrees. It is shown that the second solution cannot represent the real coordinates of the cells in a RRA. Therefore, the second solution in equation (3.7) can be excluded. By solving the equation (3.2, 3.4) and (3.6, 3.7), the z'' coordinate is obtained:

$$z'' = \frac{x''^2 + \left(\frac{\cos\alpha - \sqrt{(\cos\alpha)^2 - \frac{\sin\alpha}{h_f}\left(y'' + \frac{x''^2}{4h_f}\right)}}{\frac{\sin\alpha}{2h_f}}\right)^2}{4h_f}\cos\alpha + \left(\frac{\cos\alpha - \sqrt{(\cos\alpha)^2 - \frac{\sin\alpha}{h_f}\left(y'' + \frac{x''^2}{4h_f}\right)}}{\frac{\sin\alpha}{2h_f}}\right)\sin\alpha \tag{3.8}$$

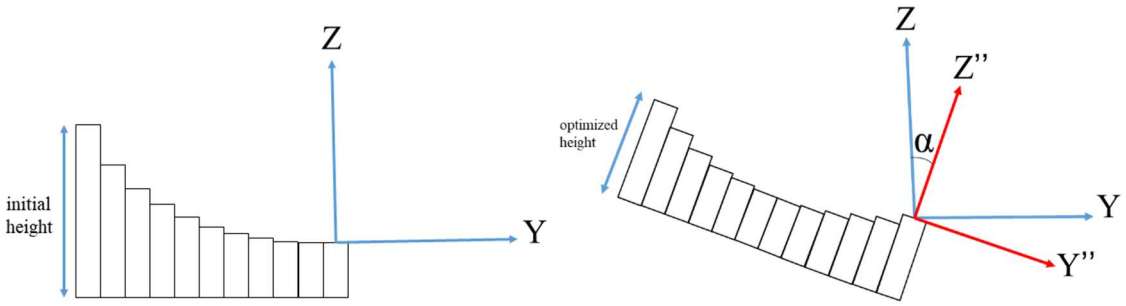

a) b)

Fig.3.34 Rotation of the coordinate system (sectional view). a) The configuration before rotation. b) The configuration after rotation.

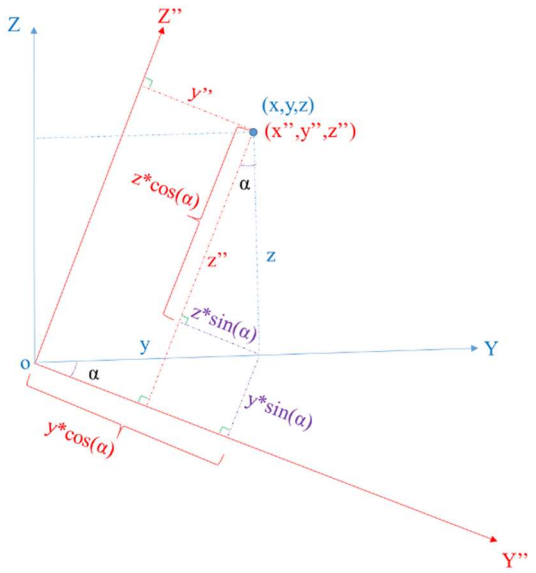

Fig.3.35 Transformation of the coordinates before and after rotation.

In the new coordinate system, the cells in the RRA are also regularly arranged with a periodicity of 3.75mm in the x''oy'' plane. The z'' coordinate of each cell can be calculated from equation (3.7).

In order to reduce the height of the RRA as much as possible, the rotation angle (α) is optimized. The height *H* of RRA is defined by:

$$H = z''_{max} - z''_{min} + 7.2 \tag{3.9}$$

where z''_{max} is the maximum z'' coordinate of a cell in the RRA and z''_{min} is the minimum z'' coordinate of a cell in the RRA. The number '7.2' is the sum of the reserved height used to tune the phase and the thickness of the ground plane. The relationship between the height *H* of RRA and the rotation angle (α) is shown in Fig.3.36. It shows that *H* reaches its minimum value when α is equal to 11 degrees. The achieved height at this rotation angle is 15.23mm. As a consequence, the rotation angle α is set to 11 degrees. The calculated z'' coordinate of each cell based on this specific rotation angle is shown in Fig.3.37. The direction of the main beam in each frequency band and the coordinate of the focal point, as tabulated in Table 3.3, are of course also changed after the rotation of the coordinate system.

Table 3.3: Configuration of RRA before and after rotating coordinate system.

	Before rotation	After rotation
Coordinates of wave vector for the main beam at 20GHz	(0, 0, 1)	(0, sin(11°), cos(11°))
Coordinates of wave vector for the main beam at 40GHz	(0, sin(10°), cos(10°))	(0, sin(21°), cos(21°))
Coordinates of focal point	(0, 0, h_f)	(0, h_f* sin(11°), h_f* cos(11°))
Incident angle of the cell in the center of RRA	22.54°	11.53°

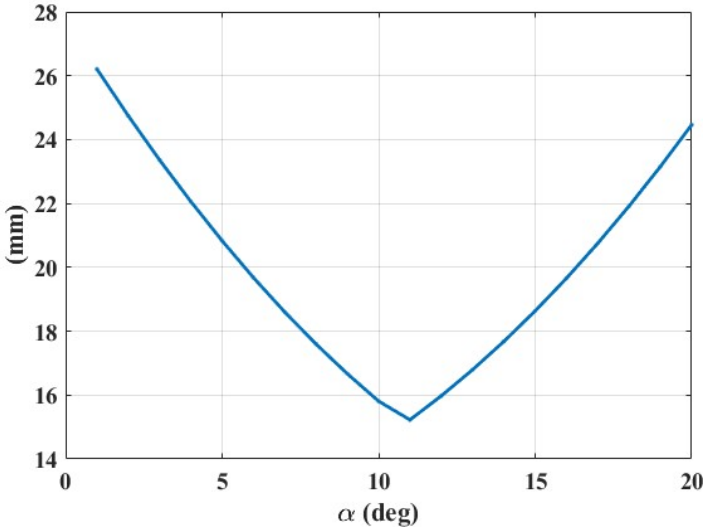

Fig.3.36 Height *H* of RRA versus rotation angle (α).

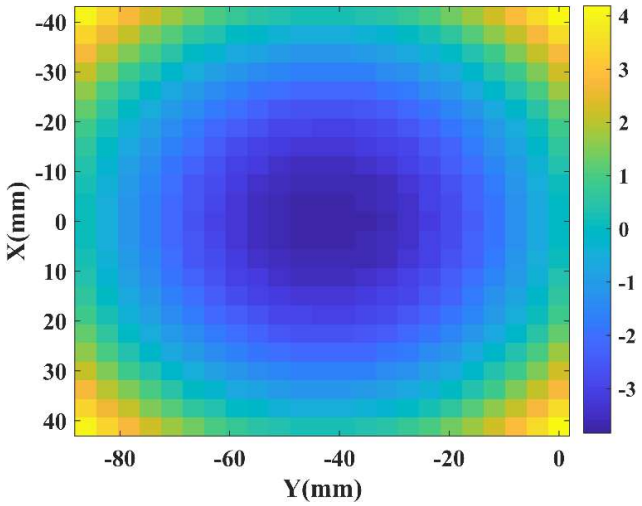

Fig.3.37 The z'' coordinate of each cell after the rotation of coordinate system (mm).

3.7.2 Performances evaluation

Since the incident angle on the cell in the center of the RRA has been changed to 11.53°, a new database at 40GHz (as shown in Fig.3.38) is established. The RRA after the rotation of the coordinate system is thus synthesized based on the configuration of Table 3.3 and the database in Fig.3.38. Note that the synthesis process is the same as the one used for RRA0. The RRA after the rotation of coordinate system is referred to as RRA4 in this chapter. As illustrated in Fig.3.39, the height of the RRA is significantly reduced (about 45.12%) after the rotation of coordinate system. The details of RRA4 are summarized in Fig.3.40. It can be seen from Fig.3.40c and d that the number of the cells with a loss greater than 2dB in RRA4 is lower than that in RRA0 (see Fig.3.19). Also, the phase error distribution over the cells in RRA4 is similar to that in RRA0 (see Fig.3.25a).

RRA4 with 3D radiated field is shown in Fig.3.41. It can be observed that the main beams at 20GHz and 40GHz are globally compliant with expectations. The comparison between RRA0 and RRA4 in the lower frequency band are summarized in Fig.3.42. It can be seen that the radiation patterns for both RRAs are quite similar and the gain after rotation in the lower band is reduced a bit. Fig.3.43 summarizes the performances of RRA0 and RRA4 in the higher frequency band. It can be seen that the side lobe level is increased by 1.8dB and the gain in the upper frequency band is increased a bit after rotation. As a summary, the performances of RRAs before and after the rotation of coordinate system are quite similar and the rotation of the coordinate system mainly contributes to reduce the height of RRA and make the fabrication easier.

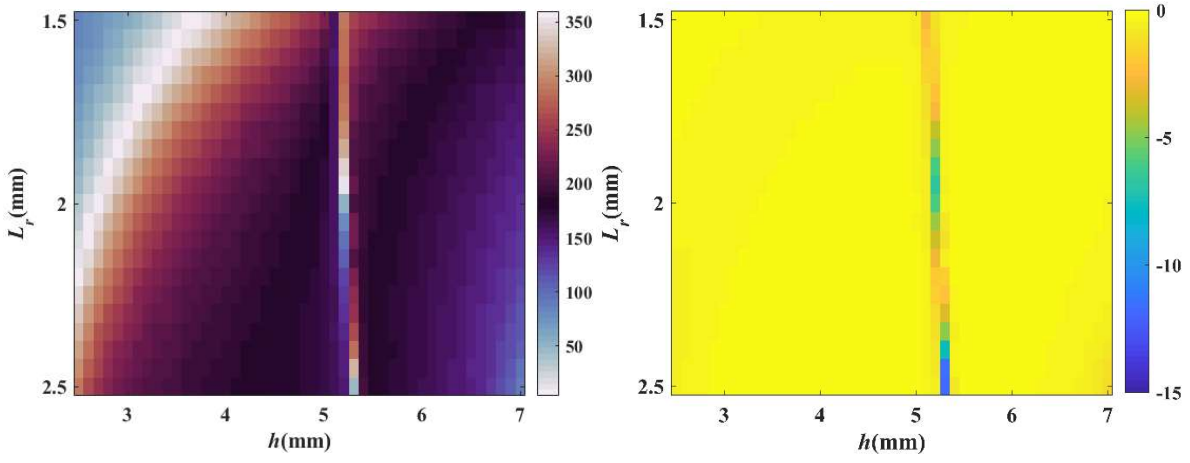

a) b)

Fig.3.38 Reflection phase and magnitude of the unit cell under oblique incidence (ϕ_{inc}=90°, θ_{inc}=11.53°, TM case). a) Reflection phase (deg). b) Magnitude (dB).

Fig.3.39 Comparison of the heights of RRAs before (right) and after (left) the rotation of coordinate system.

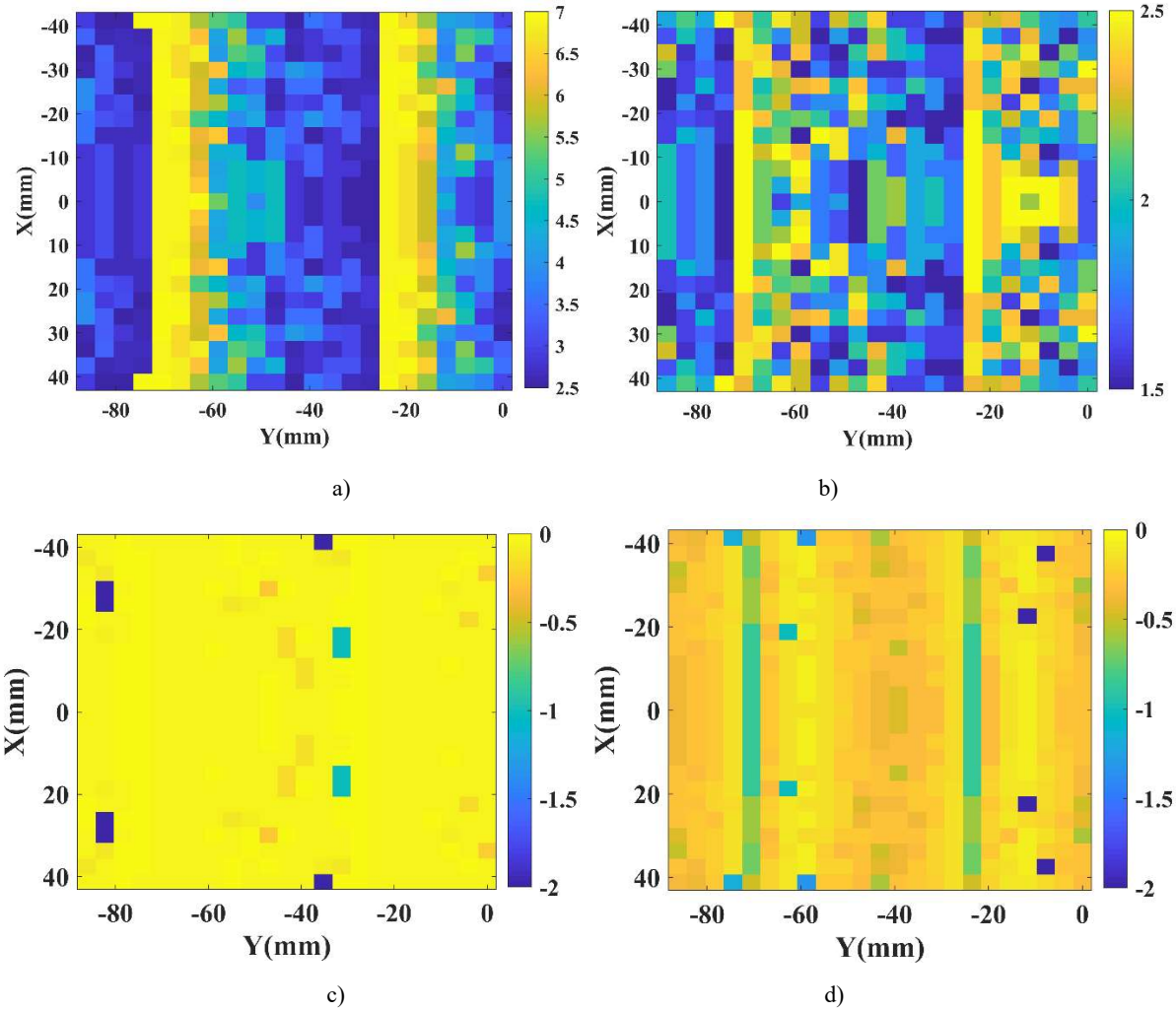

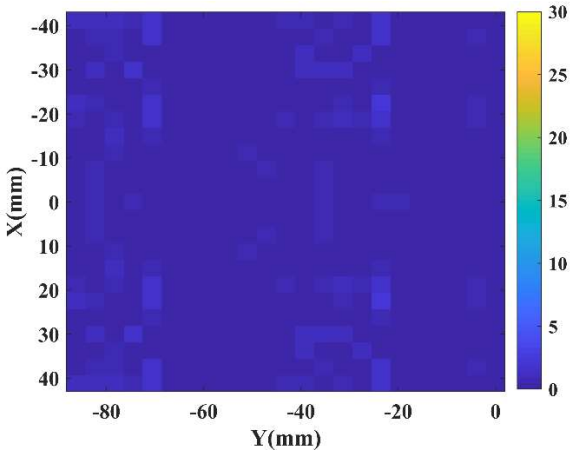

e)

Fig.3.40 Details of RRA4. a) Cell geometries for h (mm). b) Cell geometries for L_r. c) Loss at 20GHz (dB). d) Loss distribution over the cells at 40GHz (dB). e) Phase error distribution over the cells at 40GHz (deg).

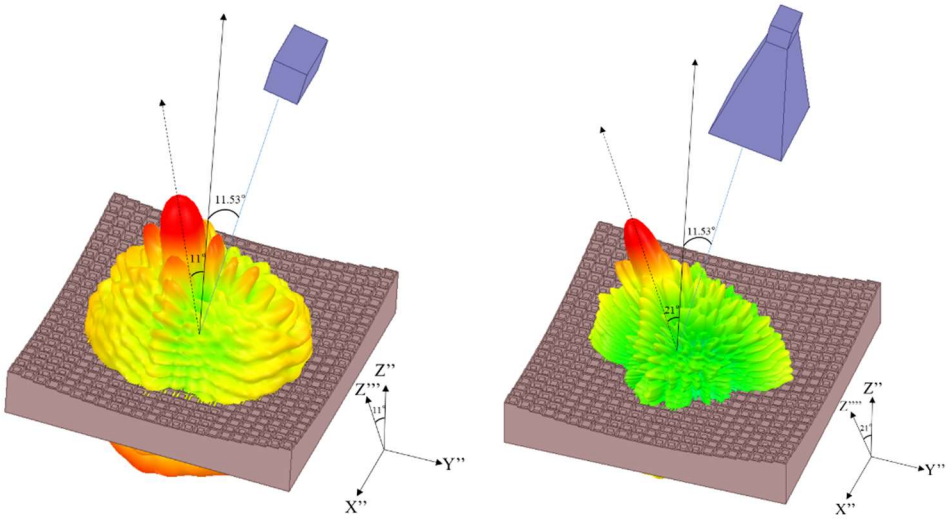

a) b)

Fig.3.41 Radiation field of RRA4. a) 20GHz. b) 40GHz.

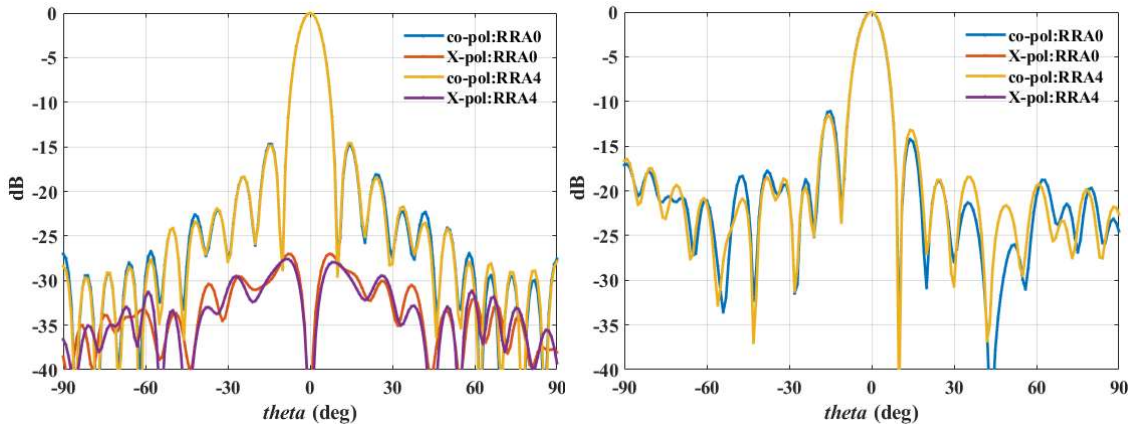

a) b)

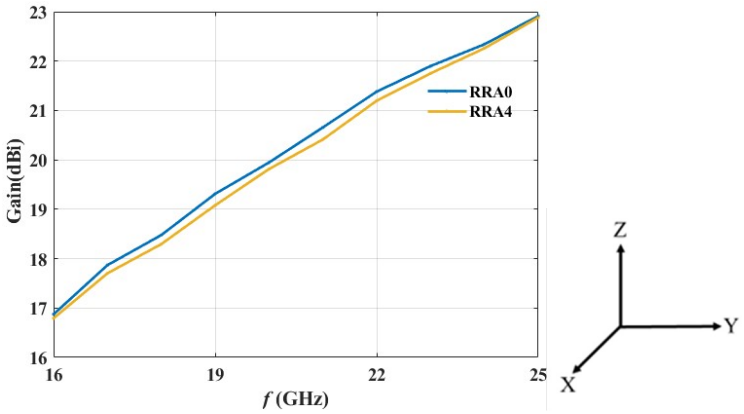

c)

Fig.3.42 Comparison between the performances of RRA0 and RRA4 in the lower frequency band. a) Radiation pattern at 20GHz (xoz plane). b) Radiation pattern at 20GHz (yoz plane). c) Gain versus frequency.

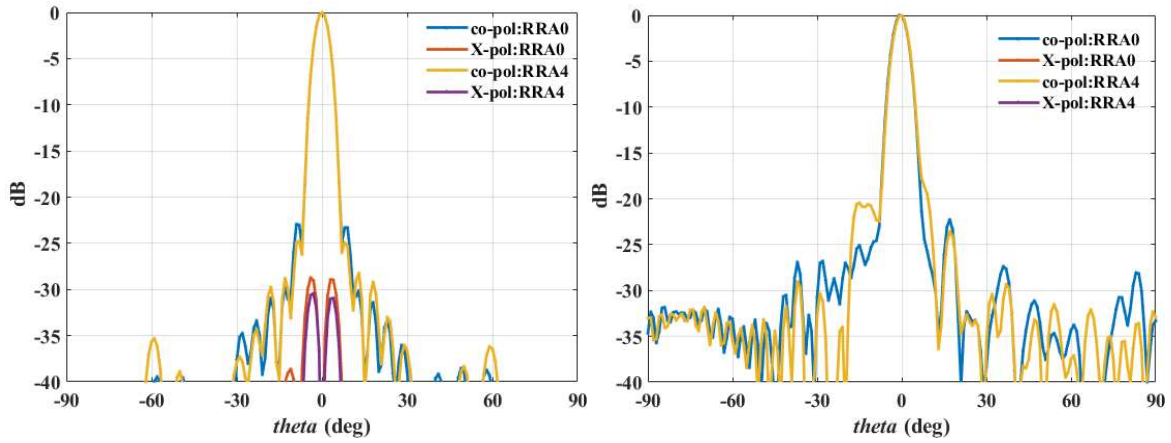

a) b)

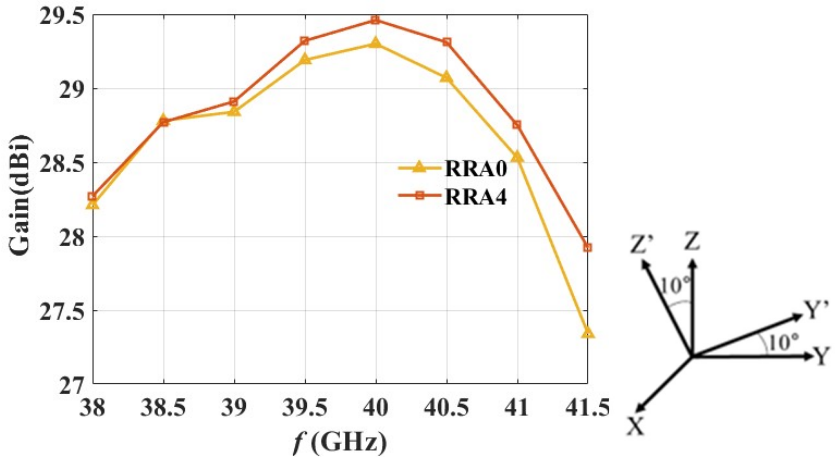

c)

Fig.3.43 Comparison between the performances of RRA0 and RRA4 in the upper frequency band. a) Radiation pattern at 40GHz (xoz' plane). b) Radiation pattern at 40GHz (y'oz' plane). c) Gain versus frequency.

3.7.3 Conclusion

In this section, the coordinate system is rotated to make RRA0 more compact and easier to be fabricated. The analytical solution of the coordinates after the rotation of coordinate system is given. The best rotation angle is proved to be 11 degrees. The height of RRA is reduced by 45.12% after the rotation of coordinate system. The RRAs before and after the rotation of coordinate system have nearly

similar performances. These results demonstrate that the rotation of the coordinate system mainly contributes to reduce the height and the weight of the RRA and makes the fabrication easier.

3.8 Fabrication and measurements

3.8.1 Antenna fabrication

After the comparison in the previous sections, the RRA after rotation (RRA4) is decided to be fabricated. The SLM 3D printing technology which has been introduced in chapter 1 is used to fabricate the antenna. The used material is stainless steel powder (316L). The antenna owns a parabolic surface and a flat bottom. Obviously, not all metal in the antenna is useful. At the same time, the metal with great thickness may cause warping due to the different cooling rates on the metallic surface [72]. Based on the principle of dual band antenna, only the waveguides with short circuit termination contribute to the functionality of the antenna (see Fig.3.44a). However, as shown in Fig.3.44a, the useful part cannot be fabricated directly because the waveguides need something else to support them. The model for final fabrication is shown in Fig.3.44b. In this model, the thickness of ground plane below each waveguide is increased. Also, some additional supports are added.

Some photos during fabrication and post-processing are shown in Fig.3.45 and 46 to illustrate the whole process. The SLM machine is shown in Fig.3.45 a). As illustrated in Fig.3.45 b-c), the RRA4 is fabricated layer by layer on a metal plate. After fabrication, the antenna needs some post-processing. As shown in Fig.3.46 a), the antenna is separated from the metal plate using wire cutting. Also, the supports on the bottom of the antenna are removed during post-processing (see Fig.3.46b). After this, the bottom of RRA4 is polished. RRA4 after the post-processing is shown in Fig.3.46 c). Similarly, the horn antenna and the waveguide are fabricated and post-processed as shown in Fig.3.47.

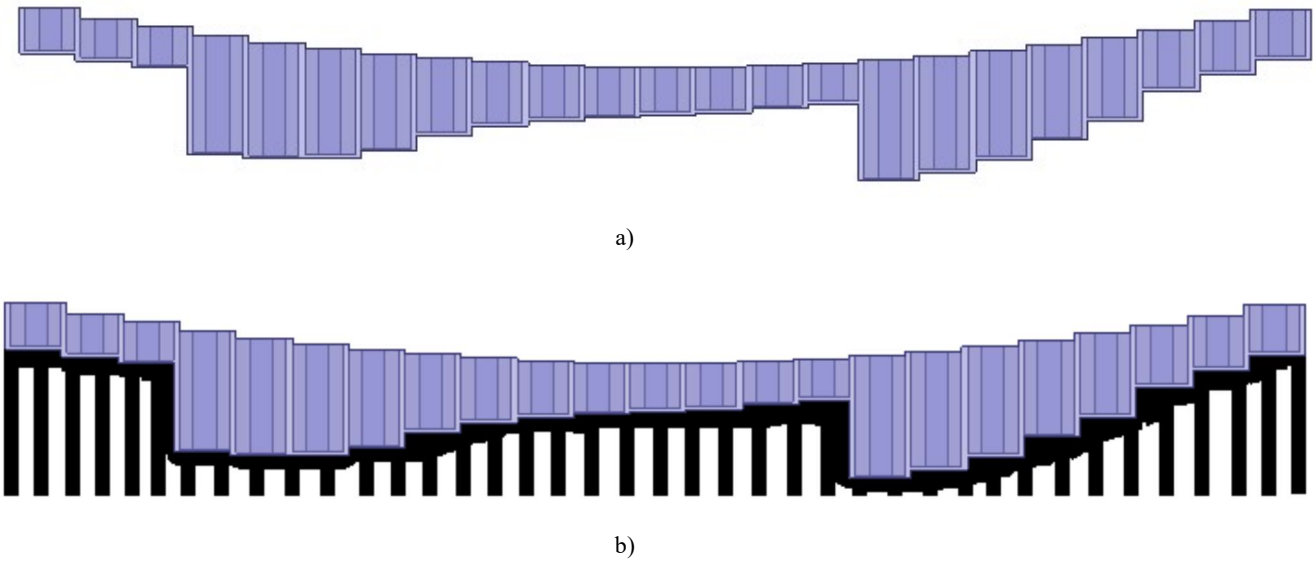

a)

b)

Fig.3.44 Antenna models (sectional view; central row). a) Useful part. b) Fabrication model.

a)

b)

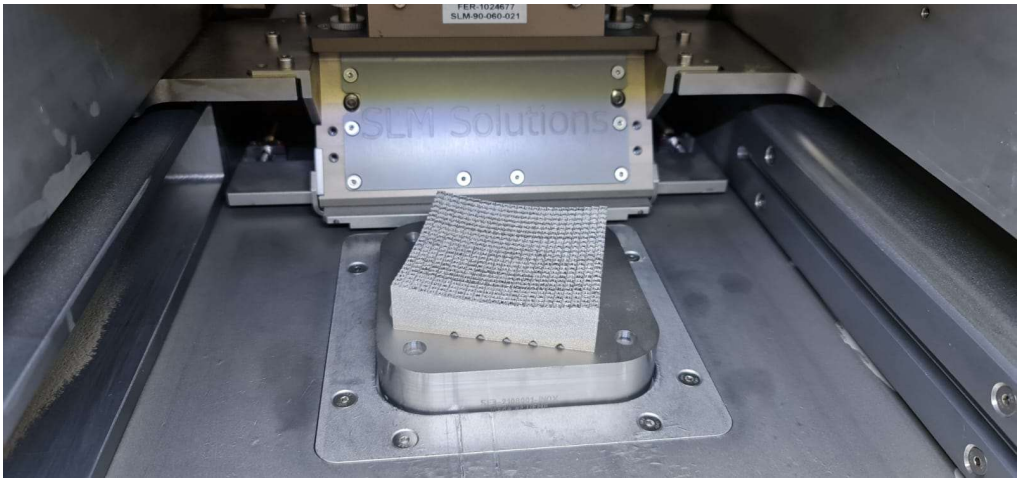

c)

Fig.3.45 Fabrication of RRA4. a) SLM machine. b) Initial stage of fabrication process. c) End of fabrication process

a)

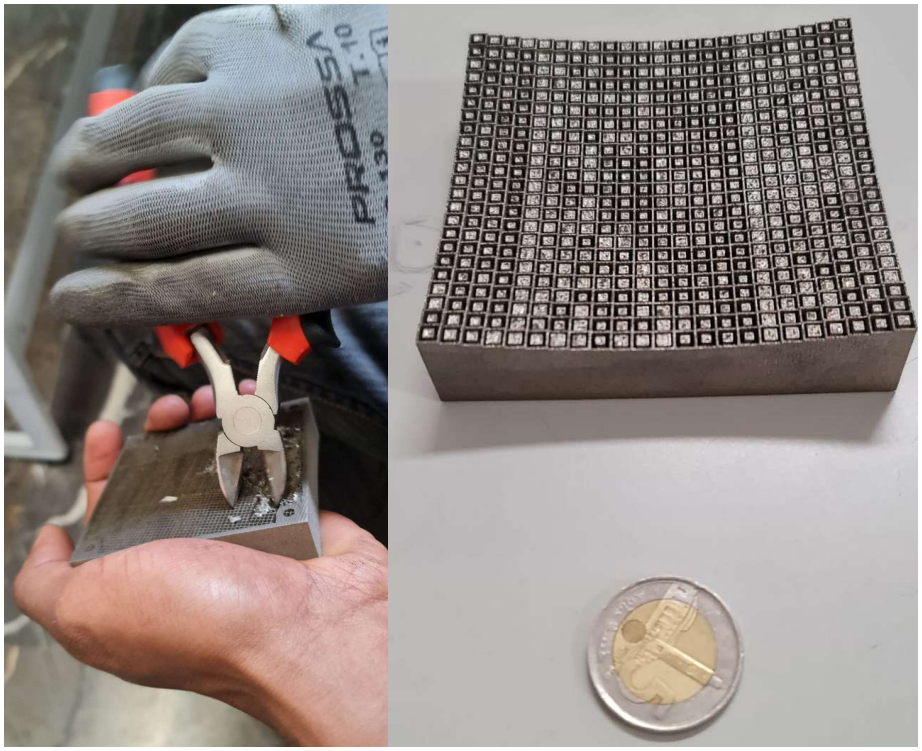

b) c)

Fig.3.46 Post-processing of RRA4. a) Separation from metal plate. b) Removal of support. c) RRA4 after post-processing.

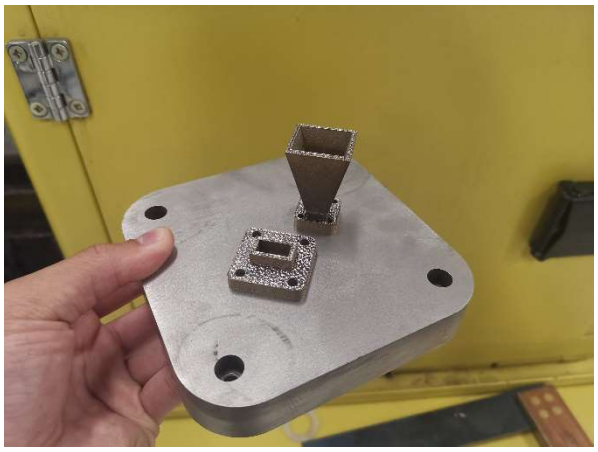

Fig.3.47 Fabrication of horn antenna and waveguide.

3.8.2 Antenna measurement

The photographs of the manufactured MORRA and its measurement setup are shown in Fig.3.48. Also, the comparisons of normalized radiation patterns between full wave simulations and measurements at lower frequency bands are shown in Fig. 3.49. It can be seen that although the measured side lobe levels at target frequencies are a bit higher that the simulated ones, the agreement between them is globally acceptable. In the target frequency band, the measured side lobe and cross polarization are lower than -10.24dB and -27.97dB, respectively. In addition, the gain response in lower frequency band is shown in Fig.3.50. It can be seen that the gain drop in the target frequency band (from 17-25GHz) is less than 3dB. It can also be seen that the gain difference between simulation and measurement is significantly increased when frequency is greater than 22GHz. This can be explained by the measured S11 parameter in Fig.3.51 It can be seen that the measured magnitude of S11 significantly increases with frequency when frequency is greater than 22GHz. Therefore, the gain drops (when frequency is greater than 22GHz) in Fig.3.50 is due to the mismatch of input port. Also, the measured directivity in lower frequency band is shown in Fig.3.50 to better characterize the capability of the fabricated antenna. It can be seen that the measured directivity increases with frequency, which suggests the antenna can operate as a parabolic reflector in lower frequency band.

Fig.3.48 Photographs of manufactured MORRA and its measurement setup.

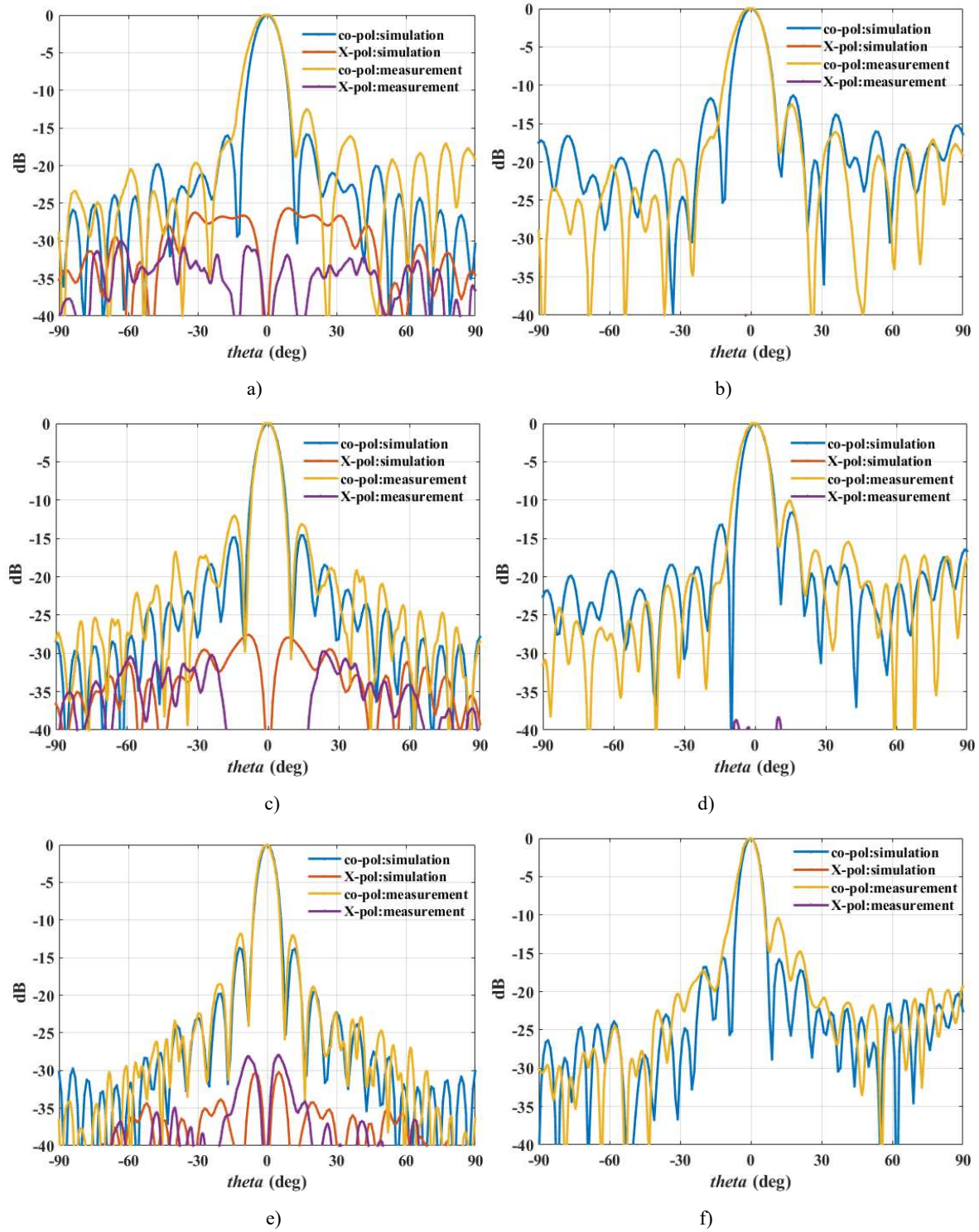

Fig.3.49 Radiation patterns in lower frequency band. a) xoz plane (17GHz). b) yoz plane (17GHz). c) xoz plane (20GHz). d) yoz plane (20GHz). e) xoz plane (25GHz). f) yoz plane (25GHz).

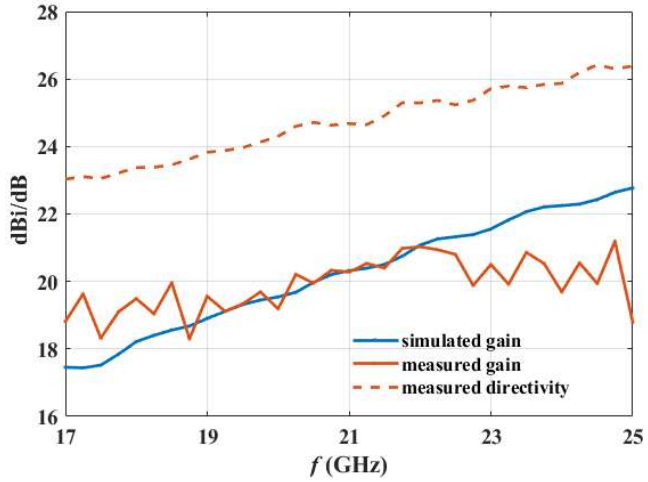

Fig.3.50 Gain and directivity in lower frequency band.

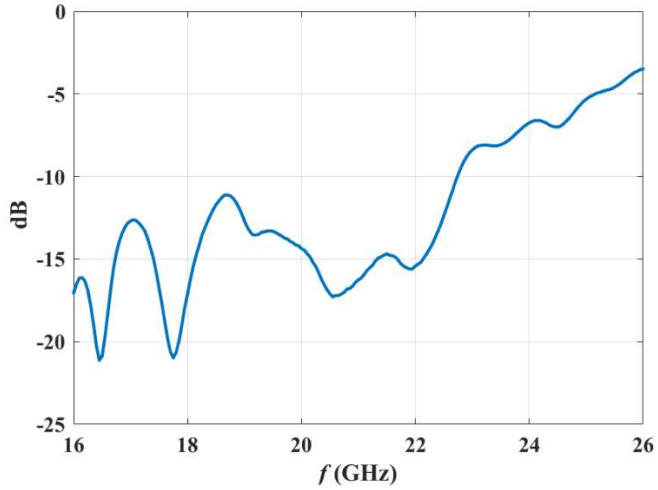

Fig.3.51 Measured S11 in lower frequency band.

Now the measurement results in upper band are analyzed. Due to the limitation of the signal generator in our lab, the measurements are conducted below 40GHz. Fig.3.52 shows the simulated radiation patterns at 38 and 40GHz. It can be seen from Fig.3.52a and that the agreement at 38GHz is acceptable. However, Fig.3.52d shows that the measured side lobe level at 40GHz is -8.45dB, which is 12dB higher than the simulated one. Also, the directivity in upper band is shown in Fig.3.53. Note that the measured gain is not given due to the absence of the gain of the corresponding reference antenna in our lab. It can be seen from Fig.3.53 that the measured directivity is significantly lower than the simulated one, e.g., the difference at 40GHz is about 2.5dB.

In general, the performance in lower band is quite acceptable while that in upper band is disappointing.

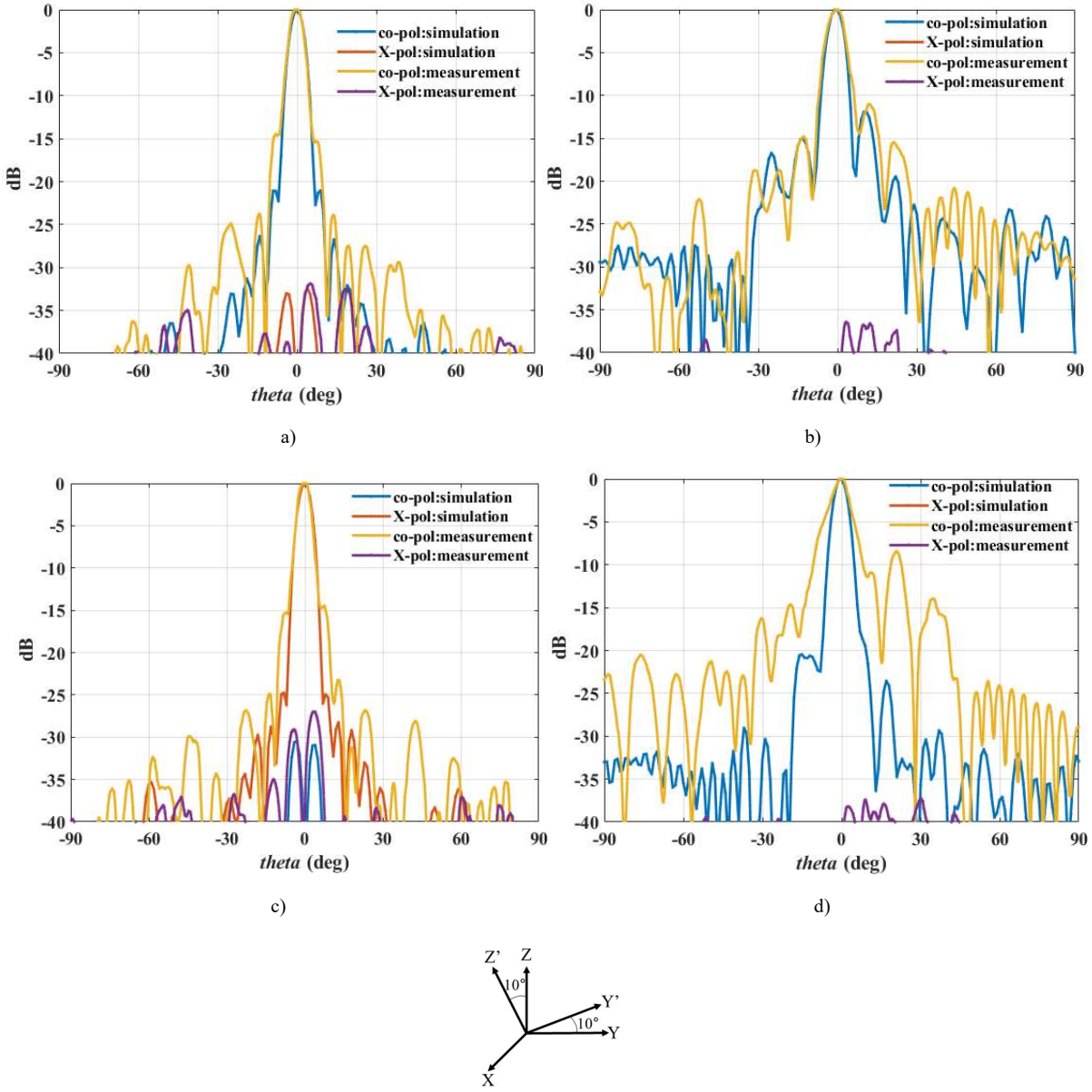

Fig.3.52 Radiation patterns in upper frequency band. a) xoz' plane (38GHz). b) y'oz' plane (38GHz). c) xoz' plane (40GHz). d) y'oz' plane (40GHz).

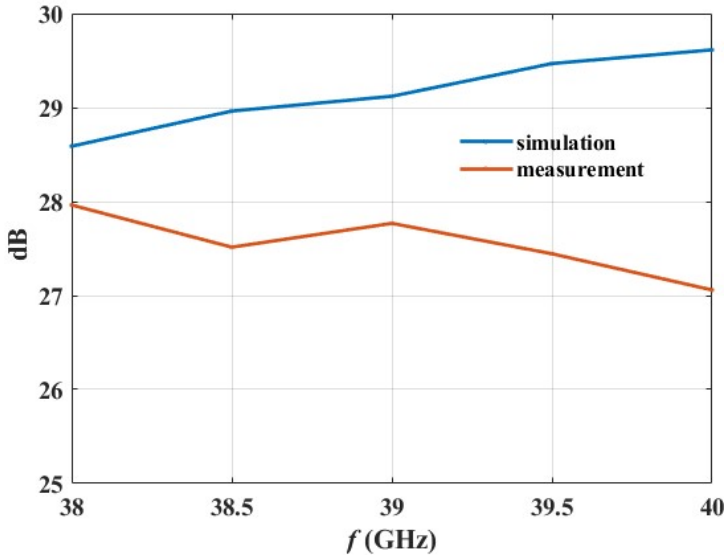

Fig.3.53 Directivity in upper band.

3.8.3 Optimized antenna made of unit cells with fixed cross-section

The performance of the measured antenna in the previous subsection is not as good as expected. It can be deduced that the large difference between simulation and measurement is mainly due to fabrication errors. Fig.3.54 compares the sensitivities of L_r and h on the reflection phase. For Fig.3.54a, h is fixed at 5mm, and the range of L_r is from 1.5 to 2.5mm. For Fig.3.54b, L_r is fixed at 2mm, and h is from 4.5 to 5.5mm. Obviously, the phase range in Fig.3.54b is smaller than that in Fig.3.54a, which demonstrates that the reflection phase is more sensitive to L_r than h. The subsequent analysis focuses on L_r. Since the waveguides in both antennas operate below cutoff in lower frequency band, the fabrication error in L_r does not have a significant effect on the antenna performance at lower frequencies and it mainly affects the upper frequency band. Different cells with the same L_r should have a similar systematic fabrication error, which means they should all preserve the same L_r (even if different from the desired one). Globally, for a constant L_r (whatever its value), the reflected phase varies quite linearly with h. This means a systematic error in L_r preserving a constant value for all cells does not modify too much the phase law on the aperture. However, in the previous antenna with variable L_r, as the phase variation with L_r is nonlinear, the perturbation in the phase distribution is quite random. The measured performance of the antenna thus has a significantly degradation. Therefore, a dual band antenna made of unit cells with fixed cross-section (L_r) is designed, fabricated, and measured in this subsection to verify these analyses. The only difference with last antenna is that the cross-section of the cells in the optimized antenna is fixed at 2mm. In this case, h is varied from 2.5 to 8mm. This subsection mainly analyzes its performance as the design and fabrication process has been introduced in previous sections in detail.

Fig.3.55 and Fig.3.56 show the performance of optimized antenna in both lower and upper bands. It can be seen from Fig.3.55a and b that the achieved side lobe level and cross polarization at 20GHz are -11.38dB and -27.61dB, which is similar to the previous antenna (see Fig.3.49). Also, the achieved directivity (see Fig.3.55c) increases with frequency and is close to that of the previous antenna (see Fig.3.50).

It can be seen from Fig.3.56a and b that a good agreement between simulated and measured radiation patterns at 40GHz is achieved. Also, the achieved side lobe level is -23.41dB at 40GHz which is significantly lower than the previous antenna (see Fig.3.52). It can be seen from Fig.3.56c that the difference between simulated and measured directivities in upper frequency band is less 0.5dB. Also, the achieved directivity of the optimized antenna (see Fig.3.56c) is obviously higher than the previous one (see Fig.3.53).

As a summary, the performances of both the optimized and the previous antennas are similar in lower frequency band while not in upper frequency band, which suggests that it's better to keep a constant cross-section.

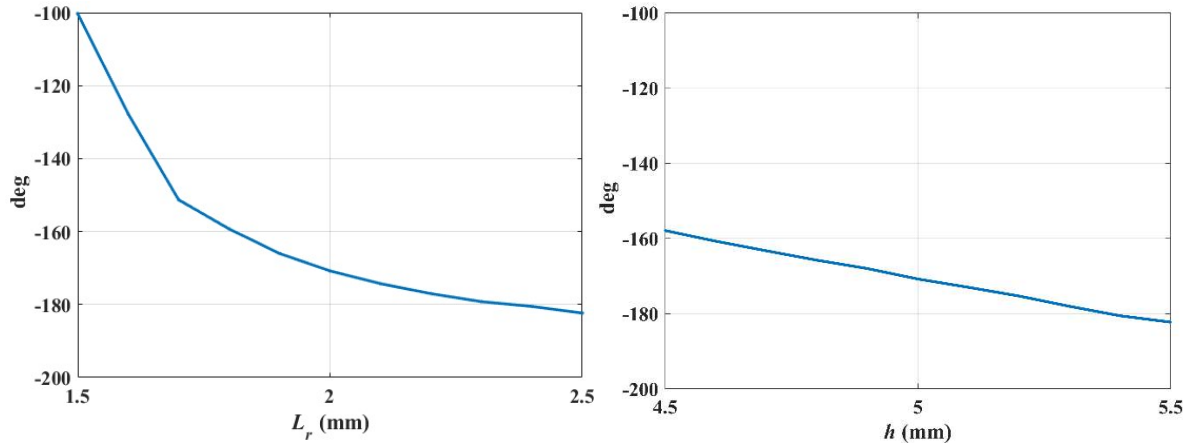

a) b)

Fig.3.54 Comparison of the sensitivity of geometry on reflection phase. a) Reflection phase vs L_r (mm). b) Reflection phase vs h (mm).

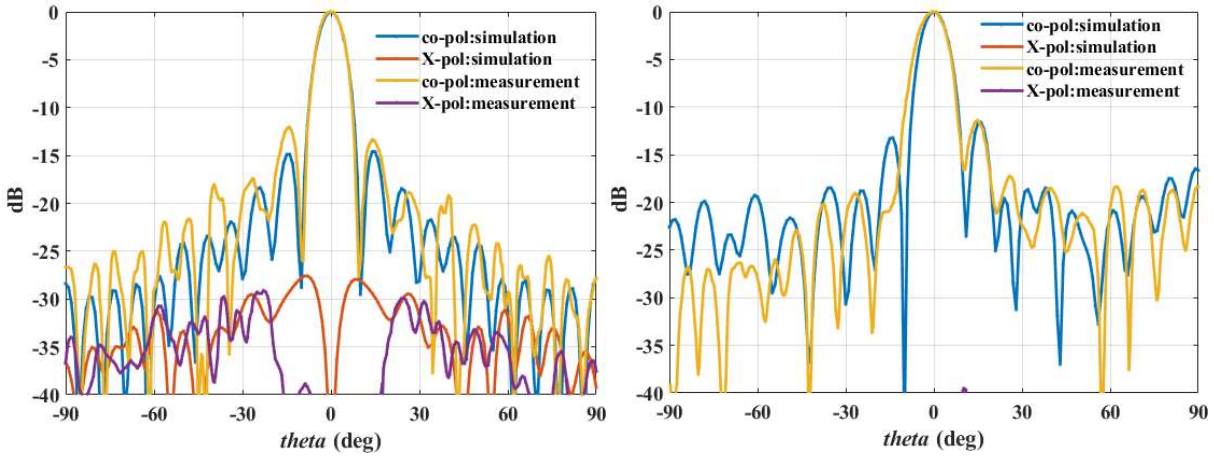

a) b)

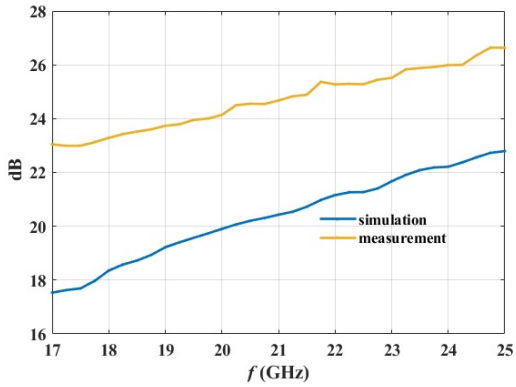

c)

Fig.3.55 Performance of optimized antenna in lower band. a) Radiation pattern at 20GHz (xoz plane). b) Radiation pattern at 20GHz (yoz plane). c) Gain and directivity.

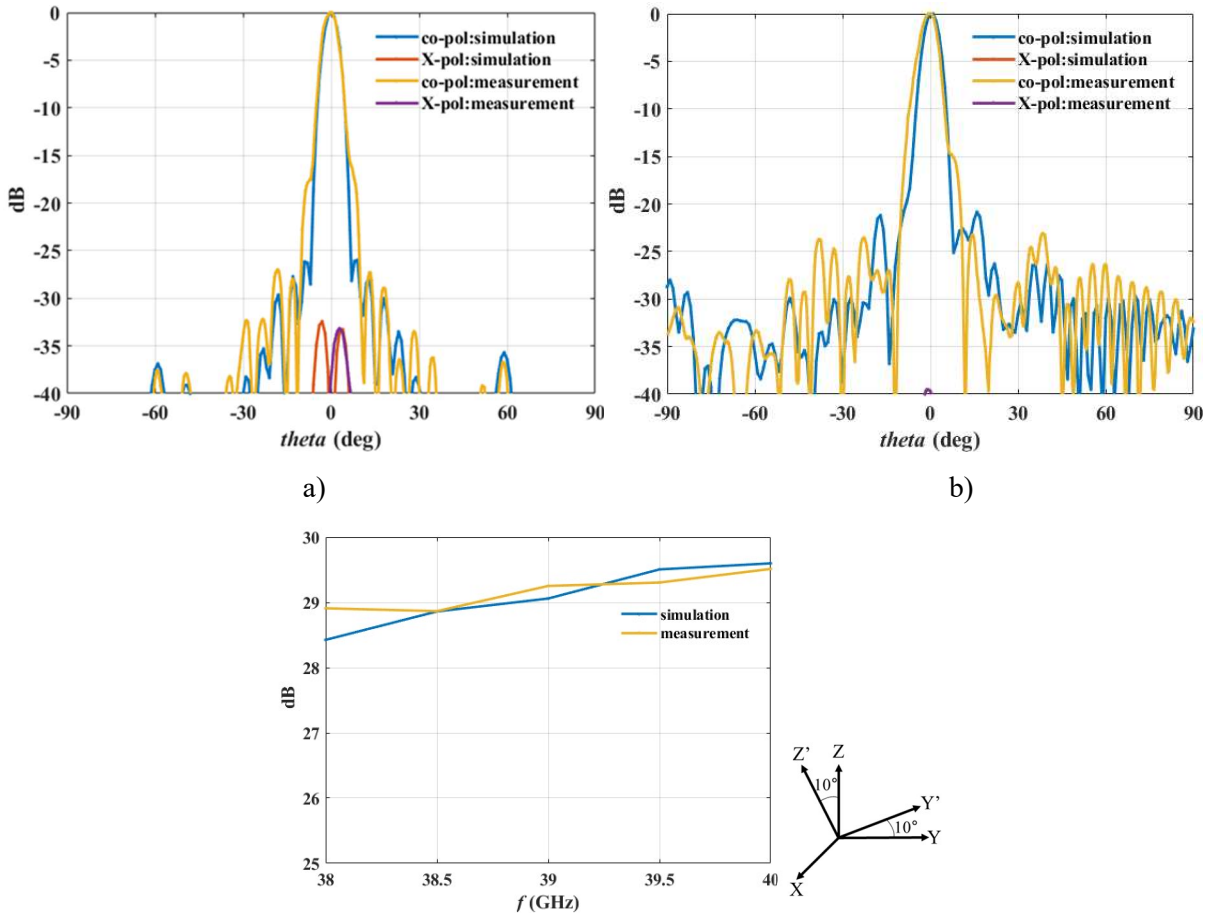

Fig.3.56 Performance of optimized antenna in upper band. a) Radiation pattern at 40GHz (xoz'). b) Radiation pattern at 40GHz (y'oz'). c) Directivity.

3.9 Conclusion

The concept of dual band RRA is described first. In the upper band, the dual band antenna is a RA that collimates the reflected beam by varying the phase distribution over the cells. In the lower frequency band, the dual band antenna operates as a parabolic reflector where the reflected beam is determined by the paraboloid. The beams in the two frequency bands can be steered in two different directions. The SCSW introduced in chapter 2 is used to design the proposed dual band antenna. Its performances are analyzed in detail. Simulation results show that oblique incidence may cause additional resonances referred to as TEM resonances.

A MORRA is synthesized using the database with TEM resonant cells. Simulation results show that the directions of the main beam in both bands are pointing in the target directions. The gain increases with frequency in the lower frequency band. The gain drop in the upper frequency band is less than 1.1dB. These results demonstrate the capability of the proposed MORRA. In addition, the number of cells with a loss greater than 2dB is very small in the designed MORRA, which means the TEM resonance does not significantly affect the designed MORRA. To further analyze the impact of TEM resonances, two MORRAs are synthesized using the database without TEM resonances. Also, a MORRA is synthesized using the modified unit cell to avoid TEM resonances. Simulation results show that it is not necessary to avoid the TEM resonances here because the initial array involves only a few cells with resonances.

The profile of the initial array is reduced by 45.12% after the rotation of coordinate system. Simulation results demonstrate that the rotation of the coordinate system mainly contributes to reduce

the height and the weight of the RRA and makes the fabrication easier. A first array with reduced profile is fabricated using SLM technology. The agreement between the simulation results and measured results is not very good. Finally, an optimized antenna made of unit cells with fixed cross-section is designed, fabricated, and measured. A good agreement between simulation and measurement is achieved. Also, the optimized antenna has a better performance than the previous one.

Chapter 4 - Single Band Antennas made of Phoenix Cells

4.1 Introduction 120

4.2. Metal-only reflectarray antenna using 3D phoenix cells 121

4.2.1 Design process of metal-only reflectarray antenna 121
4.2.2 Horn antenna design 121
4.2.3 Performances evaluation 123
4.2.4 Fabrication and measurements 125
4.2.3 Conclusion 129

4.3. Transmit-reflect-arrays using 3D phoenix cells 129

4.3.1 Design process 129
4.3.2 Performances analysis 132
4.3.3 Conclusion 139

4.4 Bandwidth enhancement of metal-only reflectarray antenna 140

4.4.1 Database 140
4.4.2 Initial design approach and analysis 141
4.4.3 Improved design approach and analysis 141
4.4.4 Conclusion 145

4.5 Conclusion 146

Chapter 4 - Single Band Antennas made of Phoenix Cells

4.1 Introduction

In chapter 2, two different waveguide-based MO cells (SC and PC) are introduced. The SCSW is used as a phase shifting cell to synthesize the RRAs in chapter 3. In this chapter, the capability of PC is demonstrated by using it to synthesize RAs and TRAs.

Section 4.2 describes the design, fabrication and measurement of a MORA operating at 20GHz. The achieved aperture efficiency and 1-dB gain bandwidth are 49.3% and 17.5% respectively. Then, the design and simulation of two different MOTRAs are discussed in section 4.3. Section 4.4 presents a detailed analysis of the effect of the height of the 3D PC on the performance of MORAs and provides an improved design approach. Finally, a conclusion is made in section 4.5.

The center frequency of all antennas in this chapter is 20GHz. As shown in Fig.4.1, the radiating aperture is $13\lambda_0 \times 13\lambda_0$ (the wavelength at center frequency, 20GHz) with an element spacing of 0.5 λ_0. The illumination is achieved by a linearly polarized horn antenna with an offset angle of 25° with respect to the normal of the panel. The f/D ratio is 1.183.

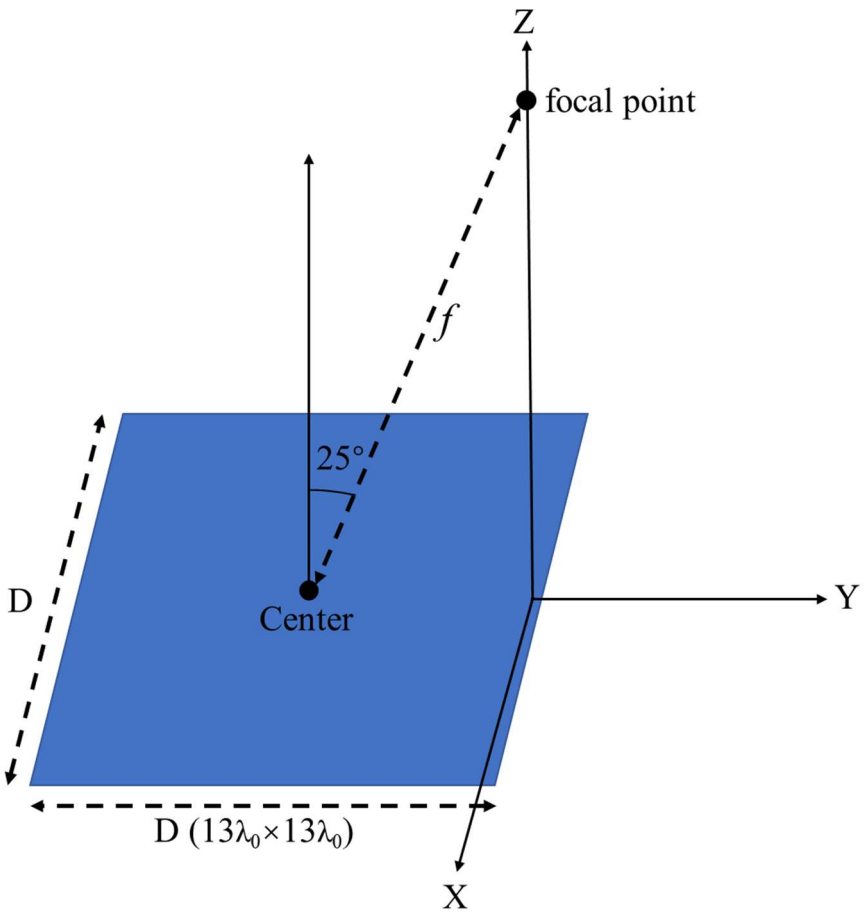

Fig.4.1 Configuration of proposed antennas.

4.2. Metal-only reflectarray antenna using 3D phoenix cell

4.2.1 Design process of metal-only reflectarray antenna

First, a RA is designed to validate the PCSW shown in Fig.2.15. To make the fabrication easier, the thicknesses of the walls in the 3D PC are increased compared to parameters in table 2.2 and the detailed parameters are tabulated in Table 4.1. The direction of the main beam has a tilt angle of 25°, opposite to the offset angle of horn antenna. The synthesis process derives from the one used in [135]. It consists in selecting the geometry for each cell in the RA in order to achieve best the desired phase. The desired phase law at frequency f is calculated using equation (1.3).

Table 4.1 Detailed parameters of the 3D MO PC for fabrication.

Parameter	L_c	L_r	L_p	w_{in}	w_{ex}
Value (mm)	7.5	1-7.5 (step=0.05)	1	0.3	0.2

Note that the phase offset $\emptyset_{off}$ (as defined in equation 1.3) is optimized during the synthesis process to minimize the average phase error $\bar{\varepsilon}$:

$$\bar{\varepsilon} = \frac{1}{N_f}\sum_{i=1}^{N_f}\sum_{m=1}^{N_c}\frac{I_m(f_i)}{\sum_{m=1}^{N_c} I_m(f_i)}\left|\phi_m^{ach}(f_i) - \phi_m^{des}(f_i)\right| \tag{4.1}$$

where N_f is the number of frequencies (f_i) for which the optimization is done, N_c is the number of cells, ϕ_m^{ach} and I_m are the achieved phase and illumination intensity for cell m. This latter one is the magnitude of the electric field from the feed antenna.

In the calculation of the I_m, the field from the feed is approximated by $\cos^q$ with q=19.574 at 20GHz. This specific value of q is selected such that the edge taper is less than -10dB, which will be shown later. Also, two frequencies (f_1=19.5GHz and f_2=20.5 GHz) are used for enlarging the bandwidth around f_0=20GHz. Fig.4.2 shows the desired phase shift distribution at these two frequencies.

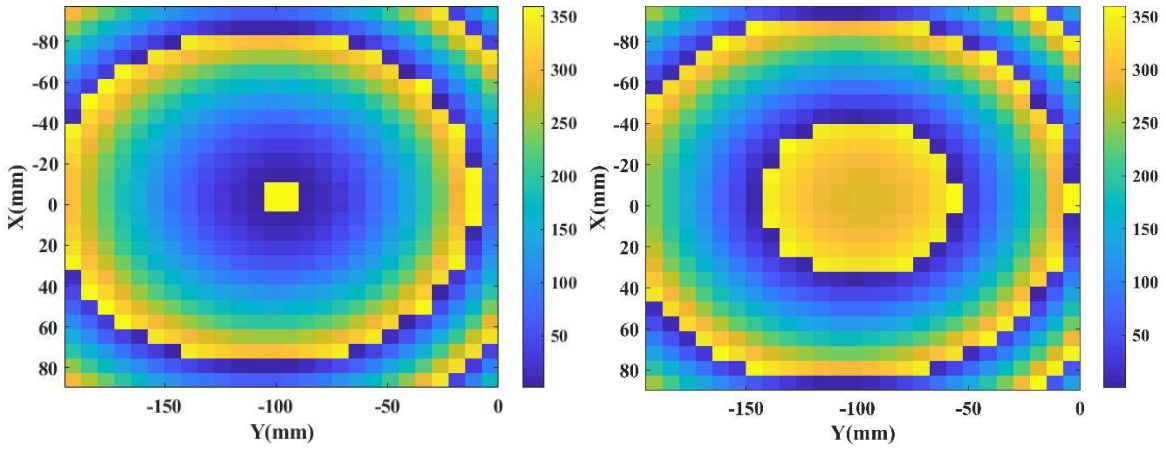

a) b)

Fig.4.2 Distribution of the required phase shift over the RA cells (deg). a) 19.5GHz. b) 20.5GHz.

4.2.2 Horn antenna design

A horn antenna is designed based on the first two steps of the design process in section 3.4.2. Fig.4.3 shows the designed horn antenna which is used to illuminate all the antennas in this chapter.

Fig.4.4 summarizes the illumination intensity at 19.5GHz, 20GHz and 20.5GHz. It can be seen that the edge taper is less than -10dB in the target frequency range.

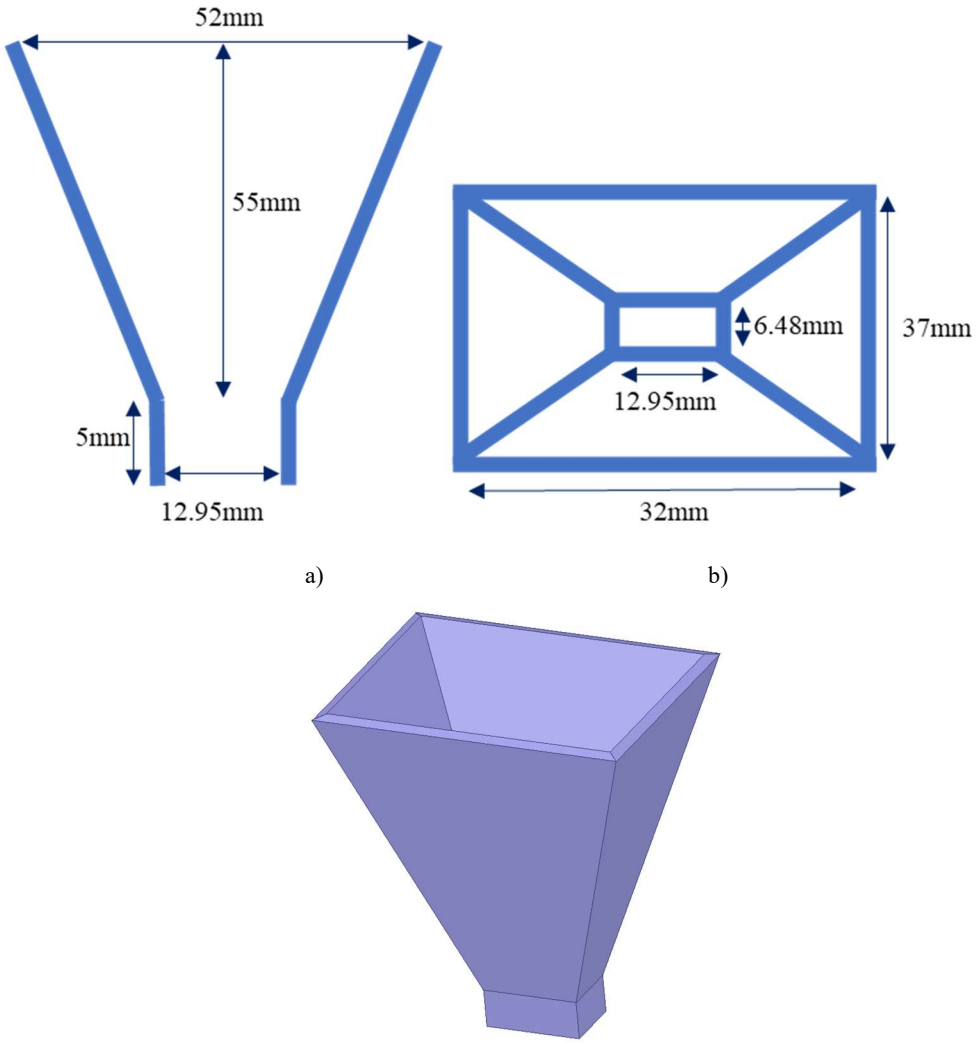

Fig.4.3 The designed horn antenna. a) Sectional view. b) Top view. c) 3D view

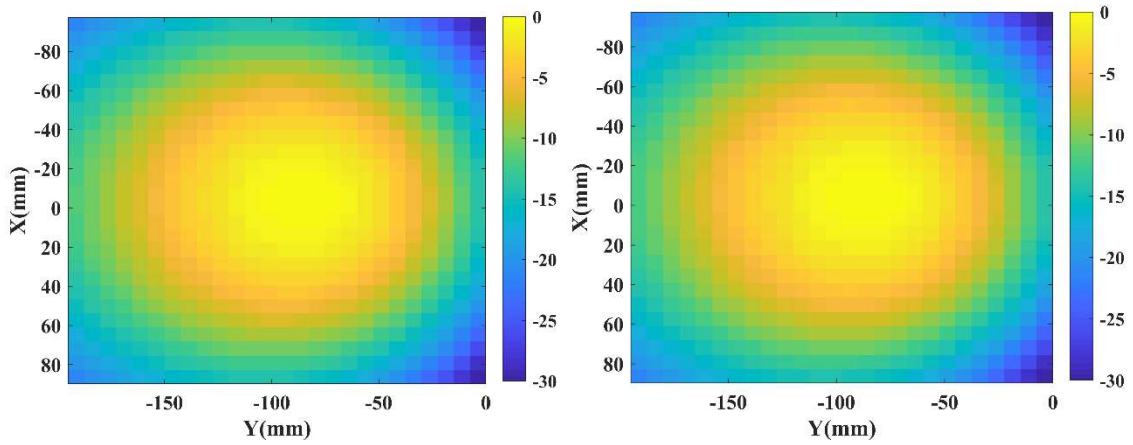

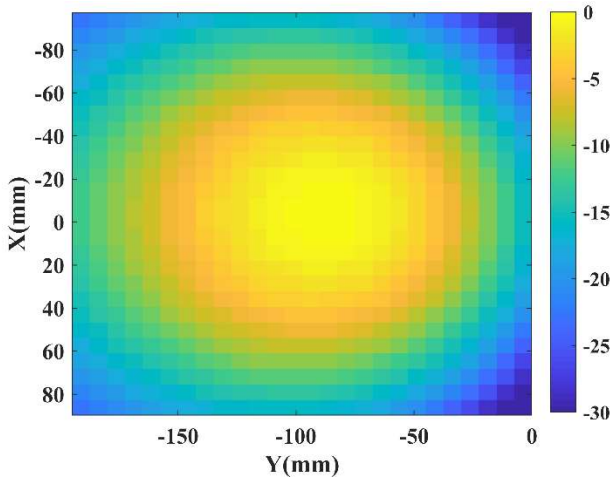

c)

Fig.4.4 Illumination intensity (dB). a) 19.5GHz. b) 20GHz. c) 20.5GHz.

4.2.3 Performances evaluation

Fig.2.16 shows that the complete phase cycle is achieved when h is greater than 4 mm. As a trade-off between antenna thickness and achieved phase range, the height of the PCSW is fixed to 6 mm for all cells. Then, the reflection phase is only controlled by L_r. The conductivity of conductors is now set to 1.33×10^6 S/m in simulations (instead of the PEC in section 2.2), as the metal used for fabrication is stainless steel.

A database is first established to characterize the response of the cell versus L_r. It is calculated with HFSS® assuming oblique incidence and y-polarization for the incident wave. The incident angle is set to the value at the array's center (25°) where the illumination is the highest. The simulated reflection coefficients at f_1 and f_2 are summarized in Fig.4.5. It can be seen that the complete phase cycle is achieved at both frequencies and the maximum loss is less than 0.25 dB. Note that the jump in magnitude when L_r=7.1 mm is due to the disappearance of the outer waveguide.

To limit fabrication issues, cells where the gap between two metal walls is less than 0.2 mm are not accepted in the final design. Cells with such a narrow gap between the inner and outer waveguides are simply removed from the database. For those where the narrow gap is located between the inner waveguide and the metallic block, the treatment is different because the associated phase is not so sensitive. Consequently, in this case, the gap is suppressed (filled with metal).

The RA is then synthesized using the database in Fig.4.5. The phase offset and the achieved average phase error after optimization at 19.5/20.5GHz are 265°/295° and 6.17°/8.28°. Fig.4.6 shows the used geometries for all cells over the panel together with the achieved magnitude of the reflection coefficient (at both frequencies). Having in mind that cells with either a small or a large L_r have a quite similar geometry, it can be said that a smooth variation is achieved (see Fig.4.6a). Also, the loss at 19.5GHz is a bit higher than that at 20.5GHz (see Fig.4.6b and c), which is consistent with the results in Fig.4.5. The designed MORA with its 3D radiated field is shown in Fig.4.7. It can be observed that the main beam at 20GHz is globally compliant with expectation. The simulated radiation patterns and gain response are summarized in section 4.2.2 for comparison with the measured results.

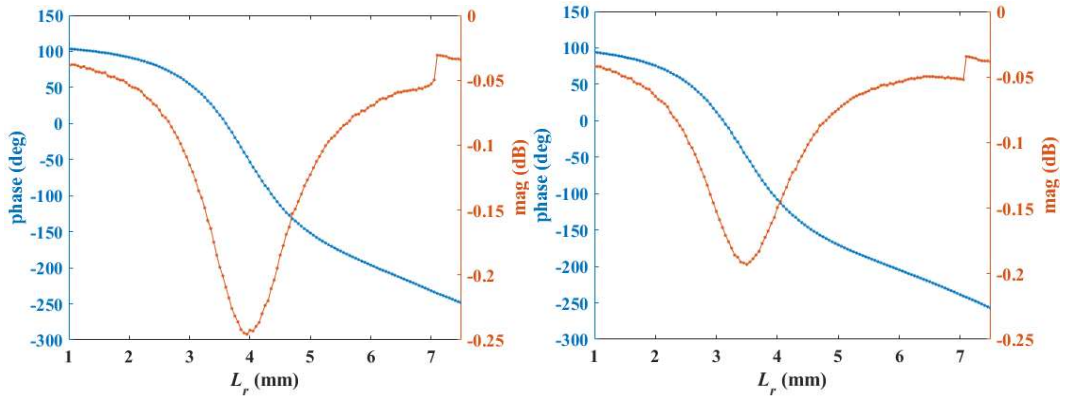

a) b)

Fig.4.5 The reflection phase of PCSW (y-polarization, ϕ_{inc}=90°, θ_{inc}=25°). a) 19.5GHz. b) 20.5GHz.

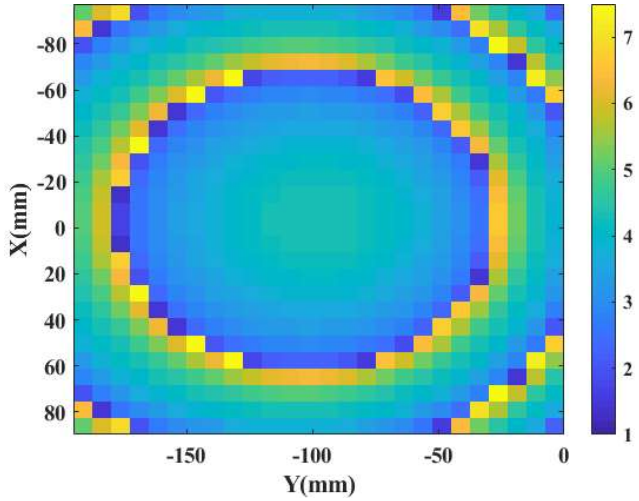

a)

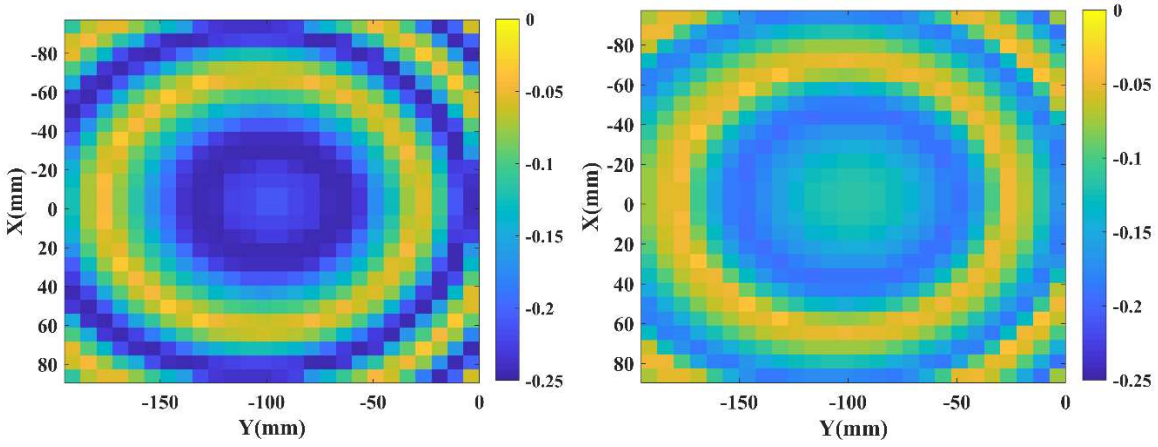

b) c)

Fig.4.6 a) Cell geometries (value of L_r in mm). b) Magnitude of the reflection coefficient over the cells at 19.5GHz (dB). c) Magnitude of the reflection coefficient over the cells at 20.5GHz (dB).

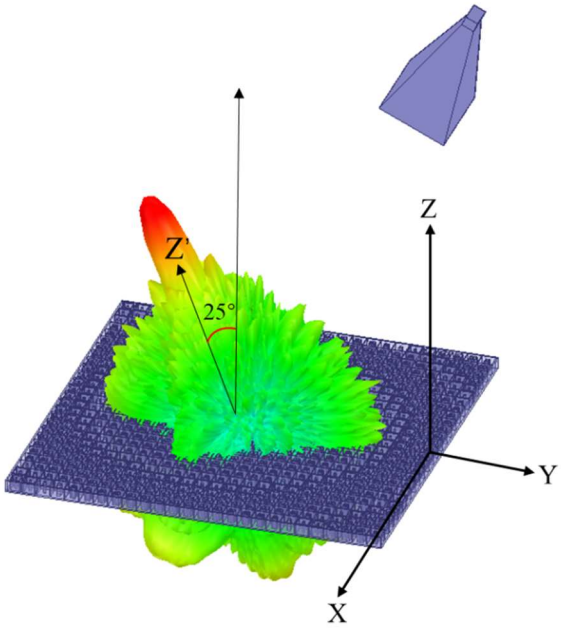

Fig.4.7 Radiation field of the designed RA at 20GHz

4.2.4 Fabrication and measurements

The RA and horn antenna are fabricated layer by layer using selective laser melting 3D printing technology. The detailed fabrication and post-processing have been introduced in chapter 1 and section 3.8 and will not be repeated here. The fabricated MORA and horn antennas are shown in Fig.4.8. The photographs of manufactured MORA and its measurement setup are shown in Fig.4.9.

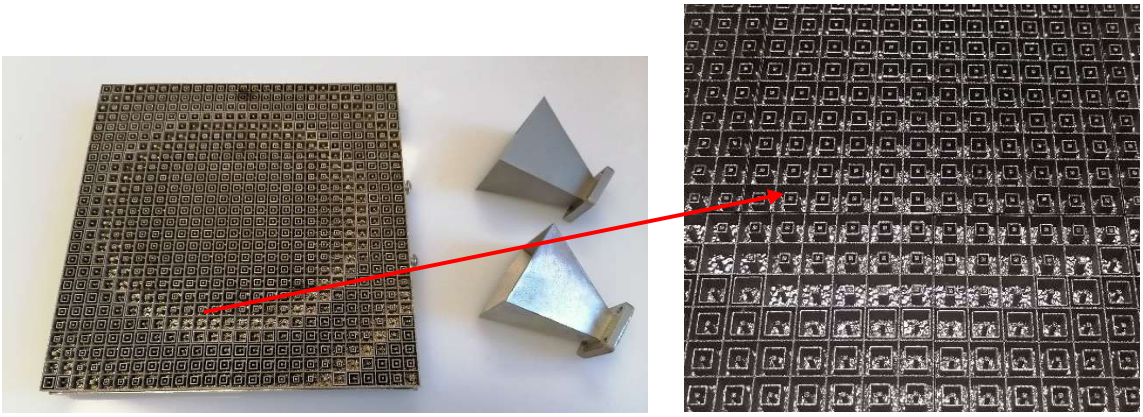

Fig.4.8 The fabricated RA and horn antennas

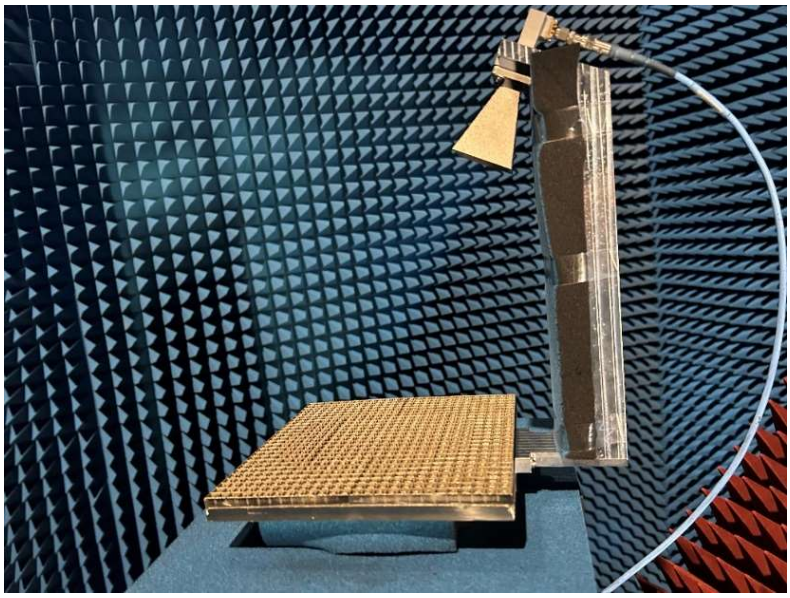

Fig.4.9 Photographs of manufactured MORA and its measurement setup.

The gain response and aperture efficiency are summarized in Fig. 4.10. The gain discrepancy is less than 0.53 dB from 18 GHz to 22 GHz, which is completely acceptable. The measured realized gain at 19.5 GHz is 30.3 dBi with a maximum aperture efficiency of 51.17 %. The measured 1-dB gain bandwidth is 15% (from 19 to 22GHz).

The direction of maximum beam in the target frequency range is tabulated in Table 4.2. The deviation from the desired direction (25°, 270°) is caused by two reasons. The first is the fabrication and assembly, which can directly vary the location of phase center of the feed antenna. The direction of main beam is strongly affected by the phase center. The second is the fabrication of the RA itself, which may produce additional phase errors. However, the deviation is less than 2° demonstrating the feasibility of such an antenna.

In addition, the comparisons of normalized radiation patterns between full wave simulations and measurements are shown in Fig. 4.11. The agreement is globally very good. Higher discrepancy can be seen when theta is greater than 25° due to blockage from the horn antenna and arm. Figures 4.11 b and c show that the measured side lobe and cross-polarization at 20 GHz are about 21.15 dB and 25.20 dB below the main beam respectively. These levels stay lower than 13.57 dB / 24.39 dB in the frequency range from 19 GHz to 22 GHz. The degradation of the side lobe level at 22 GHz (see Fig. 4.11e) is mainly due to the gradual increase in phase error as the frequency moves away from the optimized frequency.

Some existing MORAs are summarized in Table 4.3. Now the measured results of proposed MORA are compared to the ones in Table 4.3. It can be seen that only 3D cells (either metallic blocks [58, 59] or the proposed MORA) can achieve an aperture efficiency higher than 50% while allowing dual-polarization. In addition, the achieved bandwidth is very high compared to all the other published MORAs.

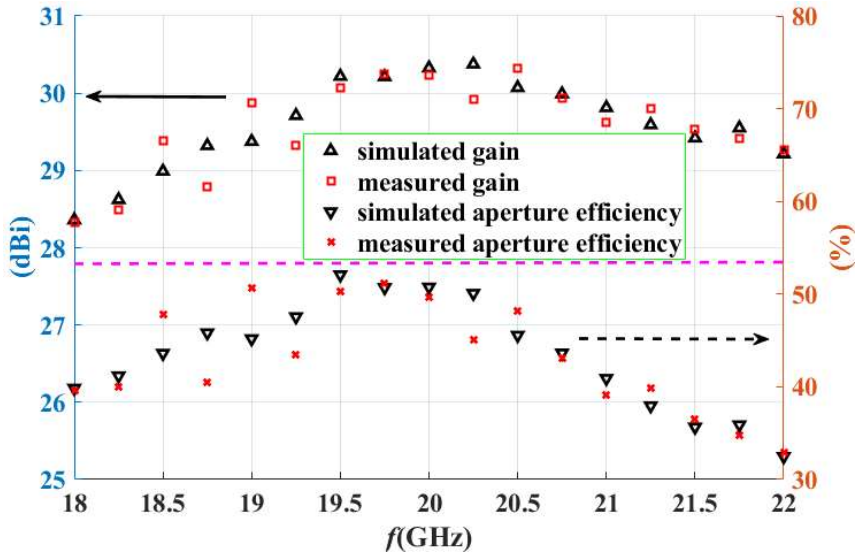

Fig.4.10 Gain response (left) and aperture efficiencies (right)

Table 4.2 Direction of maximum beam.

f (GHz)	18	19	20	21	22
(theta, phi)	(25.88°, 269.80°)	(26.35°, 270.03°)	(26.09°, 270.82°)	(26.18°, 271.44°)	(26.05°, 271.44°)

Table 4.3 Comparison of state-of-the-art MORAs

	Type (2D or 3D)	**Polarization**	**Freq (GHz)**	**Gain (dBi)**	**1-dB Gain Bandwidth (%)**	**3-dB Gain Bandwidth (%)**	**Aperture Efficiency (%)**	**3D printing**
[11]	Sot (2D)	Dual Linear	12.5	32.5	8.3	-	-	No
[12]	Slot (2D)	Single Linear	12.5	33.9	12.8	-	53.8	No
[14]	Slot (2D)	Circular	20	31.4	6.85	10.15	35	No
[18]	Waveguide (3D)	Single linear	75	42.3	-	-	30.2	No
[24]	Waveguide (3D)	Single linear	60	27.9	-	-	40.5	Yes
[25]	Metallic block (3D)	Dual linear	12.2	33.2	-	-	50	No
[26]	Metallic block (3D)	Dual Linear	100	28	-	-	50.1	No
[30]	Metallic block (3D)	Circular	24/32	24.3/24.5	-	10/9.3	38/26	Yes
This work	Waveguide (3D)	Dual linear	20	30.25	15	-	51.17	Yes

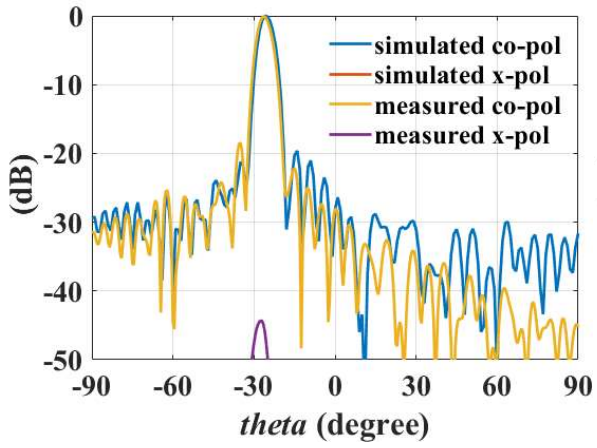
simulated co-pol
simulated x-pol
measured co-pol
measured x-pol
(dB)
theta (degree)

a)

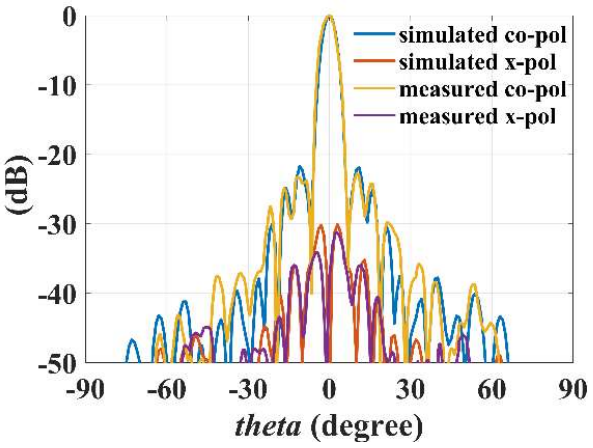
simulated co-pol
simulated x-pol
measured co-pol
measured x-pol
(dB)
theta (degree)

b)

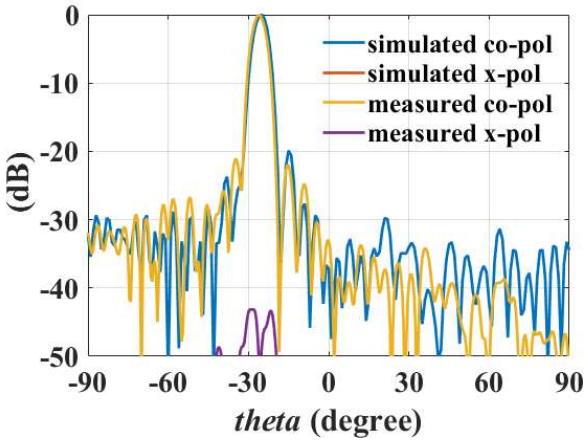
simulated co-pol
simulated x-pol
measured co-pol
measured x-pol
(dB)
theta (degree)

c)

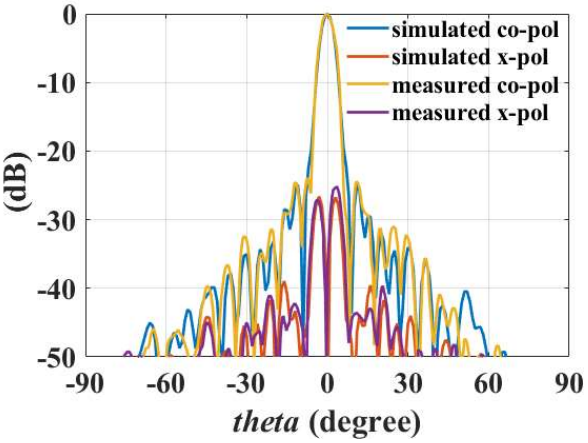
simulated co-pol
simulated x-pol
measured co-pol
measured x-pol
(dB)
theta (degree)

d)

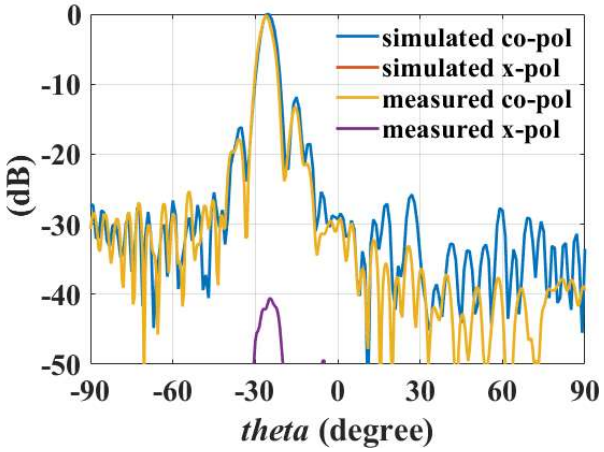
simulated co-pol
simulated x-pol
measured co-pol
measured x-pol
(dB)
theta (degree)

e)

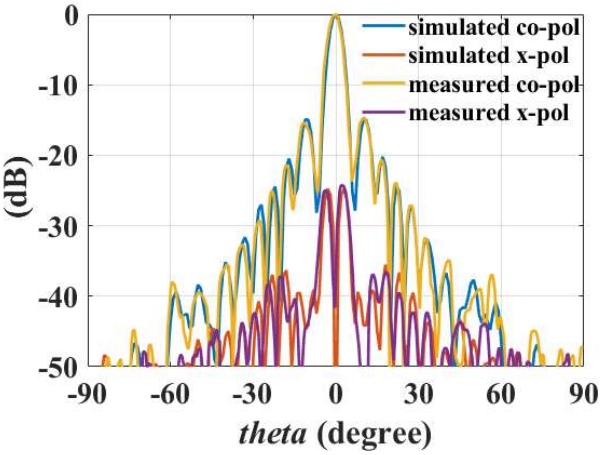
simulated co-pol
simulated x-pol
measured co-pol
measured x-pol
(dB)
theta (degree)

f)

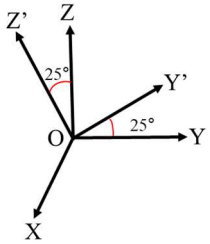
Z'
Z
25°
Y'
O
25°
Y
X

Fig.4.11 Normalized radiation pattern of the designed RA. a) yoz plane (19 GHz). b) xoz' plane (19GHz). c) yoz plane (20 GHz). d) xoz' plane (20 GHz). e) yoz plane (22 GHz). f) xoz' plane (22 GHz)

4.2.3 Conclusion

This section first has introduced the design process of a MORA. It is synthesized using the 3D PCSWs with a fixed height of 6 mm. The synthesis process consists in optimizing the offset phases to minimize the average phase error. The designed MORA is illuminated by a linearly polarized horn antenna. Both the MORA and the horn antenna are fabricated using SLM 3D printing technology. A quite good agreement between the simulations and the measurements is obtained. The achieved maximum gain and maximum aperture efficiency are 30.3dBi and 51.17% respectively. These results validate the design process and demonstrate the potentialities of this structure.

4.3. Transmit-reflect-arrays using 3D phoenix cells

4.3.1 Design process

Two TRAs made of PCOWs (see Fig.2.17) are now designed to validate this configuration of the cell. Both produce a reflected beam at 25° from broadside but they differ by the direction of the transmitted beam. As summarized in Table 4.4, TRA1 produces a transmitted beam that is symmetrical to the reflected one while TRA2 steers the transmitted beam in a different direction and a different plane.

The synthesis process is basically the same as for the RA shown in previous section, except that it now minimizes the total phase error ε, defined as:

$$\varepsilon = \sum_{m=1}^{N_c} I_m\left[|S_{11}^m|\left|\phi_{R,m}^{ach} - \phi_{R,m}^{des}\right| + |S_{21}^m|\left|\phi_{T,m}^{ach} - \phi_{T,m}^{des}\right|\right] \tag{4.2}$$

where index R and T refer to the TA and RA phases respectively while S_{11}^m and S_{21}^m , which have been introduced in section 2.2.2, are the scattering parameters of cell m. Note that, for the sake of simplicity, the optimization is done here for the central frequency only (20 GHz). The distributions of required phase shift over the cells in TRA1 and TRA2 are shown in Fig.4.12.

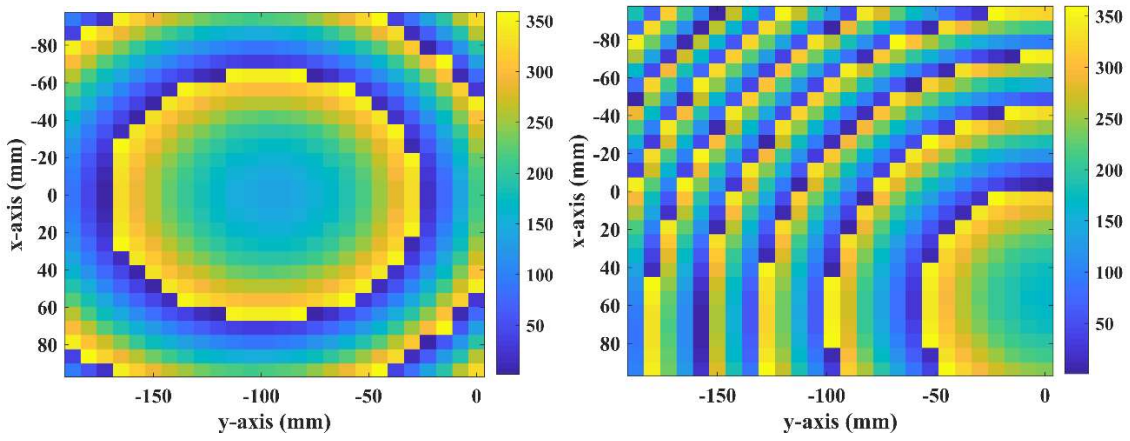

a) b)

Fig.4.12 Distribution of required phase shift over the cells. a) Reflected and transmitted beams in TRA1 and reflected beam in TRA2. b) Transmitted beam in TRA2.

As already pointed out from Fig.2.19, a large h is needed to provide a 360° range for the transmission phase. Consequently, h is now set to 10 mm. Also, the incident wave is now x-polarized to comply with the additional constraint brought by the lateral metallic wall at the middle of the cells.

The simulated database at 20 GHz is given in Fig.4.13. It shows certain cells (typically those with $|S_{11}|$>-2dB) seem best suited for reflection and other ones ($|S_{21}|$>-2dB) for transmission. The remaining ones are neither optimal for reflection nor transmission. Also, the total magnitude ($\sqrt{|S_{11}|^2+|S_{21}|^2}$) in Fig.4.13c shows that the loss is less than 0.2dB, which is completely acceptable. In the end, it must be highlighted that it is the optimization process itself that decides whether a cell is used for TA or RA and this is done automatically by minimizing the weighted phase error as given by (4.2).

Table 4.4 Beams directions of the two TRAs.

	Direction of transmitted beam	*Direction of reflected beam*
TRA1	(155°, 270°)	(25°, 270°)
TRA2	(165°, 0°)	(25°, 270°)

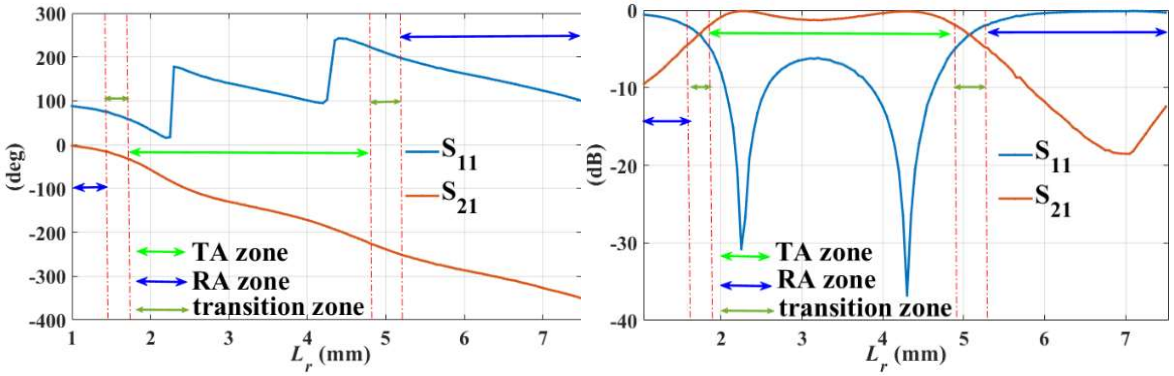

a) b)

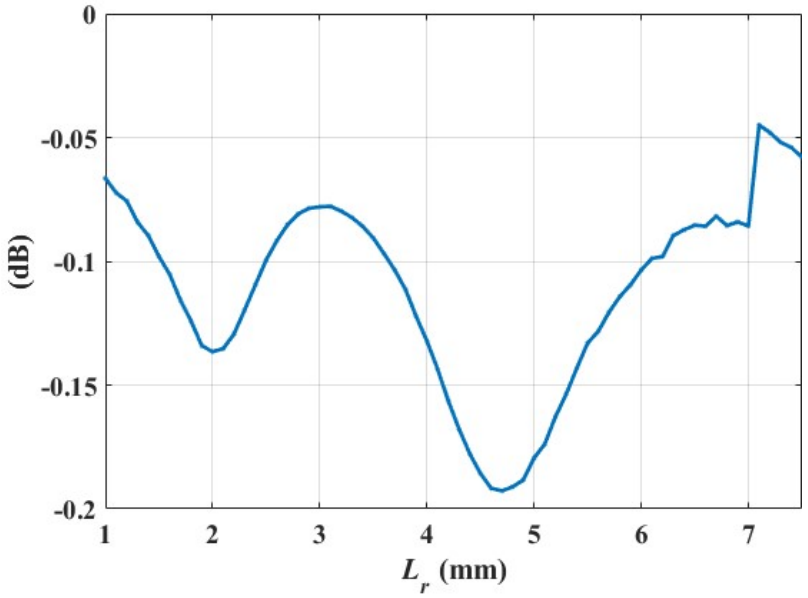

c)

Fig.4.13 The simulated S-parameters of the PCOW (h=10 mm, step=0.05 mm, f=20 GHz, x-polarization, ϕ_{inc}=90°, θ_{inc}=25°). a) Phase. b) Magnitude. c) Total magnitude ($\sqrt{|S_{11}|^2+|S_{21}|^2}$)

As a final figure of merit, the average achieved phase error is defined as:

$$\bar{\varepsilon}=\sum_{m=1}^{N_c} I_m\left[\frac{|S_{11}^m|}{\sum_{m=1}^{N_c} I_m|S_{11}^m|}\left|\phi_{R,m}^{ach}-\phi_{R,m}^{des}\right|+\frac{|S_{21}^m|}{\sum_{m=1}^{N_c} I_m|S_{21}^m|}\left|\phi_{T,m}^{ac}-\phi_{T,m}^{des}\right|\right] \quad (4.3)$$

The achieved average phase errors of both TRAs are 8.76° and 42.11° respectively. Note that, if the directions of both reflected and transmitted beams are symmetrical, the required phases for reflection and transmission are identical. In this case, it is quite easy to select offset phases for reflection (ϕ_R^{off}) and transmission (ϕ_T^{off}) so that each cell almost meets the required phases for both beams simultaneously. Therefore, the total phase error in (4.2) can easily be minimized. As a result, a much lower phase error is obtained for TRA1.

The cell geometries for both TRAs are summarized in Fig.4.14. Since the two beams are symmetrical, a smooth geometrical evolution is achieved in TRA1 (see Fig.4.14a). The distribution of the total magnitude over the cells in both TRAs are shown in Fig.4.15. It can be seen that the loss in both TRAs is less than 0.2dB, which is completely acceptable. Also, the distributions of TA cells and RA cells in the two TRAs are shown in Fig.4.16. The green color, the blue color and the dark green color in Fig.4.16 represent the TA cells, the RA cells and the transition cells respectively. Obviously, the number of TA cells is higher than that of RA cells in both TRAs, which suggests that the performances of TA may be better than that of RA. In addition, Table 4.5 compares the two TRAs in terms of average phase error, number of cells and total weighting coefficient in each operating mode. These results are prepared for the analysis of the performances of designed TRAs in next subsection.

Table 4.5 Comparison between both TRAs.

		AvgError ($\sum_{m=1}^{N_c} \frac{I_m\lvert S_{11}^m\rvert\lvert\phi_{R,m}^{ach}-\phi_{R,m}^{des}\rvert}{\sum_{m=1}^{N_c} I_m\lvert S_{11}^m\rvert}$ or $\sum_{m=1}^{N_c} \frac{I_m\lvert S_{21}^m\rvert\lvert\phi_{T,m}^{ach}-\phi_{T,m}^{des}\rvert}{\sum_{m=1}^{N_c} I_m\lvert S_{21}^m\rvert}$)	Number of cells	Total weighting coefficient ($\sum_{m=1}^{N_c} I_m\lvert S_{21}^m\rvert$ or $\sum_{m=1}^{N_c} I_m\lvert S_{11}^m\rvert$)
TRA1	TA	7.24°	324	0.6968
	RA	1.52°	314	0.6032
TRA2	TA	24.65°	436	0.7587
	RA	17.46°	224	0.4950

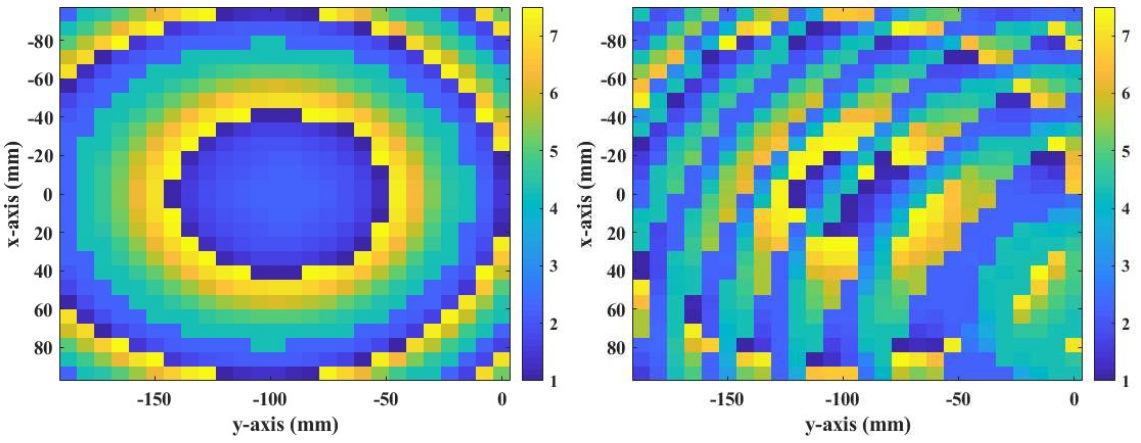

a) b)

Fig.4.14 Variation of the cell geometry over the aperture (L_r in mm). a) TRA1. b) TRA2.

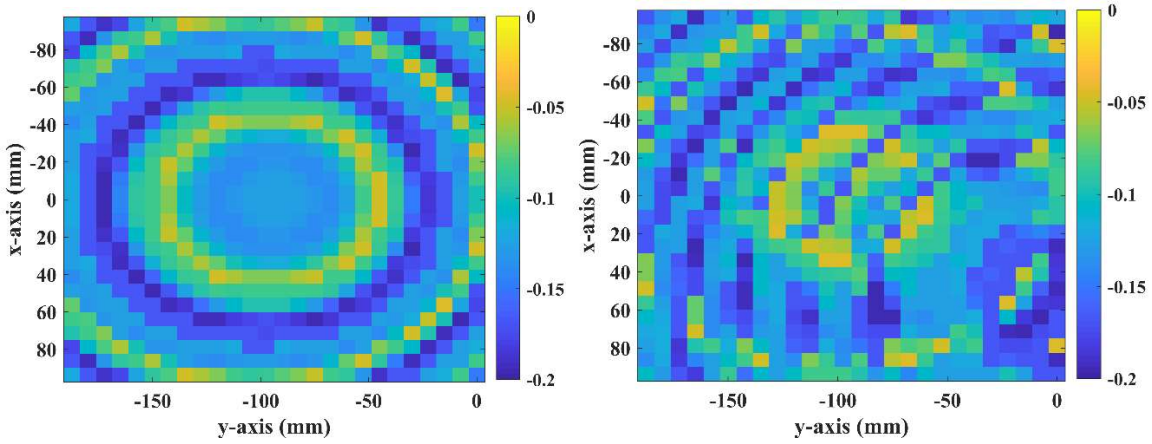

a) b)

Fig.4.15 Total magnitude distribution over the cells. a) TRA1. b) TRA2.

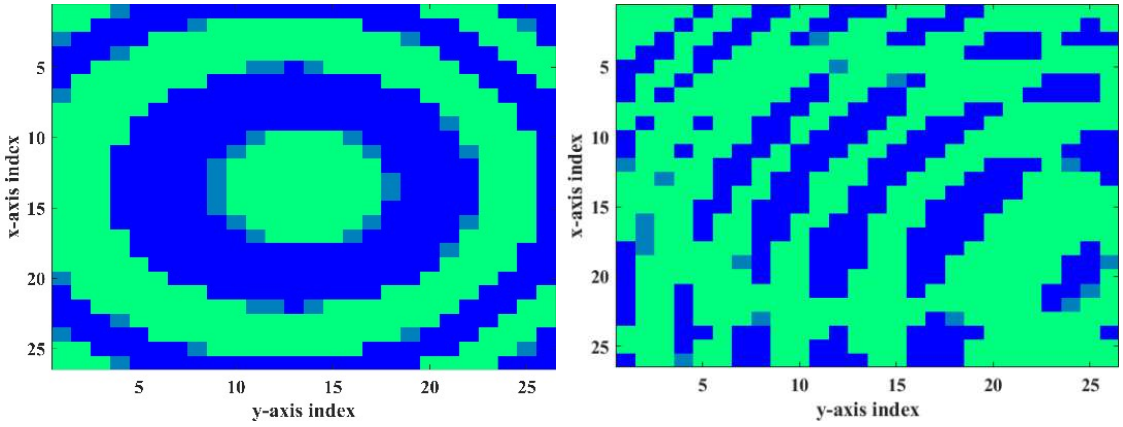

a) b)

Fig.4.16 The distribution of TA cells (green), RA cells (blue) and transition cells (dark green). a) TRA1. b) TRA2.

4.3.2 Performances analysis

The performances of TRA1 are evaluated first. Fig. 4.17 shows TRA1 with the associated radiated field at 20 GHz. It can be seen that both transmitted and reflected beams are produced simultaneously.

The normalized radiation patterns at 20GHz are shown in Fig.4.18. Z' and Z'' indicate the directions of reflected beam and transmitted beam respectively. It can be seen that the beams are produced in the desired directions, which demonstrates the ability of the proposed PC to design TRAs. Also, the level of the reflected beam is just 0.75dB below the one of the transmitted beam, which is consistent with the quite similar characteristics obtained in Table 4.3 regarding the cell numbers and weighting coefficients for both configurations. The side lobe and the cross-polarization levels are lower than -14.3dB and -30.76dB respectively. In addition, the normalized radiation patterns at 19 and 21GHz are shown in Fig.4.19 and 20, respectively. Obviously, the reflected and transmitted beams are always pointing to the desired directions in the given frequency range, which demonstrates the stable performances of the designed TRA. It can be seen from Fig.4.19 that the side lobe and cross polarization at 19GHz are lower than -15.71dB and -26.26dB respectively, which are similar to that at 20GHz. However, the level of the reflected beam gradually decreases with frequency. At 21GHz, it is lower than the transmitted beam by 3.3dB and it is only 7.71dB higher than the side lobe. To fully compare the performances of the two beams, their gains and aperture efficiencies versus frequency are summarized in Fig.4.21. It can be seen that the performances of the transmitted beam are globally better than that of the reflected one. The achieved gain for transmission and reflection at 20GHz is 26.4dBi and 25.7dBi respectively. The corresponding aperture efficiency is 20.55% and 17.29% respectively. The aperture

efficiency of TRA1 is defined as the sum of both reflected beam and transmitted beam. Therefore, the achieved aperture efficiency for TRA1 is 37.84%.

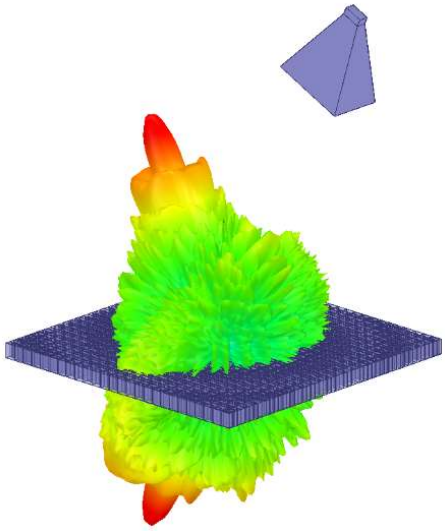

Fig.4.17 TRA1 with symmetrical beams at 20GHz and horn antenna.

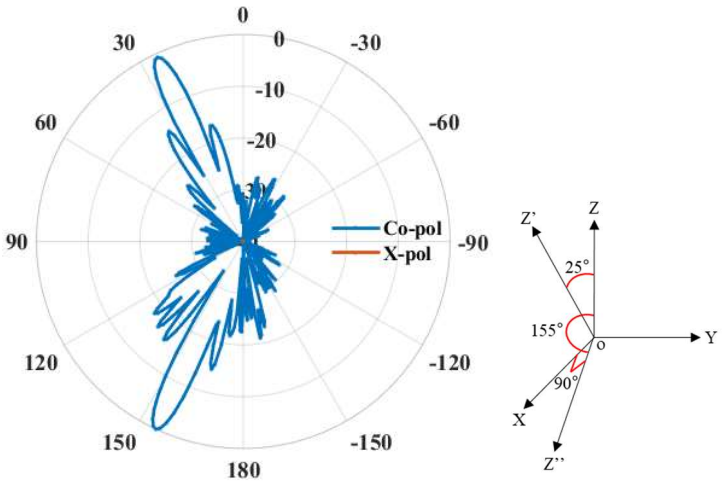

a)

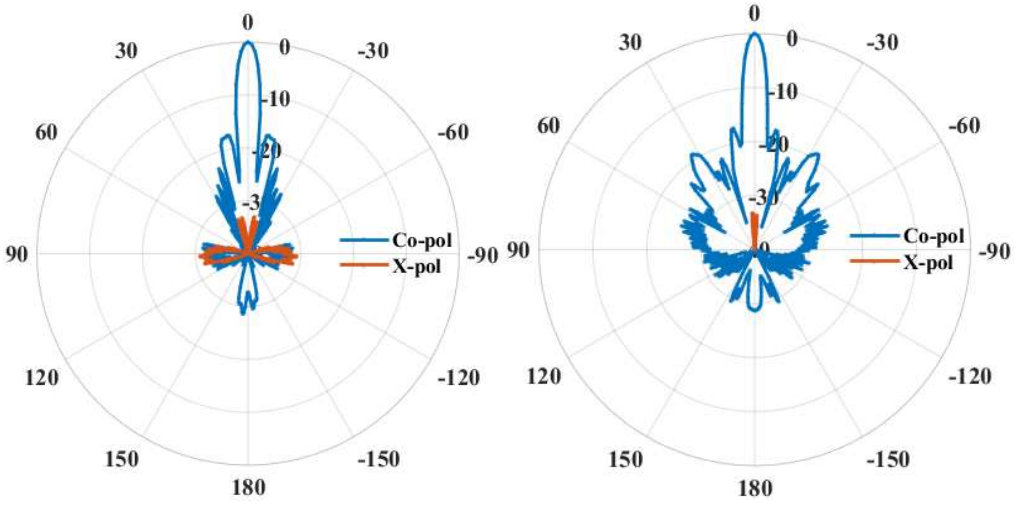

b)

c)

Fig.4.18 Normalized radiation patterns of TRA1 (dB) at 20 GHZ. a) yoz plane. b) xoz’ plane. c) xoz’’ plane.

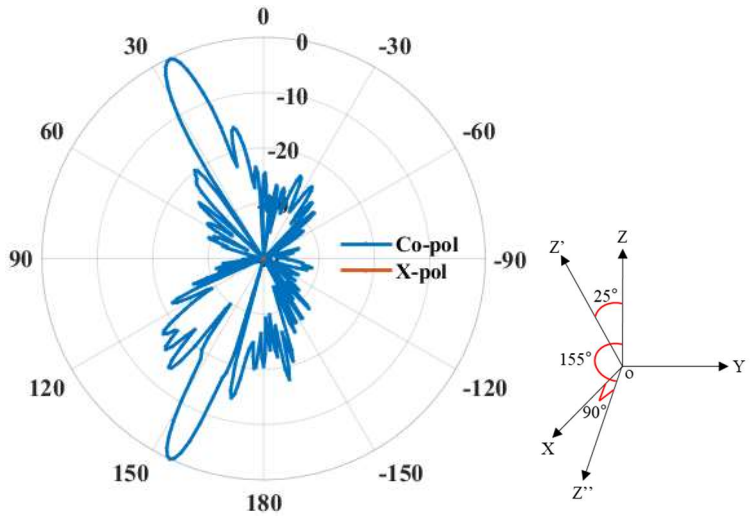

a)

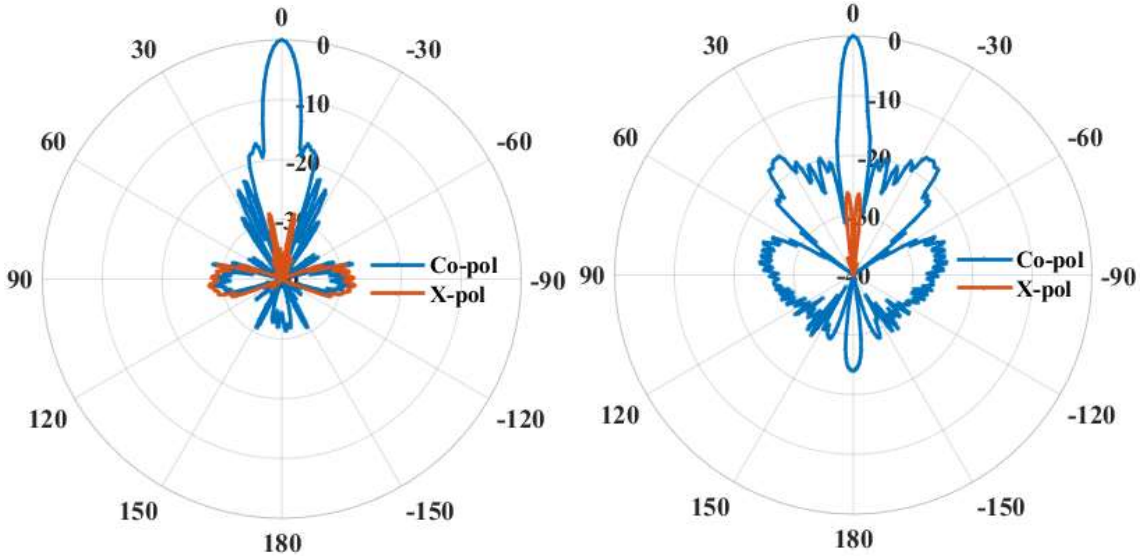

b) c)

Fig.4.19 Normalized radiation patterns of TRA1 (dB) at 19 GHZ. a) yoz plane. b) xoz’ plane. c) xoz’’ plane.

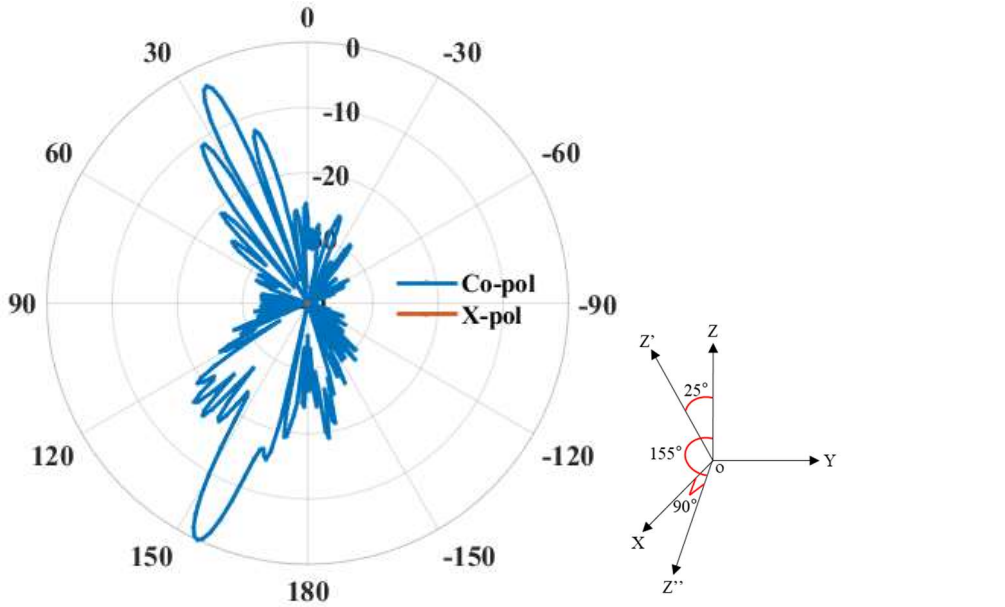

a)

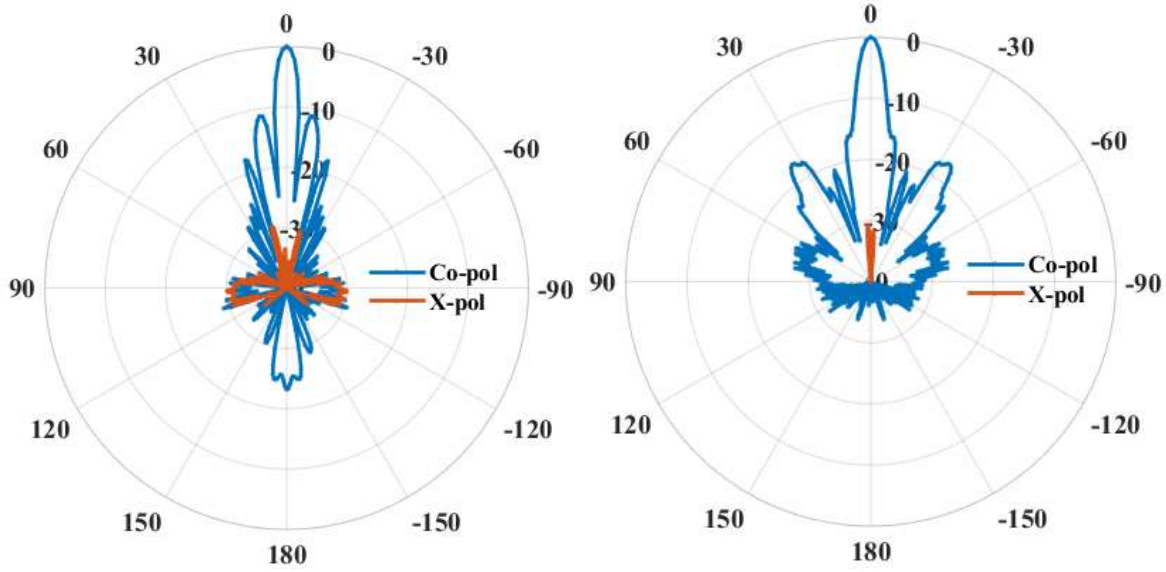

b) c)

Fig.4.20 Normalized radiation patterns of TRA1 (dB) at 21 GHZ. a) yoz plane. b) xoz' plane. c) xoz'' plane.

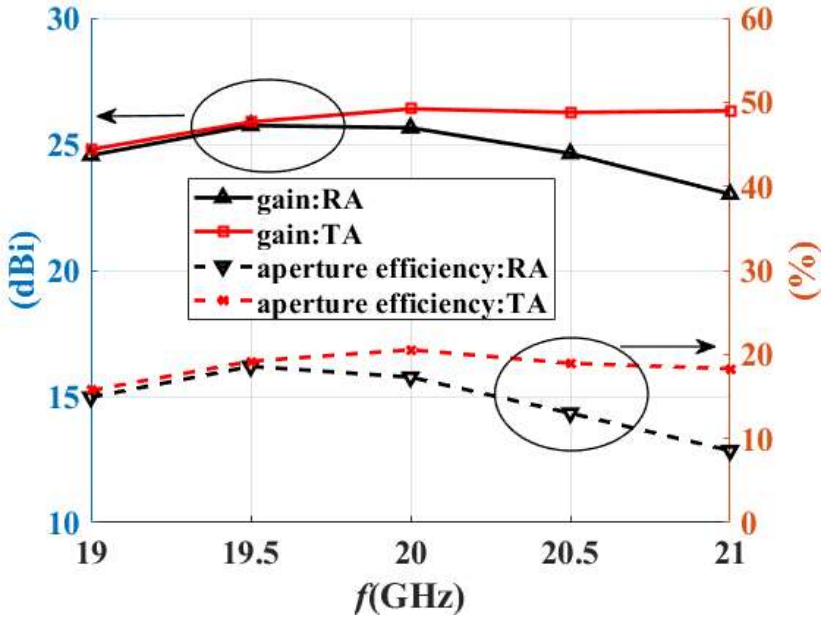

Fig.4.21 Gain and aperture efficiency of TRA1.

Now the performances of TRA2 are analyzed. The normalized radiation patterns at 20, 19 and 21GHz are summarized in Fig.4.22, 23 and 24. It can be seen from Fig.4.22 that the side lobe and the cross-polarization levels at 20GHz are lower than -10.23dB and -28.09dB respectively. Also, the side lobe level is -12.05dB at 19GHz (see Fig.4.23). However, as the frequency increases, the side lobe level degrades to -7.2dB at 21GHz (see Fig.4.24). The gains and aperture efficiencies versus frequency of both beams in TRA2 are summarized in Fig.4.25 to further compare their performances. As for TRA1, the transmitted beam in TRA2 is globally better than the reflected beam. The gain difference between the two beams is about 3dB, which is consistent with the double number of cells used for transmission (see Table 4.4). The achieved gains for transmission and reflection at 20GHz are 26.1 dBi and 23.1 dBi respectively (see Fig.4.25). The corresponding total aperture efficiency is 28.53%. The achieved aperture efficiency of TRA2 is reduced compared to TRA1, which is due to the significant increase in average phase error (see Table. 4.4).

As a summary, the proposed PCOW is more suitable for an application that requires two symmetrical beams. The achieved aperture efficiency of TRA1 is 8.84% higher than that in [71] and 16.84% higher than that in [64]. The performances of the proposed TRAs in this thesis can be further improved by optimizing the structure of PCOW to increase its phase range of reflection coefficient.

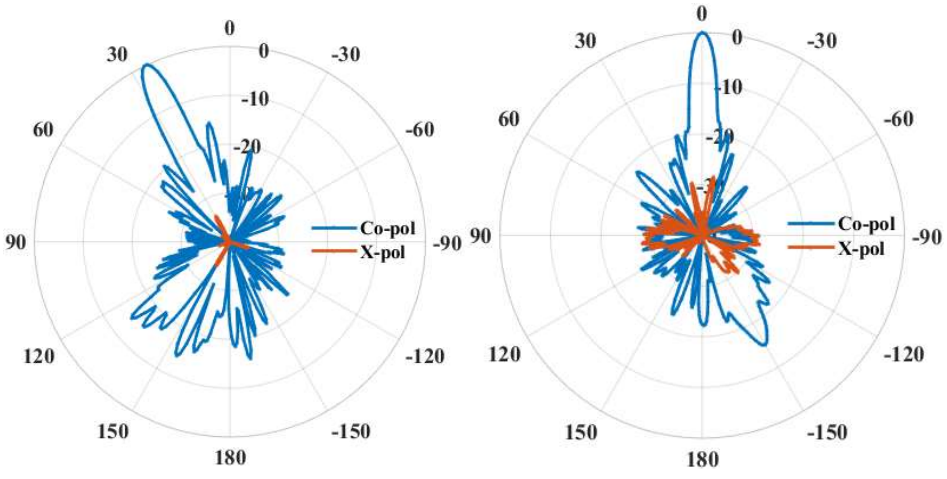

a) b)

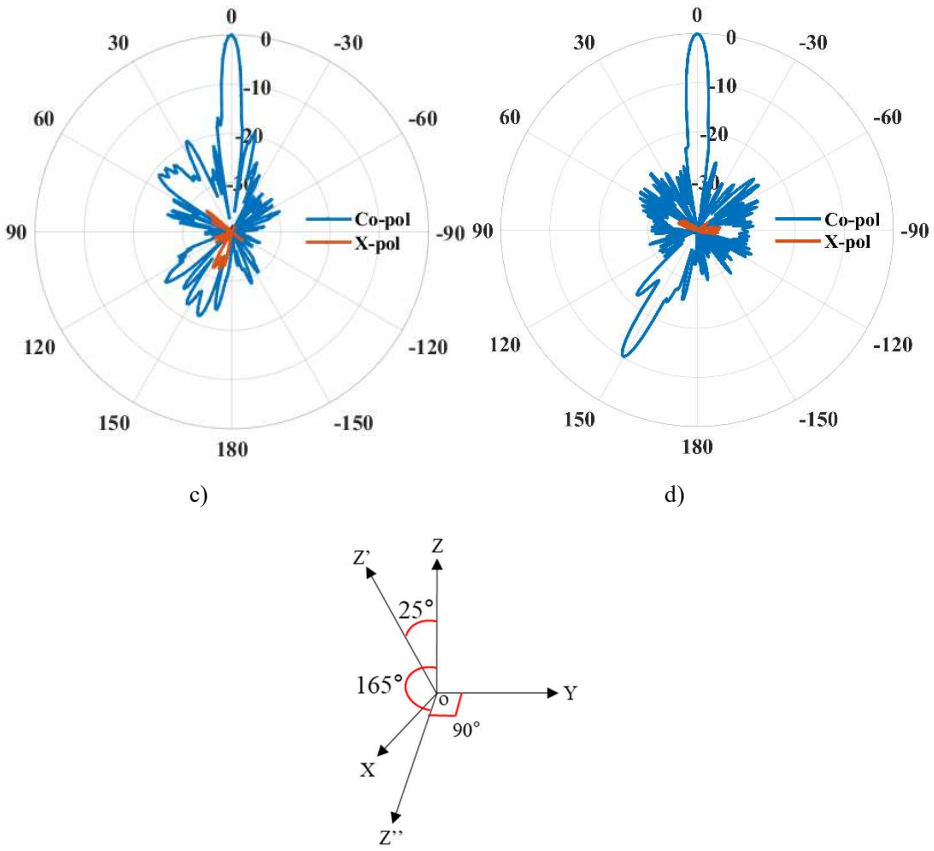

Fig.4.22 Normalized radiation patterns of TRA2 (dB) at 20 GHz - a) yoz plane (reflected beam). b) xoz' plane (reflected beam). c) yoz'' plane (transmitted beam). d) xoz'' plane (transmitted beam)

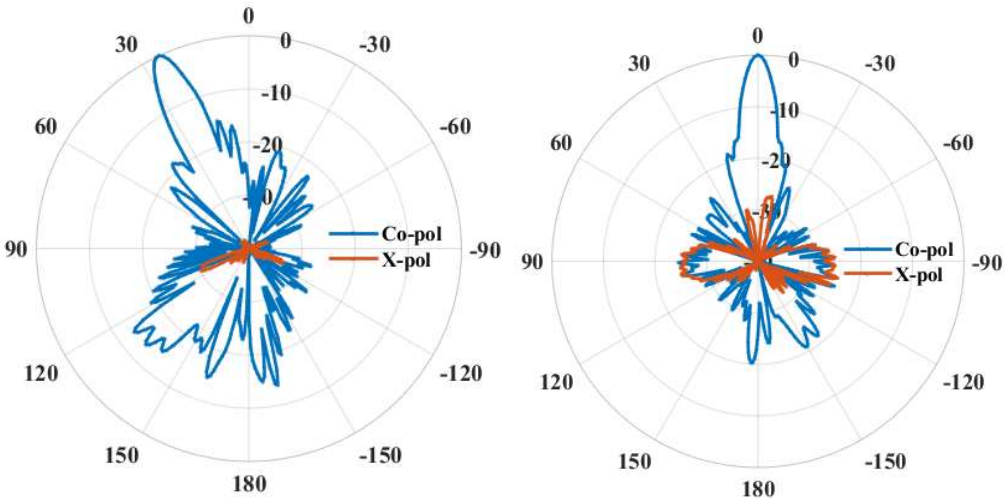

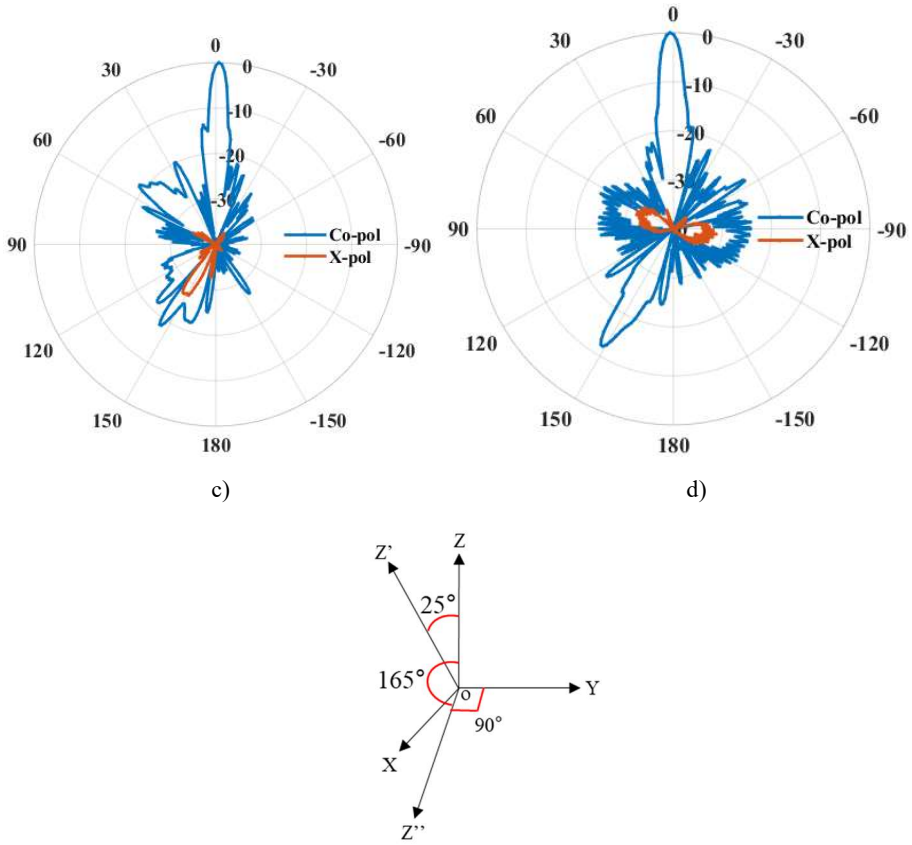

Fig.4.23 Normalized radiation patterns of TRA2 (dB) at 19 GHz - a) yoz plane (reflected beam). b) xoz' plane (reflected beam). c) yoz'' plane (transmitted beam). d) xoz'' plane (transmitted beam)

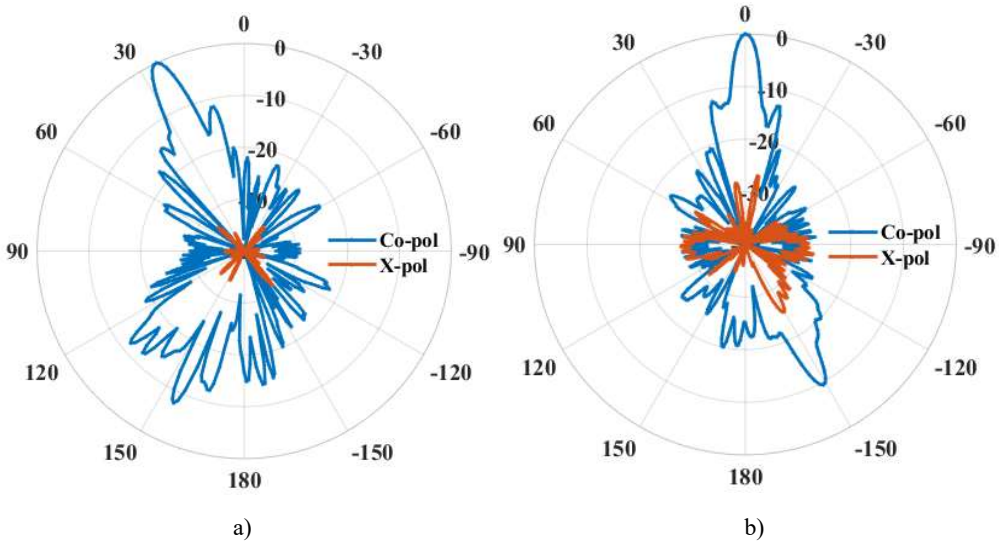

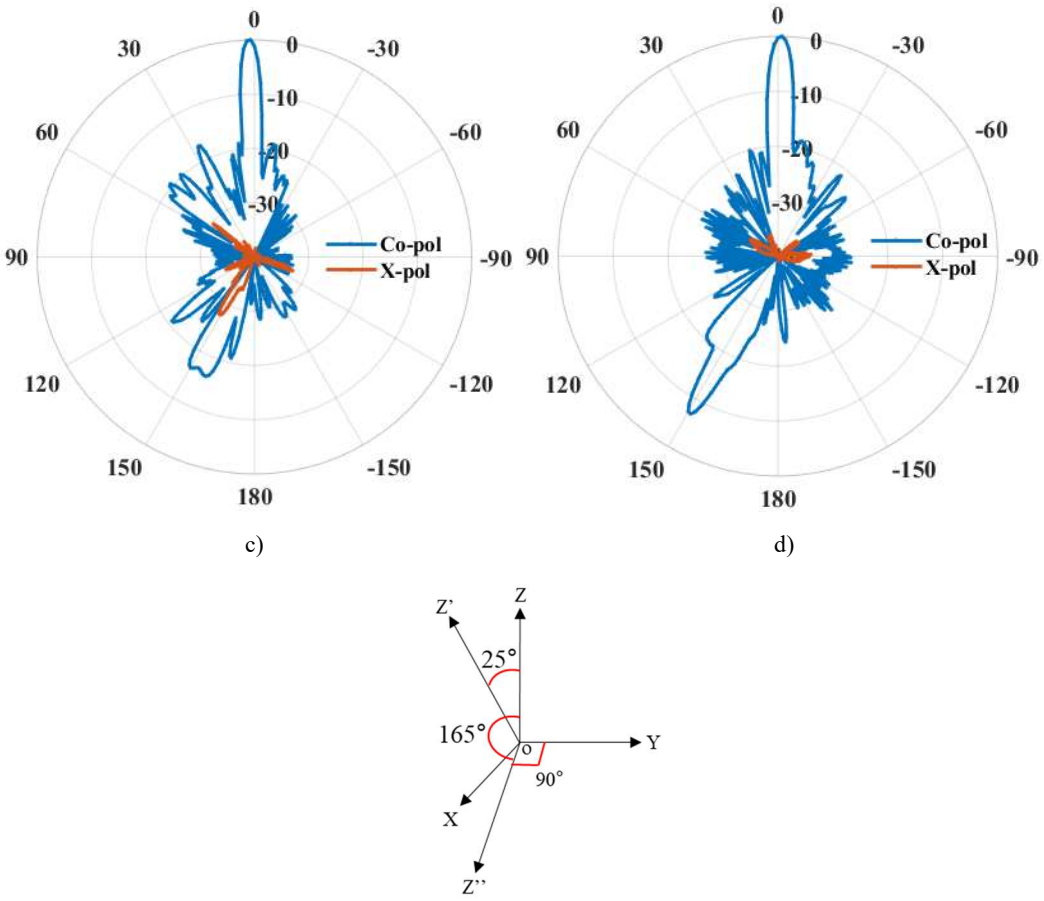

Fig.4.24 Normalized radiation patterns of TRA2 (dB) at 21 GHz - a) yoz plane (reflected beam). b) xoz' plane (reflected beam). c) yoz'' plane (transmitted beam). d) xoz'' plane (transmitted beam)

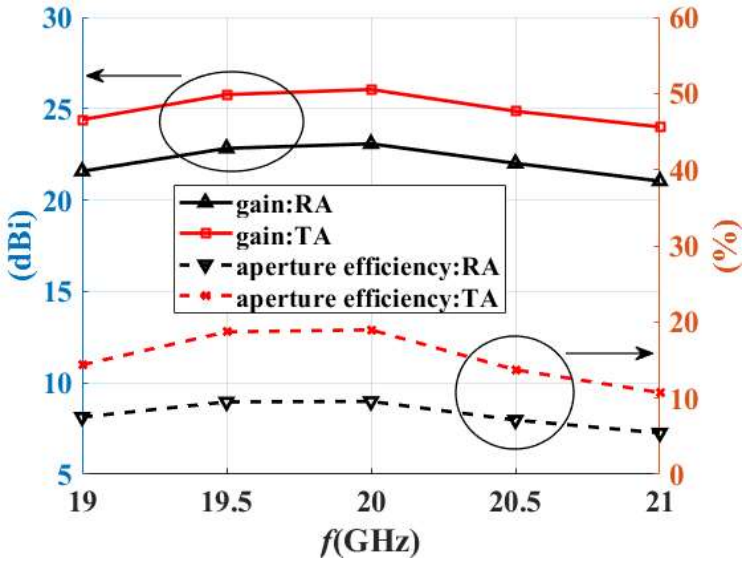

Fig.4.25 Gain and aperture efficiency of TRA2.

4.3.3 Conclusion

In this section, two MOTRAs made of PCOWs are designed and simulated. They are synthesized by minimizing the total phase error. Simulation results show that they have the ability to produce both transmitted and reflected beams simultaneously. When the directions of both beams are symmetrical,

their performances are similar. When the directions of both beams are asymmetrical, the performance of the reflected beam is significantly degraded. The degradation is the results of the large increase in average phase error. These two MOTRAs fully demonstrate the performance of the proposed 3D MO PCOW.

4.4 Bandwidth enhancement of metal-only reflectarray antenna

4.4.1 Database

In section 4.2, a MORA is designed using PCSWs (see Fig.2.12 and Fig.2.15) with a fixed height of 6 mm. This section aims at improving the performance of this MORA by exploiting another degree of freedom in the 3D PCSW, namely its height. More generally speaking, this section offers a detailed analysis of the effect of the height of the 3D PCSW on the performance of MORAs.

Five RAs (RA1, RA2, RA3, RA4 and RA5) are designed in this section. The design process of RAs in this section is the same as that in section 4.2.1 where the phase offsets at 19.5 GHz and 20.5 GHz are optimized during the synthesis process to minimize the average phase error. The only difference is the used database.

Table 4.6 summarizes the detailed parameters of the 3D PCSW used in this section. Since the antennas in this section will not be fabricated, the used thickness of inner wall (w_{in}) is not increased to 0.3mm, just to verify the proposed optimization method from simulation results. The simulated S-parameters are shown in Fig.4.26. The results once again prove the conclusion in section 2.4 that losses are higher around the resonant area (white curve in Fig.4.26a and b). Note that the cells with a loss greater than 1dB are filtered out before the synthesis process of MORAs.

Table 4.6 Detailed parameters of the 3D PCSW

Parameter	L_c	L_r (step 0.1)	L_p	h (step 0.1)	w_{in}	w_{ex}
Value(mm)	7.5	1-7.5	1	4-10	0.2	0.2

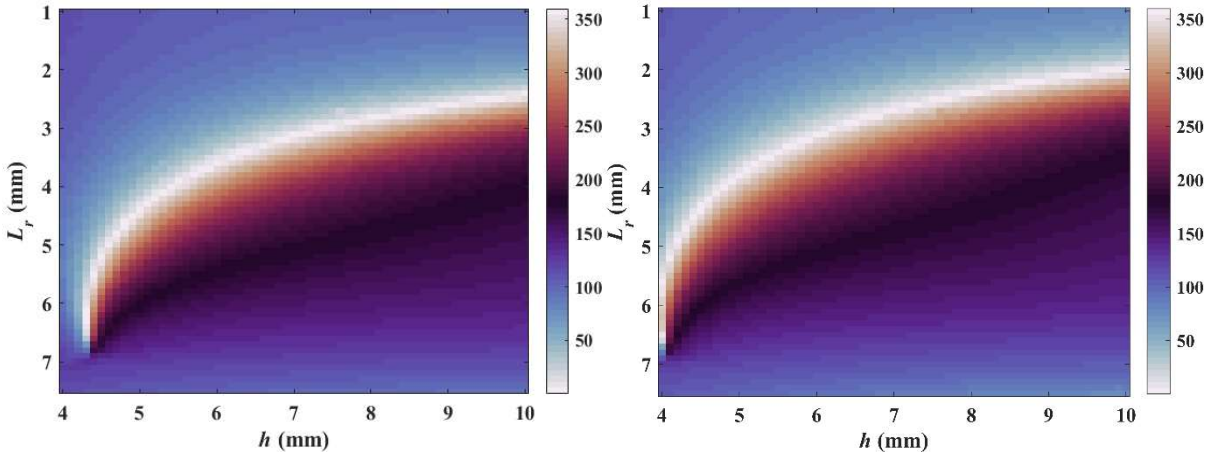

a) b)

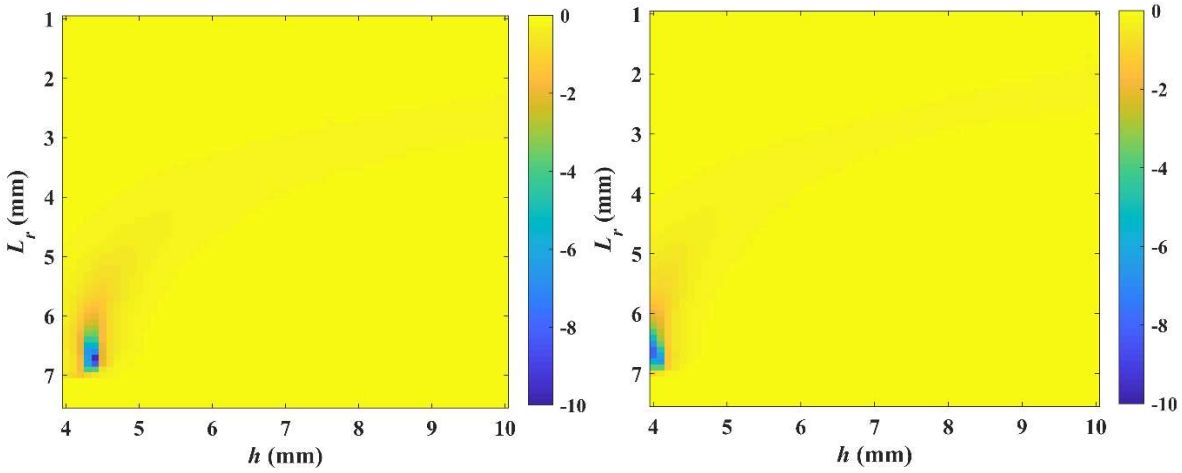

Fig.4.26 S-parameters of the PCSW (x-polarization, ϕ_{inc}=90°, θ_{inc}=25°). a) Phase (S_{11}) at 19.5GHz. b) Phase (S_{11}) at 20.5GHz. c) Mag (S_{11}) at 19.5GHz. d) Mag (S_{11}) at 20.5GHz.

4.4.2 Initial design approach and analysis

Firstly, two different RAs are designed. The first RA (RA1) has a fixed height (h=6 mm) while the second one (RA2) is designed using PCSWs with a variable height ($h\in$ [4, 10] mm). The detailed parameters of these two RAs are tabulated in Table 4.6. Fig.4.27 depicts the gain versus frequency in the direction of maximum radiation.

Table 4.7 shows that the average phase error of RA2 is much smaller than that of RA1 at both frequencies which demonstrates the ability to better control the phase thanks to this second degree of freedom. However, it can also be seen from Fig.4.27 that the gain of RA2 is lower than that of RA1 except for a few frequency points. This dysfunction of the design process can be understood by analysing the variation of the cell geometry in both RAs. To do so, Fig.4.28a presents the optimized values of L_r for RA1 while Fig.4.28b and c show that of L_r and h in RA2. It appears that the introduction of a new degree of freedom (h) resulted in a more chaotic distribution of the successive geometries. This is particularly visible in Fig.4.28c where isolated cells with large h (yellow dots) can be observed within the panel. Such abrupt variations in the geometry between two adjacent cells in RA2 may decrease the accuracy of the phase predictions, and subsequently result in a gain drop and a bandwidth reduction. Also, Fig.4.29 summarizes the magnitude distributions at 19.5GHz and 20.5GHz. It can be seen from Fig.4.29a, b, c, and d that the loss in RA2 is obviously higher than that in RA1, which further explains the gain drop in RA2. To better characterize the loss of each RA in this section, the average loss is calculated using the following equation:

$$avg\_loss = -dB\left(\frac{I_{low}\cdot M_{low}+I_{up}\cdot M_{up}}{2}\right) \tag{4.4}$$

where I_{low} and I_{up} are the matrices of normalized illumination intensity over the RA cells at 19.5 and 20.5GHz (see Fig.4.4), respectively. M_{low} and M_{up} are the matrices of achieved magnitude over the RA cells at 19.5 and 20.5GHz (see Fig.4.29). It can be seen from table 4.5 that the average loss of RA2 is 0.25dB higher than that of RA1.

4.4.3 Improved design approach and analysis

The previous subsection shows that reducing the phase error is not sufficient to enhance the antenna performance. Preserving a smooth geometry evolution in the array remains an imperative factor. This section aims to expand the design process, in order to fully benefit from the capability of the 3D PCSW

with variable height to improve the bandwidth of the RA. The idea relies in finding a method that permits to reduce the average phase error while preserving this smooth geometry variation.

In order to reduce the difference in the geometry between two adjacent cells, a predefined limitation is added to the process to design a RA. There are two variables for each cell: L_r and h. Since a smooth L_r distribution can easily be obtained (as shown in Fig.4.28a for RA1), the improvement of the design process focuses on the height h of the cells. More precisely, it is proposed to limit the variation in the value of h between two adjacent cells. The maximum difference between two such cells (dh) is adjusted to find a better balance between the average phase error and the smoothness of the cell geometries over the RA. In this process, L_r and h are derived successively. Also, since the cells in the center have stronger illumination intensity, the geometry of these cells is determined first. Fig.4.30 shows the order of selection. It travels a spiral path from the center to the outside of RA. As a consequence, for any two adjacent cells, the difference of h is no more than the predefined dh.

In order to verify the aforementioned optimization process, three additional RAs (RA3, RA4, RA5) are designed. They differ by the used value of dh (0.5, 1 and 1.5 mm respectively). It can be seen from Table 4.7 that the average phase error decreases with the increases of dh, which is consistent with the fact free variations in h provide an additional degree of freedom to reduce the error. It can be seen from Fig.4.17 that there is no obvious change in gain between RA1 (fixed height) and RA3 (when dh is equal to 0.5 mm). On the contrary, when dh is increased more significantly (typically for RA4 and RA5), the performance is much better. For instance, the 1-dB bandwidth is increased from 15% (RA1) to 18% (RA5 where dh is equal to 1.5 mm), although the average loss is increased by 0.01dB (see Table 4.7). At the same time, the gain of RA5 has also been significantly improved compared with RA2 (variable height with no dh limitations). These results confirm the cell height h is an interesting additional degree of freedom, but its variations have to be limited in order to prevent from a chaotic cell distribution in the aperture. A good trade-off has to be found between cell regularity and achieved phase error. The proposed optimization process is a possible solution to reach such a compromise.

Table 4.7 Average phase error and average loss versus h and dh for the five RAs

	dh **(mm)**	***h*** **(mm)**	**average phase error (°)**	**Average loss (dB)**
RA1	---	6	15.26	0.1505
RA2	---	4-10	8.05	0.2750
RA3	0.5	4-10	14.60	0.1532
RA4	1	4-10	14.59	0.1575
RA5	1.5	4-10	14.55	0.1617

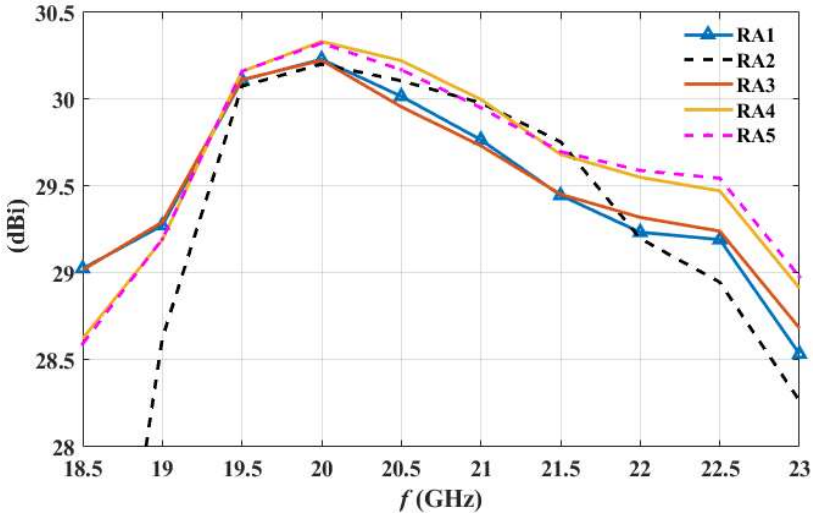

Fig.4.27 The gain versus frequency of five RAs.

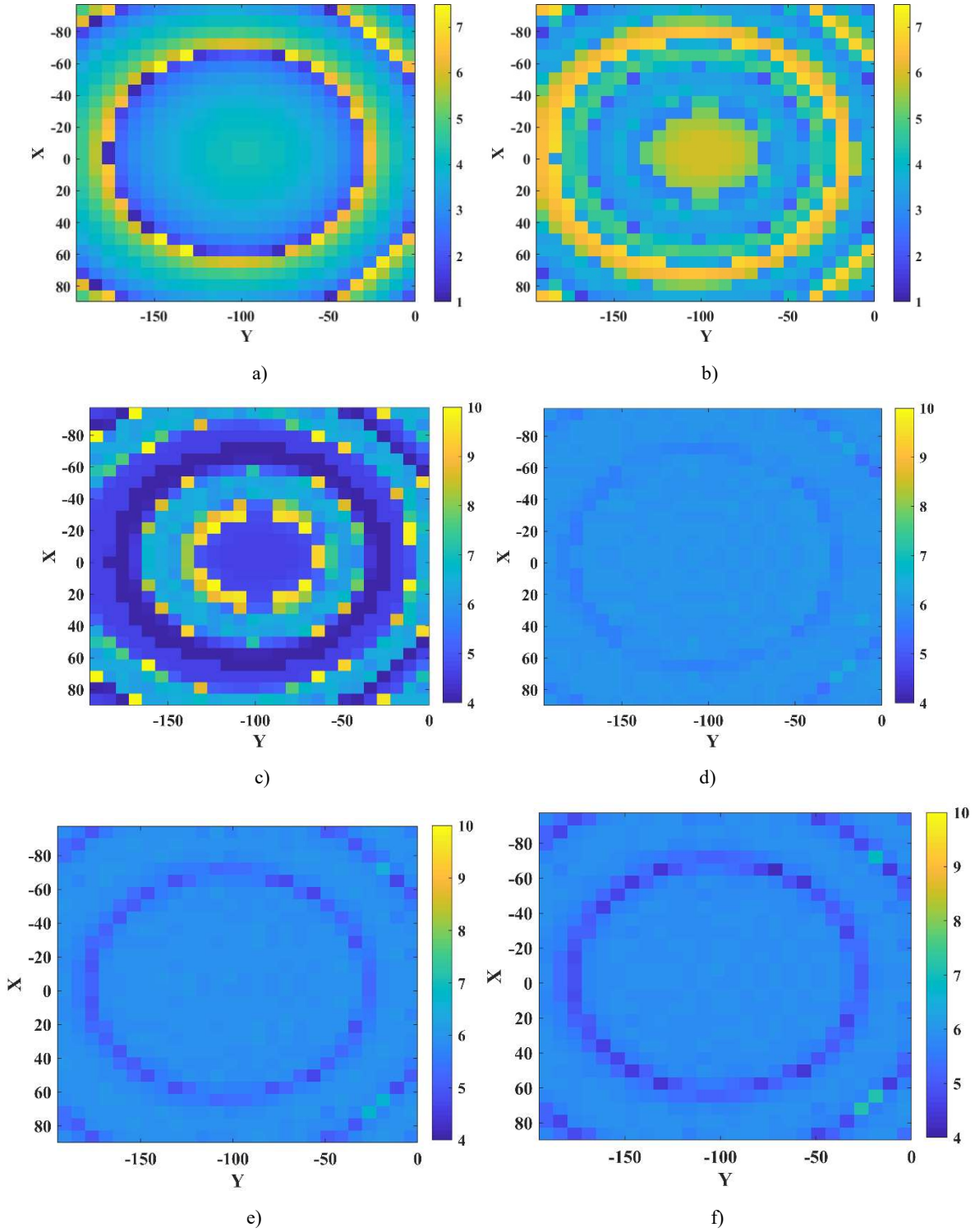

Fig.4.28 Cell geometry of five RAs. a) L_r of RA1. b) L_r of RA2. c) h of RA2. d) h of RA3 e) h of RA4 f) h of RA5

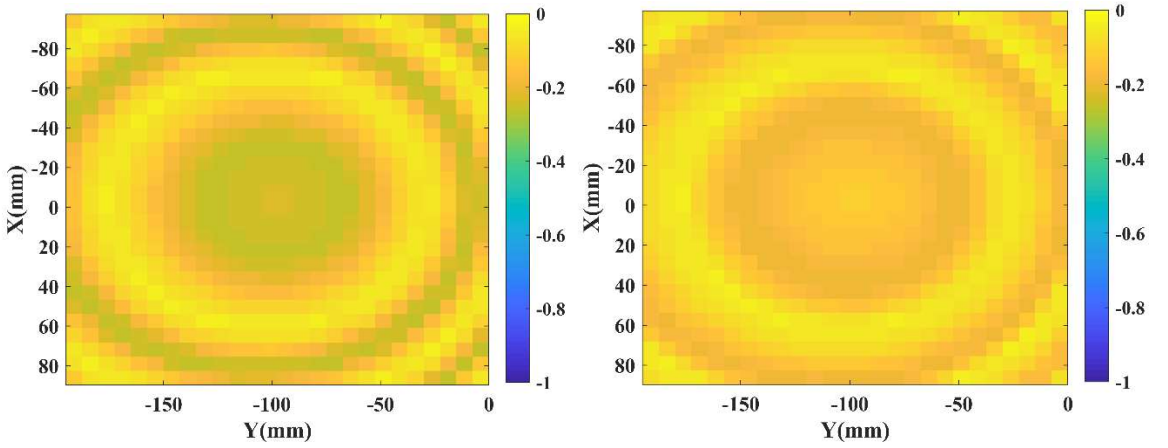
X(mm)
Y(mm)
-80
-60
-40
-20
0
20
40
60
80
-150
-100
-50
0
-0.2
-0.4
-0.6
-0.8
-1

a) b)

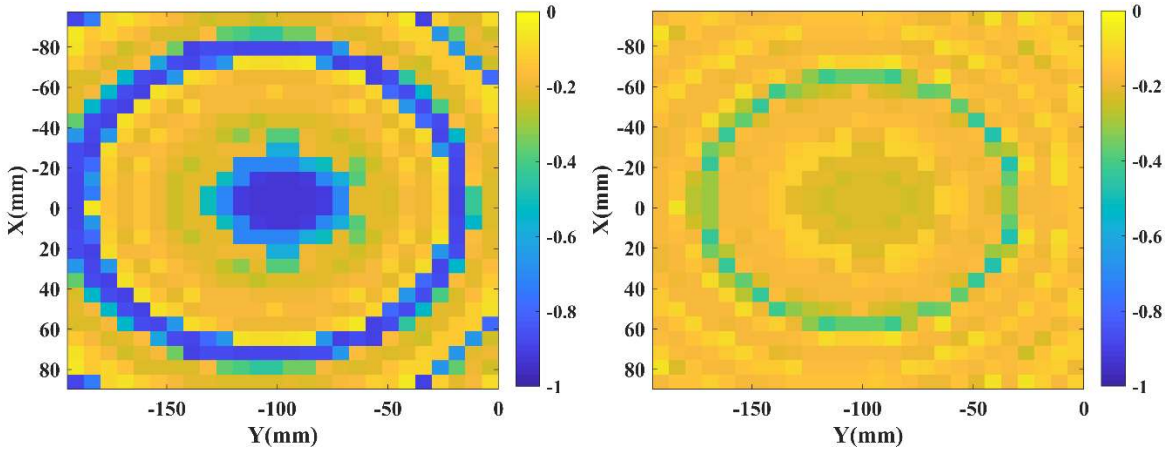
X(mm)
Y(mm)
-80
-60
-40
-20
0
20
40
60
80
-150
-100
-50
0
-0.2
-0.4
-0.6
-0.8
-1

c) d)

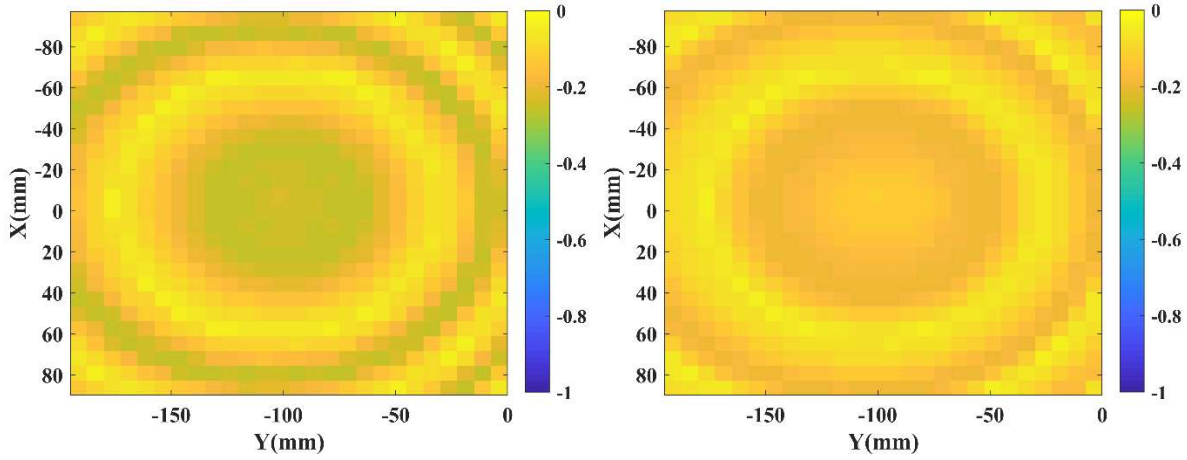
X(mm)
Y(mm)
-80
-60
-40
-20
0
20
40
60
80
-150
-100
-50
0
-0.2
-0.4
-0.6
-0.8
-1

e) f)

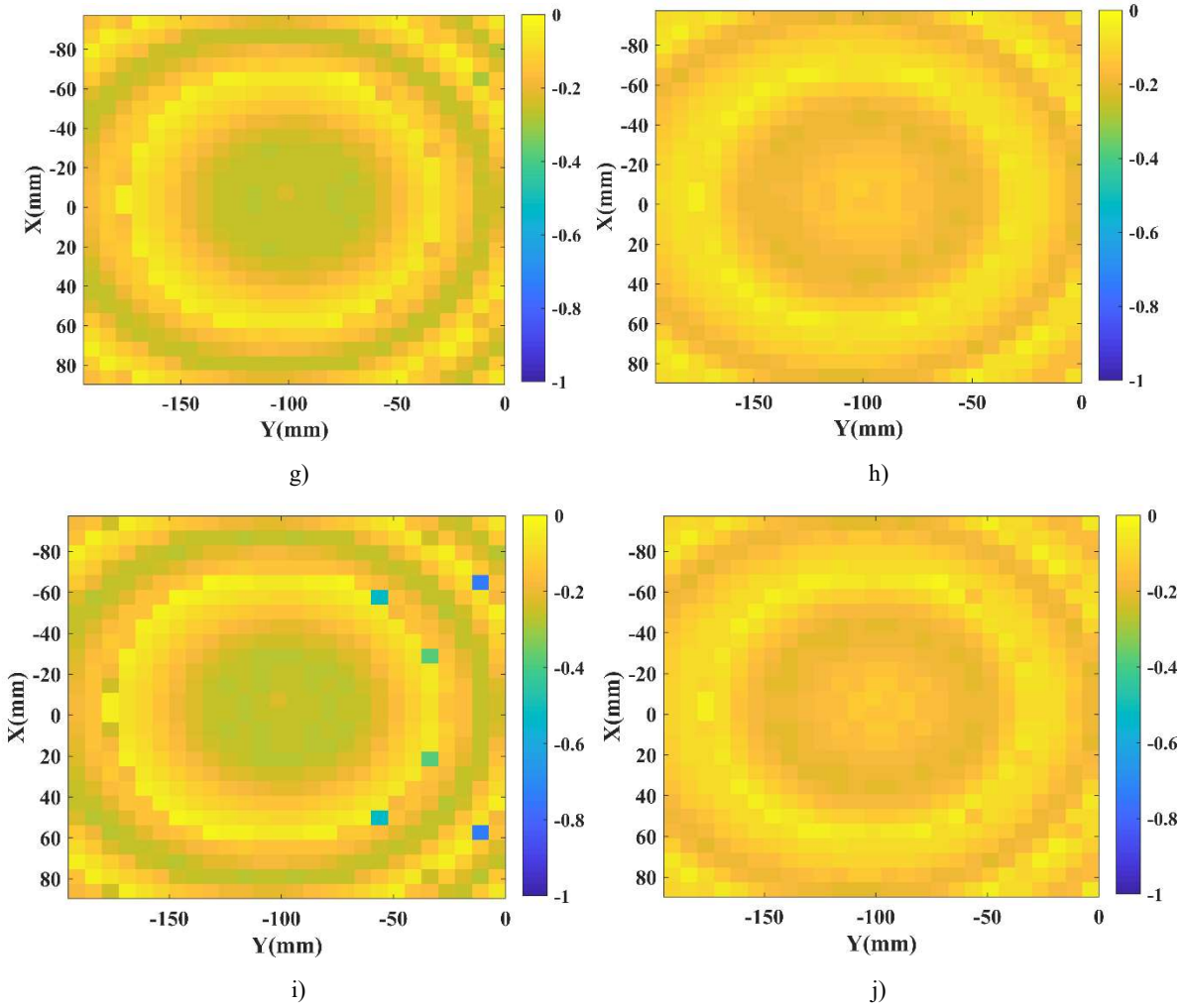

Fig.4.29 Magnitude distribution over the cells (dB). a) RA1 at 19.5GHz. b) RA1 at 20.5GHz. c) RA2 at 19.5GHz. d) RA2 at 20.5GHz. e) RA3 at 19.5GHz. f) RA3 at 20.5GHz. g) RA4 at 19.5GHz. h) RA4 at 20.5GHz. i) RA5 at 19.5GHz. j) RA5 at 20.5GHz.

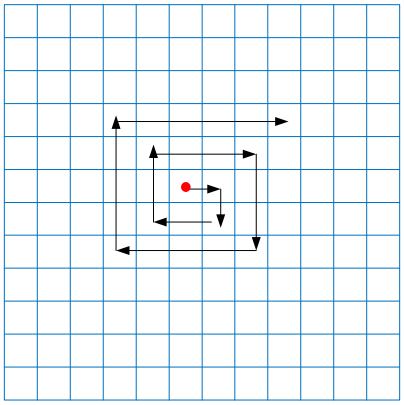

Fig.4.30 The order of selection.

4.4.4 Conclusion

In this section, five different RAs are designed to investigate the effect of the height of the 3D PC on the performance of MORAs. Simulation results show that the gain of MORAs can be optimized by selecting an appropriate height for each cell, provided that geometric variations between adjacent cells are limited. A design methodology is proposed and validated by improving the bandwidth from 15 to 18%.

4.5 Conclusion

This chapter demonstrated the capability of the proposed 3D PC to design MORA and MOTRA. First, a MORA made of PCSWs was designed by minimizing the average phase error. It was fabricated using SLM 3D printing technology and measured. A quite good agreement between the simulations and measurements is achieved. The achieved maximum gain and maximum aperture efficiency are 30.3dBi and 51.17% respectively. Then, two MOTRAs made of PCOWs are designed and simulated. They are synthesized by minimizing the total phase error. Simulation results show that they have the ability to produce both transmitted and reflected beams simultaneously. Finally, five different MORAs were designed to investigate the effect of the height of the 3D PC on the performance of MORAs. Simulation results show that the gain of MORAs can be optimized by selecting an appropriate height for each cell, provided that geometric variations between adjacent cells are limited. A design methodology is proposed and validated. It improves the bandwidth from 15% to 18%.

Chapter 5 - Dual Band and Dual Beam Antennas made of Modified Phoenix Cells

5.1 Introduction 148

5.2 Dual band metal-only reflectarray antenna 149

5.2.1 Cell analysis 149
5.2.2 Horn antenna design 151
5.2.3 Dual band reflectarray antenna design and analysis 153
5.2.4 Performances evaluation 155
5.2.5 Conclusion 158

5.3 Dual beam metal-only reflectarray antenna 159

5.3.1 Cells Description 159
5.3.2 Cells performances 159
5.3.3 Antenna synthesis and analysis 160
5.3.4 Conclusion 164

5.4 Conclusion 164

Chapter 5 - Dual Band and Dual Beam Antennas made of Modified Phoenix Cells

5.1 Introduction

Last chapter validated the two main operating modes of the 3D PC and provided an experimental validation. This chapter tries to further explore the capabilities of this cell by investigating additional degrees of freedom or slightly modified topologies. More precisely, two new versions of the 3D PCSW are discussed, leading to two new RA designs.

Firstly, it can be known from section 2.2 that the 3D PC consists of two imbricated waveguides. In all the previous designs, the heights of both waveguides are identical. However, if we tune them independently, another degree of freedom is obtained to control the reflection phase. This is what is done in section 5.2 where a dual band antenna (20/25GHz) is designed by taking advantage of the two available waveguide heights. Secondly, section 5.3 proposes a modified topology to control both linear polarizations separately. As an application, a RA that generates two different beams with orthogonal linear polarizations at 25GHz is designed. Finally, a conclusion is drawn.

Due to the lack of time, only simulations are carried out in this chapter. The (maximum) center frequency of all antennas in this chapter is 25GHz. As shown in Fig.5.1, the radiating aperture is $15\lambda_0 \times 15\lambda_0$ (λ_0 being the free space wavelength at 25GHz) with an element spacing of $0.5\lambda_0$. All the antennas and cells are supposed made of stainless steel with a conductivity of 1.33×10^6 S/m and simulated in HFSS®. The illumination is achieved by a linearly polarized horn antenna with an offset angle of 15° with respect to the normal of the panel. The f/D ratio is 1.

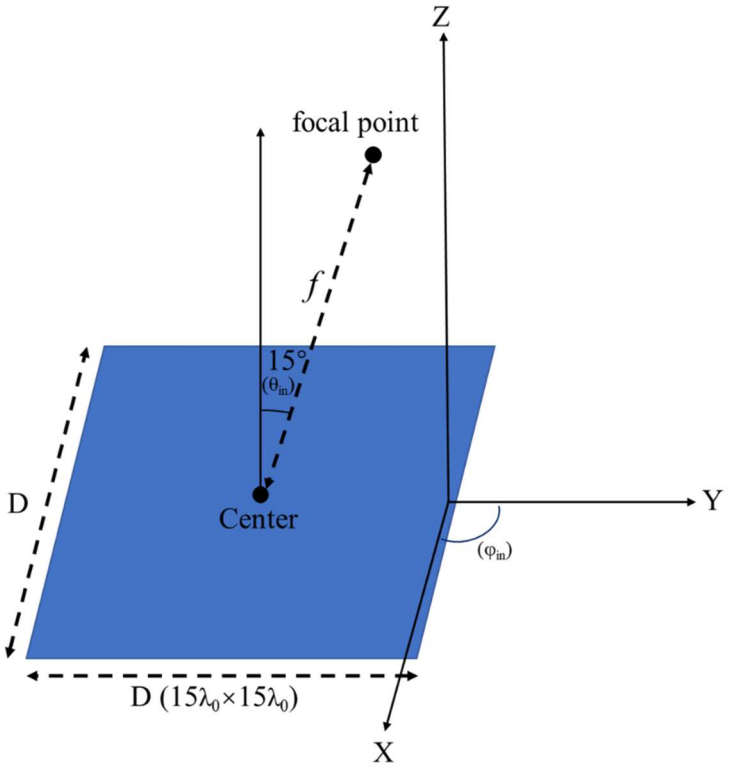

Fig.5.1 Configuration of RAs in chapter 5.

5.2 Dual band metal-only reflectarray antenna

5.2.1 Cell analysis

This subsection introduces a modified PCSW used to design a dual band MORA. As shown in Fig.5.2, the proposed cell consists of two square waveguides and a metallic block in the center (like the PCSW in Fig.2.15). The only novelty here is that the cross-section of the cell is fixed, and the reflection phase is tuned by varying the heights of both waveguides. The detailed parameters of this dual band cell are tabulated in table 5.1. Since the two target frequencies are 20 and 25GHz, the size of the external waveguide (L_c) is fixed at 6mm (half wavelength at 25GHz) to prevent from grating lobes. The size of inner waveguide (L_r) should be large enough so that the inner waveguide can also be used to control the reflection phase. At the same time, its value should not be too large as a too small gap between inner and external waveguides may increase fabrication error. Therefore, a medium value (4.5mm) is selected for L_r. Similarly, the value of L_p is fixed at 2.7 mm, which allows the incident wave to propagate in the inner waveguide and leaves enough space between inner waveguide and metallic block to reduce possible fabrication error.

Now the selected ranges of the heights of both waveguides (h_{in} and h_{ex}) are analyzed. The two waveguides are simulated using the same way as in section 2.4.1. Their detailed characteristics are tabulated in table 5.2. It can be seen that only the external waveguide operates in propagative mode at 20GHz while both waveguides allow propagation at 25GHz. Therefore, the reflection phase at 20GHz is mainly controlled by the external waveguide while both waveguides are influent at 25 GHz. It can be deduced from equation (2.1) that the required height for each waveguide to achieve the complete range is equal to $\frac{\pi}{\beta}$ where β is the imaginary part of propagation constant at target frequency. Since the reflection phase at 20GHz is controlled only by the external waveguide, its range is determined first. The calculated range of h_{ex} is equal to 11.43mm. Once h_{ex} is chosen, h_{in} is changed to tune the reflection phase at 25 GHz and the calculated range of h_{in} is 17.65 mm. Note that the calculated ranges for both waveguides are a little bit different from the finally used ones (used to produce complete phase ranges) shown in table 5.2. This comes from two reasons. Firstly, the phase is also affected by the discontinuity effects (see section 2.3) at the entrance of the dual band cell. Secondly, at the higher frequency, both waveguides contribute simultaneously, which means the effects of h_{in} and h_{ex} get mixed.

Fig.5.3 shows the simulated reflection coefficients of the unit cell at 20 and 25GHz. Note that the used ϕ_{inc} and θ_{inc} corresponds to the incident angle of the cell in the center (see Fig.5.1). The phase and loss at 20GHz are first analyzed. As expected, the response of the cell at this frequency is independent from h_{in}. It can also be seen from Fig.5.3a and c that the complete phase range is achieved, and the loss is less than 1.22dB. As introduced in section 2.4, the loss is associated to the resonances caused by the propagation of the quasi TE_{10} mode. It can be deduced from equation 2.1 and table 5.2 that the resonance occurs when h_{ex} is equal to 5.72mm ($\frac{\lambda}{4}$) at 20GHz. The expected h_{ex} is quite close to the full wave simulation result in Fig.5.3a (the position of the white curve).

Next, the phase and loss at 25GHz are analyzed. It can be seen from Fig.5.3b that the complete phase range at 25GHz can always be achieved by varying h_{in} for each fixed h_{ex} except for the value of h_{ex} that causes resonances. Since the incident wave propagates in both waveguides at 25 GHz, both may cause resonances, which can be seen in Fig.5.3b (horizontal white curve for h_{in} and vertical white curve for h_{ex}). It can be seen from Fig.5.3b that the value of h_{ex} that causes resonances is reduced due to the increase of β at 25GHz (see table 5.2). It can also be seen from Fig.5.3b that once one of the two waveguides causes a resonance, the reflection phase is hardly affected by the other waveguide.

Since both waveguides cause resonances at 25GHz, the number of cells with high losses is significantly increased (see Fig.5.3d). To mitigate the impacts of these resonances on the performances

of the designed RA, all cells with a loss greater than 1dB are removed from the database before the synthesis of the dual band RA.

Table 5.1: Detailed parameters of 3D PC

f	L_c	L_r	L_p	h_{in}	h_{ex}	w_{in}	w_{ex}	h
20/25 GHz	6 mm	4.5 mm	2.7 mm	0-16.5, step=0.25 mm	0-12, step=0.2 mm	0.3 mm	0.2 mm	16.7 mm

Table 5.2: Detailed parameters of the two waveguides in the dual band cell

			Inner waveguide	External waveguide
20GHz	γ=α+jβ	α (NP/mm)	0.26	0.0015
		β (deg/mm)	0.12	15.75
	$Z_c=R_c+jX_c$	R_c (Ω)	1.09	51.91
		X_c (Ω)	97.90	0.08
25GHz	γ=α+jβ	α (NP/mm)	0.0035	0.0013
		β (deg/mm)	10.20	23.90
	$Z_c=R_c+jX_c$	R_c (Ω)	192.59	42.46
		X_c (Ω)	3.62	-0.01

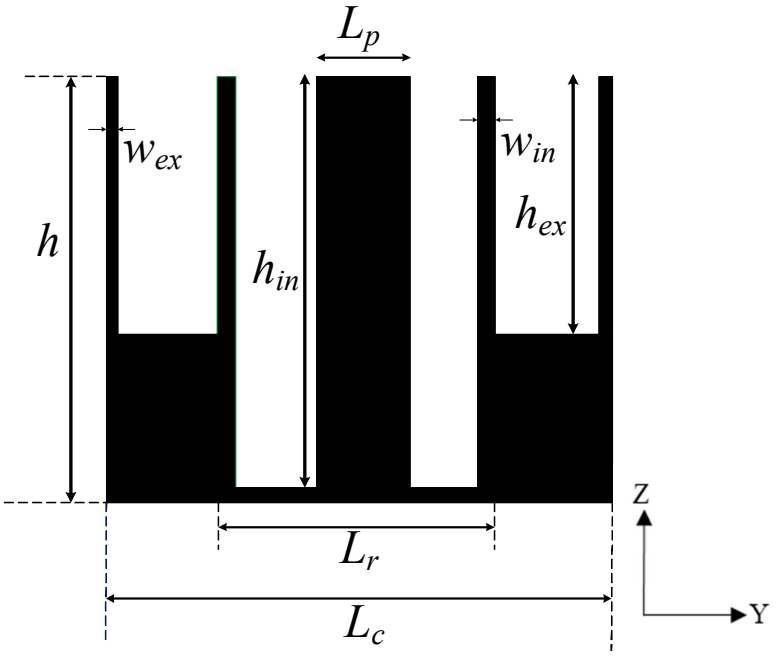

Fig.5.2 Proposed dual band cell (sectional view).

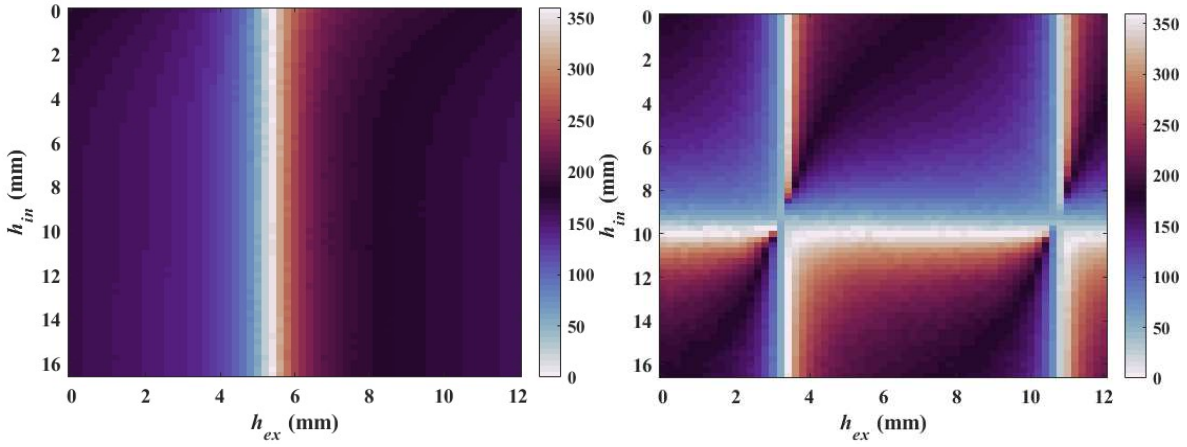

a) b)

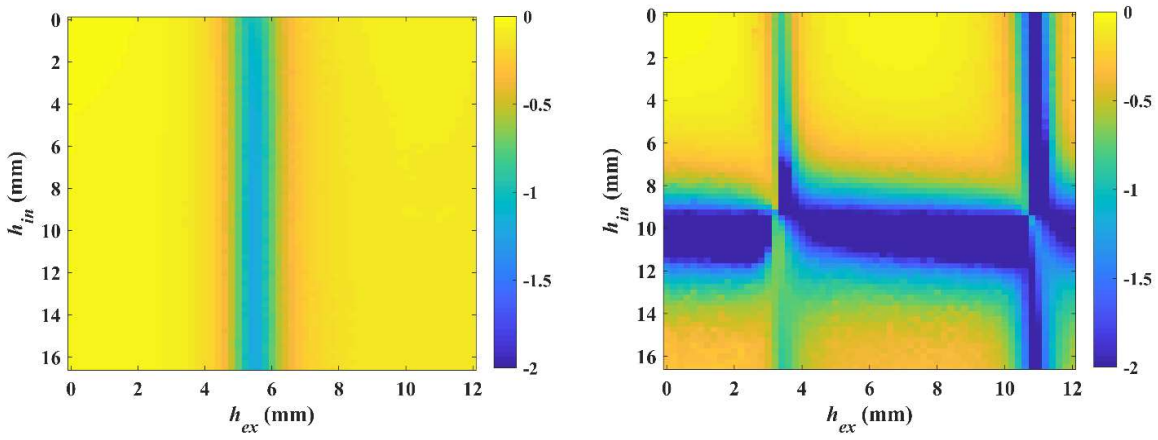

c) d)

Fig.5.3 Simulated reflection coefficient (x-polarization, ϕ_{inc}=90°, θ_{inc}=15°). a) Phase at 20GHz (deg). b) Phase at 25GHz (deg). c) Mag at 20GHz (dB). d) Mag at 25GHz (dB).

5.2.2 Horn antenna design

Before the synthesis of the dual band RA, two different horns for the two frequency bands are designed in this subsection. The design process is exactly the same as that in section 3.4.2. The designed two horns are shown in Fig.5.4 and Fig.5.5. Their corresponding illumination intensities over the cells in the dual band RA are summarized in Fig.5.6. It can be seen that the edge taper is less than -10 dB at both frequencies.

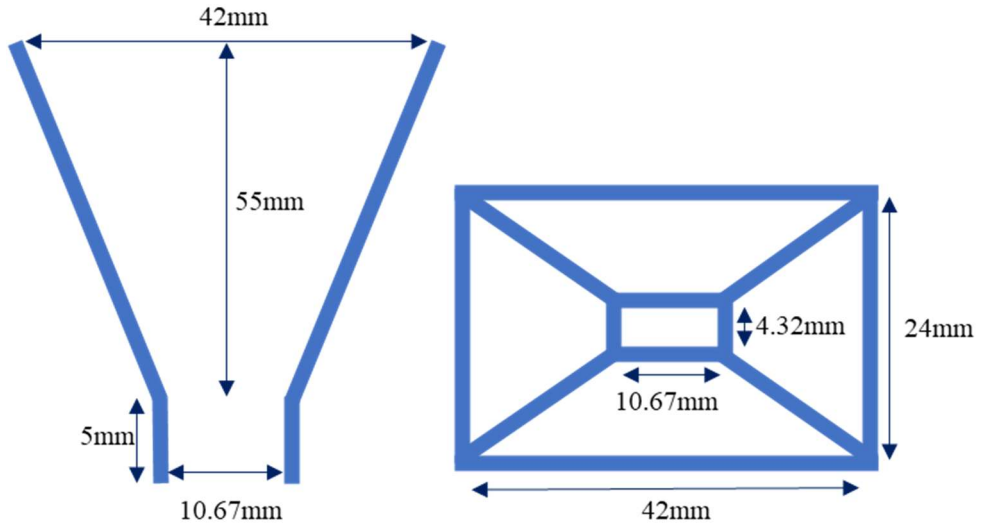

a) b)

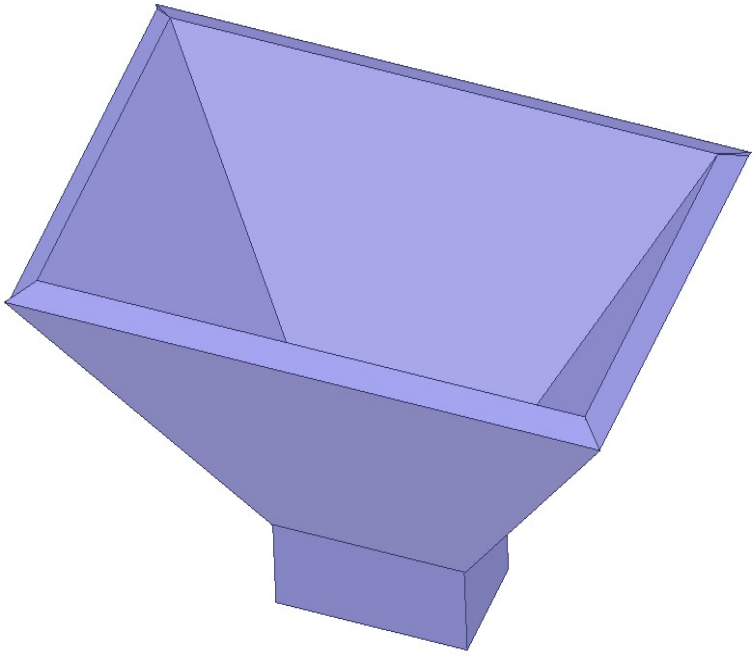

c)

Fig.5.4 Designed horn antenna (20GHz). a) Sectional view. b) Top view. c) 3D view.

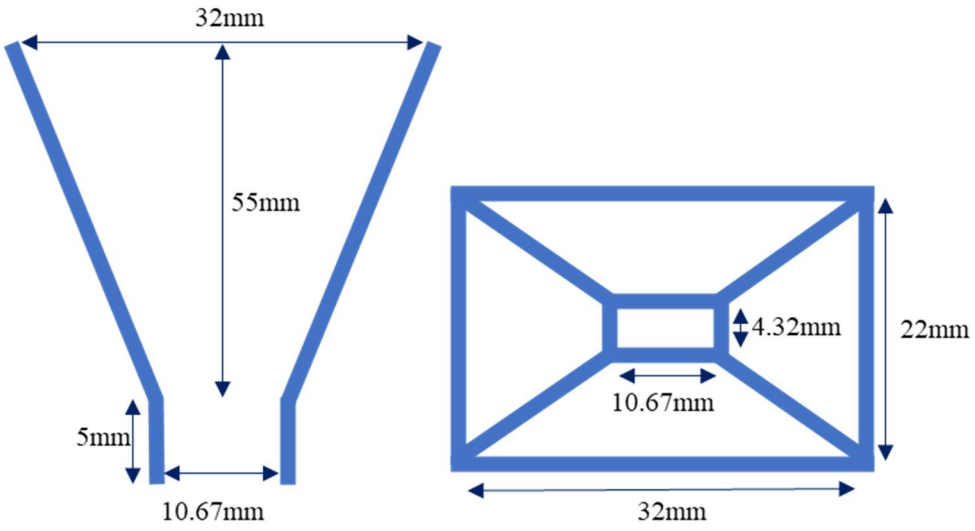

a) b)

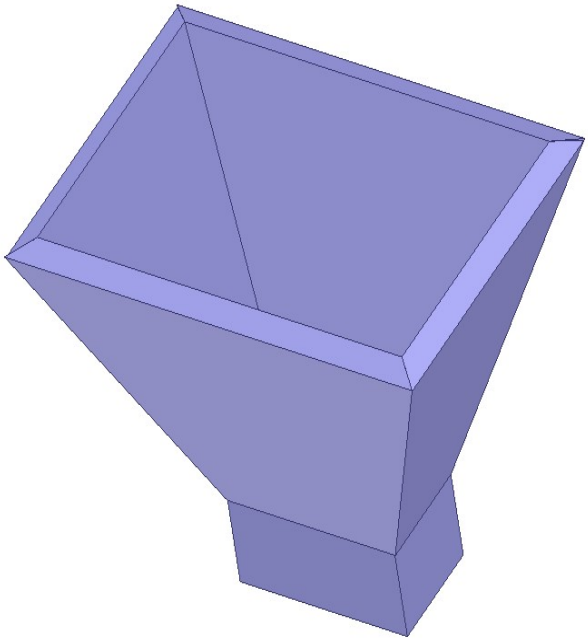

c)

Fig.5.5 Designed horn antenna (25GHz). a) Sectional view. b) Top view. c) 3D view.

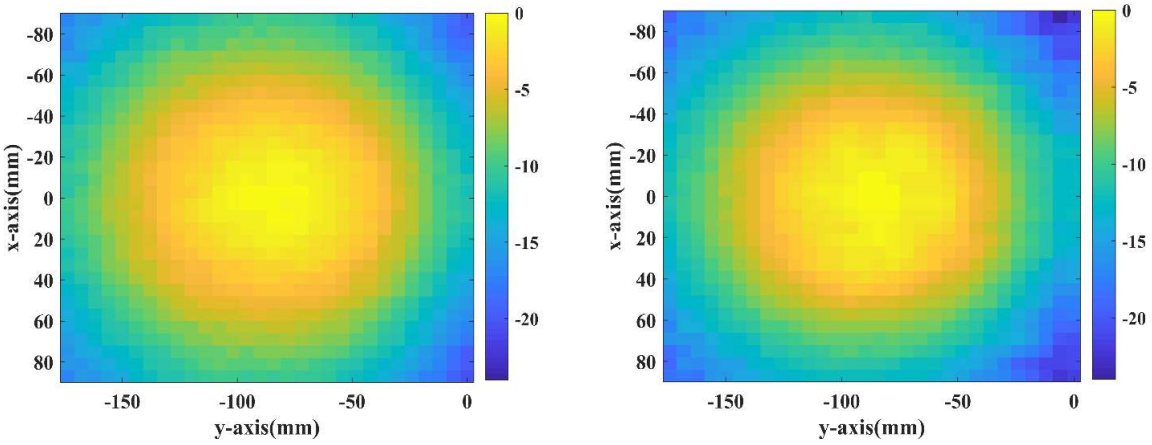

a) b)

Fig.5.6 Illumination intensity over the cells in the dual band RA (dB). a) 20GHz. b) 25GHz.

5.2.3 Dual band reflectarray antenna design and analysis

A dual band RA is now designed to validate the proposed cell. The used database is shown in Fig.5.3. The design process is similar to that in section 4.2.1 where two offset phases are optimized to minimize the average phase error at two target frequencies. During the synthesis process, the cell geometries (h_{in} and h_{ex}) are selected simultaneously. The only difference is that the target frequencies are changed to 20GHz and 25GHz, instead of 19.5 and 20.5GHz, to achieve the dual band functionality. The direction of main beam at both frequencies is (15°, 270°). The required phase shift distributions at both frequencies, calculated by equation (1.3), are shown in Fig.5.7. The offset phases at 20 and 25 GHz after optimization are 218° and 49°, respectively. Also, the achieved average phase errors at both frequencies are 11.68° and 7.98°, respectively. Obviously, the average phase error at 20GHz is higher than that at 25GHz, which suggests that the performances in the upper frequency band may be better than that in the lower one.

The cell geometries of the designed dual band RA are shown in Fig.5.8. It can be seen that there are some undesired abrupt variations in the designed dual band RA, e. g. the yellow color and the blue color next to each other in Fig.5.8a. For the original PCSW (see Fig.2.15), the complete phase range can be achieved only by varying the size of the inner waveguide (L_r). In this case, the geometry of a cell with a large L_r is quite close to that with a small L_r thanks to its rebirth ability, and a smooth geometric variation can easily be achieved for the designed RA, as shown in Fig.4.6a. For the modified PCSW (dual band cell), however, the cross-section is fixed, and the reflection phase is tuned by the heights of both waveguides. In this case, a large height and a small height do not produce a similar geometry and the dual band cell no longer has the 'rebirth' ability (the phase range is limited to 360°). Since the reflection phase at 20GHz is mainly controlled by h_{ex}, the abrupt variations in cell geometries are inevitable (at least for h_{ex}), which is a drawback of the dual band cell compared to the original PCSW with fixed height. These abrupt variations may degrade the performances of the designed RA as demonstrated in section 4.4. The achieved magnitudes over the cells in the dual band RA are shown in Fig.5.9, and the average loss at 20/25GHz calculated by equation 4.4 is 0.54/0.60dB.

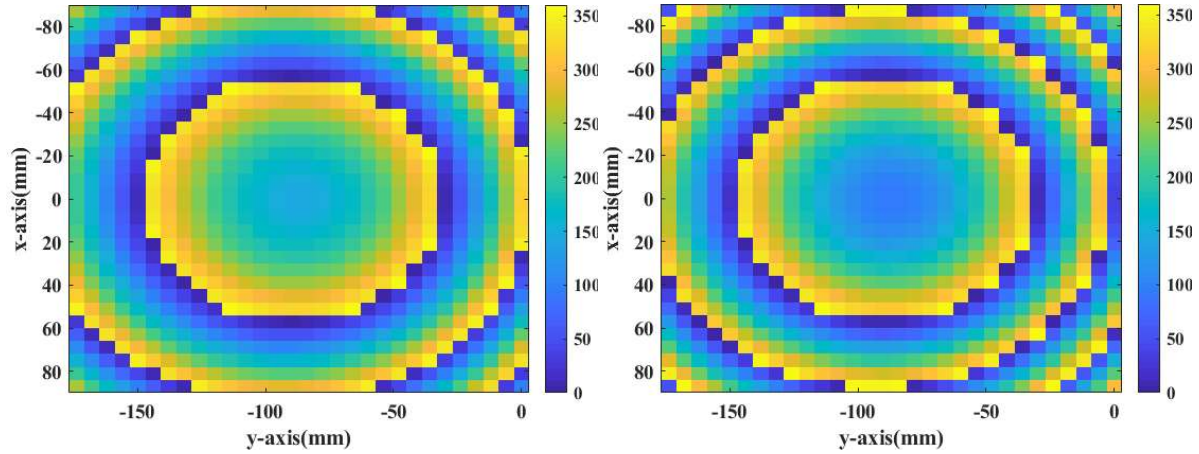

a) b)

Fig.5.7 Distribution of required phase shift over the cells (deg). a) 20GHz. b) 25GHz.

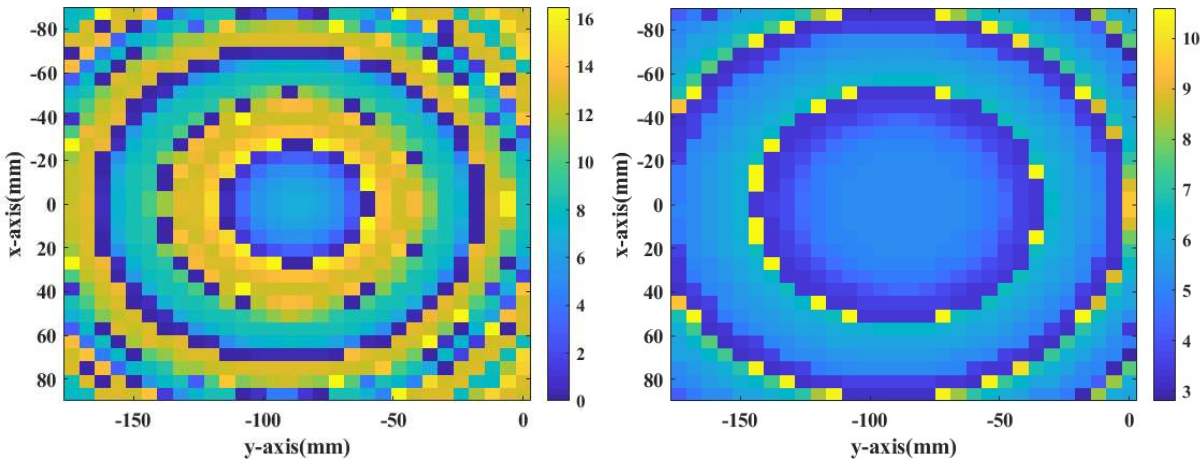

a) b)

Fig.5.8 Cell geometries of dual band RA (mm). a) h_{in}. b) h_{ex}

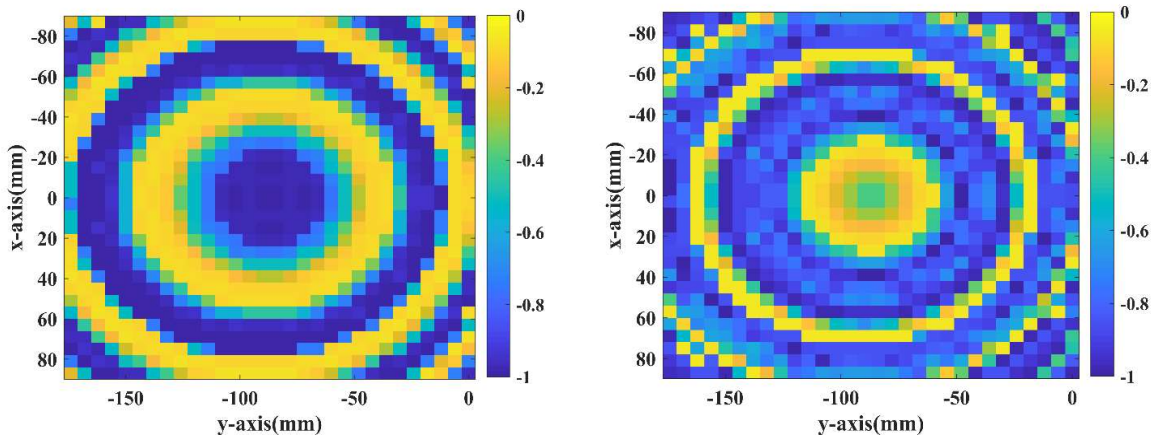

a) b)

Fig.5.9 Achieved magnitude over the cells in dual band RA (dB). a) 20GHz. b) 25GHz.

5.2.4 Performances evaluation

The dual band RA with its 3D radiated fields are shown in Fig.5.10 as a preliminary illustration of its behavior. It can be seen that the main beams are pointing to the desired directions at 20 and 25GHz. The detailed performances in the lower frequency band are summarized in Fig.5.11. It can be seen from Fig.5.11c and d that the achieved side lobe and cross polarization at 20GHz are below -20.21dB and -33.4dB respectively. It can also be seen from Fig.5.11a, b, e and f that the side lobe is not higher than -11.12dB in the range from 19 to 21GHz. In addition, Fig.5.11g shows that the gain at 20GHz is 28.1dBi with an aperture efficiency of 35.74% and the 1-dB gain bandwidth is about 5%.

Now the performances in the upper frequency band, as shown in Fig.5.12, are analyzed. It can be seen from Fig.5.12c and d that the achieved side lobe and cross polarization at 25GHz are below -24.56dB and -36.06dB respectively. It can also be seen from Fig.5.12a, b, e and f that the side lobe is not higher than -12.45dB in the range from 24 to 26GHz. In addition, Fig.5.12g shows that the gain at 25GHz is 30.9dBi with an aperture efficiency of 43.94% and the 1-dB gain bandwidth is about 5%.

These results can demonstrate that the designed RA can operate in two different frequency bands.

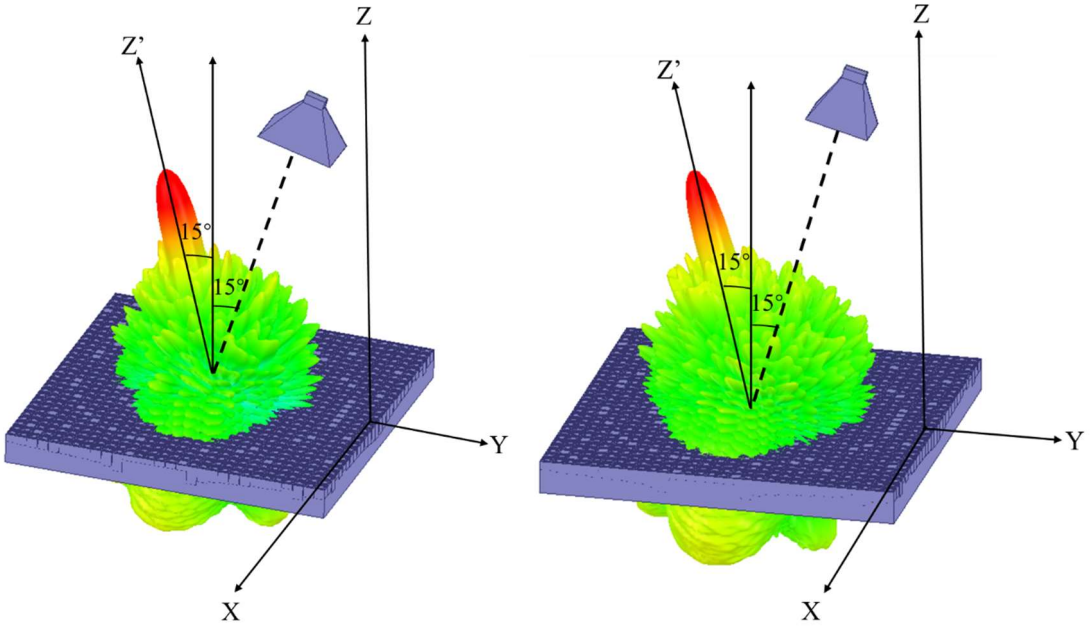

a) b)

Fig.5.10 Dual band antenna with radiation field. a) 20GHz. b) 25GHz.

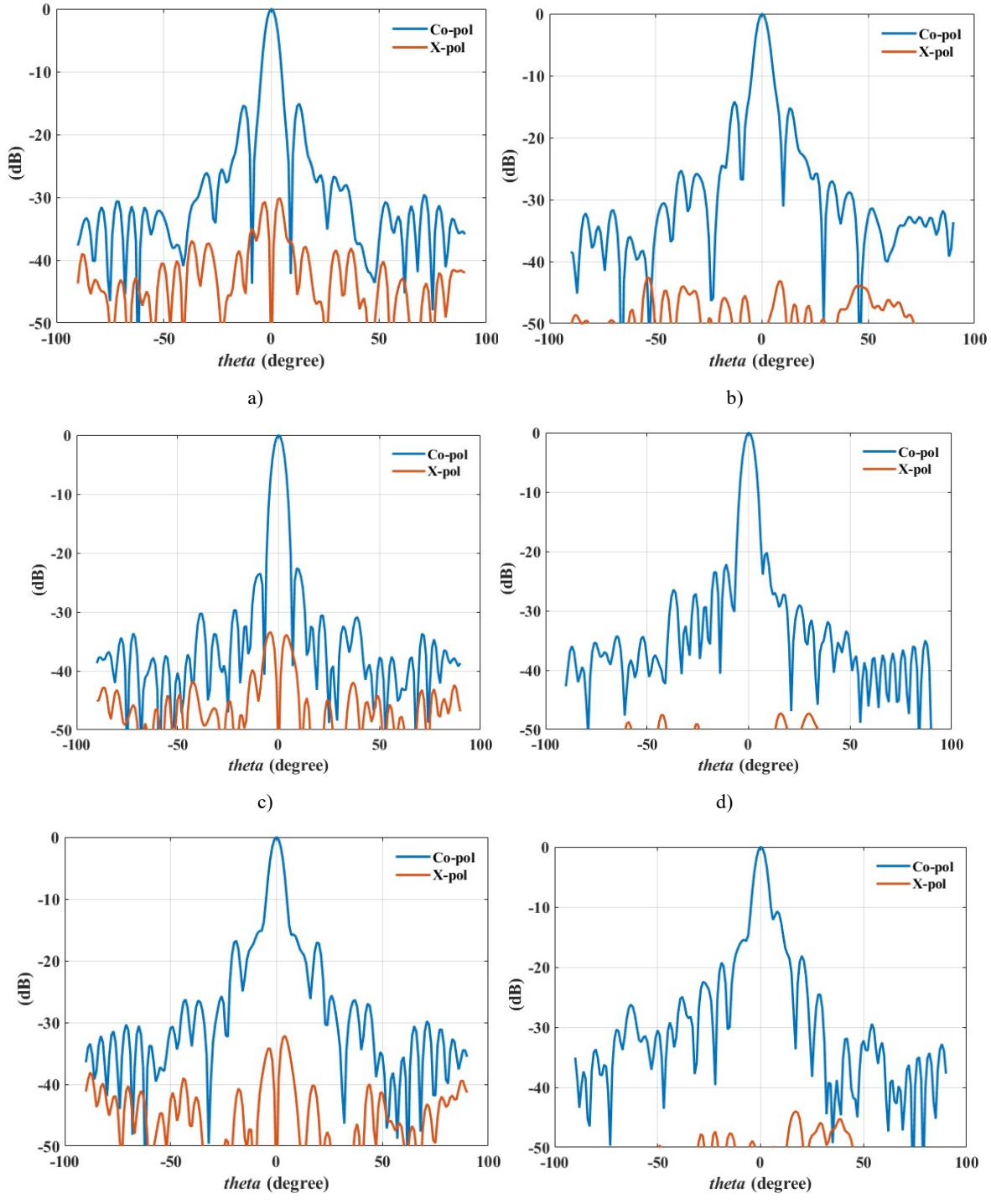

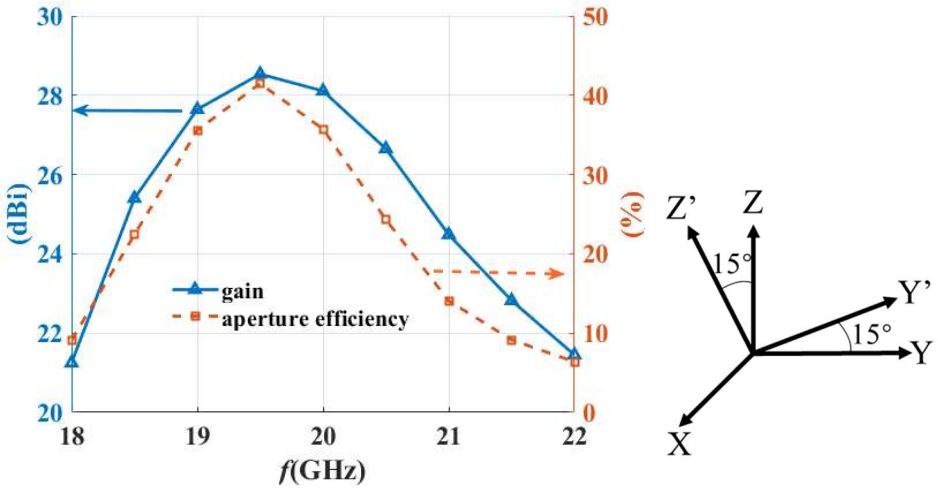

g)

Fig.5.11 Performances in lower frequency band. a) Radiation pattern in xoz' plane (19GHz). b) Radiation pattern in y'oz' plane (19GHz). c) Radiation pattern in xoz' plane (20GHz). d) Radiation pattern in y'oz' plane (20GHz). e) Radiation pattern in xoz' plane (21GHz). f) Radiation pattern in y'oz' plane (21GHz). g) Gain response and aperture efficiency.

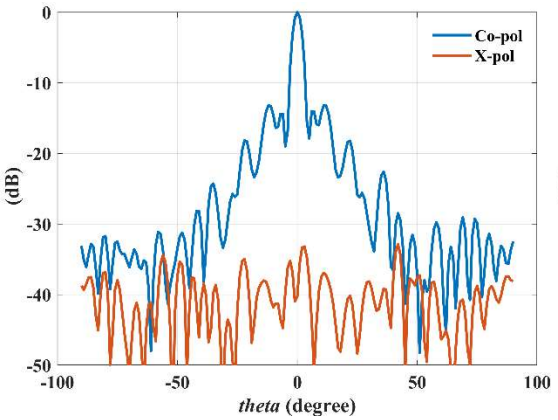

a)

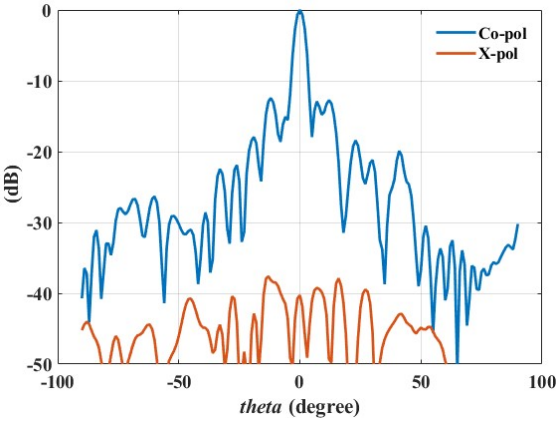

b)

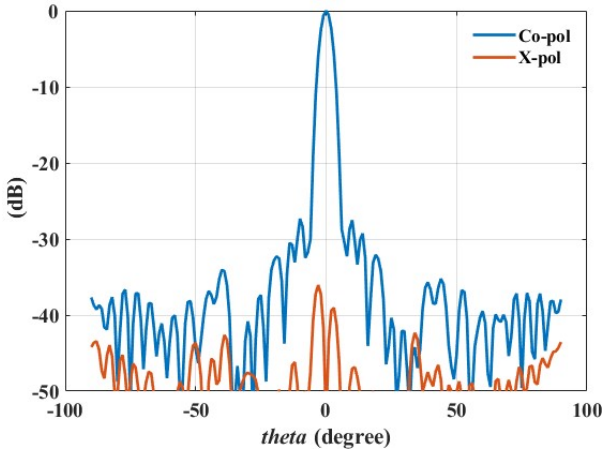

c)

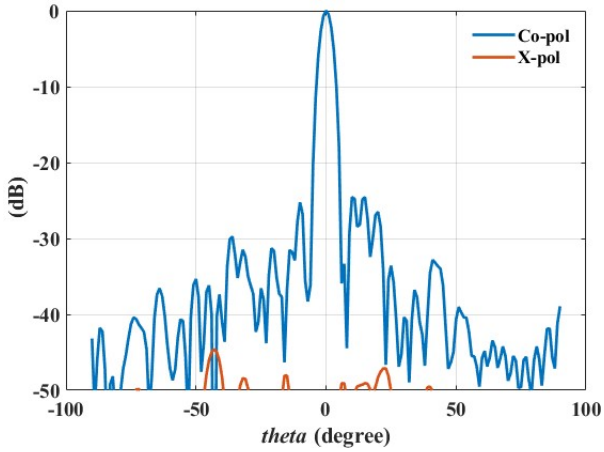

d)

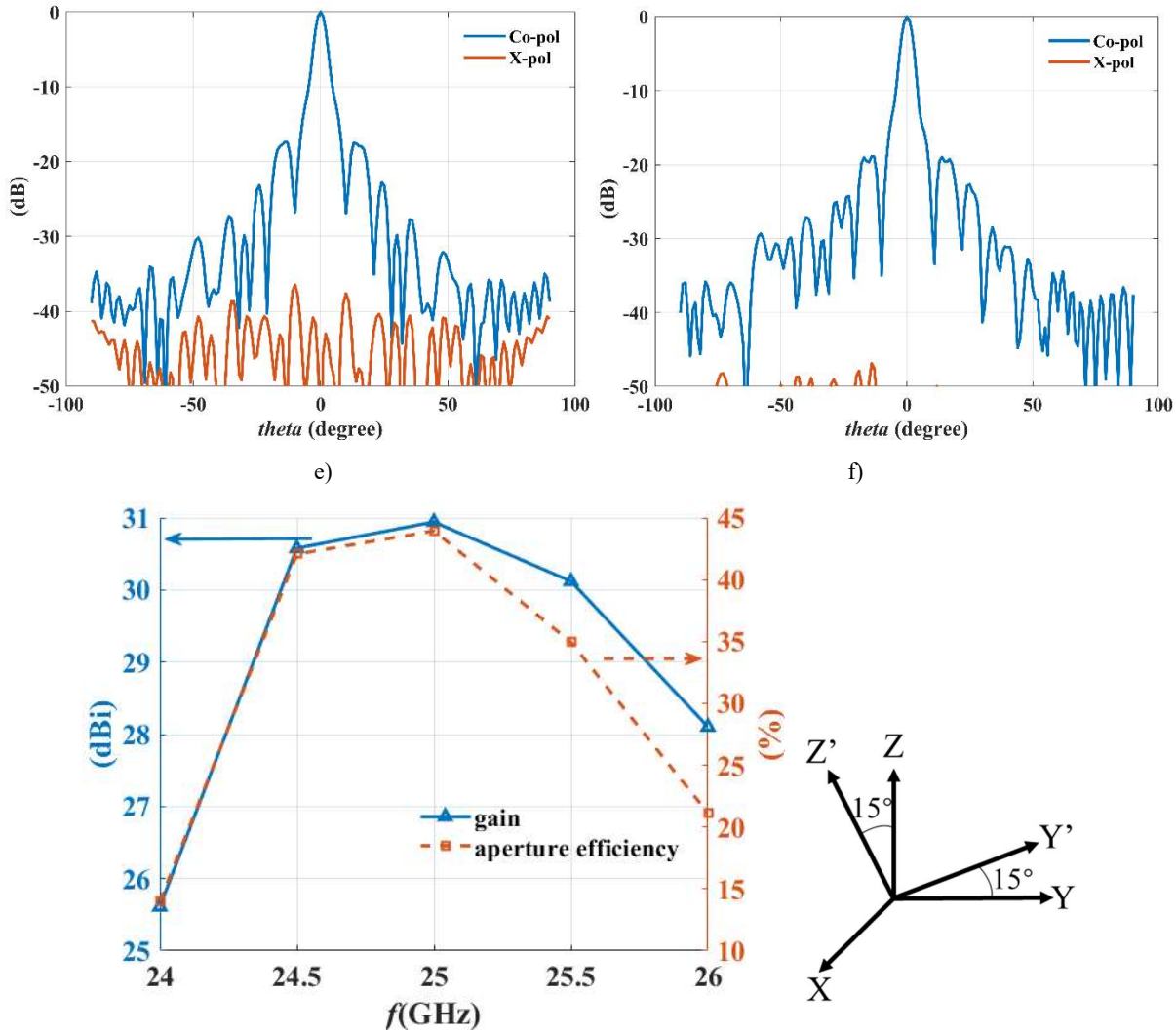

Fig.5.12 Performances in upper frequency band. a) Radiation pattern in xoz' plane (19GHz). b) Radiation pattern in yoz' plane (19GHz). a) Radiation pattern in xoz' plane (20GHz). b) Radiation pattern in y'oz' plane (20GHz). a) Radiation pattern in xoz' plane (21GHz). b) Radiation pattern in y'oz' plane (21GHz). c) Gain response and aperture efficiency.

5.2.5 Conclusion

In this section, a dual band RA is designed and analyzed. The unit cell is a modified PCSW where the heights of both waveguides, instead of the size of the inner waveguide, are used to control the reflection phases in two frequency bands. The complete phase ranges are achieved at both 20 and 25GHz. The dual band RA is synthesized by optimizing the offset phases to minimize the average phase error at 20 and 25GHz. At this stage, this study is still preliminary, the way of defining the optimal ranges for h_{in} and h_{ex} is still open. Also, the selection process of both heights could certainly be improved further (typically by selecting hex first to control the phase at the lower frequency and then using h_{in} to provide the additional degree of freedom to tune the phase at the higher frequency). However, the already achieved performances demonstrate that this concept is feasible and suggest interesting directions for further investigations.

5.3 Dual beam metal-only reflectarray antenna

5.3.1 Cells Description

This section proposes a MORA allowing to generate two pencil beams with orthogonal polarizations. The unit cell is similar to the dual band cell in Fig.5.2. The only difference, as shown in Fig.5.13, is that four walls are added to split the two waveguides into two parts. This modification allows the proposed cell to independently control incident waves with orthogonal linear polarizations. In addition, the reflection phase is controlled by tuning independently the heights of both waveguides (h_{in} and h_{ex}).

The cross-section of the cell is first designed so that the inner or external waveguides are both propagative at the considered operating frequency, f_0 = 25 GHz. The external waveguide supports a horizontally polarized mode (along y) while the inner one supports a vertically polarized one (along x). Note that the cutoff frequency of the inner waveguide is reduced below f_0 thanks to the square metallic block (L_p) whose size is optimized to make propagation possible. Then, the reflection phase at f_0 for both modes is controlled by adjusting only the heights of the waveguides: h_{in} controls the phase of x polarization while h_{ex} deals with the y polarization. In order to eliminate the coupling between both waveguides and to control the reflection phase independently in both polarizations, four walls have been added to the original cell (they are highlighted in red in Fig. 5.13). These four walls impose that the modes in the inner and external waveguides are orthogonally polarized. As a result, the proposed MO cell has two degrees of freedom to control the reflection phase independently and it can be used to design a MORA providing two independent beams with orthogonal polarizations.

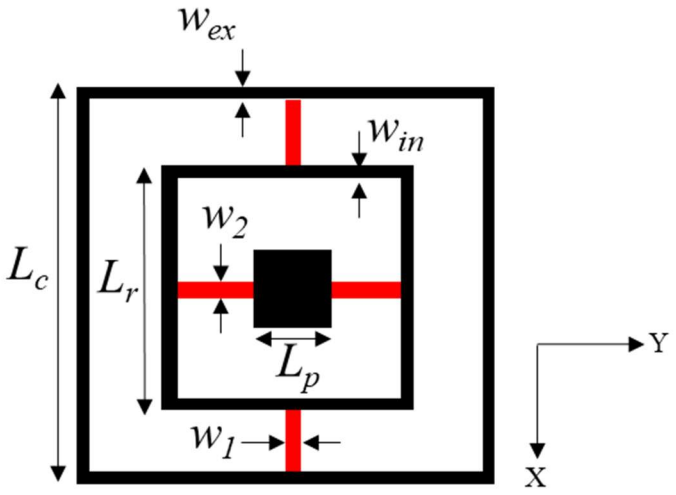

Fig.5.13 Top view of dual beam cell.

5.3.2 Cells performances

Before the design of the dual-beam MORA, the performance of the proposed unit cell is verified. The detailed parameters of the cell are tabulated in Table 5.3. Fig.5.14 shows the simulated reflection coefficients of the unit cell at normal incidence and at 25GHz. Note that the electric field direction is parallel to the x-axis for Fig.5.14a and to the y-axis for Fig.5.14b. As it can be seen, the complete 360º phase range can be achieved by increasing the height of the inner waveguide up to 15mm, and up to 9mm for the external one. Furthermore, Fig. 14a shows that the reflected phase for the x-polarization is almost independent of h_{ex} (the maximum phase variation is 4° when varying h_{ex} from 1 to 9 mm). The opposite is true (see Fig. 14b for different h_{in}). This demonstrates that h_{in} and h_{ex} can almost independently control the reflection phase in both polarizations. It can also be seen that the loss for the

x-polarized mode is significantly higher than that of y-polarized one, which may deteriorate the gain of designed RA. The high losses are certainly due to the small cross section and larger length of the inner waveguide that is used for this mode.

The reflection coefficients at different incident angles are shown in Fig.5.15. The parameters h_{ex} and h_{in} are set to 5mm (Fig.5.15a) and 8mm (Fig.5.15b), respectively. A maximum phase difference of 19° is obtained when varying θ_{inc} for h_{in}=10.25mm, which is completely acceptable for the design of a RA.

Table 5.3: Detailed parameters of the dual beam cell.

Parameter	L_c	L_r	L_p	h_{in}	h_{ex}	w_{in}	w_{ex}	w_1	w_2
Value (mm)	6	4.7	3	0-15	0-9	0.3	0.2	1.6	0.4

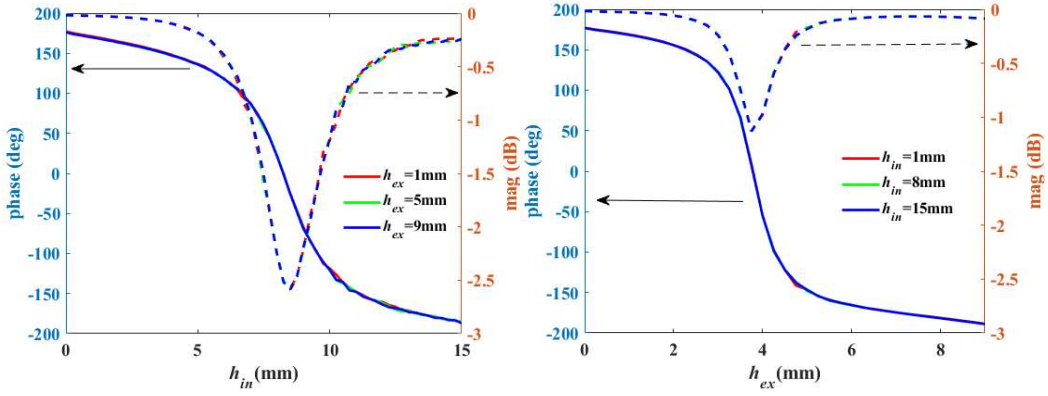

a) b)

Figure 5.14. Simulated reflection coefficients of the cell (f_0=25GHz, normal incidence). a) Inner waveguide (x-polarized excitation). b) External waveguide (y-polarized excitation).

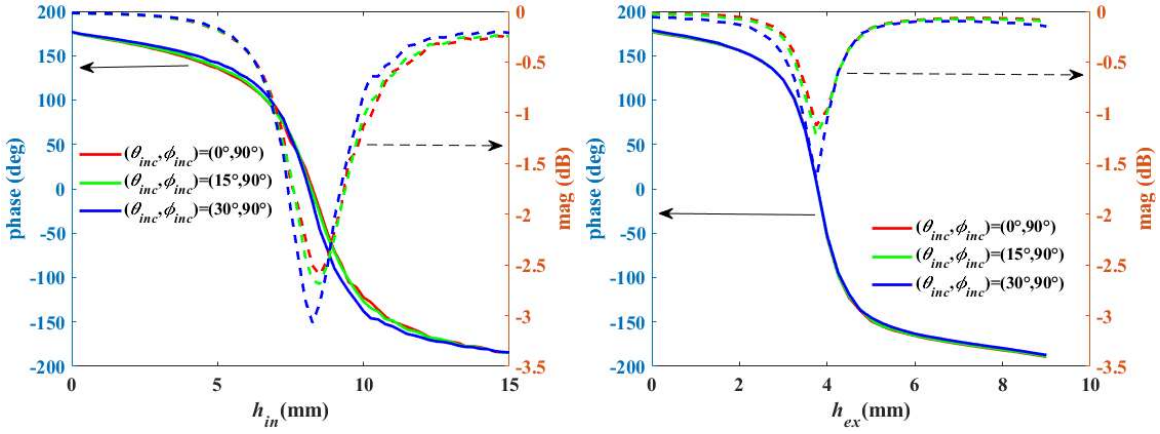

a) b)

Figure 5.15 Simulated reflection coefficients of the cell (f_0=25GHz, oblique incidence). a) Inner waveguide (x-polarized excitation). b) External waveguide (y-polarized excitation).

5.3.3 Antenna synthesis and analysis

For the database used to design the proposed RA, the incident angles are set to the ones at the center of the panel (15°, 90°). It corresponds to the green curves in Fig.5.15. The directions of the beams are set to (15°, 225°) and (15°, 315°) respectively. The h_{in} and h_{ex} heights of each cell are selected one by one to meet the required phase distributions for both beams (h_{in} for beam (15°, 315°) and h_{ex} for (15°,

225°)). The required phase distributions for both beams are shown in Fig.5.16. Also, the cell geometries and the magnitude distributions over the cells in the dual band RA are shown in Fig.5.17 and 18.

Similarly to what was observed for the dual band RA, the yellow color and the blue color next to each other in Fig.5.17 represent abrupt variations in cell geometries, which may degrade the performances of the dual beam RA. As expected, Fig. 5.18 shows that the achieved losses for beam (15°, 315°) are obviously higher than that for (15°, 225°), which suggests that the associated gain may be lower.

The dual beam RA with its radiated fields at 25GHz are shown in Fig.5.19. It can be observed that the direction of the main beam depends on the polarization of the incident wave, which is compliant with expectations. The normalized radiation patterns for both beams are summarized in Fig.5.20 and 21. It can be seen that the main beams are pointing to the desired direction from 24 to 26GHz. First, the beam controlled by the inner waveguide is analyzed. It can be seen from Fig.5.20b that the side lobe and cross polarization levels are lower than -26.73dB and -34.63dB respectively. As the frequency varies, the side lobe deteriorates to -13.17dB at 26GHz (see Fig.5.20c). Now, the beam controlled by external waveguide is analyzed. It can be seen from Fig.5.21b that the side lobe and cross polarization levels are lower than -27.19dB and -39.57dB respectively. The side lobe level remains below -23.32dB in the range from 24 to 26GHz. Obviously, the side lobe and cross polarization levels of the beam controlled by the external waveguide are better than that by the inner waveguide.

The achieved gains and aperture efficiencies of the two beams are summarized in Fig.5.22. It can be seen that the gain of the beam controlled by the external waveguide is globally better than that by the inner waveguide, which can be explained by the higher losses in the inner waveguide (see Fig.5.15 and 18). These results demonstrate that the designed dual beam RA can generate two beams with orthogonal polarizations.

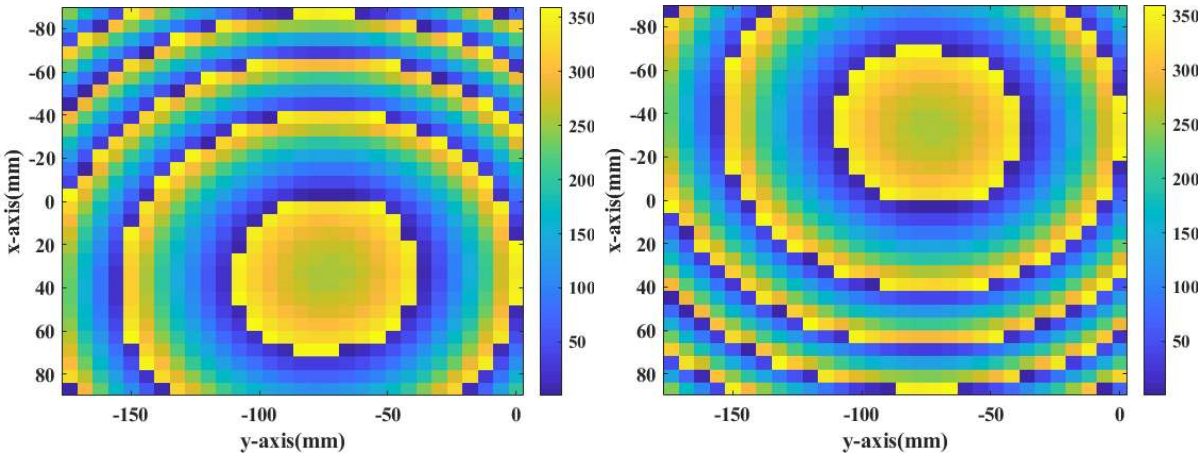

a) b)

Fig.5.16 Distribution of required phase shift over the cells (deg). a) For beam (15°, 315°). b) For beam (15°, 225°)).

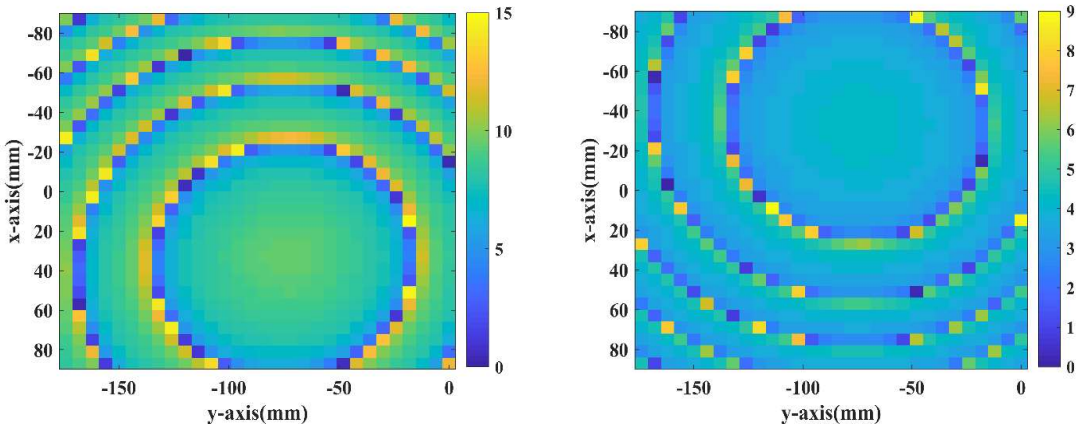

a) b)

Fig.5.17 Cell geometries of dual beam RA (mm). a) h_{in}. b) h_{ex}.

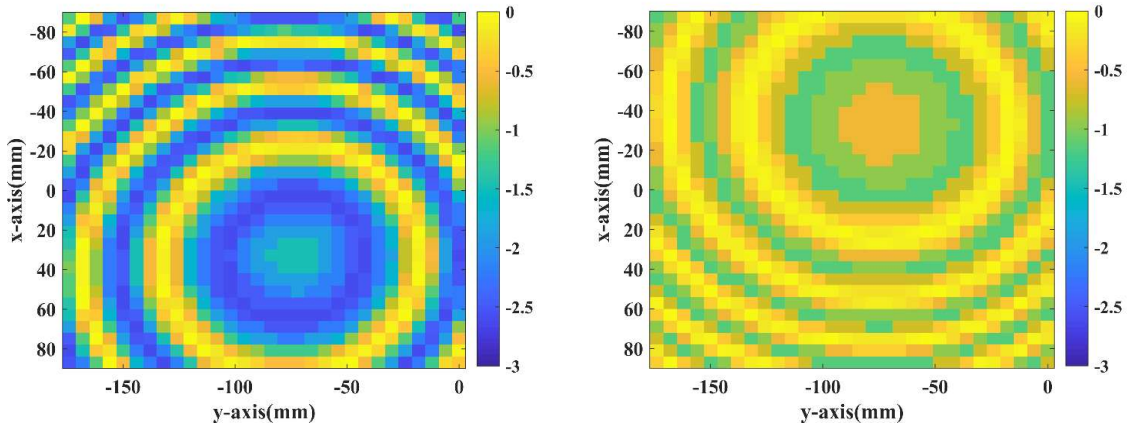

a) b)

Fig.5.18 Achieved magnitudes of dual band RA (dB). a) For beam (15°, 315°) (inner waveguide). b) For beam (15°, 225°) (external waveguide).

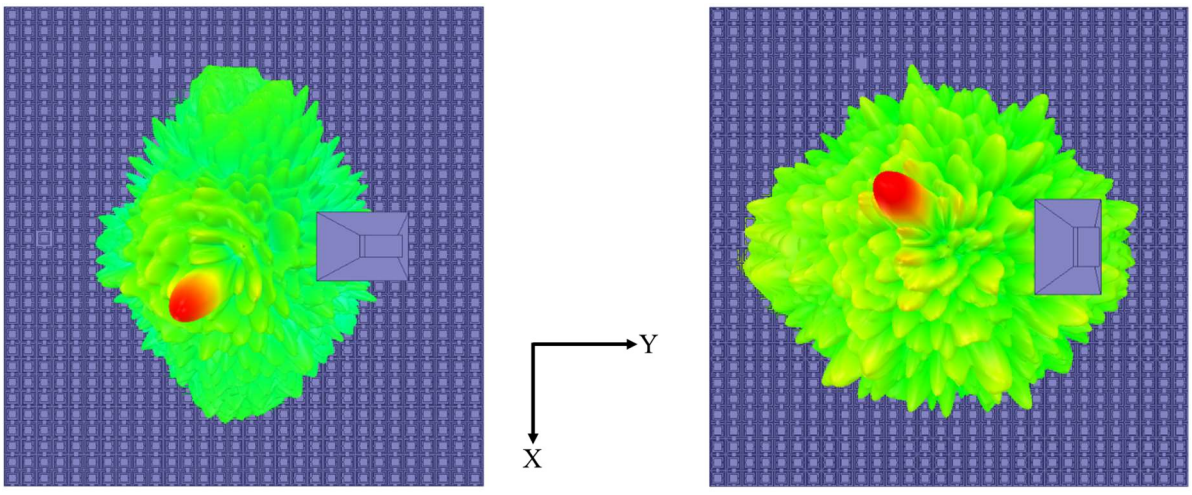

a) b)

Fig.5.19 RA with radiated fields at 25GHz. a) Beam controlled by inner waveguide (x-polarized excitation). b) Beam controlled by external waveguide (y-polarized excitation).

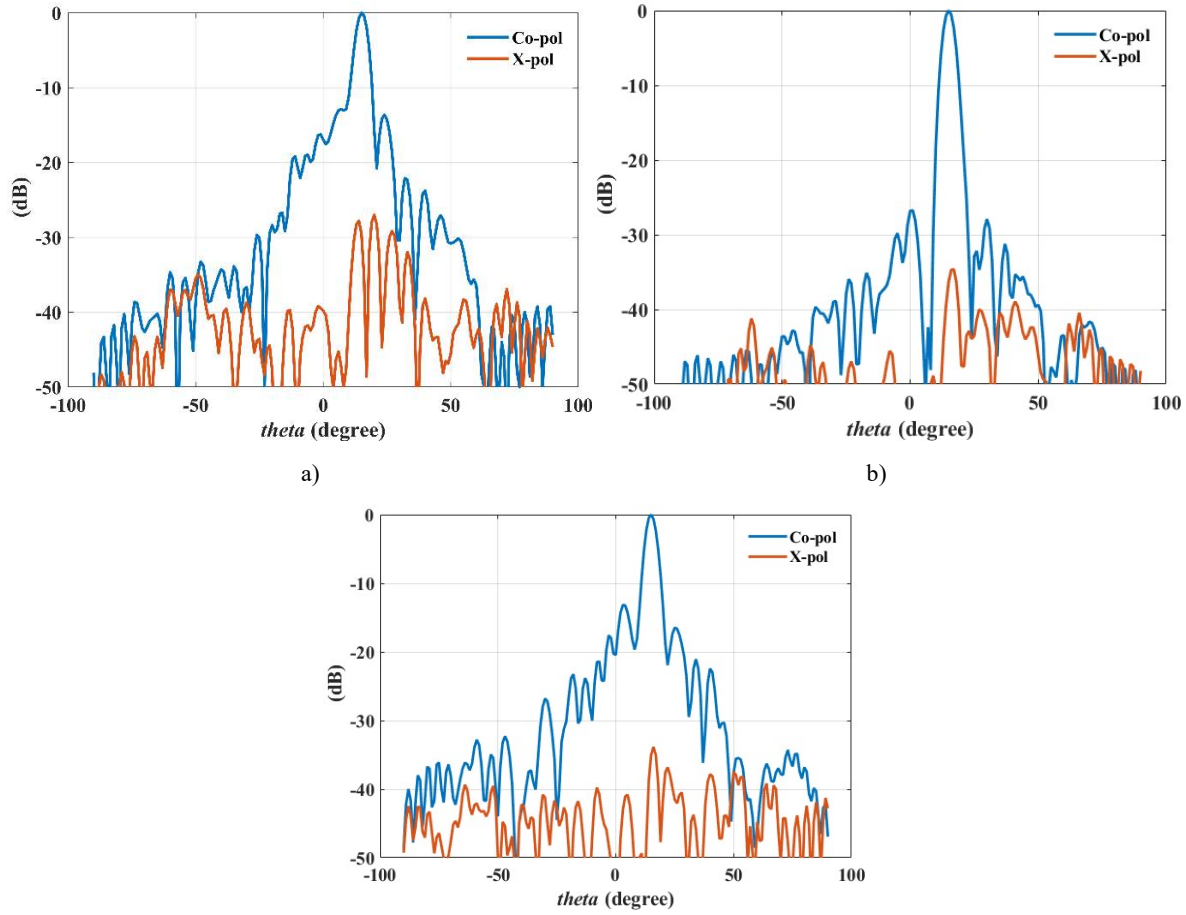

Fig.5.20 Simulated normalized radiation pattern: the beam controlled by inner waveguide (phi=315°, x-polar excitation). a) 24GHz. b) 25GHz. c) 26GHz.

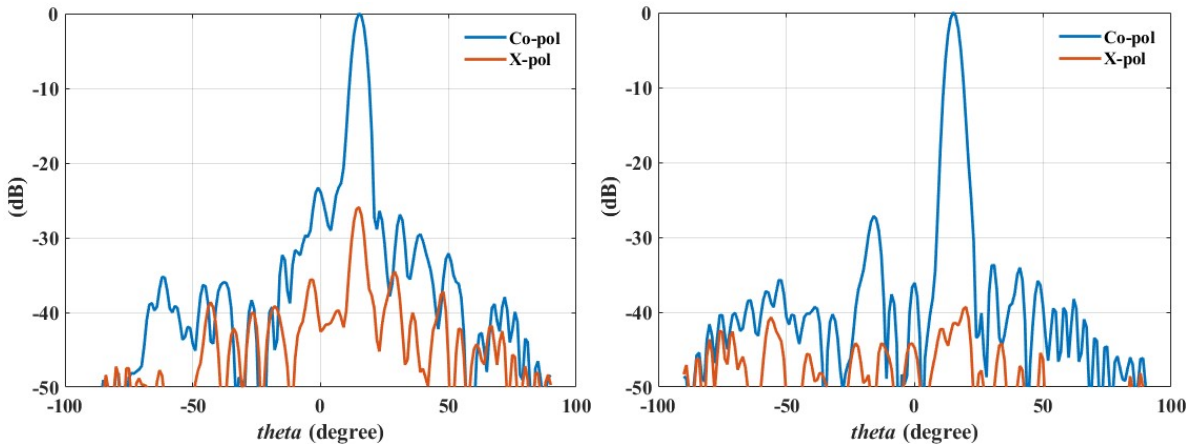

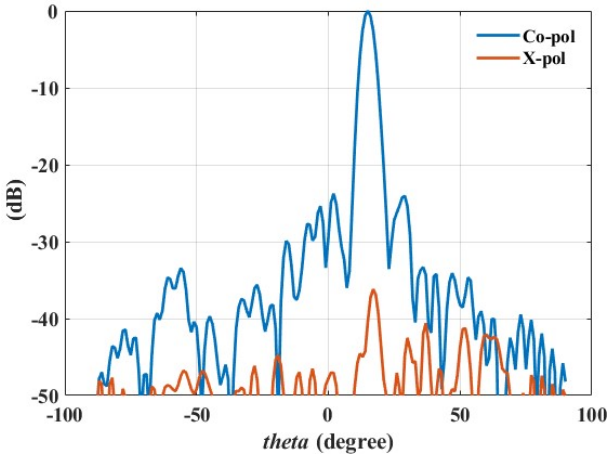

c)

Fig.5.21 Simulated normalized radiation pattern: the beam controlled by external waveguide (phi=225°, y-polar excitation). a) 24GHz. b) 25GHz. c) 26GHz.

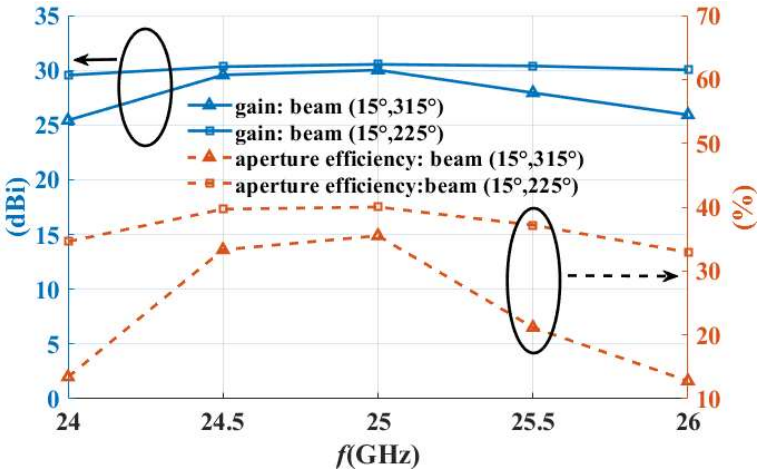

Fig.5.22 Gain responses and aperture efficiencies of two beams.

5.3.4 Conclusion

In this section, a dual-polarized antenna is designed and analyzed. Compared to the unit cell in section 5.2, four walls are added to split the two waveguides into two parts, which allows the proposed cell to independently control incident waves with orthogonal linear polarizations. The beam direction of the designed RA then depends on the polarization of the incident wave. Although the feasibility of such a concept has been clearly demonstrated, further optimizations would be needed to improve performances.

5.4 Conclusion

In this chapter, the PCSW is modified to design two different RAs cells where the cross-section is fixed, and the reflection phase is controlled by the heights of the two waveguides. The advantages of using this additional degree of freedom have been illustrated by the preliminary design of two antennas. Some possible limitations have also been identified. Firstly, the proposed modification makes the rebirth ability trickier and may cause abrupt variations in the cell geometries of designed RA. In addition, a large height may be required to achieve the complete phase range (e.g. 15mm for h_{in} of dual beam cell at 25GHz), which significantly increases the losses. This suggests additional work is still required to fully exploit the new possibilities offered by this degree of freedom and possibly to combine it with simultaneous variations in the cross section of the cell.

In any case, the chapter shows dual band and dual polarized RAs are feasible and the PCSW is a good candidate for designing antennas with advanced features.

General Conclusion

In this thesis, the capabilities of 3D MO PCs have been investigated and various antenna designs have been proposed accordingly. Since the SLM technology is available in our collaborative lab in Fez, some of the designed antennas in this thesis have been fabricated and measured, thus providing a complete experimental validation.

More precisely, the main contributions in this thesis are as follows:

A new concept of 3D MO waveguide-based PC, including its simplified version, is proposed. The proposed PC is analyzed in detail. Its principle is explained by observing the electric field distribution. The resonant phenomena are explained by theoretical S-parameters and some solutions are given to get rid of these resonances or to limit their impact. An equivalent circuit for the PC is established to predict the reflection phase. A good agreement between equivalent circuit and full wave simulation results is achieved. Different degrees of freedom (cross-section and height) in the PC are investigated. The performances are evaluated by full wave simulation results.

A dual band MORRA (operating both at 20 and 40GHz) is designed, simulated, fabricated and measured. The profile of the dual band antenna is significantly reduced by rotating the coordinate system. The dual band antenna is fabricated using SLM technology. The agreement between simulated and measured results is quite good. A single band MORA (operating at 20GHz) is designed, simulated, fabricated and measured. The antenna is designed by minimizing the average phase error. An optimization methodology is also proposed, and the 1-dB gain bandwidth is improved by 3% after optimization. A good agreement between simulations and measurements is achieved. Two different MOTRAs (operating at 20GHz) are designed and simulated as a first demonstration of this antenna topology when using PCs. The antennas are synthesized by minimizing the total phase error. Simulation results show that the proposed MOTRAs can produce both transmitted and reflected beams simultaneously, and the produced beams can be symmetrical or asymmetrical.

A modified PC cell for dual band application is proposed, and a dual band MORA (operating both at 20 and 25GHz) is designed and simulated. Its performances are evaluated by full wave simulations. The dual band antenna is synthesized by minimizing the average phase error. Simulation results show that it can work in two different frequency bands. A modified PC for dual polarization is also proposed, and a dual beam MORA (operating at 25GHz) is designed and simulated. The unit cell can independently tune the reflection phases for two orthogonal linear polarizations. Its performances are evaluated by full wave simulations. The antenna is synthesized by selecting the corresponding geometry for each beam respectively. Simulation results show that the direction of main beam can be changed by rotating the feed horn.

The main conclusions are the following:

The results in this thesis demonstrate that different functionalities can be realized by making full use of the different degrees of freedom in the PC e.g., the cross-section of the PC and the height of different waveguides in the PC. The 3D PC may be used in many different configurations (RA, TA, RA/TA, RA/parabolic reflector), which suggests additional studies are still required to fully explore all its capabilities.

The cell offers many degrees of freedom, which also requires a specific attention when designing an array. Firstly, its cross-section has to be chosen carefully as it controls the cut-off frequency of the propagating modes. Secondly, the height can be involved in the triggering of parasitic resonances. Finally, the best solution to tune the phase is to combine variations in heights and cross-section but a trade-off is required to preserve a smooth geometrical variation over the array aperture. At the moment, advanced optimization schemes are still needed to fully manage the synthesis process.

Possible future research lines are the following:

First, the thesis focuses on the unit cells based on square metal waveguides. Other types of waveguides could be considered to tune phase e.g., parallel plate waveguides. In chapter 2, only the PCSW is modelled by an equivalent circuit. The other cells can also by represented by equivalent circuits. In this way, a comprehensive understanding of the proposed waveguide-based cells can be achieved.

Since the proposed PC owns several degrees of freedom, further study is required to find the best way to select the geometry of each cell to design antennas with the best performances e.g., the best trade-off between minimum loss, minimum error and smooth geometry needs to be found. Antennas with more functionalities can be designed by making full use of the different degrees of freedom provided by the PC.

References

[1] H. Jasik , Antenna Engineering Handbook , Chapters 12 and 15, MaGraw - Hill , New York , 1961

[2] Moustafa L, Gillard R, Peris F, et al., "The phoenix cell: A new reflectarray cell with large bandwidth and rebirth capabilities, ". *IEEE Antennas and wireless propagation letters*, vol. 10, pp. 71-74, January 2011.

[3] Guha, D., Chattopadhya, S., & Siddiqu, J. Y. (2010). Estimation of gain enhancement replacing PTFE by air substrate in a microstrip patch antenna [antenna designer's notebook]. IEEE Antennas and Propagation Magazine, 52(3), 92-95.

[4] Coonrod, J., & Davis, J. (2014). Sending Circuit Materials Into Space. *Microwave Journal*.

[5] Chahat, N., Cook, B., Lim, H., & Estabrook, P. (2018). All-metal dual-frequency RHCP high-gain antenna for a potential Europa Lander. IEEE Transactions on Antennas and Propagation, 66(12), 6791-6798.

[6] Deng, R., Yang, F., Xu, S., & Li, M. (2016). A low-cost metal-only reflectarray using modified slot-type Phoenix element with 360° phase coverage. *IEEE Transactions on antennas and propagation*, *64*(4), 1556-1560.

[7] Huang, Y., Gong, X., Hajela, S., & Chappell, W. J. (2005, July). Layer-by-layer stereolithography of three-dimensional antennas. In *2005 IEEE Antennas and Propagation Society International Symposium* (Vol. 1, pp. 276-279). IEEE.

[8] Schulwitz, L., & Mortazawi, A. (2008, July). A compact millimeter-wave horn antenna array fabricated through layer-by-layer stereolithography. In *2008 IEEE Antennas and Propagation Society International Symposium* (pp. 1-4). IEEE.

[9] Zhu, X., & Zhang, B. (2019, May). A low-cost stereolithography printed X-band antenna with metallic-plated surface. In *2019 International Conference on Microwave and Millimeter Wave Technology (ICMMT)* (pp. 1-3). IEEE.

[10] Liang, M., Ng, W. R., Chang, K., Gbele, K., Gehm, M. E., & Xin, H. (2014). A 3-D Luneburg lens antenna fabricated by polymer jetting rapid prototyping. *IEEE Transactions on Antennas and Propagation*, *62*(4), 1799-1807.

[11] Ferrando-Rocher, M., Herranz-Herruzo, J. I., Valero-Nogueira, A., & Bernardo-Clemente, B. (2021). Selective laser sintering manufacturing as a low cost alternative for flat-panel antennas in millimeter-wave bands. *IEEE Access*, *9*, 45721-45729.

[12] Benge, M. D., Huck, R. C., & Sigmarsson, H. H. (2014, July). X-band performance of three-dimensional, selectively laser sintered waveguides. In *2014 IEEE Antennas and Propagation Society International Symposium (APSURSI)* (pp. 13-14). IEEE.

[13] Rahmat-Samii, Y., & Haupt, R. (2015). Reflector antenna developments: a perspective on the past, present and future. *IEEE Antennas and Propagation Magazine*, *57*(2), 85-95.

[14] Volakis, J. L. (2007). *Antenna engineering handbook*. McGraw-Hill Education.

[15] Haupt, R. L., & Rahmat-Samii, Y. (2015). Antenna array developments: A perspective on the past, present and future. *IEEE Antennas and Propagation Magazine*, *57*(1), 86-96.

[16] Fleming, J. A. (1919). *The principles of electric wave telegraphy and telephony*. Longmans, Green.

[17] Marconi, G. (1906). On methods whereby the radiation of electric waves may be mainly confined to certain directions, and whereby the receptivity of a receiver may be restricted to electric waves emanating from certain directions. *Proceedings of the Royal Society of London. Series A, Containing Papers of a Mathematical and Physical Character*, *77*(518), 413-421.

[18] Braun, K. F. (1909). Electrical oscillations and wireless telegraphy. *Nobel Lecture, December*, *11*(1909), 226-245.

[19] Adcock, F. (1919). Improvement in means for determining the direction of a distant source of electromagnetic radiation. *British patent*, *130490*.

[20] Deschamps, G. A. (1953). Microstrip microwave antennas. In *Proceedings of the Third Symposium on the USAF Antenna Research and Development Program, Oct* (pp. 18-22).

[21] Huang, J., & Encinar, J. A. (2007). *Reflectarray antennas*. John Wiley & Sons.

[22] Berry, D., Malech, R., & Kennedy, W. (1963). The reflectarray antenna. *IEEE Transactions on Antennas and Propagation*, *11*(6), 645-651.

[23] Phelan, H. R. (1977). Spiraphase reflectarray for multitarget radar. *Microwave Journal*, *20*, 67.

[24] Mailloux, R. J. (2017). *Phased array antenna handbook*. Artech house.

[25] Skolnik, M. I. (2008). *Radar handbook*. McGraw-Hill Education.

[26] Nayeri, P., Yang, F., & Elsherbeni, A. Z. (2018). Reflectarray antennas: theory, designs, and applications.

[27] Pozar, D. M., Targonski, S. D., & Pokuls, R. (1999). A shaped-beam microstrip patch reflectarray. *IEEE Transactions on Antennas and Propagation*, *47*(7), 1167-1173.

[28] Encinar, J. A., & Zornoza, J. A. (2004). Three-layer printed reflectarrays for contoured beam space applications. *IEEE Transactions on Antennas and Propagation*, *52*(5), 1138-1148.

[29] Nayeri, P., Yang, F., & Elsherbeni, A. Z. (2011). Design and experiment of a single-feed quad-beam reflectarray antenna. *IEEE transactions on antennas and propagation*, *60*(2), 1166-1171.

[30] Abdelrahman, A. H., Yang, F., Elsherbeni, A. Z., & Nayeri, P. (2017). Analysis and design of transmitarray antennas. *Synthesis Lectures on Antennas*, *6*(1), 1-175.

[31] Malagisi, C. S. (1978). Microstrip disc element reflect array. In *EASCON'78; Electronics and Aerospace Systems Convention* (pp. 186-192).

[32] Chang, D. C., & Huang, M. C. (1995). Multiple-polarization microstrip reflectarray antenna with high efficiency and low cross-polarization. *IEEE Transactions on Antennas and Propagation*, *43*(8), 829-834.

[33] Javor, R. D., Wu, X. D., & Chang, K. (1995). Design and performance of a microstrip reflectarray antenna. *IEEE transactions on antennas and propagation*, *43*(9), 932-939.

[34] Chen, K. C., Tzuang, C. K., & Huang, J. (2001, July). A higher-order microstrip reflectarray at Ka-band. In *IEEE Antennas and Propagation Society International Symposium. 2001 Digest. Held in conjunction with: USNC/URSI National Radio Science Meeting (Cat. No. 01CH37229)* (Vol. 3, pp. 566-569). IEEE.

[35] Bialkowski, M. E., & Song, H. J. (2002). Investigations into a power-combining structure using a reflectarray of dual-feed aperture-coupled microstrip patch antennas. *IEEE Transactions on Antennas and Propagation*, *50*(6), 841-849.

[36] Carrasco, E., Barba, M., & Encinar, J. A. (2007). Reflectarray element based on aperture-coupled patches with slots and lines of variable length. *IEEE Transactions on Antennas and Propagation*, *55*(3), 820-825.

[37] Gonzalez, D. G., Pollon, G. E., & Walker, J. F. (1990). *U.S. Patent No. 4,905,014*. Washington, DC: U.S. Patent and Trademark Office.

[38] Pozar, D. M., & Metzler, T. A. (1993). Analysis of a reflectarray antenna using microstrip patches of variable size. *Electronics Letters*, *29*(8), 657-658.

[39] Encinar, J. A. (2001). Design of two-layer printed reflectarrays using patches of variable size. *IEEE Transactions on Antennas and Propagation*, *49*(10), 1403-1410.

[40] Encinar, J. A., & Zornoza, J. A. (2003). Broadband design of three-layer printed reflectarrays. *IEEE Transactions on Antennas and Propagation*, *51*(7), 1662-1664.

[41] Vosoogh, A., Keyghobad, K., Khaleghi, A., & Mansouri, S. (2014). A high-efficiency Ku-band reflectarray antenna using single-layer multiresonance elements. *IEEE Antennas and Wireless Propagation Letters*, *13*, 891-894.

[42] Mohammadirad, M., Komjani, N., Chaharmir, M. R., Shaker, J., & Sebak, A. R. (2013). Phase error analysis of the effect of feed movement on bandwidth performance of a broadband X-Ku band reflectarray. *International Journal of RF and Microwave Computer-Aided Engineering*, *23*(5), 517-526.

[43] Milon, M. A., Gillard, R., & Legay, H. (2007, April). Rigorous analysis of the reflectarray radiating elements: Characterisation of the specular reflection effect and the mutual coupling effect. In *29th ESA Antenna Workshop on Multiple Beams and Reconfigurable Antennas*.

[44] J. Huang and R. J. Pogorzelski, "A Kaband microstrip reflectarray with variable rotation angles," IEEE Trans. Antennas and Propagation, Vol. 46, No. 5, pp. 650–656, May, 1998.

[45] An, W., Xu, S., & Yang, F. (2014). A metal-only reflectarray antenna using slot-type elements. *IEEE Antennas and Wireless Propagation Letters*, *13*, 1553-1556.

[46] Henderson, K. Q., & Ghalichechian, N. (2020). Circular-polarized metal-only reflectarray with multi-slot elements. *IEEE Transactions on Antennas and Propagation*, *68*(9), 6695-6703.

[47] Antonov, Y. G., Sugak, M. I., Ballandovich, S. V., Kostikov, G. A., & Liubina, L. M. (2020, March). Design of wideband reflectarray antennas. In *2020 14th European Conference on Antennas and Propagation (EuCAP)* (pp. 1-5). IEEE.

[48] Mazingue, G., Mangenot, L., Romier, M., & Capet, N. (2022, March). Full-metal X-band Reflectarray for Small Satellite Constellations. In *2022 16th European Conference on Antennas and Propagation (EuCAP)* (pp. 1-3). IEEE.

[49] Cho, Y. H., Byun, W. J., & Song, M. S. (2010). Metallic-rectangular-grooves based 2D reflectarray antenna excited by an open-ended parallel-plate waveguide. *IEEE transactions on antennas and propagation*, *58*(5), 1788-1792.

[50] Wang, D., Gillard, R., & Loison, R. (2015, April). A 60GHz passive repeater array with endfire radiation based on metal groove unit-cells. In *2015 9th European Conference on Antennas and Propagation (EuCAP)* (pp. 1-4). IEEE.

[51] Cho, Y. H., Byun, W. J., & Song, M. S. (2011). High gain metal-only reflectarray antenna composed of multiple rectangular grooves. *IEEE Transactions on Antennas and Propagation*, *59*(12), 4559-4568.

[52] Mei, P., Zhang, S., & Pedersen, G. F. (2020). A low-cost, high-efficiency and full-metal reflectarray antenna with mechanically 2-D beam-steerable capabilities for 5G applications. *IEEE Transactions on Antennas and Propagation*, *68*(10), 6997-7006.

[53] Zhao, X., Bi, S., Zhang, Q., Sun, Y., Zhang, J., & Yuan, C. (2022). An All-Metal, Circularly Polarized Reflectarray Antenna for High-Power Microwave Applications. *IEEE Transactions on Plasma Science*, *50*(10), 3525-3528.

[54] Bi, S., Xu, L., Cheng, X., Sun, Y., Zhang, Q., & Yuan, C. (2022). An All-Metal, Simple-Structured Reflectarray Antenna with 2-D Beam-Steerable Capability. *IEEE Antennas and Wireless Propagation Letters*, *22*(1), 129-133.

[55] Zhu, J., Liao, S., Li, S., & Xue, Q. (2022). Additively Manufactured Metal-Only Millimeter-Wave Dual Circularly Polarized Reflectarray Antenna with Independent Control of Polarizations. *IEEE Transactions on Antennas and Propagation*, *70*(10), 9918-9923.

[56] Palomares-Caballero, A., Molero Jiménez, C., Padilla, P., García-Vigueras, M., & Gillard, R. (2023). Wideband 3-D-Printed Metal-only Reflectarray for Controlling Orthogonal Linear Polarizations.

[57] Wu, G. B., Zeng, Y. S., Chan, K. F., Chen, B. J., Qu, S. W., & Chan, C. H. (2019). High-gain filtering reflectarray antenna for millimeter-wave applications. *IEEE Transactions on Antennas and Propagation*, *68*(2), 805-812.

[58] Chou, H. T., Lin, C. Y., & Wu, M. H. (2015). A high efficient reflectarray antenna consisted of periodic all-metallic elements for the Ku-band DTV applications. *IEEE Antennas and Wireless Propagation Letters*, *14*, 1542-1545.

[59] Deng, R., Yang, F., Xu, S., & Li, M. (2015). A 100-GHz metal-only reflectarray for high-gain antenna applications. *IEEE Antennas and Wireless Propagation Letters*, *15*, 178-181.

[60] Lee, W., & Yoon, Y. J. (2016). A broadband dual-metallic-reflectarray antenna for millimeter-wave applications. *IEEE antennas and wireless propagation letters*, *16*, 856-859.

[61] Chou, H. T., Chen, Y. J., & Ho, H. K. (2018). An all-metallic reflectarray and its element design: Exploring the radiation characteristics of antennas for directional beam applications. *IEEE Antennas and Propagation Magazine*, *60*(5), 41-51.

[62] Chou, H. T., & Liu, J. W. (2018). Synthesis and characteristic evaluation of convex metallic reflectarray antennas to radiate relatively orthogonal multibeams. *IEEE Transactions on Antennas and Propagation*, *66*(8), 4008-4016.

[63] Zhu, J., Liao, S., & Xue, Q. (2022). 3-D Printed Millimeter-Wave Metal-Only Dual-Band Circularly Polarized Reflectarray. *IEEE Transactions on Antennas and Propagation*, *70*(10), 9357-9364.

[64] Liu, S. L., Lin, X. Q., Yan, Y. H., & Fan, Y. L. (2021). Generation of a high-gain bidirectional transmit–reflect-array antenna with asymmetric beams using sparse-array method. *IEEE Transactions on Antennas and Propagation*, *69*(9), 6087-6092.

[65] Liu X, Yan Z, Wang E, et al. Dual-Band Orthogonally-Polarized Dual-Beam Reflect-Transmit-Array with a Linearly Polarized Feeder. IEEE Transactions on Antennas and Propagation, 2022.

[66] Li X, Huang Q, Yang L, et al. Dual-band wideband reflect-transmit-array with different polarizations using three-layer elements. IEEE Antennas and Wireless Propagation Letters, 2021, 20(7): 1317-1321.

[67] Yang W, Chen K, Feng Y. Multifunctional Metasurface for Broadband Reflect-Transmit-Array Antenna at 5G Millimeter-Wave Band. 16th European Conference on Antennas and Propagation (EuCAP). IEEE, 2022: 1-5.

[68] Feng J, Yan Z, Yang S, et al. Reflect-Transmit-Array Antenna With Independent Dual-Circularly Polarized Beam Control. IEEE Antennas and Wireless Propagation Letters, 2022.

[69] Song W, Xue Q, Cai Y, et al. A Single-Layer Reflect-Transmit-Array Antenna With Polarization-Dependent Operation. IEEE Access, 2021, 9: 167928-167935.

[70] Liu S, Chen Q. A wideband, multifunctional reflect-transmit-array antenna with polarization-dependent operation. IEEE Transactions on Antennas and Propagation, 2020, 69(3): 1383-1392.

[71] Yang, F., Deng, R., Xu, S., & Li, M. (2018). Design and experiment of a near-zero-thickness high-gain transmit-reflect-array antenna using anisotropic metasurface. *IEEE transactions on antennas and propagation*, *66*(6), 2853-2861.

[72] https://www.hubs.com/3d-printing/

[73] Noorani, R. (2017). 3D printing: technology, applications, and selection. CRC Press.

[74] Yang, L., Hsu, K., Baughman, B., Godfrey, D., Medina, F., Menon, M., & Wiener, S. (2017). Additive manufacturing of metals: the technology, materials, design and production (pp. 45-61). Cham: Springer.

[75] Gao, W., Zhang, Y., Ramanujan, D., Ramani, K., Chen, Y., Williams, C. B., ... & Zavattieri, P. D. (2015). The status, challenges, and future of additive manufacturing in engineering. *Computer-Aided Design*, *69*, 65-89.

[76] Gunasekaran, K. N., Aravinth, V., Kumaran, C. M., Madhankumar, K., & Kumar, S. P. (2021). Investigation of mechanical properties of PLA printed materials under varying infill density. *Materials Today: Proceedings*, *45*, 1849-1856.

[77] Nassar, I. T., Tsang, H., Church, K., & Weller, T. M. (2014, January). A high efficiency, electrically-small, 3-D machined-substrate antenna fabricated with fused deposition modeling and 3-D printing. In *2014 IEEE Radio and Wireless Symposium (RWS)* (pp. 67-69). IEEE.

[78] Fawaz, M., Jun, S., Oakey, W. B., Mao, C., Elibiary, A., Sanz-Izquierdo, B., ... & McClelland, A. (2018). 3D printed patch Antenna for millimeter wave 5G wearable applications.

[79] Castro, J., Rojas-Nastrucci, E. A., Ross, A., Weller, T. M., & Wang, J. (2017). Fabrication, modeling, and application of ceramic-thermoplastic composites for fused deposition modeling of microwave components. *IEEE Transactions on Microwave Theory and Techniques*, *65*(6), 2073-2084.

[80] Castro, J., Rojas, E., Ross, A., Weller, T., & Wang, J. (2016, May). High-k and low-loss thermoplastic composites for Fused Deposition Modeling and their application to 3D-printed Ku-band antennas. In *2016 IEEE MTT-S International Microwave Symposium (IMS)* (pp. 1-4). IEEE.

[81] Aksimsek, S., Ozek, E. A., & Ozpinar, H. (2021). Laser ablation cutting-based metal patterning technique enabling 3d-printed broadband antennas for sub-6 ghz wireless communications applications. *IEEE Transactions on Components, Packaging and Manufacturing Technology*, *11*(9), 1506-1513.

[82] Kacar, M., Wang, J., Mumcu, G., Perkowski, C., Church, K., Wu, B. I., & Weller, T. (2019, July). Phased array antenna element with embedded cavity and MMIC using direct digital manufacturing. In *2019 IEEE International Symposium on Antennas and Propagation and USNC-URSI Radio Science Meeting* (pp. 81-82). IEEE.

[83] Spence, T. G., Ford, A. L., & Roberts, C. C. (2020, July). Prototyping an S-Band Conformal Line Array Antenna on a Partial Wing Surface. In *2020 IEEE International Symposium on Antennas and Propagation and North American Radio Science Meeting* (pp. 1409-1410). IEEE.

[84] Yao, H., Fang, L., & Henderson, R. (2018, January). Evaluating conductive paint performance on 3-D printed horn antennas. In *2018 IEEE Radio and Wireless Symposium (RWS)* (pp. 191-193). IEEE.

[85] Bose, S., Ke, D., Sahasrabudhe, H., & Bandyopadhyay, A. (2018). Additive manufacturing of biomaterials. *Progress in materials science*, *93*, 45-111.

[86] Silva, J. S., Garcia-Vigueras, M., Debogović, T., Costa, J. R., Fernandes, C. A., & Mosig, J. R. (2017). Stereolithography-based antennas for satellite communications in Ka-band. *Proceedings of the IEEE*, *105*(4), 655-667.

[87] Wang, X., Jiang, M., Zhou, Z., Gou, J., & Hui, D. (2017). 3D printing of polymer matrix composites: A review and prospective. *Composites Part B: Engineering*, *110*, 442-458.

[88] Menéndez, L. G., Kim, O. S., Persson, F., Nielsen, M., & Breinbjerg, O. (2015, April). 3D printed 20/30-GHz dual-band offset stepped-reflector antenna. In *2015 9th European Conference on Antennas and Propagation (EuCAP)* (pp. 1-2). IEEE.

[89] Kong, M., & Yoon, I. J. (2017, July). A 3D printed low profile magnetic dipole antenna. In *2017 IEEE International Symposium on Antennas and Propagation & USNC/URSI National Radio Science Meeting* (pp. 2547-2548). IEEE.

[90] Ferrando-Rocher, M., Herranz-Herruzo, J. I., Valero-Nogueira, A., & Bernardo-Clemente, B. (2021). Selective laser sintering manufacturing as a low cost alternative for flat-panel antennas in millimeter-wave bands. *IEEE Access*, *9*, 45721-45729.

[91] Benge, M. D., Huck, R. C., & Sigmarsson, H. H. (2014, July). X-band performance of three-dimensional, selectively laser sintered waveguides. In *2014 IEEE Antennas and Propagation Society International Symposium (APSURSI)* (pp. 13-14). IEEE.

[92] DebRoy, T., Wei, H. L., Zuback, J. S., Mukherjee, T., Elmer, J. W., Milewski, J. O., ... & Zhang, W. (2018). Additive manufacturing of metallic components–process, structure and properties. *Progress in Materials Science*, *92*, 112-224.

[93] DebRoy, T., Mukherjee, T., Milewski, J. O., Elmer, J. W., Ribic, B., Blecher, J. J., & Zhang, W. (2019). Scientific, technological and economic issues in metal printing and their solutions. *Nature materials*, *18*(10), 1026-1032.

[94] Addamo, G., Peverini, O. A., Paonessa, F., Virone, G., Calignano, F., & Manfredi, D. (2019, March). Additive manufacturing of K/Ka/Q/V-band feed-horns. In *2019 13th European Conference on Antennas and Propagation (EuCAP)* (pp. 1-4). IEEE.

[95] Beck, C., Gabsteiger, J., Scheitler, C., Dietz, M., Hagelauer, A., & Weigel, R. (2020, October). An additive manufactured k-band waveguide coupler and k-band antennas in slm-technology. In *2020 23rd International Microwave and Radar Conference (MIKON)* (pp. 274-277). IEEE.

[96] Peverini, O. A., Lumia, M., Calignano, F., Manfredi, D., Addamo, G., Lorusso, M., ... & Tascone, R. (2017, March). Manufacturing of waveguide components for SatCom through selective laser melting. In *2017 11th European Conference on Antennas and Propagation (EUCAP)* (pp. 563-566). IEEE.

[97] Zhang, B., Zhan, Z., Cao, Y., Gulan, H., Linner, P., Sun, J., ... & Zirath, H. (2016). Metallic 3-D printed antennas for millimeter-and submillimeter wave applications. *IEEE Transactions on Terahertz Science and Technology*, *6*(4), 592-600.

[98] Zhang, B., Wu, L., Zhou, Y., Yang, Y., Zhu, H., Cheng, F., ... & Huang, K. (2019). A K-band 3-D printed focal-shifted two-dimensional beam-scanning lens antenna with nonuniform feed. *IEEE Antennas and Wireless Propagation Letters*, *18*(12), 2721-2725.

[99] Zhang, B., & Zirath, H. (2016). A metallic 3-D printed E-band radio front end. *IEEE Microwave and Wireless Components Letters*, *26*(5), 331-333.

[100] Guan-Long, H., Shi-Gang, Z., Tan-Huat, C., & Tat-Soon, Y. (2015, May). 3-D metal-direct-printed wideband and high-efficiency waveguide-fed antenna array. In *2015 IEEE MTT-S International Microwave Symposium* (pp. 1-4). IEEE.

[101] Shamvedi, D., Danilenkoff, C., Karam, S., O'Leary, P., & Raghavendra, R. (2017, November). 3D printed periodic structures in a horn antenna for side-lobe reduction using direct metal laser sintering. In *Loughborough Antennas & Propagation Conference (LAPC 2017)* (pp. 1-4). IET.

[102] Huang, G. L., & Yuan, T. (2017, October). Application of 3-D metal printing to microwave components and antennas. In *2017 Sixth Asia-Pacific Conference on Antennas and Propagation (APCAP)* (pp. 1-3). IEEE.

[103] Chio, T. H., Huang, G. L., & Zhou, S. G. (2016). Application of direct metal laser sintering to waveguide-based passive microwave components, antennas, and antenna arrays. *Proceedings of the IEEE*, *105*(4), 632-644.

[104] Guennou-Martin, A., Quéré, Y., Rius, E., Fourtinon, L., Person, C., Lesueur, G., & Merlet, T. (2016, October). Design and manufacturing of a 3-D conformal slotted waveguide antenna array in Ku-band based on direct metal laser sintering. In *2016 IEEE Conference on Antenna Measurements & Applications (CAMA)* (pp. 1-4). IEEE.

[105] Sanchez-Olivares, P., Garcia-Marin, E., & Masa-Campos, J. L. (2022). Direct Metal Laser Sintering Conformal Waveguide Array Antenna for Millimeter-Wave 5G Communications. *IEEE Antennas and Wireless Propagation Letters*, *21*(5), 1012-1016.

[106] Huang, G. L., Zhou, S. G., Chio, T. H., & Yeo, T. S. (2015). Fabrication of a high-efficiency waveguide antenna array via direct metal laser sintering. *IEEE Antennas and Wireless Propagation Letters*, *15*, 622-625.

[107] Zhang, B., Zhan, Z., Cao, Y., Gulan, H., Linner, P., Sun, J., ... & Zirath, H. (2016). Metallic 3-D printed antennas for millimeter-and submillimeter wave applications. *IEEE Transactions on Terahertz Science and Technology*, *6*(4), 592-600.

[108] Rojas-Nastrucci, E. A., Nussbaum, J., Weller, T. M., & Crane, N. B. (2016, December). Metallic 3D printed Ka-band pyramidal horn using binder jetting. In *2016 IEEE MTT-S Latin America Microwave Conference (LAMC)* (pp. 1-3). IEEE.

[109] Huang, G. L., Zhou, S. G., & Yuan, T. (2017). Development of a wideband and high-efficiency waveguide-based compact antenna radiator with binder-jetting technique. *IEEE transactions on components, packaging and manufacturing technology*, *7*(2), 254-260.

[110] Rojas-Nastrucci, E. A., Nussbaum, J. T., Crane, N. B., & Weller, T. M. (2017). Ka-band characterization of binder jetting for 3-D printing of metallic rectangular waveguide circuits and antennas. *IEEE Transactions on Microwave Theory and Techniques*, *65*(9), 3099-3108.

[111] Nayeri, P., Liang, M., Sabory-Garcı, R. A., Tuo, M., Yang, F., Gehm, M., ... & Elsherbeni, A. Z. (2014). 3D printed dielectric reflectarrays: Low-cost high-gain antennas at sub-millimeter waves. *IEEE Transactions on Antennas and Propagation*, *62*(4), 2000-2008.

[112] Da Wu, M., Li, B., Zhou, Y., Liu, Y., Wei, F., & Lv, X. (2018). Design and measurement of a 220 GHz wideband 3-D printed dielectric reflectarray. *IEEE Antennas and Wireless Propagation Letters*, *17*(11), 2094-2098.

[113] Li, B., Mei, C. Y., Zhou, Y., & Lv, X. (2020). A 3-D-printed wideband circularly polarized dielectric reflectarray of cross-shaped element. *IEEE Antennas and Wireless Propagation Letters*, *19*(10), 1734-1738.

[114] Mei, P., Zhang, S., & Pedersen, G. F. (2020). A wideband 3-D printed reflectarray antenna with mechanically reconfigurable polarization. *IEEE Antennas and Wireless Propagation Letters*, *19*(10), 1798-1802.

[115] Zhu, J., Yang, Y., Mcgloin, D., Liao, S., & Xue, Q. (2021). 3-D printed all-dielectric dual-band broadband reflectarray with a large frequency ratio. *IEEE Transactions on Antennas and Propagation*, *69*(10), 7035-7040.

[116] Thomson, J. J. (1893). *Notes on recent researches in electricity and magnetism: intended as a sequel to Professor Clerk-Maxwell's Treatise on electricity and magnetism*. Cambridge University Press.

[117] Rayleigh, L. (1897). XVIII. On the passage of electric waves through tubes, or the vibrations of dielectric cylinders. *The London, Edinburgh, and Dublin Philosophical Magazine and Journal of Science*, *43*(261), 125-132.

[118] Sommerfeld A. Fortpflanzung elektrodynarnischer Wellen an einenzylindrischen Leiter[J]. Ann. d. Phys, 67: 223.

[119] Pozar, D. M. (2011). *Microwave engineering*. John wiley & sons.

[120] Hsu, S. H., Han, C., Huang, J., & Chang, K. (2007). An offset linear-array-fed Ku/Ka dual-band reflectarray for planet cloud/precipitation radar. *IEEE transactions on antennas and propagation*, *55*(11), 3114-3122.

[121] You, B. Q., Liu, Y. X., Zhou, J. H., & Chou, H. T. (2012). Numerical synthesis of dual-band reflectarray antenna for optimum near-field radiation. *IEEE Antennas and Wireless Propagation Letters*, *11*, 760-762.

[122] Zhao, J., Li, T., Cui, X., Zhao, X., Li, H., Hu, B., ... & Liu, Q. (2017). A low-mutual coupling dual-band dual-reflectarray antenna with the potentiality of arbitrary polarizations. *IEEE Antennas and Wireless Propagation Letters*, *16*, 3224-3227.

[123] Smith, T., Gothelf, U., Kim, O. S., & Breinbjerg, O. (2013). Design, manufacturing, and testing of a 20/30-GHz dual-band circularly polarized reflectarray antenna. *IEEE Antennas and Wireless Propagation Letters*, *12*, 1480-1483.

[124] Qu, S. W., Chen, Q. Y., Xia, M. Y., & Zhang, X. Y. (2013). Single-layer dual-band reflectarray with single linear polarization. *IEEE Transactions on antennas and Propagation*, *62*(1), 199-205.

[125] Hamzavi-Zarghani, Z., & Atlasbaf, Z. (2014). A new broadband single-layer dual-band reflectarray antenna in X-and Ku-bands. *IEEE Antennas and Wireless Propagation Letters*, *14*, 602-605.

[126] Deng R, Mao Y, Xu S, et al. A single-layer dual-band circularly polarized reflectarray with high aperture efficiency[J]. IEEE Transactions on Antennas and Propagation, 2015, 63(7): 3317-3320.

[127] Guo, L., Tan, P. K., & Chio, T. H. (2016). Single-layered broadband dual-band reflectarray with linear orthogonal polarizations. *IEEE Transactions on Antennas and Propagation*, *64*(9), 4064-4068.

[128] Deng, R., Xu, S., Yang, F., & Li, M. (2016). Single-layer dual-band reflectarray antennas with wide frequency ratios and high aperture efficiencies using phoenix elements. *IEEE Transactions on antennas and Propagation*, *65*(2), 612-622.

[129] Su, T., Yi, X., & Wu, B. (2019). X/Ku dual-band single-layer reflectarray antenna. *IEEE Antennas and Wireless Propagation Letters*, *18*(2), 338-342.

[130] Chen, Y., Chen, L., Wang, H., Gu, X. T., & Shi, X. W. (2013). Dual-band crossed-dipole reflectarray with dual-band frequency selective surface. *IEEE Antennas and Wireless Propagation Letters*, *12*, 1157-1160.

[131] Xu, P., Li, L., Li, R., & Liu, H. (2021). Dual-circularly polarized spin-decoupled reflectarray with FSS-back for independent operating at Ku-/Ka-bands. *IEEE Transactions on Antennas and Propagation*, *69*(10), 7041-7046.

[132] Deng, R., Yang, F., Xu, S., & Li, M. (2016). An FSS-backed 20/30-GHz dual-band circularly polarized reflectarray with suppressed mutual coupling and enhanced performance. *IEEE Transactions on Antennas and Propagation*, *65*(2), 926-931.

[133] Deng, R., Xu, S., Yang, F., & Li, M. (2017). Design of a low-cost single-layer X/Ku dual-band metal-only reflectarray antenna. *IEEE Antennas and Wireless Propagation Letters*, *16*, 2106-2109.

[134] Chou, H. T., Lertwiriyaprapa, T., Akkaraekthalin, P., & Torrungrueng, D. (2020). Flexible dual-band dual-beam radiation of reflector antennas by embedding resonant phase alignment elements for power refocusing. *IEEE Transactions on Antennas and Propagation*, *68*(6), 4259-4270.

[135] Mao, Y., Xu, S., Yang, F., & Elsherbeni, A. Z. (2015). A novel phase synthesis approach for wideband reflectarray design. *IEEE transactions on antennas and propagation*, *63*(9), 4189-4193.

Acknowledgement

I would like to express my deepest gratitude to my esteemed supervisors, Raphaël Gillard, Tony Makdissy, and María García Vigueras, whose invaluable guidance has been instrumental in shaping the outcome of my academic endeavors. Their unwavering support, patience, and insightful inputs have greatly enriched my research work and scholarly growth.

I extend my sincere appreciation to the esteemed reviewers of my thesis, Régis GUINVARC'H, Xavier BEGAUD, and Paola PIRINOLI, for their valuable time, expertise, and critical evaluation of my work. Their meticulous examination, thoughtful comments, and constructive suggestions have significantly contributed to the refinement and overall improvement of my thesis.

I am deeply grateful to Sébastien Vaudreuil and Yassine el Ansary for their dedicated assistance and expertise in the intricate process of antenna fabrication. Their meticulous attention to detail, technical acumen, and collaborative spirit have played an integral role in the successful realization of my research objectives.

I would also like to express my profound appreciation to Jérôme SOL and Laurent Le Coq for their unwavering support and technical assistance during the extensive series of measurements conducted on the prototype. Their expertise, meticulousness, and willingness to share their knowledge have yielded substantial insights and favorable outcomes, enhancing the credibility and robustness of my research findings.

Finally, I wish to extend my heartfelt gratitude to my beloved family. Their unwavering belief in my abilities, constant encouragement, and unconditional love have been the cornerstone of my academic journey. Over the course of 23 years dedicated to attaining my doctoral degree, I have not only gained invaluable knowledge and skills in my field but also profound insights into life itself. I wholeheartedly embrace this thesis and the conferred degree as a stepping stone, marking the commencement of a promising future in both my professional pursuits and personal endeavors.

Appendix 1: Acronyms

RA: Reflectarray Antenna

SC: Simple Cell

SCOW: Simple Cell with Open-ended Waveguides

SCSW: Simple Cell with Short-ended Waveguides

PC: Phoenix Cell

PCOW: Phoenix Cell with Open-ended Waveguides

PCSW: Phoenix Cell with Short-ended Waveguides

TA: Transmitarray Antenna

MO: Metal-only

MOPC: Metal-only Phoenix Cell

MORA: Metal-only Reflectarray Antenna

TRA: Transmit-reflect-array

MOTRA: Metal-only Transmit-reflect-array

AM: Additive Manufacturing

SLM: Selective Laser Melting

FDM: Fused deposition modeling

SLA: Stereolithography

UV: Ultraviolet.

MJ: Material Jetting

SLS: Selective Laser Sintering

DMLS: Direct Metal Laser Sintering

PEC: Perfect Electric Conductor

PBC: Periodic Boundary Condition

RRA: Reflector reflectarray antenna

MORRA: Metal-only Reflector reflectarray antenna

CP: Circularly Polarization

LHCP: Left-hand Circular Polarization

RHCP: Right-hand Circular Polarization

COLLEGE MATHS, TELECOMS
DOCTORAL INFORMATIQUE, SIGNAL
BRETAGNE SYSTEMES, ELECTRONIQUE

INSA INSTITUT NATIONAL DES SCIENCES APPLIQUÉES RENNES

Titre : Antennes directives 3D entièrement métalliques et constituées d'arrangements quasi-périodiques de cellules Phénix de type guide d'onde

Mots clés : réseau réflecteur, cellule Phénix, gain élevé, structure quasi-périodique, fabrication additive métallique

Résumé : Un réseau réflecteur peut être considéré comme une combinaison entre antenne réflecteur et antenne réseau. Il présente les avantages d'un gain élevé, d'un faible encombrement, d'un coût réduit et d'une fabrication facile. De plus, il est possible de manipuler la forme et la direction du faisceau principal en contrôlant la géométrie des cellules unitaires constituant le réseau. Cette opération s'effectue beaucoup plus simplement que pour un réseau à rayonnement direct où elle nécessite de concevoir un répartiteur de puissance complexe. Parmi les solutions possibles, la cellule Phénix est une topologie de cellule de réseau réflecteur avec un fort potentiel. Parce qu'elle permet de revenir à la géométrie initiale après un cycle complet de 360°, la cellule Phénix permet d'éviter les brusques variations de géométrie sur l'ouverture rayonnante. Cette thèse explore les possibilités offertes par la fabrication additive dans la conception d'antennes métalliques 3D réelles. Une cellule Phénix de type guide d'ondes 3D a été proposée, analysée et modélisée à l'aide d'un circuit équivalent. Différentes antennes à gain élevé fabriquées à partir de cellules Phénix 3D ont été conçues, simulées et analysées, dont deux ont été fabriquées pour démontrer leurs performances. Une bonne concordance entre les simulations et les mesures a été obtenue.

Title : 3D Printed Metal-only High-gain Antennas made of Quasi-periodic Arrangements of Waveguide-type Phoenix Cells..... .....

Keywords : reflectarray, phoenix cell, high gain, quasi-periodic structure, full-metal additive-manufacturing

Abstract : Reflectarray antenna can be seen as a combination of reflector antenna and array antenna. It has the advantages of high gain, low profile, low cost and easy manufacturing. Also, it is able to manipulate the main beam by controlling the geometrical pattern of the unit, including its shape and direction. In contrast to phased array antennas, such manipulation of the radiation is obtained in reflectarray without increasing the complexity of the array beamforming network. Among possible solutions, the phoenix cell is a topology of reflectarray cell with high potential. The geometric variation over the reflectarray aperture is smoothed out owing to the rebirth ability of the phoenix cell. This thesis explores the possibilities offered by additive manufacturing in designing actual 3D metal-only antennas. A 3D waveguide-type phoenix cell has been proposed, analyzed, and modeled using an equivalent circuit. Different high-gain antennas made of 3D phoenix cells have been designed, simulated, and analyzed, two of which have been fabricated to further demonstrate their performance. Good agreement between simulations and measurements has been achieved.